CHARACTERIZATION OF MICROSTRUCTURE AND SLIP BEHAVIOR OF NIOBIUM USED TO FABRICATE ACCELERATOR CAVITIES

By

Di Kang

A DISSERTATION

Submitted to
Michigan State University
in partial fulfillment of the requirements
for the degree of

Materials Science and Engineering—Doctor of Philosophy

2019

ABSTRACT

CHARACTERIZATION OF MICROSTRUCTURE AND SLIP BEHAVIOR OF NIOBIUM USED TO FABRICATE ACCELERATOR CAVITIES

By

Di Kang

Large grain niobium (Nb) has been used to fabricate superconducting radiofrequency (SRF) cavities for particle accelerators over the past couple of decades, as a promising alternative to the well-established but expensive approach of using rolled polycrystalline sheet Nb. While the large grain approach to make cavities provides a reduced cost process, the performance is comparable to fine grain cavities. Cavities fabricated from both approaches exhibit variability in performance, a costly yet common issue. Understanding the origin of the variability will enable informed design decisions to be made, which necessitates studying the underlying physical metallurgy of Nb.

One source of the variability is the starting material for fabricating cavities. Large and fine grain Nb was characterized to determine if ingots have commonalities and examine how different ingots result in heteogeneity in the microstructure of rolled sheets. Eight large grain ingots were analyzed using electron backscatter diffraction (EBSD) and Laue X-ray diffraction. The lack of similarity in crystal orientations and grain boundary misorientations of the ingots suggests random orientation nucleation/growth, which gives rise to variability in subsequent forming and processing.

Fine grain rolled Nb sheets to be used for the Facility for Rare Isotope Beams (FRIB) were evaluated using tensile tests and EBSD to ensure the acceptability of the material. With these data, performance variability in future FRIB cavities can be traced to the initial microstructure. While the mechanical properties and texture vary significantly from one batch to another, correlations between texture, microstructure, and mechanical properties are generally weak.

A multi-crystal rolling experiment was devised to investigate the connection between ingot and sheet microstructure. Wedged pieces from an ingot were rolled flat, from which samples with different amounts of cold work were extracted and analyzed with EBSD before and after annealing. Bands with orientations different from the parent grains developed due to rolling, and small grains nucleated from the bands upon annealing. The banding and recrystallization patterns approximate those observed in sheets subjected to more rolling passes, which implies that the microstructural heterogeneity in the rolled sheets originated from the randomly oriented large grains in the ingots.

Hot spots are regions in a cavity with a localized temperature increase that may destroy the superconducting state. To identify sources of hot spots and performance variability in large grain cavities, EBSD was used to examine the cross-sections at the equator and iris of a cavity half-cell. The results suggest that cavity surface damage (locations with higher dislocation content reflected by greater orientation gradients) associated with the friction from deep drawing depends on crystal orientation, and the magnitude of such damage is different at the iris and equator. The orientation gradients at the equator were not uniformly removed after annealing at 1000 °C/2hr. This explains why the equator is more susceptible to hot spots in additional to it having a higher magnetic field and suggests that annealing at higher temperatures or longer times may be necessary.

Modeling microstructural evolution during cavity processing can help predict performance variability and reduce the number of trial and error experiments. A fundamental understanding of deformation mechanisms of Nb is needed to establish such a model. For this purpose, two sets of single crystals with the same orientations were extracted from an ingot slice, and one set was heat treated to alter the initial condition. Both sets of samples were deformed to about 40% engineering strain in uniaxial tension. The differences in flow stress, crystal rotation, and active slip systems between the two sets are likely due to the removal of preexisting dislocations caused by the anneal.

ACKNOWLEDGMENTS

This work was supported by the U.S. Department of Energy, Office of High Energy Physics, through Grant No. DE-S0004222.

I would like to express my sincere appreciation for my advisor Dr. Thomas Bieler for his mentorship, support, encouragement, understanding, and patience throughout the years. It would have been impossible for me to be where I am without him. I have gone through several struggles, and he has always given me a hand. His natural curiosity, enthusiasm for science, and approach to life have influenced me greatly.

I would also like to express my deep gratitude for my guidance committee members Dr. Martin Crimp, Dr. Carl Boehlert, and Dr. Neil Wright for their devotion, insights into my research, and constant feedback on how I can improve.

I would also like to thank my collaborators, Chris Compton at the Facility for Rare Isotope Beams and Gigi Ciovati at Jefferson Lab, for their tremendous assistance with my experiments as well as numerous valuable discussions.

I would also like to thank my fellow graduate students for their friendship, inspiration, and help over the past years.

Finally, I would like to thank my parents for always believing in me and providing me with unconditional support during tough times.

TABLE OF CONTENTS

LIST	OF TABLES	vii
LIST	OF FIGURES	viii
I.	INTRODUCTION	1
II.	LITERATURE REVIEW	4
a.	Accelerator Technology and Niobium	4
b.	Progress in Improving Cavity Performance	6
c.	Dislocations and Cavity Performance	8
d.	Ingot Production and Initial Grain Orientation	13
e.	Large Grain Approach to Forming Cavities	20
f.	Microstructure of Fine Grain Nb Sheets	22
g.	Cavity Fabrication and Surface Studies	
h.	Active Slip Systems in Nb	
i.	Observation of Dislocations in Nb	42
j.	Evaluation of GNDs using cross-correlation EBSD	45
k.	Opportunities for Research	47
III.	MATERIALS AND METHODS	50
a.	Large Grain Nb Ingots Characterized by EBSD and Laue Camera	50
b.	Fine Grain Nb Sheets Characterized by EBSD and Mechanical Tests	57
c.	Rolled Multi-Crystal Nb Samples Characterized by EBSD and Laue Camera.	59
d.	Nb Cavity Samples Characterized by EBSD	
e.	Nb Single Crystals Characterized by <i>in-Situ</i> Tensile Tests	65
IV.	RESULTS	70
a.	Crystal Orientation of Large Grain Nb Ingots	70
b.	Texture and Stress-Strain Behavior of Fine Grain Nb Sheets	
c.	Microstructure of Rolled Nb Samples	107
d.	Evolution of Microstructure in Nb Cavity Samples	112
e.	Slip and Crystal Rotation in Heat-Treated Nb Single Crystals	119
V.	DISCUSSION	137
a.	Preferred Orientation and Orientation Stability in Large Grain Nb Ingots	137
b.	Texture/Property Relationship in Fine Grain Nb Sheets	
c.	Connection between Ingot and Sheet Microstructure	
d.	Effects of Processing History on Cavity Surface Damage	
e.	Effects of Heat Treatment on Preferred Slip Systems in Nb	
VI.	CONCLUSIONS	162

VII.	RECOMMENDATIONS FOR FUTURE WORK	165
APPE	NDIX	167
BIBLI	IOGRAPHY	188

LIST OF TABLES

Table 1: Information of ingots and their short names used in this work, ranked by ingot size 52
Table 2: Orientations in Bunge Euler angles (°) for the Ningxia ingot slice. The numbering is the same as Figure 24
Table 3: Orientations in Bunge Euler angles (°) for the CBMM-NSCL ingot slice. The numbering is the same as Figure 24. There are varying differences between EBSD and Laue measurements of the same grains (discussed later)
Table 4: Orientations in Bunge Euler angles (°) for the CBMM-H1 and CBMM-H2 ingot slices. The numbering is the same as Figure 25. The two slices are nearly identical in orientations 71
Table 5: Orientations in Bunge Euler angles (°) for the TD-1 and TD-2 ingot slices. The numbering is the same as Figure 25. There is a systematic difference only in ϕ 1 associated with mounting error
Table 6: Orientations in Bunge Euler angles (°) for the Heraeus ingot at locations shown in Figure 25. Orientation variation in grain 1 is small based upon five measurements
Table 7: Orientations in Bunge Euler angles (°) for the Niowave ingot at locations shown in Figure 26. Orientations do not vary much in the longitudinal direction of the ingot. After etching, the orientation of seven locations changed 1-2°, but the orientation gradients associated with the milling bands are still present.
Table 8: Orientation spread for grains with multiple Laue measurements, estimated using the average orientations (Figure 43) as the reference. The intragranular orientation variation is small compared to the Ningxia ingot (shown later).
Table 9: Summary of observed slip planes from slip trace analyses for as-received and heat-treated samples, with {112} planes in the first line, and {110} planes in the second line for each orientation. The heat-treated samples exhibited more {110} slip than the as-received samples. The numbers in parentheses indicate the Schmid factor rank (as illustrated in Figure 71) for a given slip system, and the first slip system whose Schmid factor rank is different between the two samples is indicated in the left column.
Table 10: Orientation evolution with deformation for the annealed samples T1 and V1. Numbers in red are the difference between the initial and final orientation, which shows that T1 has a greater crystal rotation than V1

LIST OF FIGURES

Figure 1: Example of a 7-cell cavity. Blue arrows on top indicate polarity changes of the electromagnetic fields within the cells [adapted from Figure I-1 in reference [16]]
Figure 2: Q_0 vs. E_{pk} measured on a 1.3 GHz single cell cavity before and after baking at 100 °C for 48 hours. The bake moved the Q-slope to higher accelerating fields and increased the Q value [Figure 1 (b) in reference [22]].
Figure 3: Local average misorientation (LAM) maps from "hot" (left) and "cold" (right) regions in a cavity. The green color corresponds to a misorientation of 2°, and blue is 0° [Figure 14 in reference [26]]
Figure 4: Local average misorientation (LAM) calculations using the 2nd nearest neighbor sampling area – for the point at the center, LAM averages the misorientations of all its neighboring points (connected by short white lines) within the kernel [Figure 3 in reference [126]]
Figure 5: Corresponding histograms for the LAM maps shown in Figure 3 [Figure 15 in reference [26]]
Figure 6: Thermal conductivity as a function of temperature for a bi-crystal sample. The original phonon peak (blue arrow) on grain 2 disappeared after 15% strain, but it was fully restored after a 1000 °C/2hr heat treatment [adapted from slide 5 in reference [32]]
Figure 7: Schematic of the electron beam melting equipment to produce and to purify Nb ingots [Figure 2 in reference [38]]
Figure 8: Ultrasonic tomography of a Nb ingot. No. 1 is near the bottom of the ingot, and No. 48 is near the top [Figure 3 in reference [44]].
Figure 9: Electron channeling contrast image of a sample from an as-received Nb ingot showing contrast arising from dislocations [Figure 8 in reference [24]]
Figure 10: Flow diagram of SRF cavity fabrication using fine grain or large grain Nb (courtesy of W.C. Heraeus, Germany) [adapted from Figure 6 in reference [37]]
Figure 11: Orientation maps of the full thickness of Nb tensile specimens from (a) Wah-Chang as-received ILC sheet (b) Wah-Chang as-received ILC sheet after annealing (c) Tokyo-Denkai as-received sheet [Figure 2 in reference [63]].
Figure 12: A half-cell (right) formed from a large grain ingot slice (left) by deep drawing, and a schematic of the process is shown in the middle [adapted from Figure 8 in reference [37]] 27

Figure 13: Representative inverse pole figures from EBSD measurements on different samples. The orientation spread is greatest after deformation and is least in the recrystallized condition [adapted from Figure 9 in reference [24]]
Figure 14: Dependence of achievable accelerating gradient on the thickness of material removed from surface, measured on a fine grain cavity [adapted from Figure 3 in reference [76]] 30
Figure 15: Change in local average misorientations (LAMs) on cavity samples due to baking. Ir each case, measurements were made on the same sample before and after baking in ultra-high vacuum [Figure 2 in reference [27]].
Figure 16: A schematic diagram showing a [111] bcc screw dislocation with its Burgers vector and line direction out of the page, and the effect of core relaxation on a slip trace: a) The core may relax on either three symmetric {112} planes (dashed lines) or three symmetric {110} planes (solid lines). Motion of the dislocation can leave a trace on a surface indicating the slip plane for: b {112} relaxation, the screw dislocation may frequently cross slip on two of the three {112} relaxation planes (each change in plane marked by a circle), while following a high resolved shear stress plane (fine dotted line). c) For {110} relaxation, the screw dislocation may frequently cross slip on two of the {110} planes, while following a high resolved shear stress plane [Figure II-13] in reference [16]]
Figure 17: Initial tensile axes for D&F and Ningxia samples on a stereographic projection section. The boundaries mark where the Schmid factors are equal between two {110} slip systems (solid lines), two {112} slip systems (dashed lines), a {110} and a {112} slip system (dotted lines). The boundary is colored green for the same slip direction, and red for intersecting slip directions. Slip systems whose Schmid factors are greatest in the area between the boundaries are labeled [Figure V-9 in reference [16]].
Figure 18: TEM micrographs of (a) dislocation cell structure in a Nb sample cold rolled to 50% (45,000× magnification) (b) dislocation networks in a Nb sample rolled to 98% and annealed a 900 °C/1h (44,000× magnification) [Figure 5 and Figure 9 in reference [110]]
Figure 19: (a) Electron channeling contrast (ECC) image of dislocations near an indent (b) GND density map of the same area generated from CC-EBSD showing similar dislocation distribution (c) Dislocation density map calculated by counting dislocations in the ECC image [Figure 3 in reference [119]]
Figure 20: Road map showing the interconnections of research activities outlined above. Letters a-e in parentheses correspond to the section headings in the next three chapters
Figure 21: Schematic of the EBSD configuration. The electron beam interacts with a sample that is tilted 70° from the beam axis. Red arrows indicate the coordinate systems used for the crystal orientation. Backscatter electrons form diffraction patterns on the EBSD camera, which are therefore processed by a computer equipped with data acquisition and analysis software. The electron beam trajectory is also controlled by the computer [adapted from Figure 1.3 in reference [124] and Figure II-15 in reference [16]]

Figure 22: Laue camera equipped with area detector, showing how an ingot slice was mounted to determine crystal orientations [Figure 3 in reference [122]]
Figure 23: A typical Laue pattern (left) and the indexing user interface (right) [Figure 4 in reference [122]]
Figure 24: Images of ingot slices characterized by EBSD. Dashed lines identify the location of faint grain boundaries. The numbers on the images of the ingots indicate IDs of the grains whose crystal orientation will be reported later. The scale bar is common to both images
Figure 25: Images of ingot slices characterized by Laue camera. The grid on the CBMM-NSCL slice illustrates how 57 measurements were systematically made with a step size of 1 inch. The TD-1 slice was measured similarly using a step size of 2 inches, yielding 19 data points (detailed in). For the Heraeus, CBMM-H1, and TD-1 slices, the numbers provide approximate locations of the orientation measurements (reported later). The scale bar is common to all images
Figure 26: Image of a slab cut along the longitudinal direction of an ingot (prepared by Niowave). The dimensions are 70 cm (W) \times 22 cm (H) \times 1 cm (T). Ten closely spaced Laue measurements (a-j) were made in addition to the numbered locations. Scan j was about half way between locations 2 and 27 [adapted from Figure 3 in reference [123]].
Figure 27: Layout of acceptance criteria list (ACL) samples extracted from (a) Tokyo-Denkai and (b) Ningxia sheets. The Tokyo-Denkai samples are oriented 45° with respect to the rolling direction, while the Ningxia samples are either perpendicular or parallel to the rolling direction. The dimensions are the same for each type of samples and are shown on the Tokyo-Denkai drawing All units are in inches except for the square samples in (a) [adapted from Figure 14 in reference [61]]
Figure 28: Schematic of a "bark" shaped sample S off the Niowave ingot used for the rolling experiment. The green dotted line indicates that the sample was cut in half part way through the rolling process due to developing a curved strip.
Figure 29: A flat piece ("A") about 1 mm thick rolled from the right half of sample S (Figure 28). End slice S1 was cut next to the top edge of the rolled piece, and its corresponding orientation map and the sense of rolling are shown on the right. The cross-sections of samples A2 and A6 were examined for the effects of rolling and annealing.
Figure 30: Locations of three samples extracted from a half-cell formed by JLab. The locations of grain boundaries (GB) and a neck are indicated in the blown-up images in Figure 31. Numbers provide approximate locations of EBSD scans on the equator and iris [adapted from Figure 2 in reference [126]]
Figure 31: Secondary electron images of the 6 areas examined by EBSD. Grain boundaries and the neck are marked in accordance with Figure 30. The numbering is also the same as Figure 30 adapted from Figure 4 in reference [126]

Figure 32: Layout of single crystal tensile samples extracted from the Ningxia ingot slice. The dimensions are shown on the left. The location of samples P1 and P3 are shown as examples of the labeling strategy [adapted from Figure III-3 in reference [16]]
Figure 33: Experimental setup of the <i>in-situ</i> tensile tests. Sample W is shown as an example. Left – tensile load frame mounted inside the MIRA3 SEM chamber, right – plan view of the sample [adapted from Figure 3.2 in reference [131]
Figure 34: Illustration of how orientation maps were generated using the TD-1 ingot slice. Red dots indicate approximate locations of the 19 measurements that are two inches apart, and each pixel in the 30x30 grid was assigned the measured orientation closest to it within a grain 75
Figure 35: Normal direction orientation maps for the CBMM-H1, Heraeus, Ningxia, and TD-1 ingot slices, as labeled. Annotations provide angle and rotation axis for grain boundary misorientations, with CSL boundaries identified with thick black boundaries and red text. The red arrow on the Heraeus slice identifies the perimeter grain that has the same orientation as the center grain. The high angle (> 15°) grain boundaries are identified with thin black lines. The scale and legend are common to all maps.
Figure 36: Normal direction orientation maps for the CBMM-NSCL slice measured by EBSD (left) and Laue camera (right). Annotations provide angle and rotation axis for grain boundary misorientations, with CSL boundaries identified with thick black boundaries and red text. The discrepancy between the two methods will be addressed in the Discussion chapter. The scale and legend are common to both maps.
Figure 37: Transverse (ingot growth) direction orientation map for the Niowave ingot slab. Annotations provide angle and rotation axis for grain boundary misorientations. The red arrow identifies the perimeter grain that has the same orientation as the center one. The high angle (> 15°) grain boundaries are identified with thin black lines. There is no CSL boundary in this ingot.
Figure 38: Grain boundary misorientation distribution functions (MODFs) for the CBMM-H1 and TD-1 ingot slices. The specific misorientations identified in Figure 35 are identified by X's. There is a trend for grain boundary misorientations to fall between 35-55°
Figure 39: Grain boundary MODFs for the Ningxia and Heraeus ingot slices. Misorientations identified in Figure 35 are identified by X's. There is a trend for grain boundary misorientations to fall between 35-55°.
Figure 40: Grain boundary MODFs for the CBMM-NSCL and Niowave ingots. Misorientations identified in Figure 36 and Figure 37 are identified by X's. There is a trend for grain boundary misorientations to fall between 35-55°

Figure 41: Density pole figures for each ingot plotted using the same color scale. Orientations of dominant grains are evident by the three red <100> poles for the Heraeus and Niowave ingots. The ingots lack commonality in orientation distributions.
Figure 42: Ingot growth (sheet normal) direction discrete inverse pole figures for each ingot. There is a lack of near <111> orientations among the ingots
Figure 43: Illustration of how orientation variation is estimated from multiple Laue measurements within a grain. The orientation deviation map on the left uses the average orientation of each grain as a reference. For example, the largest deviation for grain 1 is in the range of 2.5-3° (dark yellow), and the upper bound value (3°) is assigned to this grain as its orientation spread
Figure 44: Orientation gradients along the 18-mm gauge length of three tensile samples extracted from the Ningxia ingot slice. Y1 has the largest orientation gradient due to a low angle boundary near its right end
Figure 45: Orientation variation in Euler angles for the three samples shown in Figure 44 90
Figure 46: Grain reference orientation deviation maps showing fine scale orientation gradients for samples Y1 and U1 based on the average orientation at the center. The directionality of banding is consistent for sample U1, but less so for sample Y1. The color scale is common to all maps.91
Figure 47: Selected fine scale orientation patterns of the as-cut samples overlaid onto the image of the Ningxia slice. Black dashed lines highlight the original grain boundaries. The color scale for the maps is the same as Figure 46. There is no consistency in the directionality of the banding with respect to the ingot.
Figure 48: Fine scale orientation patterns from roughly the same regions for samples P1 and Q1 before and after an 800 °C/2h anneal. The anneal did not alter the patterning by much. The color scale is the same as Figure 46.
Figure 49: Orientation deviation maps (based upon points with minimum KAM) of the heat-treated samples S2 and T2 before deformation but after electropolishing and annealing. There are no fine scale orientation gradients like those in the as-cut samples. The color scale is the same as Figure 46
Figure 50: Half-cell deep drawn from the CBMM-H2 ingot slice. Orientations measured before and after deformation are overlaid onto the image (black – before, yellow – after). Note that the numbering of locations (hand-written on the half-cell) is different from Figure 25. The orientations did not change much after deep drawing, except for location 10 (9.8° difference). The red boxes indicate locations for which the Laue patterns will be compared before and after deep drawing (Figure 51) [adapted from Figure 2 in reference [123]]
Figure 51: Laue diffraction patterns before and after deep drawing at locations 1, 5, and 7 shown

in red boxes in Figure 50. The spots visible on the undeformed ingot slice (left three) are not as

visible and more smeared after deformation (right three). A example is shown in red circles at location 7
Figure 52: Laue diffraction patterns at positions e and d from the Niowave ingot (Figure 26). The left pattern shows distinct spots in the middle of a milling band, while the right one shows smearing of spots from the edge of a milling band.
Figure 53: Laue diffraction patterns at positions 7, 18, and 25 from the Niowave ingot (Figure 26) before and after a 100 µm etch. The spots became sharper after etching. The 1-2° orientation change is due to mounting error and the removal of a machined surface layer
Figure 54: Sheet normal direction orientation maps, engineering stress-strain curves, and density pole figures for the Tokyo-Denkai samples with extreme tensile properties. The loading direction is either horizontal, or in and out of the page with respect to the orientation maps. There is an inverse correlation between grain size and yield strength [adapted from slide 18 in reference [139]].
Figure 55: Engineering stress-strain curves for 23 Ningxia samples that were either perpendicular (red curves) or parallel (blue curves) to the rolling direction [adapted from slide 16 in reference [139]]. The yield strength vs. grain size correlation applies to the two extreme samples, but not to every other sample.
Figure 56: UTS vs. average grain size (equivalent diameter from EBSD analysis) scatter plots for Tokyo-Denkai samples (above) and Ningxia samples (below). A weak negative correlation is present. On average, the Tokyo-Denkai samples have higher UTS than the Ningxia samples [adapted from slide 17 in reference [139]].
Figure 57: Maximum ODF intensity value of γ -fiber on or near the $\phi_2 = 45^\circ$ slice (from 0-90°) for Tokyo-Denkai (above) and Ningxia (below) samples [adapted from slide 20 in reference [139]].
Figure 58: ϵ_f vs. average ODF intensity value of γ -fiber at $\phi_2 = 45^\circ$ for Tokyo-Denkai (above) and Ningxia (below) samples. Little correlation is present [adapted from slide 21 in reference [139]].
Figure 59: Orientation map of a region on the cross-section of sample A2 with ~68% reduction. The original orientation is shown on the top right corner. An original grain boundary is present in the upper area. The average confidence index (CI) before cleanup is 0.45 for this dataset. The legend on the top left applies to all following orientation maps unless otherwise specified 107
Figure 60: Orientation map of a region on the cross-section of sample A2 with ~76% reduction. Further deformation bands with distinct orientations developed, and the original orientation is no longer traceable. The average CI before cleanup is 0.54 for this dataset

The horizontal bands of different orientations and black zones in the middle resemble the layered structure observed in sheet material. The average CI before cleanup is 0.13 for this dataset 109
Figure 62: Orientation maps from matching areas on sample A2 with ~68% reduction (shown in Figure 59) before and after annealing at 800 °C/2hr. Small grains emerged inside the lower large grain due to the anneal, with orientations different from the parent grain. However, these minority orientations are the same within the pink and dark green regions
Figure 63: Orientation maps from matching areas on sample A2 with ~76% reduction (shown in Figure 60) before and after annealing at 800 °C/2hr. Similar to Figure 62, small grains with green orientations emerged on the right from the deformation bands because of the anneal. The scattered new grains again have the same orientation.
Figure 64: Normal direction orientation maps (left), LAM maps (middle), and IQ maps (right) for the three equator regions indicated in Figure 31. For each region, results for as-deep drawn, after heat treatment, and after BCP conditions are shown from top to bottom. The scale and legends are common to all images. Red arrows on the LAM map of Equator 2 indicates a scratch feature that disappeared after the heat treatment [adapted from Figure 5 in reference [126]]
Figure 65: Normal direction orientation maps (left), LAM maps (middle), and IQ maps (right) for the three iris regions indicated in Figure 31. For each region, results for as-deep drawn, after heat treatment, and after BCP conditions are shown from top to bottom. The scale is common to all images and the legends are the same as Figure 64. A grain boundary developed in Iris 1, likely during deep drawing [Figure 6 in reference [126]]
Figure 66: Point-to-origin (upper three) and point-to-point (lower three) misorientation profiles for the three colored lines drawn on Equator 2 in Figure 64. The blue ends of the colored lines in Figure 64 are the origin. In the after-BCP condition (green), the left grain exhibits an oscillation of ~2-3° as the line crosses the area with low angle grain boundaries. [Figure 7 in reference [126]].
Figure 67: LAM histograms of the six EBSD scans for as-deep drawn (top), after annealing (middle), and after BCP (bottom) conditions. The horizontal scale is common for all three plots. Before annealing, the iris had higher LAM values than the equator, but the iris changed more from annealing [Figure 8 in reference [126]
Figure 68: Engineering stress-strain curves of as-received (left) and heat-treated (right) samples. Orientations of tensile axes are indicated by corresponding colors in the triangle inset, which also provides Schmid factor contours in white for $\{110\}$ slip and gray for $\{112\}$ slip, both scaled at 0.5, 0.499, 0.49, 0.47, 0.44, 0.40, 0.36, 0.32. Dashed lines mark boundaries with equal Schmid factors (orange $-\{110\} + \{112\}$ with intersecting slip directions, red $-\{112\}$ with intersecting slip directions, blue $-\{110\} + \{112\}$ with the same slip directions) [Figure 1 in reference [130]]. 119
Figure 69: Slip trace identification on the heat-treated sample W in some of the areas examined.

Observed slip traces (solid lines) were matched with computed traces (dotted lines) based on the

measured orientations, with {110} slip traces in green, and {112} in purple. Slip traces were not apparent until ~20% engineering strain for this sample [adapted from Figure 7 in reference [58]].
Figure 70: Slip systems ranked by Schmid factors (up to 8th highest) for the as-received sample T3 (above) and heat-treated sample T2 (below). The first {110} slip system was observed in both samples and was the only apparent slip system
Figure 71: Slip systems ranked by Schmid factors (up to 8th highest) for the as-received sample V3 (above) and heat-treated sample V2 (below). A {110} and a {112} slip system were observed in V3, while only the most highly favored {110} slip system was observed in V2
Figure 72: <111>, <112>, and <110> pole figures for the heat-treated sample T2 with the tensile direction pointing out of the page. The [111] pole moved towards the tensile axis with increasing strain, while the [011] pole moved away from the tensile axis. This is consistent with the observed slip system (011) [111].
Figure 73: Orientation evolution with deformation for the as-received sample R2 and heat-treated sample R3. R2 rotated more than R3 during deformation [adapted from Figure 6 in reference [58]].
Figure 74: Prisms illustrating how the three locations of the heat-treated sample P2 (right) rotated differently with deformation over a range of ~5 mm along the gauge length. The orientations at 40% strain all differed from that of the as-received sample P3 (left). The left and right regions of sample P3 had similar opposite rotations as P2. Numbers in red show misorientations before and after deformation in corresponding areas.
Figure 75: Orientation maps from three regions for the heat-treated sample U2 before and after deformation. The left area developed orientation bands with different rotations after deformation. Annotations on the left map provide angle and rotation axis for misorientations of the deformation-induced grain boundaries.
Figure 76: Inverse pole figures showing the evolution of tensile axis orientations with deformation for as-received (triangles) and heat-treated samples (colored solid circles). The orientation change (°) from deformation is shown for each annealed sample. The as-received samples almost always exhibit more crystal rotation than the annealed samples [adapted from Figure 4 in reference [130]].
Figure 77: Optical images of the as-received (AR) and heat-treated (HT) samples in pairs taken after deformation. The scale shown for orientation W is common to all images. Both P samples had similarly opposite sense of rotation on either side of the gauge length, based on the reflections. The two U samples necked at different locations near one of the ends of the sample
Figure 78: Engineering stress-strain curves of samples T1 and V1 deformed <i>in-situ</i> . The arrows indicate where the tensile test was paused to collect CC-EBSD data. The initial hardening behavior for T1 is partly due to the pre-strain (~8.7%), and its plot is shifted to the right accordingly 134

Figure 79: GND distribution maps at each strain level obtained from CC-EBSD for samples T1 and V1. The before-deformation condition for T1 is missing as it was pre-strained to about 8.7%. The orange circle on the top right indicates an area with higher preexisting GND content for V1. There is a noticeable increase in GND density for T1, and little change for V1
Figure 80: Maximum Schmid factor maps for the 5 ingot slices for slip on {110}, {112}, or both families of planes based on biaxial tension. The scale shown next to the Heraeus slice is common to all maps. These maps provide an estimate of formability based on hard/soft orientations 141
Figure 81: Maximum Schmid factor maps for the Niowave ingot slab for slip on {110}, {112}, or both families of planes based upon biaxial tension in a slice taken perpendicular to the longitudinal direction. Slices from this ingot would likely experience more homogeneous deformation due to the huge grain at the center.
Figure 82: Fitted line of yield strength vs. grain size for the Ningxia samples shown in Figure 55. The shotgun scatter suggests that the Hall-Petch relationship is not well satisfied
Figure 83: LAM profiles in the 6 grains obtained from averaged traces on the inside and outside of the equator and iris. Damage depths up to about 200 µm is present in some regions, and the magnitude is different for the equator and iris, as well as for the outside and inside [Figure 9 in reference [126]]
Figure 84: The table on the right lists the annealed samples in the order of increasing ratio between the primary and secondary {110} slip systems, which corresponds roughly to decreasing initial hardening rates as shown in the zoomed image on the lower left [Figure 3 in reference [121]].155
Figure 85: Comparison of experimental and simulation results of several annealed samples using classical, dynamic hardening, and differential-exponential approaches. Without accounting for the Non-Schmid effects, the modeling still shows good agreement with the experiments [Figure 15 and Figure 16 in reference [149]].
Figure 86: Comparison of slip trace morphology at 40% engineering strain on the as-received and heat-treated sample X. X3 has wavier slip traces than X2
Figure 87: <111>, <112>, and <110> pole figures from three regions on the gauge length for the heat-treated samples P, Q, and R with the tensile axis pointing out of the page. The color scale for engineering strain is common and shown next to sample P
Figure 88: <111>, <112>, and <110> pole figures from three regions on the gauge length for the heat-treated samples S, T, and U with the tensile axis pointing out of the page. The color scale for engineering strain is common and shown next to sample S
Figure 89: <111>, <112>, and <110> pole figures from three regions on the gauge length for the heat-treated samples V, W, and X with the tensile axis pointing out of the page. The color scale for engineering strain is common and shown next to sample V

Figure 90: Slip trace identification on the heat-treated sample P in some of the areas examined. Observed slip traces (solid lines) were matched with computed traces (dotted lines) based on the measured orientations, with {110} slip traces in green, and {112} in purple
Figure 91: Slip trace identification on the heat-treated sample Q in some of the areas examined. Observed slip traces (solid lines) were matched with computed traces (dotted lines) based on the measured orientations, with {110} slip traces in green, and {112} in purple
Figure 92: Slip trace identification on the heat-treated sample R in some of the areas examined. Observed slip traces (solid lines) were matched with computed traces (dotted lines) based on the measured orientations, with {110} slip traces in green, and {112} in purple
Figure 93: Slip trace identification on the heat-treated sample S in some of the areas examined. Observed slip traces (solid lines) were matched with computed traces (dotted lines) based on the measured orientations, with {110} slip traces in green, and {112} in purple
Figure 94: Slip trace identification on the heat-treated sample T in some of the areas examined. Observed slip traces (solid lines) were matched with computed traces (dotted lines) based on the measured orientations, with {110} slip traces in green, and {112} in purple
Figure 95: Slip trace identification on the heat-treated sample U in some of the areas examined. Observed slip traces (solid lines) were matched with computed traces (dotted lines) based on the measured orientations, with {110} slip traces in green, and {112} in purple
Figure 96: Slip trace identification on the heat-treated sample V in some of the areas examined. Observed slip traces (solid lines) were matched with computed traces (dotted lines) based on the measured orientations, with {110} slip traces in green, and {112} in purple
Figure 97: Slip trace identification on the heat-treated sample X in some of the areas examined. Observed slip traces (solid lines) were matched with computed traces (dotted lines) based on the measured orientations, with {110} slip traces in green, and {112} in purple
Figure 98: Orientation maps from three regions for the heat-treated sample P before and after deformation
Figure 99: Orientation maps from three regions for the heat-treated sample Q before and after deformation
Figure 100: Orientation maps from three regions for the heat-treated sample R before and after deformation
Figure 101: Orientation maps from three regions for the heat-treated sample S before and after deformation.

Figure 102: Orientation maps from three regions for the heat-treated sample T before and a deformation	
Figure 103: Orientation maps from three regions for the heat-treated sample U before and a deformation	
Figure 104: Orientation maps from three regions for the heat-treated sample V before and a deformation	
Figure 105: Orientation maps from three regions for the heat-treated sample W before and a deformation	
Figure 106: Orientation maps from three regions for the heat-treated sample X before and a deformation	

I. INTRODUCTION

Particle accelerators incorporating superconducting radiofrequency (SRF) technology have a variety of scientific and industrial applications. As the performance of accelerator cavities made from niobium (Nb) approaches the theoretical limit, an increasing number of issues have arisen that cannot be explained or tackled with conventional physics. Over recent years, much research has focused on the materials science aspects of Nb in the SRF community, following the pioneering efforts by Padamasee *et al.* [1, 2]. Physical understanding of the metallurgy of Nb is necessary to develop a viable path to further enhance the performance of cavities while reducing their variability in performance.

Material considerations for SRF cavities involve three major aspects: formability, stiffness, and microstructure [3]. Good formability facilitates cavity fabrication and requires high elongation to failure; stiffness ensures dimensional stability during cavity operation (e.g., cooling down under vacuum) and requires a high Young's modulus; the final microstructure (dislocation configuration) dictates thermal conductivity and magnetic properties that are linked to cavity performance, since dislocations interfere with heat transfer and trap magnetic flux [3]. Depending on the application of a cavity, the material specification usually requires a compromise among these factors [3].

Currently, the formability and stiffness of Nb can be reasonably controlled by SRF cavity manufacturers, even though knowledge of the microstructure or metallurgical state of cavities is limited. A material model that integrates the microstructure with existing physics theories will enable a more accurate prediction of cavity performance. To build such a comprehensive model, it is vital to understand how microstructure evolves during cavity fabrication and how it affects

performance. With such a model, forming and performance issues can be anticipated or eliminated at an earlier stage, and more robust criteria for material acceptance are possible.

This work addresses some of the missing links required to establish a better material model. The initial microstructure of the material to make cavities is a prerequisite for the simulation. Then, two paths are followed – first, the microstructural evolution during processing of a cavity is investigated and correlated to its performance; second, the slip behavior is examined in the simpler case of uniaxial tension for a fundamental understanding of deformation mechanisms of Nb that govern the microstructural changes. The insights from these studies will complement prior knowledge and provide a basis for the modeling, thus enabling design strategies that will lead to more consistent cavity performance and cost reduction.

Recently, the role of dislocations in cavities has attracted increasing in the SRF community [4-6]. Dislocations are associated with variability in the starting Nb material, and such variability evolves during the forming process and may magnify variability during cavity fabrication, which eventually influences cavity performance. An improved material model will allow dislocation configuration in a cavity to identified as dislocations are both a component and consequence of the microstructural evolution.

The scope of this work follows five parallel storylines that will be set forth in the Materials and Methods, Results, and Discussion chapters: (a) crystal orientations of ingot slices, (b) texture of fine grain sheets, (c) link between the ingot and sheet microstructure, (d) orientation gradients in a large grain cavity, and (e) single crystal tensile tests. The reason for using this structure instead of having five separate chapters is that the linkages between sections a-e can be more effectively

communicated, particularly in the Discussion chapter. However, this organization brings about a disadvantage of conveying five parallel studies within each chapter.

II. LITERATURE REVIEW

a. Accelerator Technology and Niobium

The quest for superconductivity began in 1892 when James Dewar invented the Dewar flask, a vessel he later used to liquefy hydrogen successfully in 1898 [7]. Heike Onnes managed to produce liquid helium in 1908, which opened a brand-new chapter in the properties of matter at low temperatures [7, 8].

"Mercury practically zero," Onnes wrote in his lab notebook in 1911, as he discovered that the resistance of mercury was $0.034~\Omega$ at 13.9~K, $0.0013~\Omega$ at 4.3~K, and less than $0.0001~\Omega$ at 3~K [7, 9]. At that time, however, he was more into celebrating his choice of mercury to validate his theory on electrical resistivity of metals rather than realizing the birth of a new era. In 1913, the Leiden group led by Onnes found that lead and tin were also superconductors, with transition temperatures close to 6~K and 4~K, respectively [8, 10]. In the same year, Onnes was awarded the Nobel Prize in Physics for his extraordinary contribution to low-temperature physics [7].

The world of particle accelerators was almost developing in parallel [11]. Driven by high energy physics research, the history of accelerators can be traced back to 1895, when Lenard observed electron scattering in gases, signifying the transition from atomic physics to nuclear physics [11]. In the early twenties, Ernest Rutherford identified the need for "atomic projectiles" with much higher energy and intensity than what was naturally available [11]. A milestone was achieved in 1932 when Cockcroft and Walton split a lithium atom with 400 kV protons [11].

Accelerator technology entered a new stage in 1961, as Banford and Stafford started looking into "the possibility of applying superconducting principles to proton linear accelerator design" [7, 12]. In this technology, superconductivity is coupled with the existing radiofrequency

resonators, hence the term superconducting radiofrequency (SRF). Niobium (Nb) was proposed then for assessment of its potential in the application, because it has the highest superconducting transition temperature ($T_c = 9.3 \text{ K}$) among elemental metals, along with other merits such as being a type II superconductor as well as having good ductility and thermal conductivity [12].

The first Nb accelerator cavity incorporating the SRF technology was developed in 1968 at Stanford University [13], replacing traditional lead-plated copper cavities that operate at room temperature. SRF cavities enable high duty cycle or even continuous-wave operations with large accelerating gradients while minimizing beam impedance and power dissipation [14]. There are a variety of applications for SRF cavities, ranging from fundamental physics research, including nuclear physics and nuclear astrophysics, to high energy light sources such as those used in life science and materials science [2, 15].

At the core of an accelerator, cavities consist of a string of ellipsoidal cells [1]. Figure 1 shows an exemplary assembly of a 7-cell cavity [16]. The largest diameter of the ellipsoid is referred to as the equator, and the smallest diameter is the iris [1]. With radiofrequency (RF) induction, the electromagnetic field between each adjacent pair of cells keeps changing polarity as charged particles pass such that a constant accelerating direction is maintained [17]. The polarity changes are strategically timed to accommodate the increasing speed of particles. After traveling through multiple cavities, subatomic particles can nearly reach the speed of light, while larger particles can reach half the speed of light [17]. There may be tens of thousands of cavities in an accelerator such as the proposed International Linear Collider (ILC), depending on particle characteristics and the desired speed [18].

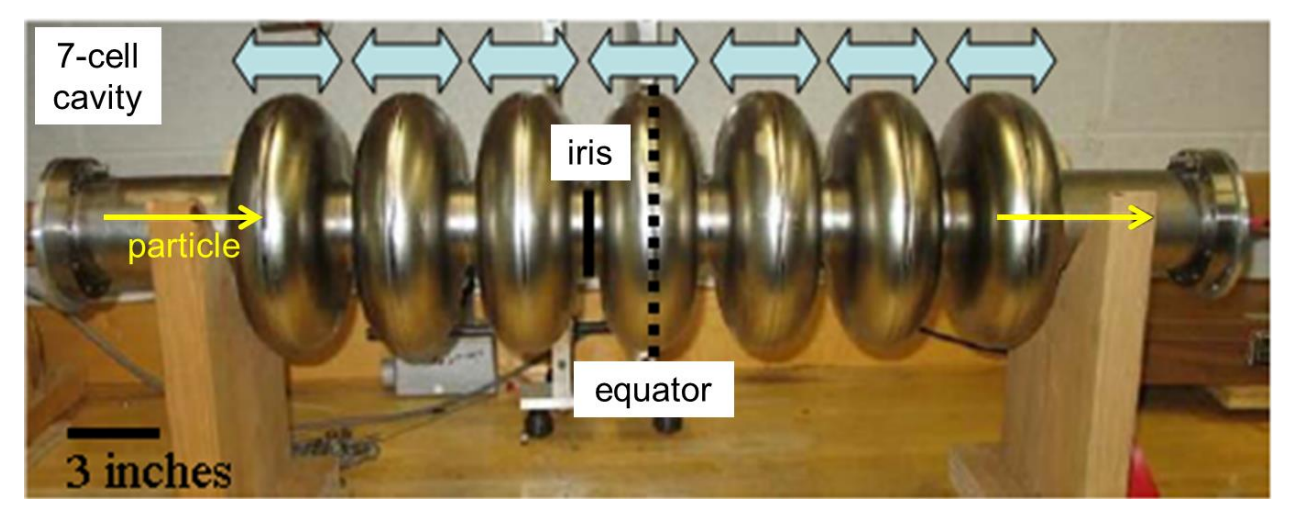


Figure 1: Example of a 7-cell cavity. Blue arrows on top indicate polarity changes of the electromagnetic fields within the cells [adapted from Figure I-1 in reference [16]].

b. Progress in Improving Cavity Performance

The performance of a cavity is typically represented by two parameters – the accelerating gradient (field) E_{acc} and the quality factor Q_0 [1]. E_{acc} denotes the capability of a cavity and Q_0 denotes its efficiency. The theoretical limit for E_{acc} is calculated to be ~55 MV/m for Nb cavities, based on the critical magnetic field, and the design of the ILC requires an E_{acc} of ~31 MV/m [19].

The quality factor Q_0 is defined as

$$Q_0 = \frac{U}{P_c}$$

where U is the energy stored in a cavity, and P_c is the energy dissipated in one RF cycle [20]. Typical Q_0 of modern cavities is on the order of 10^{10} . To provide an understanding of this value, if Galileo Galilei's experiment in the early 17^{th} century with a 1 Hz pendulum had such a Q_0 , the amplitude of the pendulum would have only decreased by about half as of today [21].

Regardless of the application, a "good" cavity is one that exhibits the highest possible E_{acc} and the highest possible Q_0 [3]. Over the years, steady improvements in both parameters have

been accomplished, thanks to the growing understanding of limiting phenomena and practical solutions. The first issue identified that affects cavity performance was multipacting, a resonant process during which electrons build up within a small region of the cavity surface [1]. These electrons absorb RF power, making it difficult to further increase the electric field by increasing the incident RF power. The electrons also impact cavity walls, leading to a substantial increase in temperature and eventually to thermal breakdown (discussed next). This multipacting issue can be overcome with a proper shape design [1].

The second issue is thermal breakdown or "quench," a significant energy loss that occurs when the local temperature of a cavity exceeds T_c [1]. Thermal breakdown typically originates at sub-millimeter-size regions of defects, where there is a small temperature increase. This leads to a higher fraction of normally conducting electrons, i.e., instability of the superconducting state [1]. The likelihood of a thermal breakdown can be reduced by improving the thermal conductivity of Nb [1].

Another issue is field emission, which is the emission of electrons from high electric field regions of a cavity [1]. The RF power is absorbed by these electrons and dissipated as heat and radiation upon impact with cavity walls. Intense field emission can initiate thermal breakdown. Therefore, field emission sites such as surface defects, need to be prevented [1].

Finally, a Q-slope is often present at high electric fields, which is a rapid drop in Q_0 when the accelerating field approaches the theoretical limit, as shown in Figure 2 [18, 22]. In general, a low-temperature bake at around 120 °C dramatically improves the high field Q_0 , although different mechanisms have been proposed to explain this effect and no agreement has been reached so far.

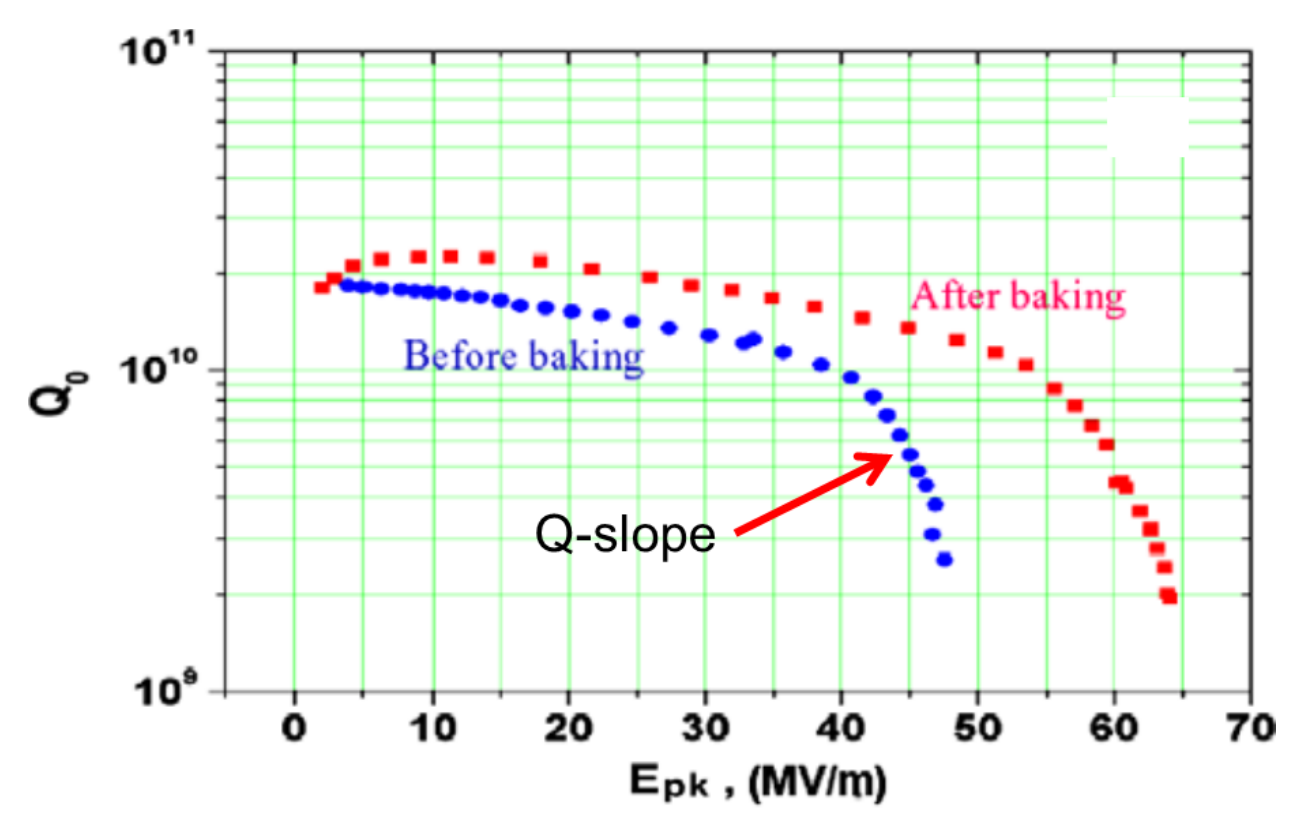


Figure 2: Q_0 vs. E_{pk} measured on a 1.3 GHz single cell cavity before and after baking at 100 °C for 48 hours. The bake moved the Q-slope to higher accelerating fields and increased the Q value [Figure 1 (b) in reference [22]].

Thermal breakdown, field emission, and Q-slope are all closely related to "defects" in a cavity. Any material imperfections that potentially lead to issues with the superconducting state and strong electromagnetic fields are categorized as defects [1]. These include inclusions (Ta, Cu, Fe, etc.), chemical or drying stains, balls and voids at electron beam welds, interstitials (O, N, C, and H) and crystalline defects. While other defects can be eliminated via careful handling and purification processes, crystalline defects are prevalent and more difficult to control [1].

c. Dislocations and Cavity Performance

It is hypothesized that dislocations have the most substantial impact on cavity performance among the various crystalline defects in Nb [23-25]. This section will discuss how dislocations could interfere with the operation of SRF cavities.

The first known mechanism is that dislocations serve as pinning centers for magnetic flux, resulting in the irreversibility of magnetization curves [1]. When an external magnetic field is applied, incoming magnetic flux is captured at pinning centers. As the magnetic field is reduced, these flux lines remain trapped, resulting in residual magnetization even when the external field vanishes. The only way of eliminating pinned flux is to heat the cavity to destroy the superconducting state, which is not practical in normal operations. Trapped flux also introduces error into measurements of the critical magnetic field H_{c1} – a drop in the apparent values for H_{c1} has been observed with post-processing steps such as etching and heat treatment, as dislocations are removed [1]. Therefore, dislocations and other pinning centers (such as interstitial impurities) for magnetic flux need to be minimized in a cavity.

Dislocations can also degrade the thermal conductivity of Nb, which contributes to thermal breakdown [1]. The temperature increase due to inadequate heat transfer introduces local thermal instability that destroys the superconducting state. Romanenko *et al.* found a correlation between high dislocation content and the hot regions of a cavity [26, 27]. Figure 3 shows the local average misorientation (LAM) maps (discussed next) from two regions on a large grain cavity [26].

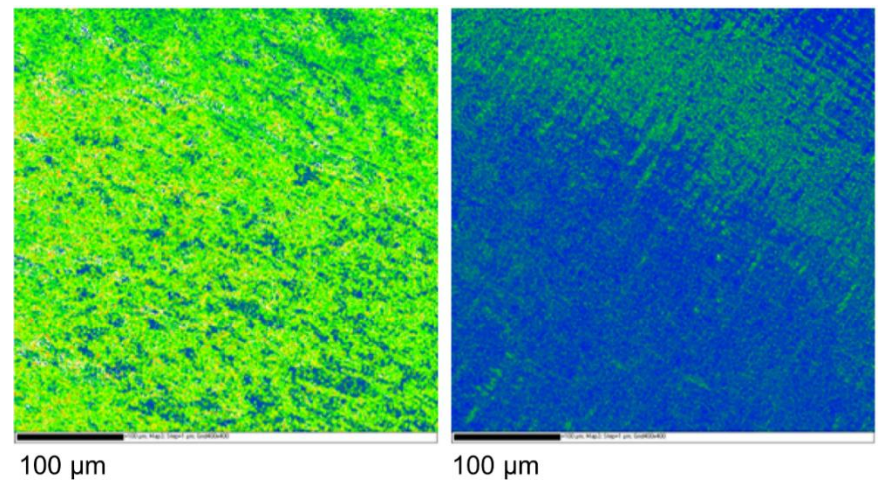


Figure 3: Local average misorientation (LAM) maps from "hot" (left) and "cold" (right) regions in a cavity. The green color corresponds to a misorientation of 2°, and blue is 0° [Figure 14 in reference [26]].

LAM provides an estimate of the dislocation content. For a given datum point, LAM reports the average misorientation between of all the neighboring points within a specified distance from the kernel [28], as illustrated in Figure 4 for the 2nd nearest neighbor sampling area. LAM information can be presented in the form of a grayscale map or a histogram. In an LAM map, each EBSD datum point is assigned a certain shade of gray between white and black, corresponding to misorientations from 0° to a user defined maximum value. In an LAM histogram, the range of misorientations is divided into bins, and the number of observed misorientations from each pixel in each bin determines its number fraction.

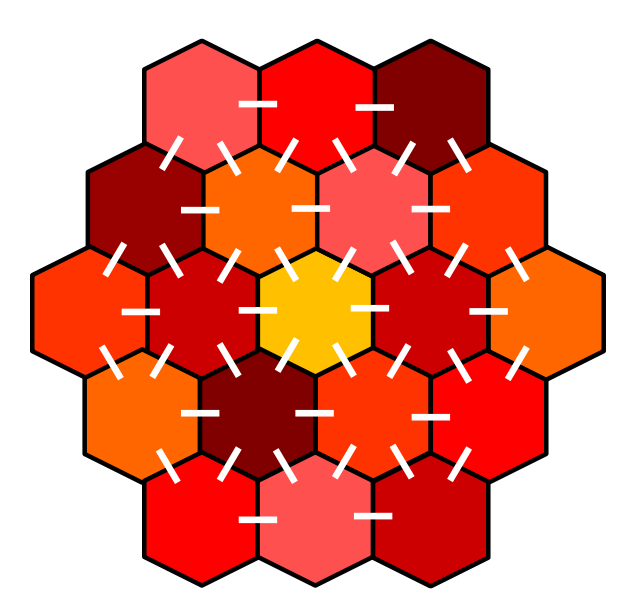


Figure 4: Local average misorientation (LAM) calculations using the 2nd nearest neighbor sampling area – for the point at the center, LAM averages the misorientations of all its neighboring points (connected by short white lines) within the kernel [Figure 3 in reference [126]].

The map on the left had larger LAM values (more dislocations), which correlated with hot regions in the cavity, while the map on the right correlated with cold regions in the cavity [26]. Figure 5 shows corresponding histograms for the LAM maps in Figure 3, where the cold region has a sharper peak at a smaller misorientation angle than the hot region [26].

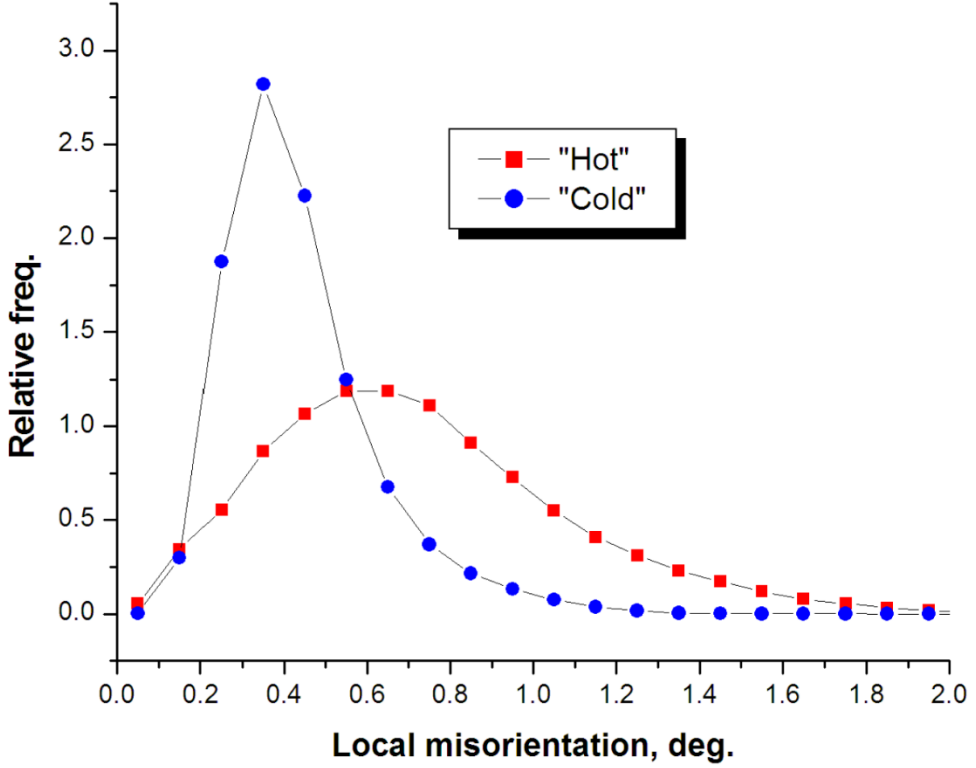


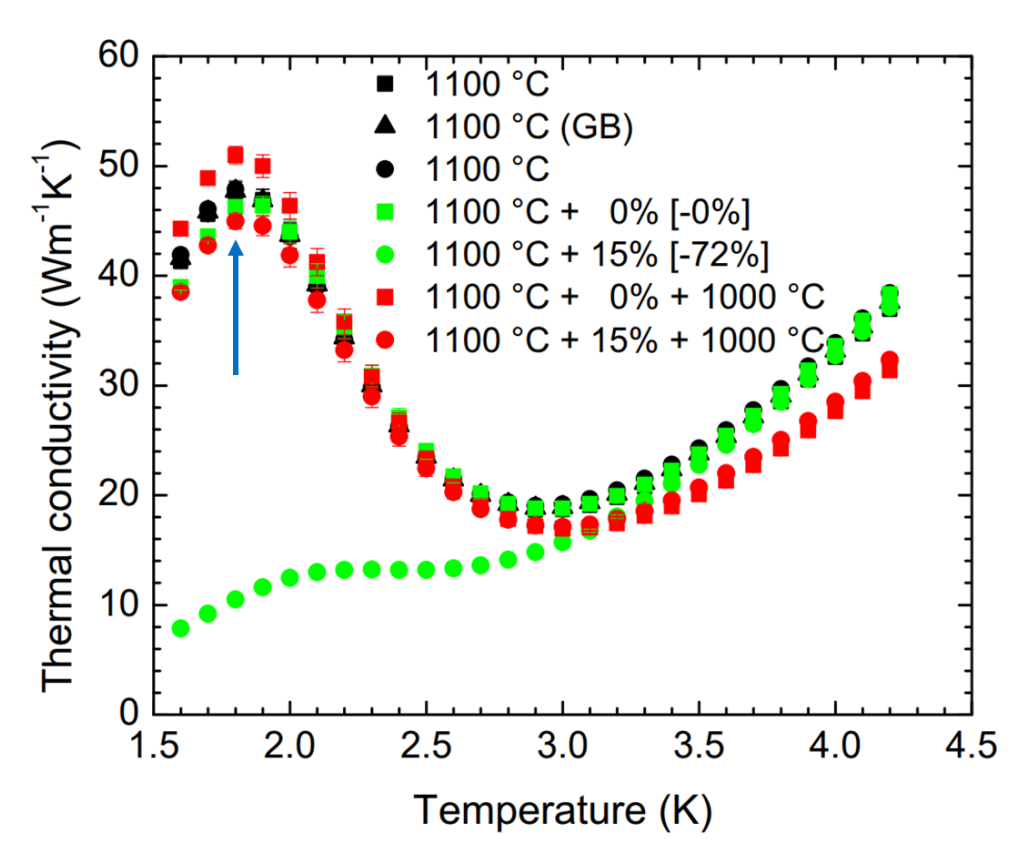
Figure 5: Corresponding histograms for the LAM maps shown in Figure 3 [Figure 15 in reference [26]].

Dislocations in crystalline materials exist in two forms [29, 30]. Geometrically necessary dislocations (GNDs) account for the lattice curvature arising from an unbalanced population of dislocations of one sign within a given region in a grain. Such lattice curvature can be revealed by a LAM map, in which a larger LAM value corresponds to a higher GND density. Statistically stored dislocations (SSDs) are slightly displaced dislocation pairs with opposite signs that do not contribute to the overall orientation gradient. When there are adequate driving forces such as an

elevated temperature, neighboring SSDs with opposite signs can move towards each other and sometimes annihilate [29, 30]. Because more dislocations are categorized as SSDs as the step size increases, the GNDs are semi-quantitatively revealed in the LAM maps.

A proposed explanation for the dislocation-induced local heating is that dislocation lines vibrate with passing phonons (lattice vibrations, the primary conducting mechanism in the superconducting state) and disperse them, thereby slowing the heat transfer [24]. This interference is most significant when dislocation lines (both edge and screw) are aligned with the direction of heat flow [24]. Evidence for this theory was provided by Chandrasekaran *et al.*, in which annealing at temperatures above 1000 °C usually led to a significant restoration of phonon peaks on deformed single crystal and bi-crystal samples [31-33]. Figure 6 shows an example of the phonon peak evolution on a bi-crystal sample that was annealed after being extracted from an ingot slice, deformed in tension, and annealed again. The phonon peak of grain 2 disappeared after 15% strain but completely recovered to its original position after the 1100 °C anneal [32]. Moreover, phonon peaks have been observed in fully recrystallized fine grain samples with a low purity [34, 35], implying that dislocations are more detrimental than impurities and grain boundaries to thermal conductivity in the superconducting state. This is another reason why it is desirable to reduce the dislocation content in a cavity.

Furthermore, near-surface dislocations may account for the benefits associated with low-temperature baking. Romanenko *et al.* speculated that dislocation annihilation might occur via a vacancy-assisted process at around 120 °C, hence the performance gain [27]. However, other mechanisms such as the elimination of excess concentration of oxygen were also proposed, and more research is needed before a consensus can be reached [2]. Dislocations could still degrade cavity performance in other ways that have not yet been explored and understood.



Grain	Abs. Schmid factor	# active slip sys.	Engg. strain
1 (■)	0.359	2	0%
2 (•)	0.481	1	15%

Figure 6: Thermal conductivity as a function of temperature for a bi-crystal sample. The original phonon peak (blue arrow) on grain 2 disappeared after 15% strain, but it was fully restored after a 1000 °C/2hr heat treatment [adapted from slide 5 in reference [32]].

For all of the reasons discussed above, one of the ultimate goals of SRF cavity processing is to minimize the dislocation content in a cavity and to align the remaining dislocations perpendicular to the direction of heat flow to minimize phonon dispersion (maximize thermal conductivity) [24].

d. Ingot Production and Initial Grain Orientation

To continue to push the limit of cavity performance, significant research has focused on materials science and surface science in the SRF community over recent years [3, 24, 36]. The

goal is to understand the metallurgical state evolution during the cavity fabrication process, with emphases on three aspects – initial crystal orientations, deep drawing, and post-processing steps, including chemical and heat treatments. It is desirable to have a model that can computationally predict the final shape and microstructure (e.g., dislocation content and arrangement) within a cavity, based upon the initial crystal orientations and processing history. With such modeling, acceptance criteria can be established or improved for materials suppliers, so that it is possible to obtain more consistent cavity performance. These three aspects will be introduced in the following sections.

Nb ingots are produced and purified by electron beam melting in vacuum [37]. Raw Nb pellets are melted by an electron beam, and the molten Nb is collected in a water-cooled copper mold to form ingots [37, 38]. Figure 7 shows a schematic diagram of this process [38-40]. The ingots are purified several times by repeated electron beam melting [37, 38].

The water cooling leads to large radial and longitudinal temperature gradients in the ingots. The resultant strain from thermal contraction causes dislocations to form [24]. Both the ingot production and ingot purification are done slowly at elevated temperatures, leading to considerable grain growth, although not to the extent that all dislocations are wiped out since thermal strains occur concurrently with grain growth due to the temperature gradient in the cooling ingot. While huge grains are present in an as-received ingot, there has not been much success in getting a grain that extends to the full diameter of an ingot [41].

It is challenging to control the grain orientations in an ingot. One of the first Nb ingots that Jefferson Lab received from CBMM had a large single crystal in the center [41]. This is a desirable configuration for deep drawing since the largest strain occurs at the center and a single crystal in

this region can help enable uniform deformation. However, it is unclear under what conditions that ingot was grown and how it could be reproduced [41].

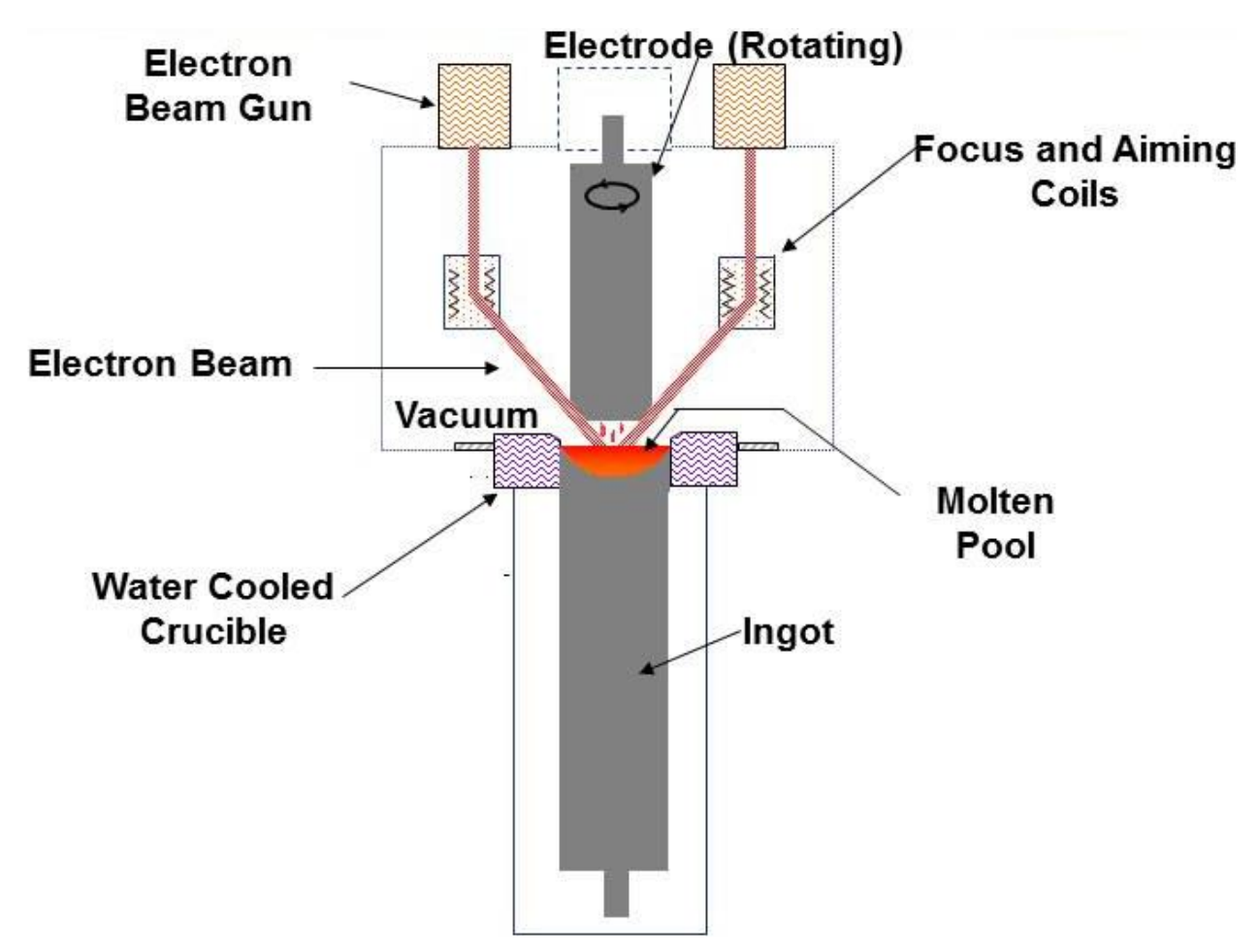


Figure 7: Schematic of the electron beam melting equipment to produce and to purify Nb ingots [Figure 2 in reference [38]].

A study at DESY on ingot slices from three suppliers (CBMM, Heraeus, and Ningxia) further demonstrated the lack of reproducibility in grain microstructures [42]. Full-penetration X-ray characterization at DESY-HASYLAB showed that the central grain of the CBMM slice had good homogeneity with a near {111} orientation – measurements at seven locations of the grain revealed minimal fluctuations, proving high quality of the single crystal. The Heraeus ingot slice

consisted of a big central grain with a near {100} orientation and small perimeter grains. The central crystal again possessed a high quality with little orientation fluctuations. In contrast, the Ningxia slice consisted of many grains with widely scattered orientations [42]. At the center of the slice, a signal splitting of reflections (indicating multiple crystals) and Debye-Scherrer rings (indicating small crystals) were observed in addition to the strong single crystal signal [42].

Due to the reduced number of grain boundaries in large grain Nb, it is expected that the contribution to thermal resistance from phonon scattering at grain boundaries will be much lower than fine grain Nb [42]. The thermal conductivity of a series of fine grain, large grain, and single crystal Nb samples was measured at low temperatures. The results showed pronounced phonon peaks on the large grain and single crystal samples from Heraeus after an 800 °C heat treatment, while no phonon peak was observed on the fine grain samples after the same heat treatment. No phonon peak was observed either on a large grain sample from Ningxia, which is likely due to its large grain consisting of many small sub-grains. This suggests that the orientation consistency of the large grains could be essential for practical superconductivity of Nb [42].

While there may be orientation variations in the plane of an ingot slice, orientations along the longitudinal direction of an ingot appear to be quite stable. Umezawa *et al.* examined 48 slices extracted from the top to the bottom of an ingot with ultrasonic tomography, as shown in Figure 8 [43, 44]. The grain orientations were almost identical, although the positioning of grain boundaries differed slightly with each slice. They concluded that the grains grew in a columnar manner and that the size and shape of a grain strongly depended on the orientations present at the base plate

[44]. This suggests that a seeding approach may work in obtaining desirable orientations for Nb ingots (discussed next).

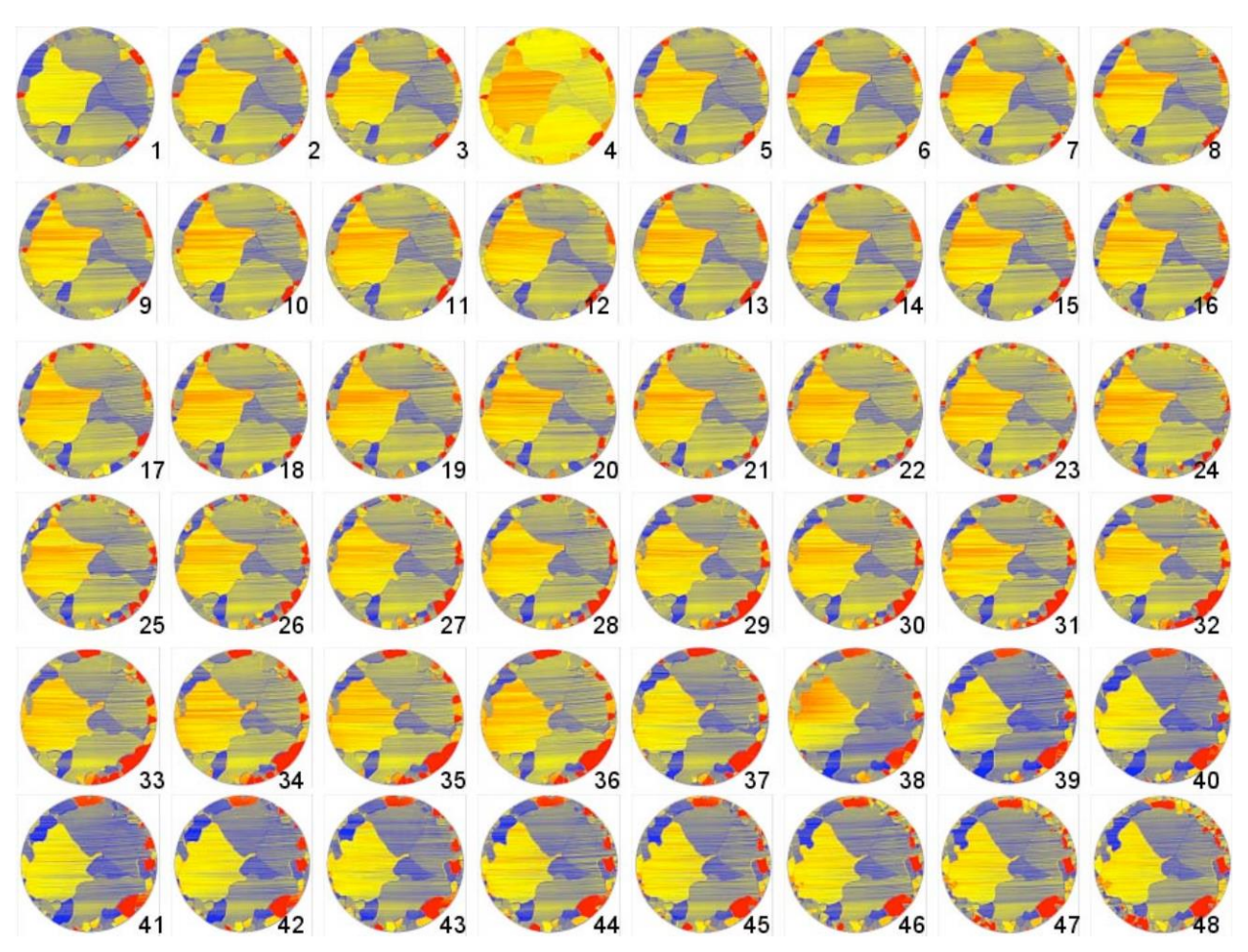


Figure 8: Ultrasonic tomography of a Nb ingot. No. 1 is near the bottom of the ingot, and No. 48 is near the top [Figure 3 in reference [44]].

In the pursuit of reducing the grain boundary area even further, efforts have been made to grow single crystal ingots. Heraeus investigated the growth parameters to reliably produce ingots with a sizeable central grain with a specified orientation [13, 45, 46]. Several variables in electron drip melting could affect the nucleation and dissolution of grains in the liquid pool, such as the pool temperature, molten pool motion, and dripping of melt stock into the pool. Their preliminary conclusion was that their melting process was not stable enough to reproducibly create a central crystal of ~150 mm in diameter with a controlled orientation throughout a whole ingot of ~2000 mm in length [13].

Tokyo-Denkai also attempted to grow single crystal ingots by placing a seed crystal onto a Nb base plate before the standard melting process [13, 44]. However, ultrasonic tomography revealed that the base plate crystals rather than the seed determined the grain growth in the ingot. It was argued that a thicker seed crystal might be necessary for a successful single crystal growth [13].

DESY demonstrated that it is possible to enlarge a single crystal without destroying its original microstructure by rolling [13, 47]. Even after being deformed into half-cells, the enlarged single crystals still maintained their orientations normal to the surface. Annealing at 800 °C did not alter the deformed single crystals either (i.e., no recrystallization), although {001} and {110} orientations were more stable than {111} orientations [13, 47]. They also observed that when the misorientation between two single crystals was within 3°, they grew into one grain upon electron beam welding [13].

Dislocations have been observed in as-received ingots. The electron channeling contrast image of a sample from an ingot slice demonstrated large populations of entangled dislocations,

as shown in Figure 9 [24, 48]. White regions indicate a high dislocation density, as electrons are backscattered towards the detector by dislocations; black areas correspond to lattice planes that are oriented for electron channeling with little distortion by dislocations. Such clusters of dislocations resemble those observed in cold-worked metals [29]. These preexisting networks of dislocations in an ingot could have an impact on deformation and microstructural evolution during subsequent forming steps.

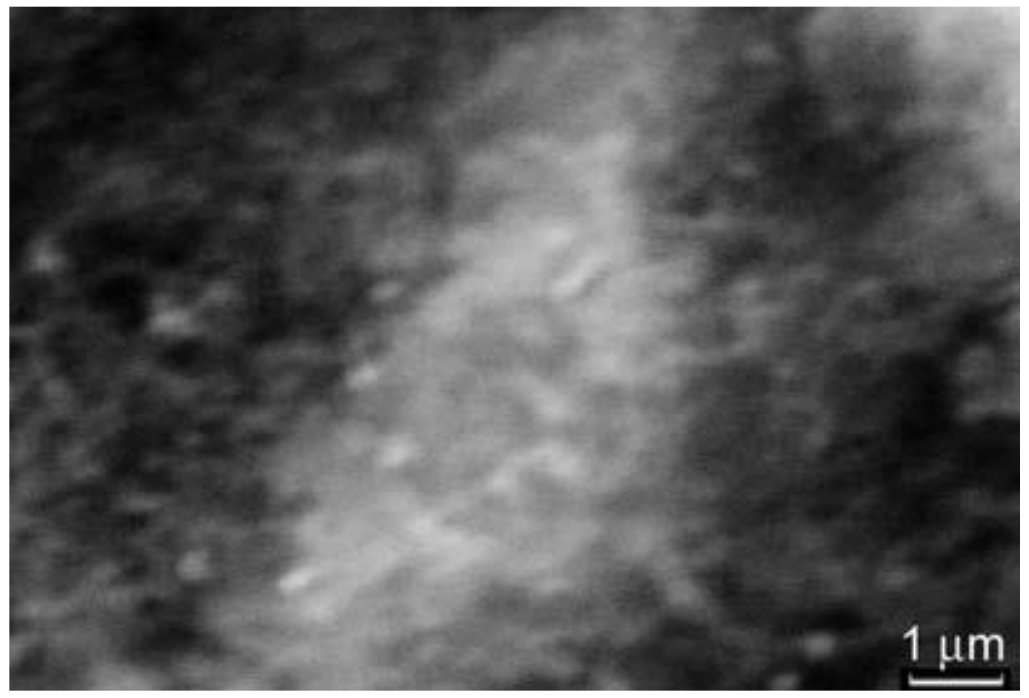


Figure 9: Electron channeling contrast image of a sample from an as-received Nb ingot showing contrast arising from dislocations [Figure 8 in reference [24]].

e. Large Grain Approach to Forming Cavities

There are mainly two approaches to forming a cavity. One is the well-established fine grain approach [37], in which Nb ingots are broken down with forging, milling, and rolling, plus intermediate heat treatments to retrieve formability. Sheet metal disks of ~3 mm in thickness and ~35 cm in diameter are produced this way for deep drawing. A small and uniform grain size of ~50 µm is generally necessary for good formability so that no excessive surface roughing occurs during deformation [13].

Alternatively, disks can be produced by directly slicing Nb ingots, namely the large grain approach [13, 41, 49]. Figure 10 shows a schematic diagram of the fine grain approach (above) and the large grain approach (below) [37]. Proposed about two decades ago, the large grain approach quickly gained attention as it significantly reduces fabrication costs by eliminating the rolling and annealing steps, and the amount of material waste to produce disks was estimated to be 15%, compared to about 45% for standard fine grain disks [41, 43, 50]. More importantly, comparable or even better performance has been achieved from large grain cavities [13, 41, 51-55]. The large grain approach was a breakthrough in the cavity manufacturing industry and could benefit many accelerator projects, including the ILC.

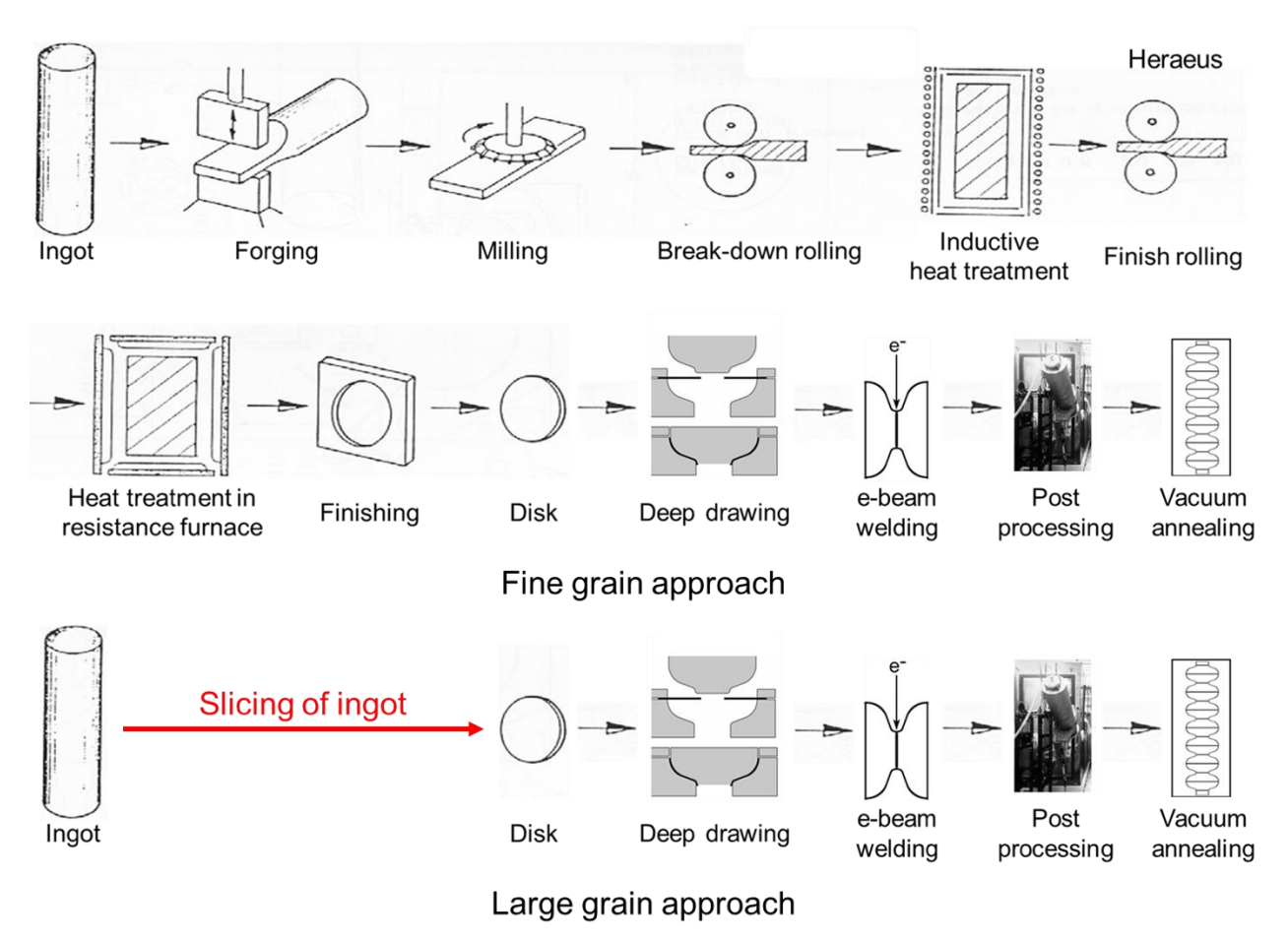


Figure 10: Flow diagram of SRF cavity fabrication using fine grain or large grain Nb (courtesy of W.C. Heraeus, Germany) [adapted from Figure 6 in reference [37]].

An apparent difference between disks obtained from the two methods is the average grain size. Fine grain disks usually have a uniform grain size of ~50 µm, while the grain size for large grain disks is much less uniform, and can be as large as 20 cm. Thus, large grain Nb tends to be more mechanically anisotropic, with formability and dimensional stability inferior to fine grain Nb. However, a study by Ciovati *et al.* [56] demonstrated that with proper heat treatments, the mechanical properties (evaluated by yield strength and burst tests) of large grain cavities could be better than fine grain cavities.

The heterogeneous deformation of large grain ingot slices is mostly accounted for by the differences in crystal orientations [16, 57]. From established principles for body-centered cubic (bcc) materials, orientations with <111> directions normal to the surface have high flow stress (hard), yet are the most stable in deep drawing, while orientations with <100> directions normal to the surface are soft and less stable [24]. From single crystal experiments, tension along <111> directions requires about twice as much stress as tension in directions more than 20° away from <111> [16, 58].

Large grain cavities may have an "orange peel" appearance (a combination of bumps and grooves) caused by the heterogeneous deformation at and near grain boundaries. This can be overcome with appropriate mechanical processing, such as barrel polishing [3]. However, after chemical treatments, even though the grain surfaces remain mostly smooth, the difference in etch rates from one orientation to another produces steps up to 500 µm between the grains, more prominent than those in fine grain cavities [3, 51]. While large grain Nb exhibits excellent ductility in uniaxial tension, its biaxial deformation properties (e.g., susceptibility to thinning) are closer to those of fine grain material rather than single crystals [3]. Therefore, one of the major concerns about the large grain approach is whether the cost reduction makes it worthwhile to tolerate the uncertainties in forming [24].

f. Microstructure of Fine Grain Nb Sheets

As the large grain approach has not been fully industrialized due to its recent introduction into the field, most SRF cavities to date are still manufactured with fine grain Nb sheets. A critical step in producing these sheets is rolling combined with heat treatments. The final microstructure of a rolled sheet is determined by both the initial grain orientations and processing history, as will be reviewed in this section.

Rolled and heat-treated Nb sheets tend to exhibit a sandwich microstructure, with {100} orientations near the surface, and {111} orientations in the middle [24]. Raabe *et al.* observed such microstructures on polycrystalline Nb rolled to 50% and 60% reduction and attributed them to slip on {110} and {112} planes [59]. A similar study by Abreu *et al.* revealed that {100} orientations increased with the amount of deformation, but not {111} orientations [60]. The discrepancy may be due in part to different starting materials – Raabe *et al.* used a weakly textured material, while Abreu *et al.* used a hot-rolled sheet [59, 60].

For manufacturing SRF cavities, it is desirable to have Nb sheets with consistent texture and grain sizes. However, there is almost always a considerable variation in the sheet microstructure, even for suppliers with mass production capability and well-controlled processing schedules [24, 61, 62]. For example, Jiang *et al.* examined ten rolled sheets from two suppliers, and all of them had different microstructures (e.g., grain size and preferred orientations) [63].

Full recrystallization that removes most dislocations generated during rolling is necessary for good formability of Nb sheets. In a study by Jiang *et al.*, one batch of material (Figure 11 (a)) was under-recrystallized compared to (b) and (c) due to the presence of elongated grains [63]. This batch showed greater mechanical anisotropy in tensile tests, and there were problems in deep drawing. The other two batches shown in Figure 11 (b) and (c) had equiaxed grains with more isotropic mechanical properties, suggesting that they would deform more homogeneously (cause less earing) during deep drawing [63].

The deformation texture of Nb can also be optimized by asymmetric rolling [64]. Ito *et al*. found that less elongated grains could be obtained by differential-speed rolling (different rotational speed of upper and lower rolls [65]) with a speed ratio of 1.4. Moreover, subsequent heat treatment

of asymmetrically-rolled samples produced an equiaxed microstructure with less α -fiber ({110} orientations), so there is less planar anisotropy in the sheets [64].

A commonality among the rolled Nb sheets is a lack of {110} (Goss) orientations [24]. These orientations cannot be achieved by rolling, as the stress state facilitates rotations towards orientations between {001} and {111} aligned with the sheet normal direction. However, unlike silicon steel, where a high fraction of {110} orientations can be obtained by recrystallization after deformation, {110} orientations are rarely observed even in annealed Nb sheets. The difference in recrystallization behavior despite other similarities between the two materials could be due to the existence of small particles in silicon steels or the opposite elastic anisotropy of Nb and Fe [24].

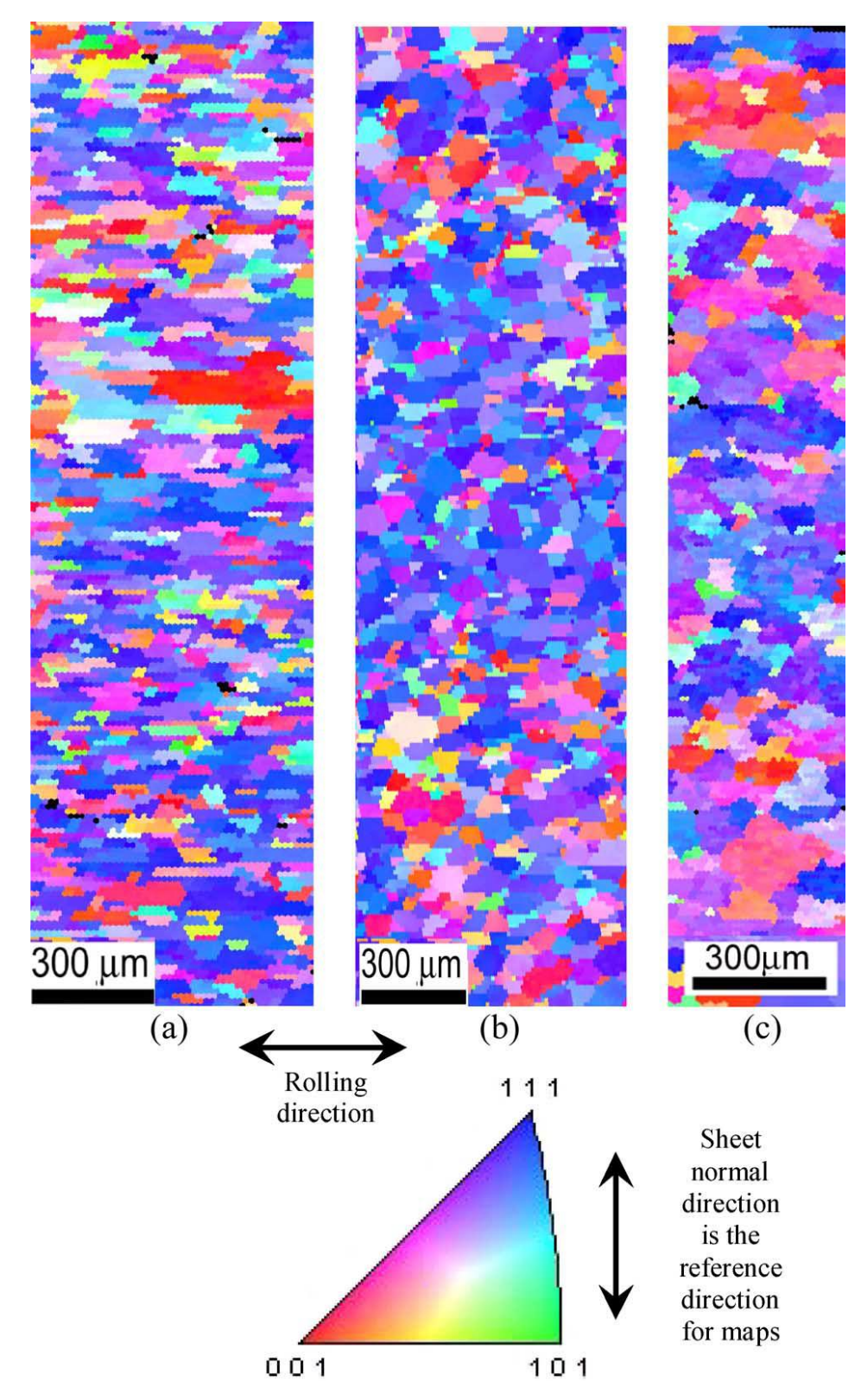


Figure 11: Orientation maps of the full thickness of Nb tensile specimens from (a) Wah-Chang as-received ILC sheet (b) Wah-Chang as-received ILC sheet after annealing (c) Tokyo-Denkai as-received sheet [Figure 2 in reference [63]].

To identify how specific orientations respond to rolling and annealing, Nb samples with much larger grains were studied. Srinivasan *et al.* rolled Nb single crystals with {001}, {110}, and {111} orientations to strains of 25-50% [66]. After deformation, the samples were annealed at 800 °C, 1000 °C, and 1200 °C for three hours. The {001} and {110} samples exhibited good orientation stability, i.e., no recrystallization occurred after annealing. This is consistent with a minor hardness increase in these samples after rolling, which indicates low work hardening and stored energy. On the other hand, the {111} samples deformed to 50% strain showed more work hardening and consequently, enhanced recovery in hardness after the 1000 °C and 1200 °C heat treatment, due to partial recrystallization. The greater residual hardness of these samples can be attributed to a higher GND content to accommodate the lattice curvature in non-recrystallized regions [66].

Sandim *et al.* also investigated orientation evolution during rolling and annealing of Nb. One of their studies used high-resolution electron backscatter diffraction (EBSD) to observe the subdivision of three neighboring grains in coarse-grained Nb rolled to 80% [67]. Results show strong orientation dependence in grain fragmentation – two of the grains developed deformation bands nearly parallel to the rolling direction, while the Goss-oriented third grain developed a more organized microstructure. Two other studies by Sandim *et al.* involved recrystallization of rolled large grain Nb [68, 69]. In both cases, highly misoriented lamellar boundaries formed due to heterogeneous deformation in rolling. Upon annealing, these boundaries served as nucleation sites for grains, but the original grain boundary in the lesser deformed bi-crystal sample (rolled to 70%) was also confirmed to be a nucleation site. Abnormal sub-grain growth was proposed to account for the formation of other grains during recrystallization [68].

g. Cavity Fabrication and Surface Studies

This section will introduce major steps in forming cavities from fine grain or large grain disks and review prior studies that correlate the microstructures with the performance of cavities.

The smallest unit of a cavity is a half-cell, formed by deep drawing as illustrated in Figure 12 [37]. Half-cells are typically formed by deep drawing Nb disks and are electron beam welded together at the equator and iris to form a series of cells. A schematic configuration of deep drawing is also shown in Figure 12 [37].

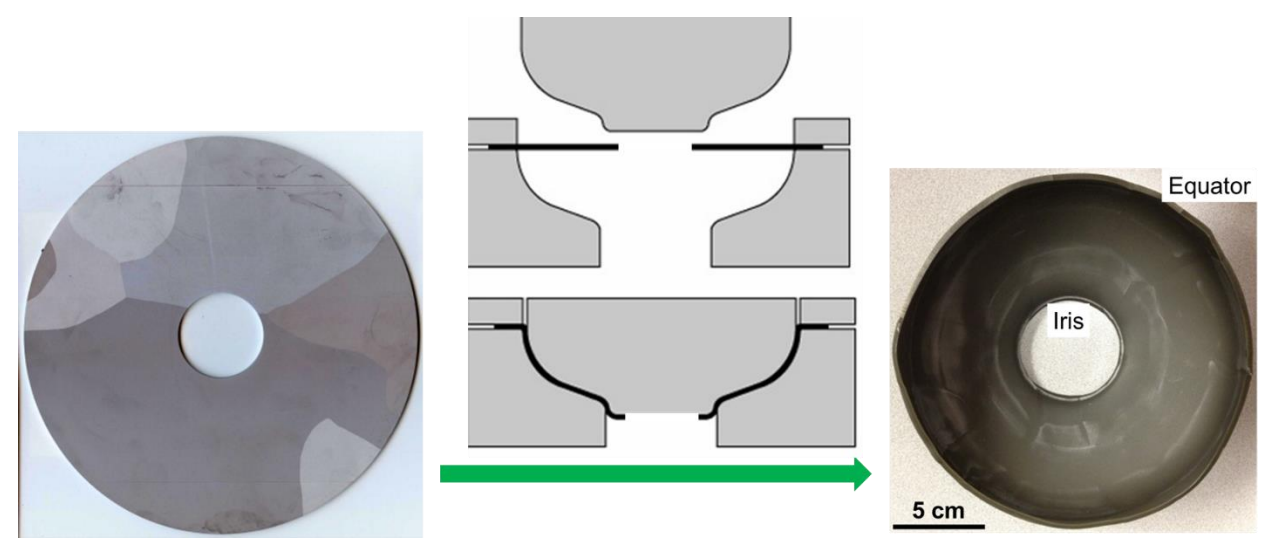


Figure 12: A half-cell (right) formed from a large grain ingot slice (left) by deep drawing, and a schematic of the process is shown in the middle [adapted from Figure 8 in reference [37]].

After welding, the inner surface of a cavity is cleaned using buffered chemical polishing (BCP) [37]. The BCP solution is a mixture of phosphoric acid, hydrofluoric acid, and nitric acid in the ratio of 1:1:2 [70]. A typical removal rate is \sim 1 μ m/min. The solution needs to be cooled in order to minimize hydrogen contamination via diffusion [37].

Next, the cavity is heat treated in a vacuum furnace to remove most of the dislocations introduced during forming. Various schedules have been used in the SRF community, such as

600 °C for 10 hours, 800 °C for two hours, and 1000 °C for two hours, and no agreement has yet been reached as to which one is the most beneficial for cavity performance [71, 72].

A thin and stable pentoxide layer tends to form on the surface of Nb with exposure to air or water. The equilibrium thickness of the oxide layer is on average ~5 nm, but is dependent on crystal orientations [3]. While the oxide itself does not greatly degrade the superconducting properties of Nb, the interface between the oxide layer and Nb can absorb contaminants, such as hydrogen [73, 74]. A vacuum anneal above 500 °C is effective in dissolving the surface oxide into the bulk [75]. The heat treatment also removes hydrogen contamination during BCP [3].

During the heat treatment of a cavity, microstructural changes occur by the mechanisms of recovery, recrystallization, or a combination of both [24, 29]. Recovery takes place when a plastically deformed material is heated to moderate temperatures. When high purity Nb is heated to 700-800 °C (about 35% of its melting point), the stored strain energy from plastic deformation is first released by local rearrangements of dislocations, where nearby dislocations with opposite signs annihilate with each other. The strain energy is further reduced as low angle boundaries (<5° misorientation) begin to form [29]. Both processes require the reduction of defect structure and climb of dislocations, so they only occur when there is enough thermal energy for local as well as long-range diffusion [24, 29].

When the heating is above a critical temperature, new grains containing few dislocations emerge in the recovered microstructure, and grains with fewer dislocations grow into those with more dislocations [24, 29]. This is the process of recrystallization, during which high angle grain boundaries (>10° misorientation) are produced [29].

The inverse pole figures in Figure 13 illustrate the effects of deformation and heat treatment [24]. The EBSD measurements were done on different samples for the four conditions, so they do not describe orientation evolution. Typically, the orientation spread is highest in the deformed condition and drops as recrystallization occurs. The orientation spread is similar to the LAM in reflecting dislocation content, but it is a larger-scale evaluation. The moderate orientation spread in the recovered state reflects the presence of sub-grains. This Figure is a simplified representation of the evolution of dislocations along the cavity fabrication path – dislocations nucleate during the ingot solidification due to the large thermal gradient; dislocation multiplication occurs during deep drawing through Frank-Read sources and cross slip; annealing removes SSDs by recovery and more dislocations by recrystallization [29]. Complete recrystallization is believed to be necessary for the optimal superconducting and mechanical properties of fine grain Nb [3].

Materials subjected to a small amount of deformation usually have large recrystallized grains upon annealing, while heavily deformed single crystals annealed at low temperatures for short times tend to have small recrystallized grains, including nanocrystals. The recrystallization temperature decreases with increasing purity [3]. It is also possible to achieve recovery without recrystallization in large grain cavities by annealing at low temperatures for a long time [3].

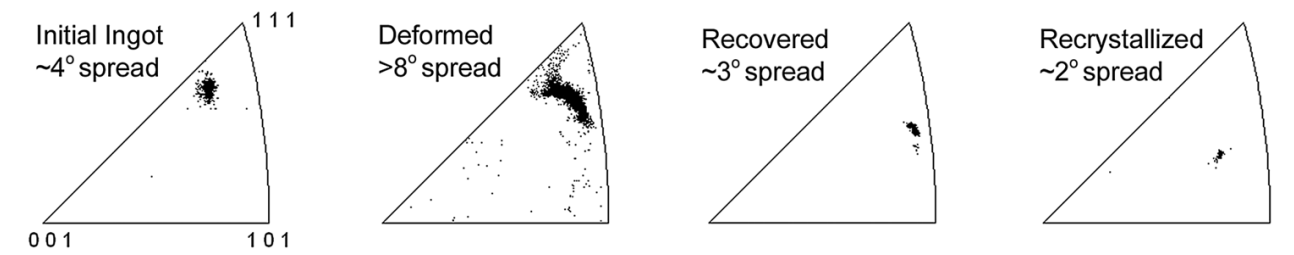


Figure 13: Representative inverse pole figures from EBSD measurements on different samples. The orientation spread is greatest after deformation and is least in the recrystallized condition [adapted from Figure 9 in reference [24]].

The surface of a cavity tends to have a higher dislocation content than the bulk due to the friction effects from the die in deep drawing, and a BCP etch is necessary to remove the surface damage layer. Kneisel *et al.* identified the dependence of achievable accelerating gradients on the amount of material removed from the cavity surface (Figure 14) [76]. The test was stopped at about 180 µm as the cavity performance was acceptable for their application. The thickness of the damage layer was estimated to be 100-200 µm. Therefore, removing surface material from deep drawn cavities via barrel polishing and chemical treatments has become normative in the SRF community.

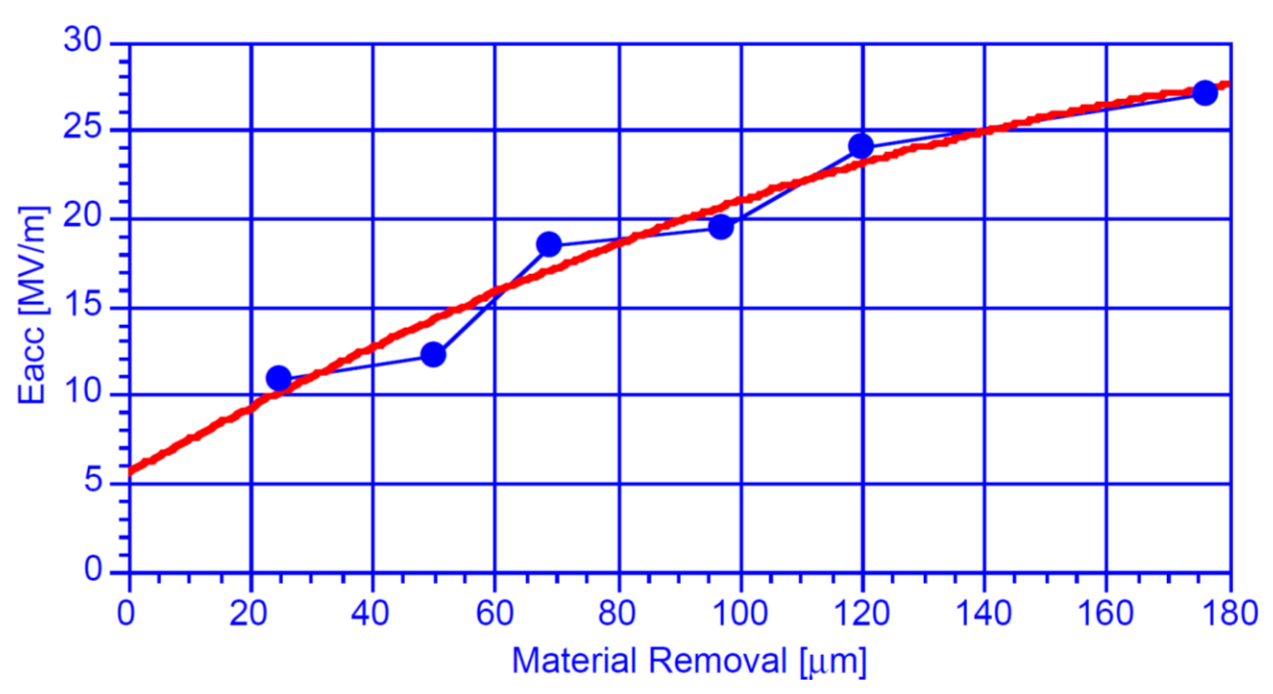


Figure 14: Dependence of achievable accelerating gradient on the thickness of material removed from surface, measured on a fine grain cavity [adapted from Figure 3 in reference [76]].

Romanenko *et al.* observed a striking effect of the low-temperature bake on dislocations [27]. Figure 15 shows the LAM values for small/large grain cavity samples cleaned by BCP or electropolishing (EP), before and after the bake [27]. Except for the small grain BCP case, LAM

values were noticeably lower after baking, suggesting that dislocations were removed. However, some grains resisted recovery/recrystallization and retained a high dislocation density [27].

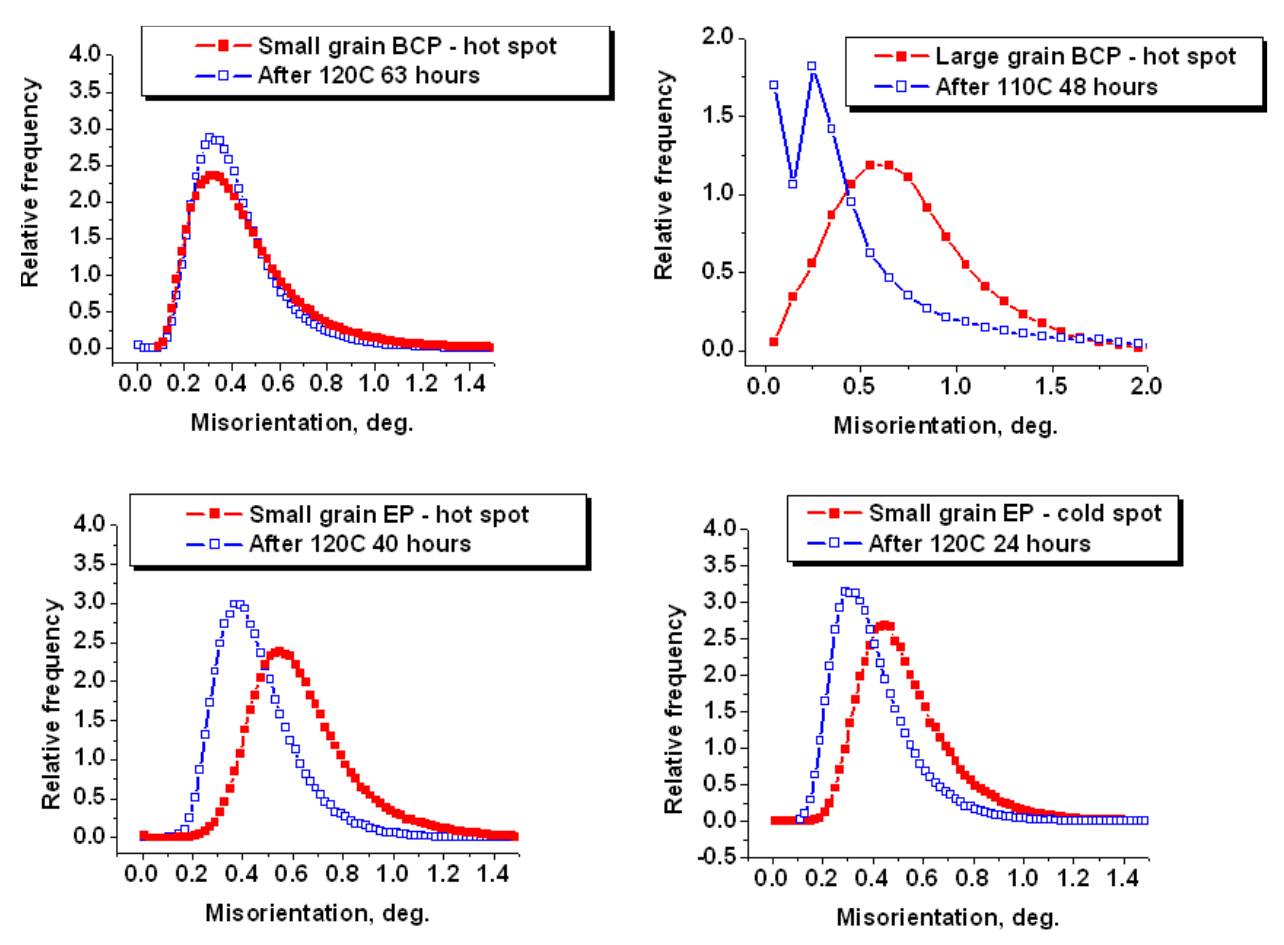


Figure 15: Change in local average misorientations (LAMs) on cavity samples due to baking. In each case, measurements were made on the same sample before and after baking in ultra-high vacuum [Figure 2 in reference [27]].

Initiation of flux penetration corresponds to RF losses during cavity tests [3, 77]. After baking, the onset of flux penetration shifted towards higher fields for both hot and cold spots, which is consistent with prior observations on dislocation density [27]. Also, hydride precipitates were identified on Nb samples cut from cavities after cryogenic RF tests, and the hydride concentration was higher on hot spots (high dislocation content) than it was on cold spots [3].

Hydrogen tends to segregate along dislocations and form "Cottrell clouds." The high local concentration of hydrogen facilitated the formation of hydrides upon RF cycling [3].

This series of cavity test results again show that dislocations play a significant role in the superconducting behavior of Nb and that reducing the dislocation content is essential to improve the reproducibility of cavity performance [3].

h. Active Slip Systems in Nb

Slip during plastic deformation is the underlying mechanism that accounts for many of the cavity performance phenomena previously discussed. This section will cover fundamental studies on slip in Nb, along with general theories on deformation in bcc metals.

In the cavity fabrication process, crystal orientations, active slip systems, dislocation substructure, and recrystallization during annealing are interrelated from the metallurgical perspective [24]. Slip behavior depends on how crystals are oriented with respect to the applied stress; slip and interactions of slip systems result in a specific dislocation substructure; the dislocation substructure determines how recovery and recrystallization proceed during heat treatments, and the remaining dislocations may be defective regions in a cavity [26, 27, 78].

Establishing the correct model for slip systems is particularly important for predicting the microstructural evolution during the cavity fabrication process. To understand slip during deep drawing of a large grain Nb disks, knowledge about slip in simpler uniaxial tension of single crystal Nb is needed to provide an initial basis. Specifically, the study of slip addresses two concerns – the effective/macroscopic slip planes (evident by slip trace analysis and crystal rotation), and planes on which kink pairs nucleate along dislocation lines (fundamental/atomic slip planes) [79].

For bcc metals, the close-packed (hence slip) directions are <111>, but there are no close-packed planes like those in face-centered cubic metals [79]. Planes containing the close-packed direction with a decreasing order of inter-planar spacing are {110}, {112}, and {123}. No stable stacking faults have been found in bcc metals due to their high stacking fault energy, so no slip planes are defined by dislocation dissociations either. Kocks described "pencil glide," in which slip occurs in <111> directions without following any particular slip planes [79, 80].

In bcc materials, edge dislocations have lower lattice friction and are more mobile than screw dislocations at room temperature, so screw dislocations are the rate-controlling mechanism during plastic deformation [24]. Since the motion of screw dislocations is thermally activated, it will likely occur by nucleation of kink pairs on well-defined atomic planes [79]. The kink pair nucleation mechanism gives rise to the temperature and strain rate dependence of flow stresses in bcc metals [79].

The low mobility of bcc screw dislocations can be partly explained by the core relaxation theory [81-85]. A <111> bcc screw dislocation core tends to spread onto three symmetric {110} or {112} planes, which results in a non-planar core structure and hinders the movement of screw dislocations [86]. Consequently, screw dislocation mobility is affected by non-glide shear stresses, resulting in a violation of the Schmid law. Due to their low mobility, long and drawn-out screw dislocations are usually left behind during plastic deformation and are observable [16].

The core relaxation in Nb depends on both the temperature and purity [87-89]. Seeger argued that fundamental slip planes change from {110} at low temperatures (<100 K) to {112} at higher temperatures due to a change in the core structure [88]. Experimental results from many bcc materials support this theory, but there are exceptions [90-94]. Interstitial impurities such as

hydrogen stabilize the {110} relaxation [85, 95]. SRF cavities are fabricated from high purity Nb at room temperature, so the {112} relaxation should be favored over {110}. However, the forming process could lead to hydrogen contamination so that both relaxations may coexist [16]. The differences between {110} and {112} relaxations account for the differences in critical resolved shear stresses between {110} and {112} planes [16].

In contrast, atomistic simulations of bcc metals predict that slip should occur fundamentally on {110} planes, regardless of the interatomic potential, boundary conditions, or material purity [79]. Atomistic simulations have been successful in predicting mechanical properties of bcc metals, e.g., in demonstrating that non-planar screw dislocation cores lead to strong lattice resistance and thermally activated plasticity [79]. Furthermore, net {112} slip could occur by the motion of screw dislocations on alternating {110} planes, and the core structure does not straightforwardly dictate apparent slip planes [79].

Another phenomenon unique to bcc metals is the twinning/anti-twinning asymmetry, in which a smaller resolved shear stress is needed to move a screw dislocation in the twinning sense of slip than in the anti-twinning sense [86, 87, 96, 97]. This asymmetry has been attributed to the energy required to displace an atom within a given slip plane in the direction of the Burgers vector. The twinning/anti-twinning asymmetry and non-planar screw dislocation cores give rise to the non-Schmid effects in bcc metals and affect the critical resolved shear stress for a given slip system to varying extents [86, 87, 96, 97]. Atomistic simulations have confirmed the presence of the twinning/anti-twinning asymmetry [79].

The relationship between slip systems may change with deformation due to the rotation of the crystal with respect to the applied stress. A general rule regarding work hardening is that if the operating slip systems have a common slip direction, little hardening results; but there will be significant work hardening if the slip systems have different slip directions. For example, the interaction of intersecting <111> slip systems could leave behind sessile dislocations with the resulting Burgers vector on a non-close packed {100} plane [79].

Slip trace analysis has been widely used in fundamental studies of slip. Deformation experiments lead to transport of material by dislocations onto a free surface, forming slip traces. These slip traces can be imaged in several ways, such as optical microscopy, scanning electron microscopy (SEM), and atomic force microscopy [79, 98, 99].

Slip trace analysis may be complicated by the tendency of bcc screw dislocations to cross slip on either {112} or {110} planes due to core relaxation [85, 95]. Figure 16 shows an illustration of this effect, where frequent changes in slip planes lead to a wavy slip trace that roughly follows the trace of a highly stressed plane [16]. This causes the problem of imitation, where cross slip occurs over a small length scale, such that the macroscopic slip trace appears straight rather than serrated and is mistaken for a slip trace of the other slip plane family. The smaller the distance between cross-slip events, which may occur at nanometer scale [85, 95], the more difficult to distinguish that a slip trace was formed by a combination of two individual slip traces.

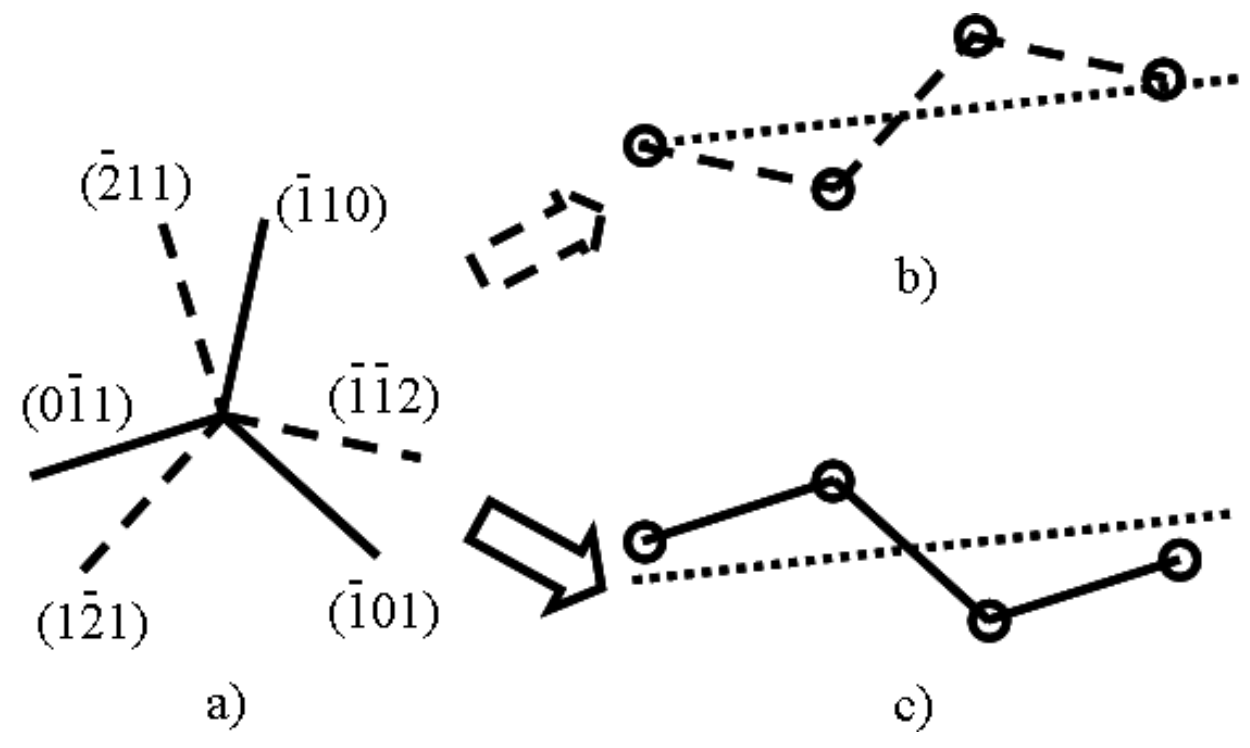


Figure 16: A schematic diagram showing a [111] bcc screw dislocation with its Burgers vector and line direction out of the page, and the effect of core relaxation on a slip trace: a) The core may relax on either three symmetric {112} planes (dashed lines) or three symmetric {110} planes (solid lines). Motion of the dislocation can leave a trace on a surface indicating the slip plane for: b) {112} relaxation, the screw dislocation may frequently cross slip on two of the three {112} relaxation planes (each change in plane marked by a circle), while following a high resolved shear stress plane (fine dotted line). c) For {110} relaxation, the screw dislocation may frequently cross slip on two of the {110} planes, while following a high resolved shear stress plane [Figure II-13 in reference [16]].

A limitation of slip trace analysis is that slip may be influenced by the presence of a free surface, as evidenced by studies using thin foils [79, 100, 101]. Vesely noticed on molybdenum thin foils that the activated slip systems have a Burgers vector nearly parallel to the surface besides having a high resolved shear stress [100, 101]. A similar outcome was obtained by Luft and Kaun [102], who studied thin foils with different exposed faces and compared the results to those obtained using cylindrical rods. For the thin foils, the slip traces were determined by the subsurface dislocations, which might not be a good representation of the bulk behavior. Therefore, slip trace analysis could be misleading in identifying slip planes for bulk plasticity [79, 100-102].

Slip in the various bcc metals has a lot in common, although each material has its subtleties [79]. Investigation of slip in Nb started over 60 years ago when several researchers deformed single crystal Nb under different experimental conditions [90, 94, 103-105]. More attention has been put into Nb over the past few decades, as it became the material of choice to build SRF cavities. The following paragraphs will concentrate on slip in high purity Nb at room temperature, which is the condition during SRF cavity manufacturing.

Maddin and Chen used optical slip trace analyses and Laue X-ray diffraction to identify slip only on {110} planes in Nb at room temperature in both tension and compression across the unit triangle [90]. In the work of Duesbery and Foxall (referred to as D&F later), slip was observed on either {110} or {112} planes depending on the stress axis and the orientation of single crystals as detailed in [104]. Baars also investigated slip systems in Nb, and his findings will be summarized in the following paragraphs [16]. Results from the D&F set will be compared to the work by Baars [16].

Baars [16] extracted 12 sets of single crystals with different orientations from a large grain Nb ingot slice supplied by Ningxia. The orientations were chosen to initially favor a single slip system or a combination of slip systems. The interstitial impurity content of the Ningxia samples is high enough such that elementary slip on both {112} and {110} planes should be considered [16, 95]. However, the results suggest that the dominant slip systems at yield are {112}. This is based upon the interpretation of the stress-strain behavior of a sample that was oriented to favor a single {110} slip system, but its initial hardening behavior resembled another sample that favored two intersecting {112} slip systems. Therefore, it was concluded that the onset of hardening in both samples was predominantly caused by two {112} slip systems interfering with each other [16]. Furthermore, samples with larger differences between the initial resolved shear stress on

intersecting {112} slip systems have a lower initial hardening slope, while those with smaller differences have a higher initial hardening slope [16]. Considering only the {110} slip systems or a combination of {110} and {112} slip systems does not give the same correlation on hardening. The rotation of tensile axes can also be explained by the dominance of {112} slip systems at yield [16].

A ratio between the shear stress of the two most-stressed intersecting {112} slip systems below 1.1 correlates well with hardening at yield, suggesting that the combined twinning/antitwinning and non-glide shear stress effects may only alter the critical resolved shear stress by a small amount [16]. Thus, incorporation of many of these details may not be necessary for practical models for the deformation of large grain Nb. Initial simulation results from Mapar *et al.* suggest that the shape change in the tensile samples can be adequately modeled (determined by slip planes and kinematics). However, the non-Schmid effects are still needed to get the stress levels correct (shown later) [106].

The dominance of {112} slip at yield followed by {110} slip for the rest of deformation appears to comply with the theory of Seeger *et al.* [16, 95], which suggests that the core relaxation of screw dislocations in high purity Nb is on {112} planes, and that impurities change the core relaxation to {110} planes. This indicates that the initial interstitial impurities of ~400 at. ppm (plus hydrogen absorbed during sample preparation) did not cause a significant amount of {110} relaxation at yield, but the additional impurities absorbed during deformation in the air (due to breakdown of the surface oxide layer that allows hydrogen to get in) changed the relaxation to {110} type [16]. The possibility that the favored slip plane could change during deformation due to absorbed impurities such as hydrogen poses a challenge to the modeling of slip in Nb [16].

Bands with distinct orientations are more evident in the deformed samples favoring intersecting slip systems than in samples with easy glide orientations [16]. This suggests that with the same amount of strain, samples can have different amounts of GNDs, which could account for delayed observation of deformation bands until strains are large. Even though uniaxial tension is not the stress state for fabricating cavities, this implies that selecting a strategic orientation may be important for minimizing dislocation content and for ensuring that dislocations are aligned desirably in a cavity. Also, samples with higher dislocation content are more prone to recrystallization, which may lead to unexpected grains upon annealing [16].

The impurity content and experimental conditions of the D&F data set are close to the Ningxia samples, except that preexisting dislocations should be minimal in the D&F set (grown by electron beam zone melting) due to their anneal before deformation [16, 104]. The lower yield stress in the D&F set is consistent with their higher purity, though the interstitial impurity content is still high enough so that {110} slip must be considered [16, 104].

The D&F set shows the same trend as the Ningxia set, in which a decreasing difference in the resolved shear stresses of the intersecting most-stressed {112} slip systems at yield correlates well with the initial hardening slope [16, 104]. However, the trend is also present in the D&F set if the intersecting most-stressed {110} slip systems or the two most-stressed systems are compared. This leaves some uncertainty about active slip systems at yield for the D&F set [104].

Figure 17 shows a stereographic projection section of the tensile axes for both the D&F and Ningxia samples, with boundaries of equal Schmid factor (resolved shear stress) between {110} and {112} slip systems whose <111> slip directions are either parallel or intersecting [16]. As the twinning/anti-twinning asymmetry and non-glide stresses could alter the critical resolved shear

stress, the boundaries with both slip systems equally active may be shifted. Some of the boundaries may not even exist depending on the experimental conditions (i.e., purity and temperature). This Figure is useful in selecting orientations that favor specific slip systems for further investigations into slip systems in Nb or for forming cavities [16].

Overall, the outcomes from the Ningxia and D&F sets are consistent with dominant {112} slip at yield [16]. The occasional {110} slip observed at yield in the D&F set may come from imitation by frequent cross slip on {112} slip planes, though this requires that the imitating (less stressed) slip systems be activated by the twinning/anti-twinning and non-glide stress effects [16]. While dislocation motion unhindered by impurities tends to occur in bursts that should be visible at the scale at which the samples were imaged, it remains unclear if this possibility of imitation can be eliminated [16, 107-109].

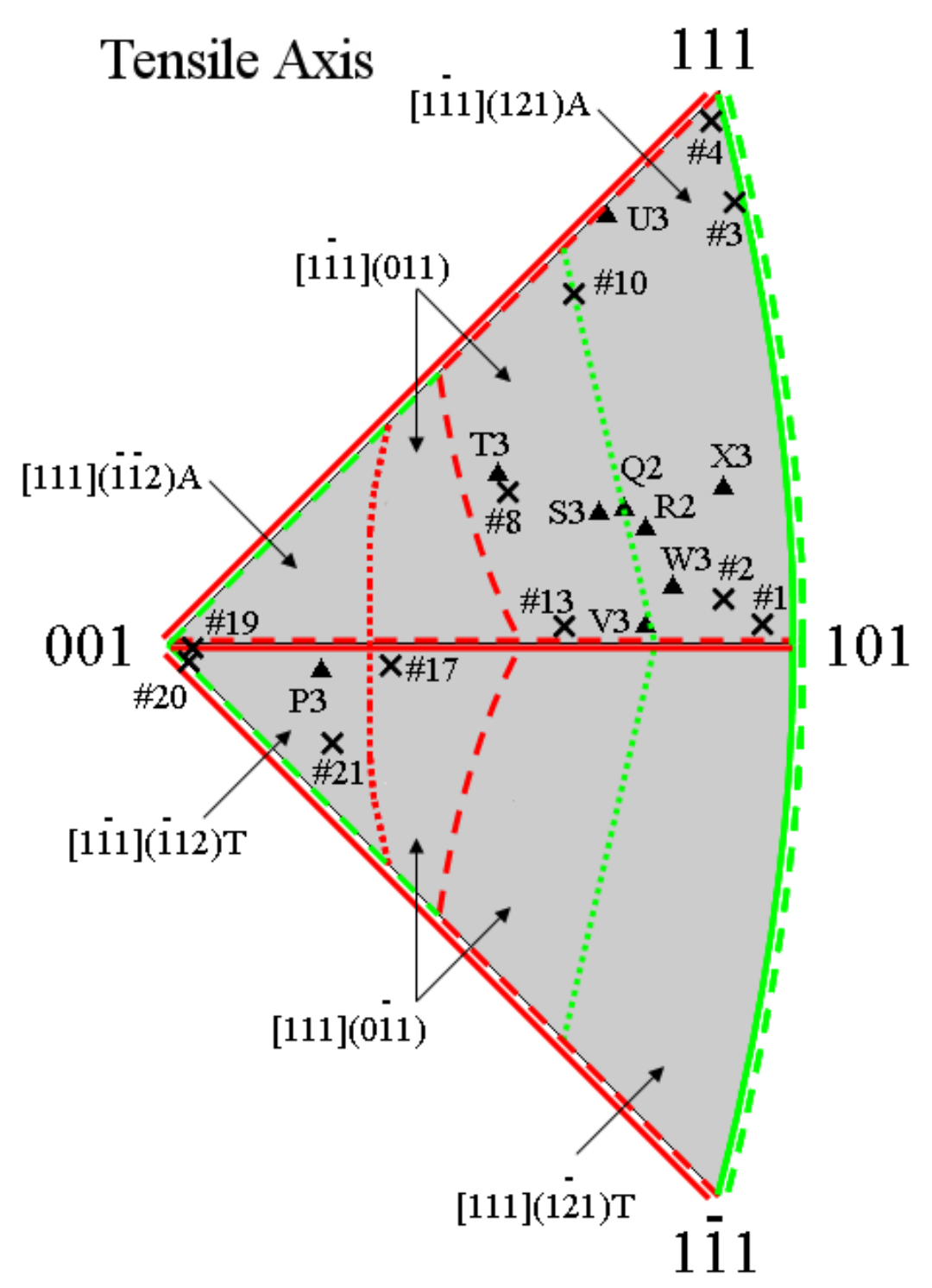


Figure 17: Initial tensile axes for D&F and Ningxia samples on a stereographic projection section. The boundaries mark where the Schmid factors are equal between two {110} slip systems (solid lines), two {112} slip systems (dashed lines), a {110} and a {112} slip system (dotted lines). The boundary is colored green for the same slip direction, and red for intersecting slip directions. Slip systems whose Schmid factors are greatest in the area between the boundaries are labeled [Figure V-9 in reference [16]].

i. Observation of Dislocations in Nb

Direct observation of dislocations complements slip analyses, since it provides additional details about the deformation mechanism. Dislocations in Nb have been imaged by transmission electron microscopy (TEM) since the 1960s, as will be reviewed in this section.

Stiegler *et al.* studied the dislocation evolution during rolling and annealing of Nb single crystals [110]. For a rolling reduction up to 10%, dislocation entanglements were confined to a ~100 µm surface layer, while the bulk developed a distinctive cell structure¹. With 80% reduction, individual cells were no longer discernible [110]. After heat treatment, dislocations inside the cells moved towards the walls to form organized networks [110]. At higher temperatures, regions with low dislocation content were formed by sweeping of dislocations out of the networks facilitated by the thermal energy [110]. Figure 18 shows the cell structure on a 50% reduction sample and the organized dislocation networks on a 98% reduction sample that was annealed at 900 °C for an hour [110].

Bowen *et al.* deformed Nb single crystals in uniaxial tension at room temperature and observed long clusters of edge dislocations on {112} slip planes in stage I work hardening [103]. During stage II, densely packed secondary dislocations built up within the cell structure, as in the case of rolling. A similar study by Foxall *et al.* also demonstrated the presence of edge dislocations in the form of dipoles and loops in stage I [94]. They further observed that dislocations in stage II were primarily distributed in tilt and twist boundaries as well as in edge multipole walls [94].

42

¹ No details about rolling were provided in the paper; as actual strain history depends on roller size, sample thickness, and strain per pass, these results may not be consistent with other studies.

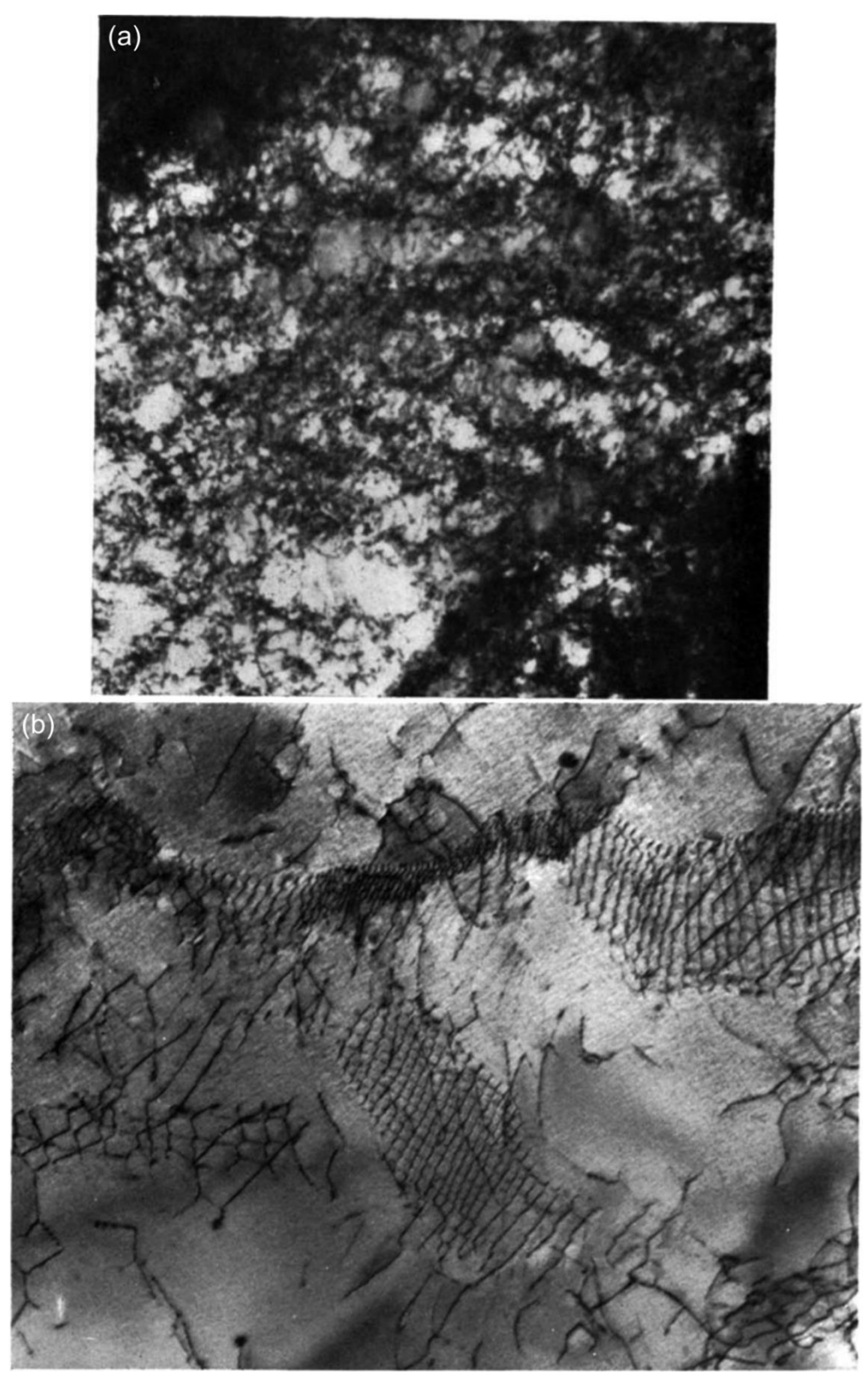


Figure 18: TEM micrographs of (a) dislocation cell structure in a Nb sample cold rolled to 50% ($45,000\times$ magnification) (b) dislocation networks in a Nb sample rolled to 98% and annealed at 900 °C/1h ($44,000\times$ magnification) [Figure 5 and Figure 9 in reference [110]].

In contrast, Ikeno *et al.* observed mainly screw dislocations on single crystal Nb thin foils stretched at room temperature (strain level not specified) [111]. They argued that the clusters of dislocation dipoles originated from jogs rather than from dislocation trapping. As their experiment was done *in-situ*, they suggested that the previously identified dislocation substructure in Nb could be partly due to artifacts during sample unloading and thinning [111]. Dislocations of screw character were also observed by Thompson *et al.* [112] on polycrystalline Nb samples deformed by cold rolling and drawing.

Louchet *et al.* conducted *in-situ* tensile tests of Nb thin foils at different temperatures [83]. They observed that screw dislocations dictate the deformation behavior below ~200 K, while the room temperature deformation is dominated by the motion of mixed dislocations with short, pure screw segments [83].

Chang *et al.* examined the interactions of glissile dislocations in Nb [113]. Even though all interactions led to sessile dislocations with <100> or <110> Burgers vectors, one interaction surprisingly facilitated slip by promoting the cross slip of a portion of one reactant mobile <111> dislocations [113]. This implies that not all interactions of intersecting slip systems would necessarily hinder the slip process, and adds to the complexity of deformation of Nb [113].

In summary, both edge and screw dislocations in cell/wall structures have been identified in deformed Nb samples by TEM. While it is generally believed that screw dislocations dictate the room temperature deformation of Nb, edge dislocations are commonly observed. Therefore, it would be desirable to characterize dislocations in Nb using nondestructive techniques such as electron channeling contrast imaging (ECCI) [114] to minimize artifacts from sample preparation, which is lacking in the literature.

j. Evaluation of GNDs using cross-correlation EBSD

In the past decade, a cross-correlation based analysis of high-resolution EBSD patterns has been developed, and it enables estimating GND content and arrangement in deformed materials [115-118]. The cross-correlation EBSD (CC-EBSD) method bridges the gap between localized imaging techniques such as TEM and macroscopic analyzing techniques such as X-ray diffraction for characterizing dislocations [116].

In CC-EBSD, variations in elastic strain and lattice curvature are calculated from subtle shifts in the positions of zone axes and other diffraction features in EBSD patterns, based upon a chosen reference pattern with zero or known strain [116]. Strains as low as 10^{-4} and rotations as low as 0.006° can be resolved [116, 117]. Even if the strain is unknown for a reference pattern, the GND distribution can still be extracted as only the gradients of strains and lattice rotations are needed for the evaluation [116].

CC-EBSD was initially applied to semiconductors due to their well-defined geometry and low dislocation density, and it has evolved to be sufficiently reliable for structural materials such as metals [116, 118]. Wilkinson *et al.* demonstrated satisfactory utility of the method for studying dislocation in four deformation modes of metallic systems – nanoindentation, phase transformation, thermal contraction, and fatigue [116].

To better understand the capabilities and limitations of CC-EBSD, Dunlap *et al.* compared the dislocation distributions calculated from CC-EBSD with direct observations from ECCI [119]. The dislocation densities measured by both methods show good agreement, though the discrepancy in spatial arrangements is more significant [119]. Figure 19 shows a comparison of ECCI and CC-EBSD from the same area near an indent, in which the approximate locations of dislocations match,

but there is no one-to-one correlation [119]. The discrepancy may result from two aspects – CC-EBSD could miss dipoles due to its inferior spatial resolution, while ECCI could miss dislocations due to invisibility criteria or may be unable to resolve clusters of dislocations [119].

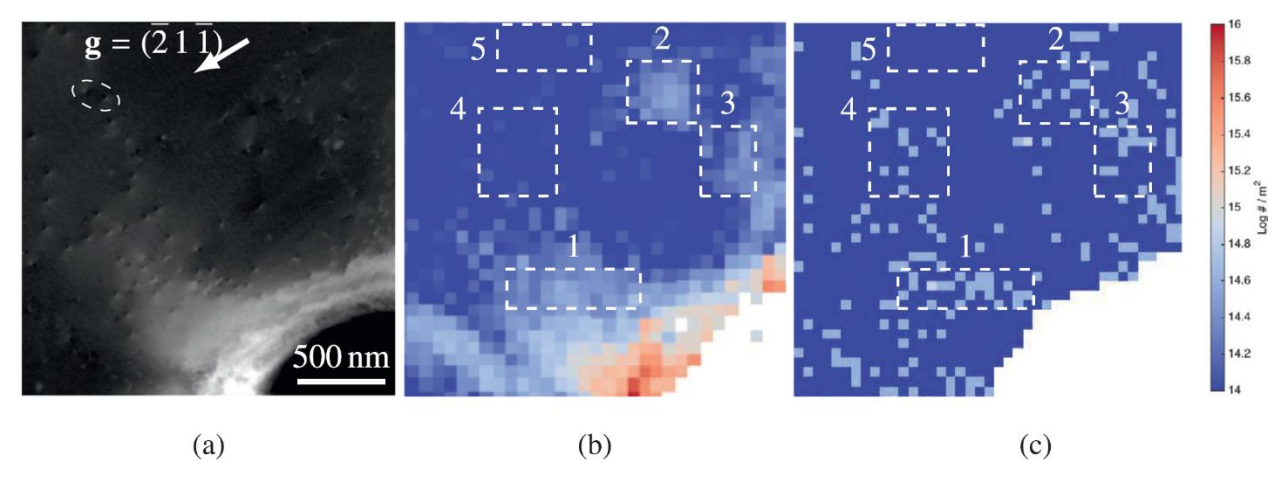


Figure 19: (a) Electron channeling contrast (ECC) image of dislocations near an indent (b) GND density map of the same area generated from CC-EBSD showing similar dislocation distribution (c) Dislocation density map calculated by counting dislocations in the ECC image [Figure 3 in reference [119]].

Estimation of GND density using CC-EBSD may be influenced by step size and binning (averaging adjacent pixels in a pattern) [120, 121]. Jiang *et al.* discovered that an increase in the step size of EBSD scans leads to lower GND density because some dislocations will be considered as SSDs [120]. GND density maps of a deformed Cu sample exhibited noticeable loss of features when the step size was changed from 0.5 to 2 μ m, as the dislocation cell size is about 1.5 μ m in the material [120]. They also found that pattern binning (up to 8x8) does not affect the calculated GND density significantly, giving the potential for speeding up CC-EBSD data acquisition.

Ruggles *et al.* modeled the change in calculated GND density as a function of step size by incorporating the transition of GNDs into SSDs due to the implicit Burgers circuit defined by step size [121]. They found a range of steps sizes where the calculated GND density is nearly constant

for a given sample, thus establishing robust criteria for step size selection [121]. Their simulations also indicate a much higher portion of GNDs in heterogeneously deformed specimens than those subjected to homogeneous deformation [121]. The model provides the potential of estimating overall dislocation content since it accounts for SSD contributions, which would be a significant advance in the EBSD-based dislocation analysis [121].

In brief, GND density and distribution in deformed materials can be conveniently assessed by the CC-EBSD method. Because of the ease of use and extensive availability of EBSD systems, this method can provide considerable insights into the field of materials science and plasticity.

k. Opportunities for Research

As reviewed in previous sections, material studies on Nb used in SRF cavities followed both science (fundamental understanding) and engineering (cavity fabrication) approaches. This combination of approaches creates opportunities for obtaining a deeper understanding of the deformation mechanisms of Nb, such that the microstructural evolution during cavity forming can be modeled, enabling prediction of cavity performance. Outlined below are efforts that have been accomplished in support of research and development programs at Michigan State University (MSU):

Characterization of more ingot slices adds to the literature on the initial condition of Nb ingots and could provide further insights into why microstructures are heterogeneous in rolled polycrystalline sheets. The differences and commonalities in ingot slices from different suppliers may reveal trends to be controlled or exploited.

Characterization of fine grain sheets for use in the Facility for Rare Isotope Beams (FRIB) ensures that the materials meet the specifications defined by FRIB [62], and enables relationships

between microstructure and mechanical properties to be explored. Such data can also be correlated with the performance of future FRIB cavities. Then, it is possible to establish a microstructure-performance model that can simulate cavity forming and operation, which would be valuable to the SRF community.

It is desirable to identify the connection between ingot and sheet microstructures. A rolling experiment of multi-crystals are conducted to make progress toward this goal. Samples with different amounts of cold work reduction are examined before and after annealing to find credible sources for the layered microstructure in the sheet metal.

Studying the microstructural changes during deep drawing and subsequent processing of Nb to supplement the surface studies is valuable, as previous work focused more on cavity testing than on the metallurgical perspective. An assessment of the effects of complex strain paths in deep drawing can be made by comparing the crystal orientations of an ingot slice before and after the deformation. Grain orientation and dislocation substructure will be examined on samples extracted from a large grain cavity that was subjected to the same chemical and heat treatments as in a real cavity. This gives a measure of dislocation evolution in a cavity, which can be correlated with cavity performance results.

On a more fundamental level, a further study of active slip systems in Nb single crystals building on the work of Baars [16] would contribute to the goal of establishing a model that can estimate the final dislocation configuration in cavities by predicting the amount of dislocation glide on various slip systems based upon crystal orientations. As Baars investigated as-received single crystals and deformed them in a conventional test frame with analysis after monotonic deformation to 40% strain, a more detailed examination with *in-situ* tensile tests on a set of neighboring samples

from the same ingot slice that has been annealed provides an opportunity to identify effects of preexisting dislocations on slip behavior. It will also enable a more straightforward interpretation of the results of Baars in the context of a lower initial dislocation density.

A road map that shows the interconnections of the above projects and aids visualization of the logic flow of this work is provided in Figure 20. The letters in parentheses (a-e) correspond to the storylines that will be followed in each of the Materials and methods, Results, and Discussion chapters.

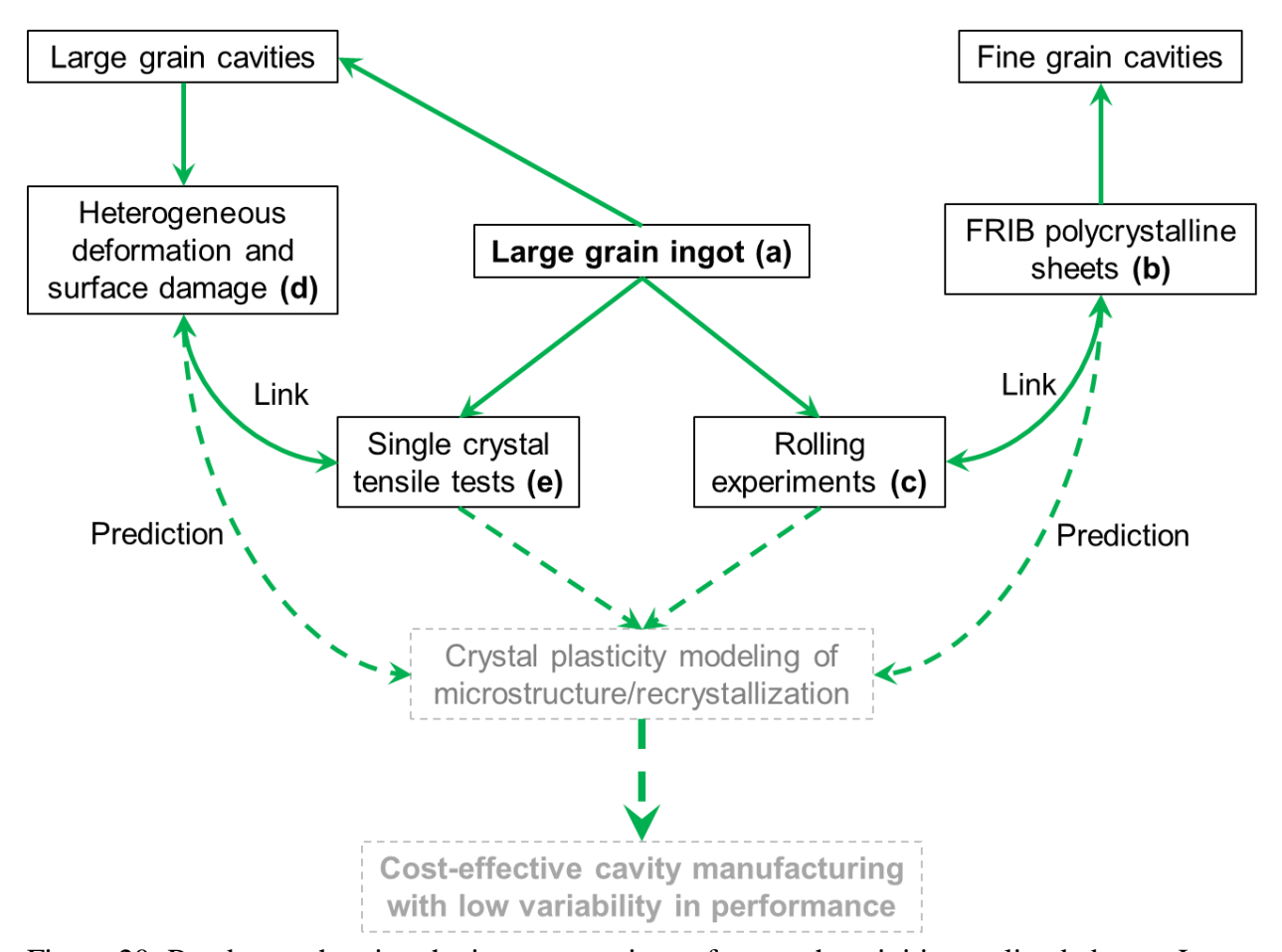


Figure 20: Road map showing the interconnections of research activities outlined above. Letters a-e in parentheses correspond to the section headings in the next three chapters.

III. MATERIALS AND METHODS

An experimental approach is employed to establish the foundation for modeling the microstructural evolution and performance of cavities, as detailed in this chapter.

a. Large Grain Nb Ingots Characterized by EBSD and Laue Camera

This section and corresponding sections in the Results and Discussion chapters are based upon previously published papers [122, 123], with additional figures and details.

Electron backscatter diffraction (EBSD) is a well-established technique for identifying crystal orientations. In EBSD, an electron beam is focused onto a flat crystalline sample whose surface normal is tilted 70° from the beam axis [124]. Electrons that are scattered by the sample in backward directions produce intersecting (Kikuchi) patterns on a fluorescent screen (EBSD camera). These patterns can be converted into crystal orientations through a Hough transform [124]. A schematic configuration of EBSD is shown in Figure 21 [16, 124].

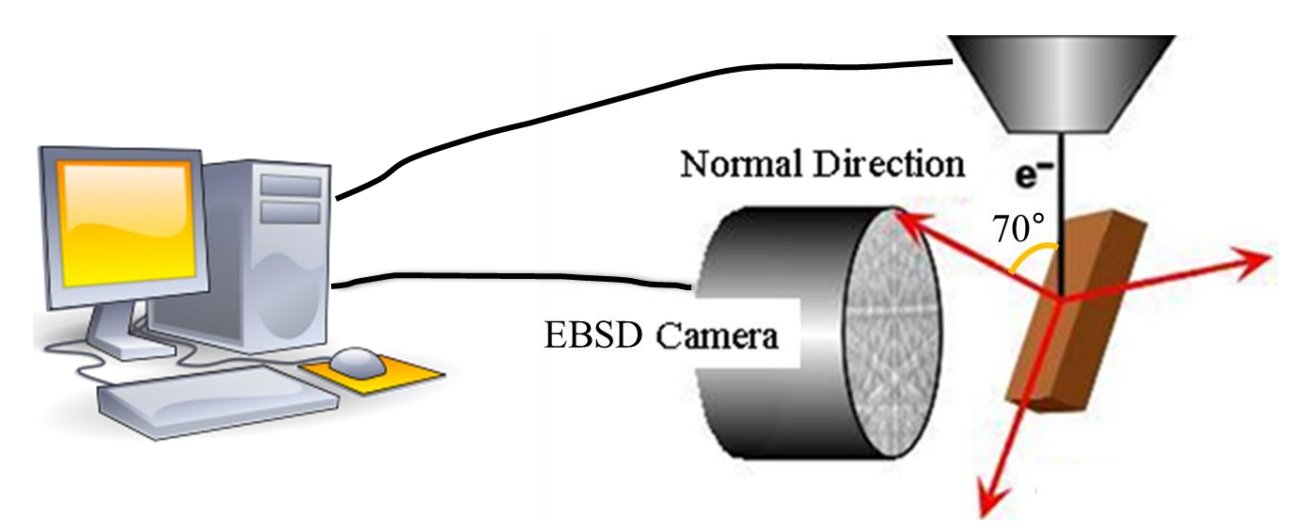


Figure 21: Schematic of the EBSD configuration. The electron beam interacts with a sample that is tilted 70° from the beam axis. Red arrows indicate the coordinate systems used for the crystal orientation. Backscatter electrons form diffraction patterns on the EBSD camera, which are then processed by a computer equipped with data acquisition and analysis software. The electron beam trajectory is also controlled by the computer [adapted from Figure 1.3 in reference [124] and Figure II-15 in reference [16]].

Rather than using EBSD to characterize ingot slices as Baars did [16], it is more practical to measure orientations using the Laue method, in which a beam of white radiation from an X-ray source shines on a sample and is diffracted according to Bragg's law [125]. X-rays diffracted in backward directions (i.e., with large Bragg angles) are recorded by an area detector. Figure 22 illustrates the experimental setup for Laue measurements, in which a Nb ingot slice was attached in front of the Laue camera (Photonic Science Laue X-ray Imaging System, Microphotonics Inc.). The slice was supported vertically by books and held in place with double stick tape on aluminum supports to ensure that the ingot surface is perpendicular to the X-ray beam. This way, the biggest mounting errors exists in the rotation about the ingot surface normal.



Figure 22: Laue camera equipped with area detector, showing how an ingot slice was mounted to determine crystal orientations [Figure 3 in reference [122]].

The collected patterns were indexed with a semi-automatic method using OrientExpress software 3.4, based on the crystal structure of Nb, the sample to detector distance, and dimensions of the area detector. Figure 23 shows an example of a Laue diffraction pattern and the indexing user interface. Typically, five points on multiple hyperbolae need to be specified for indexing a pattern. The orientations were converted to match the EBSD software coordinate system with X pointing down and Y to the right.

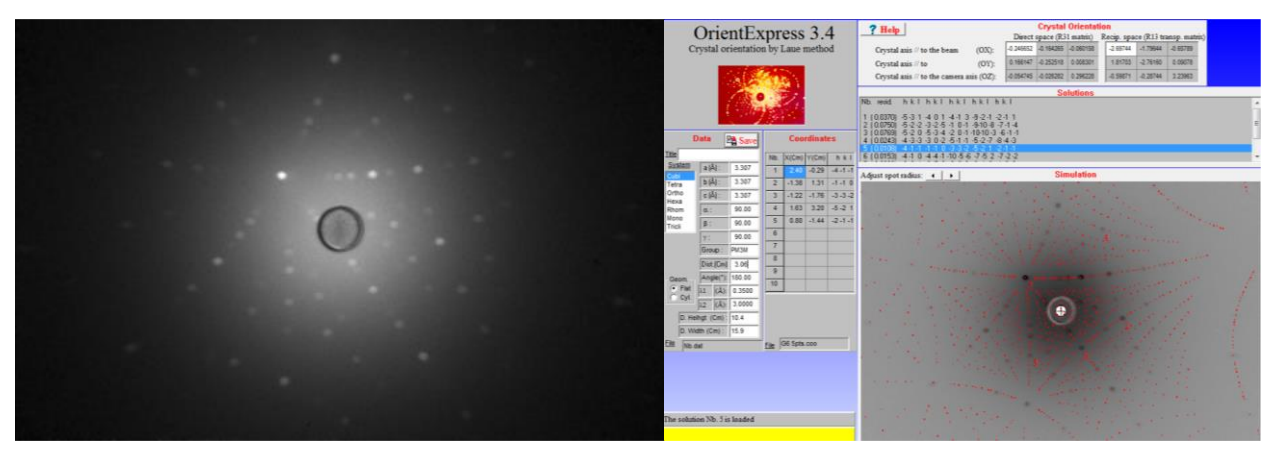


Figure 23: A typical Laue pattern (left) and the indexing user interface (right) [Figure 4 in reference [122]].

Seven ingot slices and a slab cut in the longitudinal direction of an ingot using wire electrodischarge machining (EDM) were examined to identify their crystal orientations. The supplier information for each ingot is shown in Table 1 (ranked by ingot diameter/size), with a name for each that will be used later. Except for the Niowave ingot, the ingot slices are about 3 mm in thickness. The composition (impurity elements and content) of the ingots are unknown.

Table 1: Information of ingots and their short names used in this work, ranked by ingot size.

Original supplier	Processed by	Diameter (cm)	Name used in this work
CBMM	JLab (H1)	23	CBMM-H1
CBMM	JLab (H2)	23	CBMM-H2
Tokyo-Denkai	NSCL(1)	26	TD-1
Tokyo-Denkai	NSCL (2)	26	TD-2
Ningxia	NSCL	27	Ningxia
CBMM	NSCL	28	CBMM-NSCL
Heraeus	DESY	29	Heraeus
CBMM	Niowave	70(W)x22(H)x1(T)	Niowave

The Ningxia and CBMM-NSCL ingot slices (Figure 24) were characterized by EBSD on a CamScan 44 field emission scanning electron microscope operated at 20 kV, with a working distance of 33 mm. For the Ningxia slice, a keyhole-shaped sample containing grains 1-8 were

extracted by EDM from the center, as shown in Figure 24. Orientations of the perimeter grains 9 and 10 were measured by the Laue method. For the CBMM-NSCL slice, four samples containing all five grains were extracted at grain boundaries on the perimeter (numbered 1-8). The samples were etched by buffered chemical polishing (BCP, defined in section g of Literature Review) after EDM to provide a surface suitable for EBSD. Dashed lines are overlaid on some faint grain boundaries for better visibility. As the EBSD samples were much smaller than the size of the grains, they are assumed to be "representative," i.e., that the orientations do not vary greatly within the grains. This assumption will be assessed later.

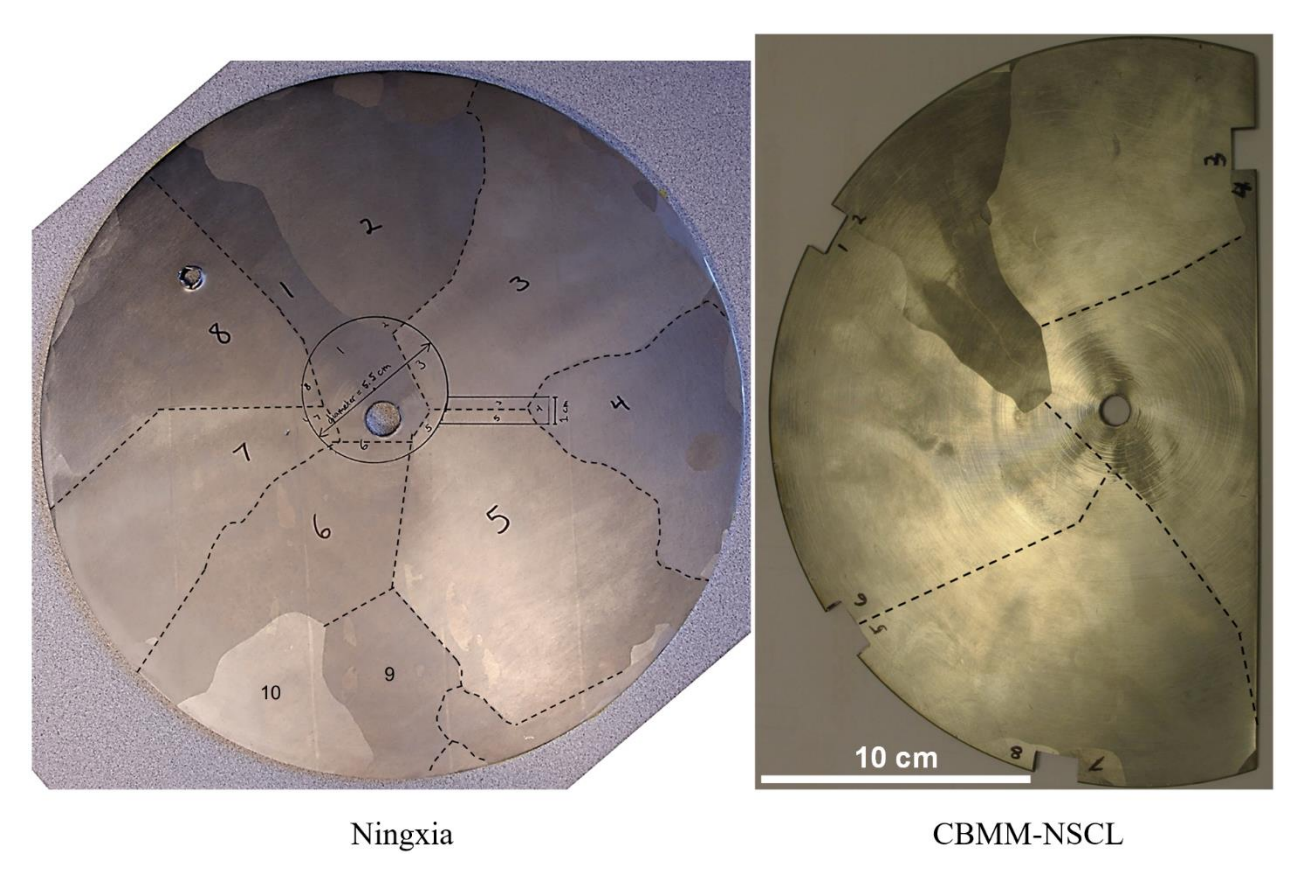


Figure 24: Images of ingot slices characterized by EBSD. Dashed lines identify the location of faint grain boundaries. The numbers on the images of the ingots indicate IDs of the grains whose crystal orientation will be reported later. The scale bar is common to both images.

The Laue method was used to study the CBMM-H1, CBMM-H2, TD-1, TD-2, CBMM-NSCL, Heraeus (Figure 25), and Niowave (Figure 26) ingot slices. The numbers on each ingot slice indicate roughly where the orientations were measured. Multiple measurements were made in some of the large grains. For example, the grid overlaid on the CBMM-NSCL slice shows the approximate locations of 57 Laue measurements that are one inch apart, where each intersection corresponds to one measurement (excluding those beyond the image of the slice). These results were compared to EBSD data from the same ingot slice. The CBMM-H1 and CBMM-H2 slices were cut adjacent to each other from an ingot, and so were the TD-1 and TD-2 slices. Thus, only the CBMM-H1 and TD-1 slices are shown in Figure 25.

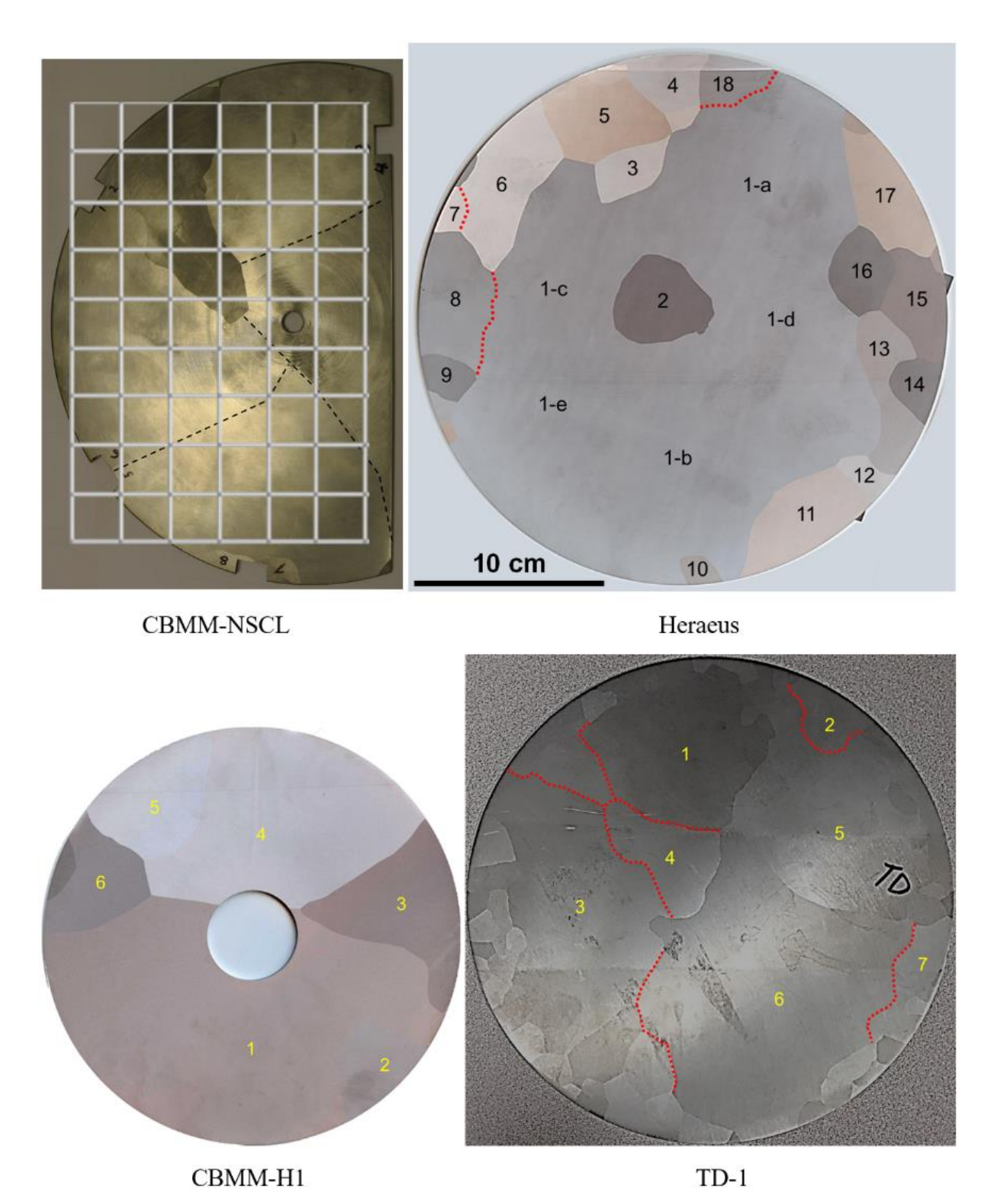


Figure 25: Images of ingot slices characterized by Laue camera. The grid on the CBMM-NSCL slice illustrates how 57 measurements were systematically made with a step size of 1 inch. The TD-1 slice was measured similarly using a step size of 2 inches, yielding 19 data points (detailed in). For the Heraeus, CBMM-H1, and TD-1 slices, the numbers provide approximate locations of the orientation measurements (reported later). The scale bar is common to all images.

To identify effects of deformation on orientations and to assess changes in the sharpness of Laue diffraction spots, the CBMM-H2 ingot slice was measured again with the Laue camera after being deep drawn into a half-cell.

The surface of the Niowave ingot slab was smoothed using an end mill after a rough saw cut, and then mechanically polished to make the grains on the surface visible (Figure 26). Besides the numbered locations, ten closely spaced orientations a-j were captured to the left of location 2 across two milling passes (the lower image of Figure 26), where orientation j was about halfway between locations 2 and 27. Seven of the locations were examined again after removing $100 \, \mu m$ from the surface by etching.

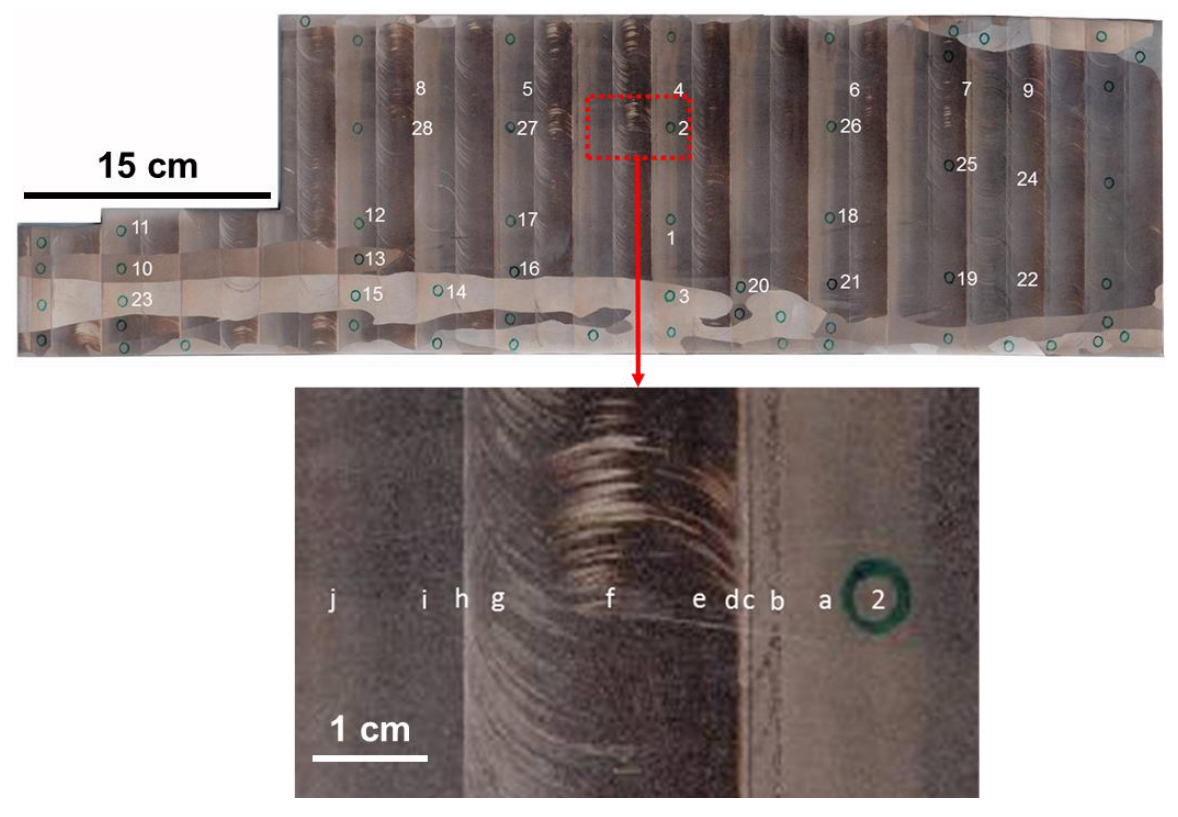


Figure 26: Image of a slab cut along the longitudinal direction of an ingot (prepared by Niowave). The dimensions are 70 cm (W) \times 22 cm (H) \times 1 cm (T). Ten closely spaced Laue measurements (a-j) were made in addition to the numbered locations. Scan j was about half way between locations 2 and 27 [adapted from Figure 3 in reference [123]].

b. Fine Grain Nb Sheets Characterized by EBSD and Mechanical Tests

The facility for rare isotope beams (FRIB) is a scientific user facility under construction at MSU funded by the U.S. Department of Energy, MSU and the State of Michigan [62]. A large quantity of fine grain Nb is being used in the construction of the FRIB, which has been procured from two suppliers – Tokyo-Denkai and Ningxia [62]. While vendors generally follow well-established material specifications for Nb, there is still a substantial variation in the properties of the incoming material. Therefore, the FRIB has developed its acceptance criteria list (ACL) to ensure the quality of Nb and to minimize potential variability issues in cavity fabrication. The ACL includes mechanical properties, purity, texture, surface finish, and electrical conductivity or residual resistivity ratio (RRR) [62].

At least one set of samples from each production lot were tested based on the ACL [62]. The samples were extracted from non-usable areas of the sheets (2-4 mm thick) using EDM, as shown in Figure 27 [61, 62]. The Tokyo-Denkai samples were cut 45° with respect to the rolling direction, while the Ningxia samples were either parallel or perpendicular to the rolling direction [62]. In each set, a standard ASTM dog-bone shaped sample was deformed to fracture in uniaxial tension using an Instron 4302 load frame, with a loading rate of 5 mm/min. The square samples were etched by BCP, and their cross-sections were examined by EBSD, using the CamScan microscope operated at 20 kV in stage-controlled scan mode. After EBSD, Vickers hardness were measured on the cross-sections of the square samples, using a Clark microhardness tester CM-100 at a load of 100 g. The other sample was used for thermal conductivity measurements and will not be discussed in this work.

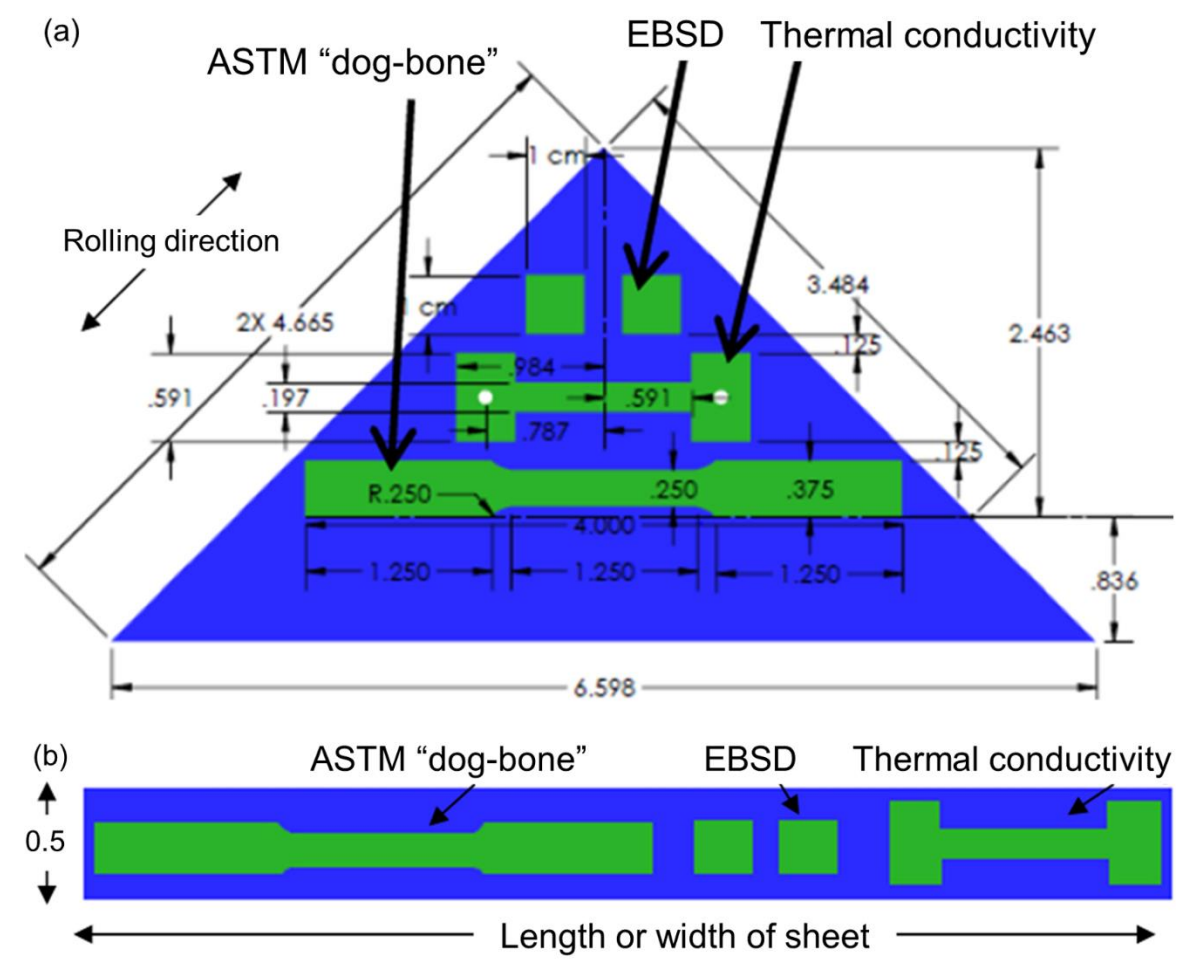


Figure 27: Layout of acceptance criteria list (ACL) samples extracted from (a) Tokyo-Denkai and (b) Ningxia sheets. The Tokyo-Denkai samples are oriented 45° with respect to the rolling direction, while the Ningxia samples are either perpendicular or parallel to the rolling direction. The dimensions are the same for each type of samples and are shown on the Tokyo-Denkai drawing. All units are in inches except for the square samples in (a) [adapted from Figure 14 in reference [61]].

Various mechanical parameters can be extracted from the tensile test data. Specifically, the ACL requirements are as follows [62]:

0.2% offset yield strength: >7000 psi (48.3 MPa)

Tensile strength (UTS): >14000 psi (96.5 MPa)

Percent elongation (ε_f): >40% in longitudinal direction and >35% in transverse direction

The EBSD data were used to assess texture, grain size, and degree of recrystallization of the sheets [62]. The ACL requirement is a predominant grain size of ASTM #5 (64 μ m) with >90% recrystallization. While texture is not part of the ACL, it can be useful in understanding potential problems during cavity forming and operation. The EBSD data were cleaned up using a single iteration of grain dilation and grain confidence index (CI) standardization with a minimum grain size of 3, and points with CI > 0.1 were used to generate the maps shown later.

For Vickers hardness (HV), ten datum points were collected on each sample mounted with one of its cross-sections (arbitrarily chosen) facing the indenter, and eight of them excluding the minimum and maximum were averaged for the hardness value reported. The ACL requires an HV of less than 60 [62].

c. Rolled Multi-Crystal Nb Samples Characterized by EBSD and Laue Camera

To investigate the origin of the heterogeneous banded texture and microstructure that varies from one lot to the next in the sheet material, a multi-crystal rolling experiment was designed. A portion of an ingot with a "bark" shape was extracted (S in Figure 28), and the initial orientations of its end slices (S1 and S2) were measured using the Laue camera. Part way through the rolling process, sample S was cut in half, and each half was further rolled to a flat piece that is about 1 mm thick, yielding a gradient of rolling reductions. One of the rolled pieces ("A") is shown in Figure 29, where S1 is next to its top edge, and S2 is next to its bottom edge. The sense of rolling and corresponding orientation map for S1 are shown on the top right corner in Figure 29.

Two samples, cut from the rolled piece, were evaluated by EBSD for the effects of rolling and annealing. Sample A2 is near the right end with zero to moderate cold work reduction, while

sample A6 is close to the maximum reduction region. Both samples were heat treated at 800 °C/2hr and examined again afterward.

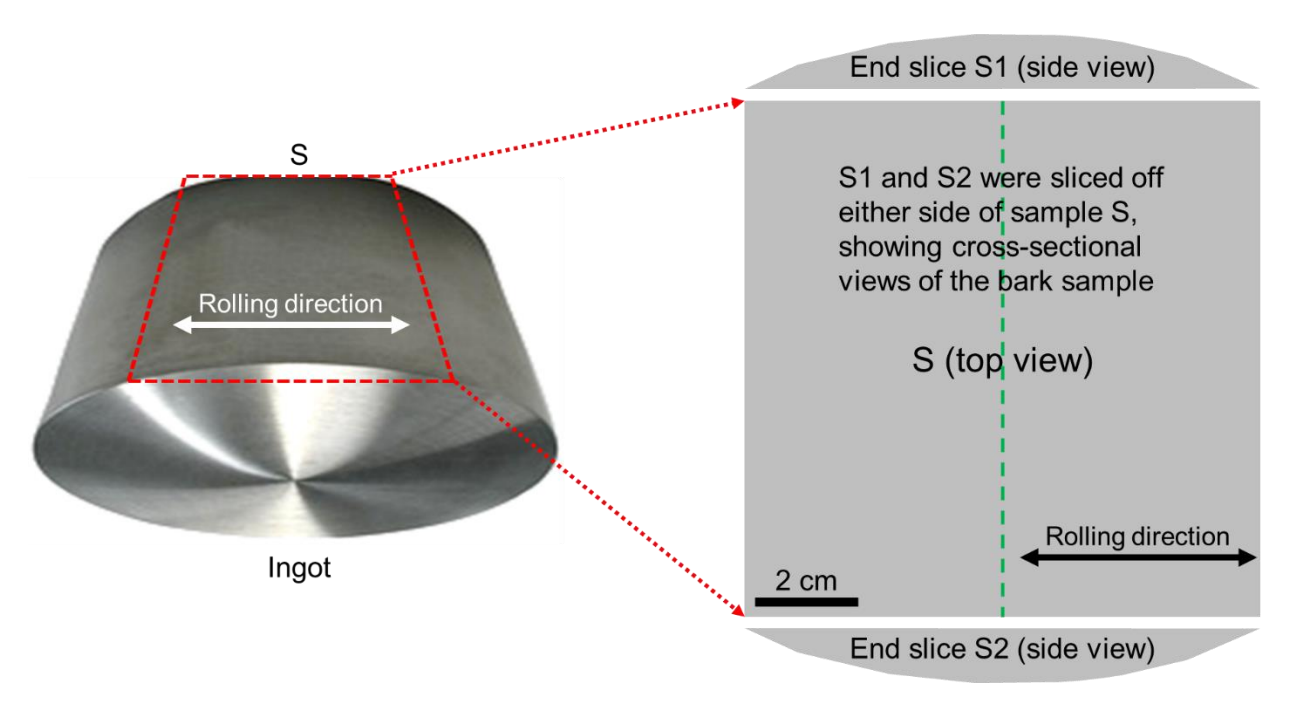


Figure 28: Schematic of a "bark" shaped sample S off the Niowave ingot used for the rolling experiment. The green dotted line indicates that the sample was cut in half part way through the rolling process due to developing a curved strip.

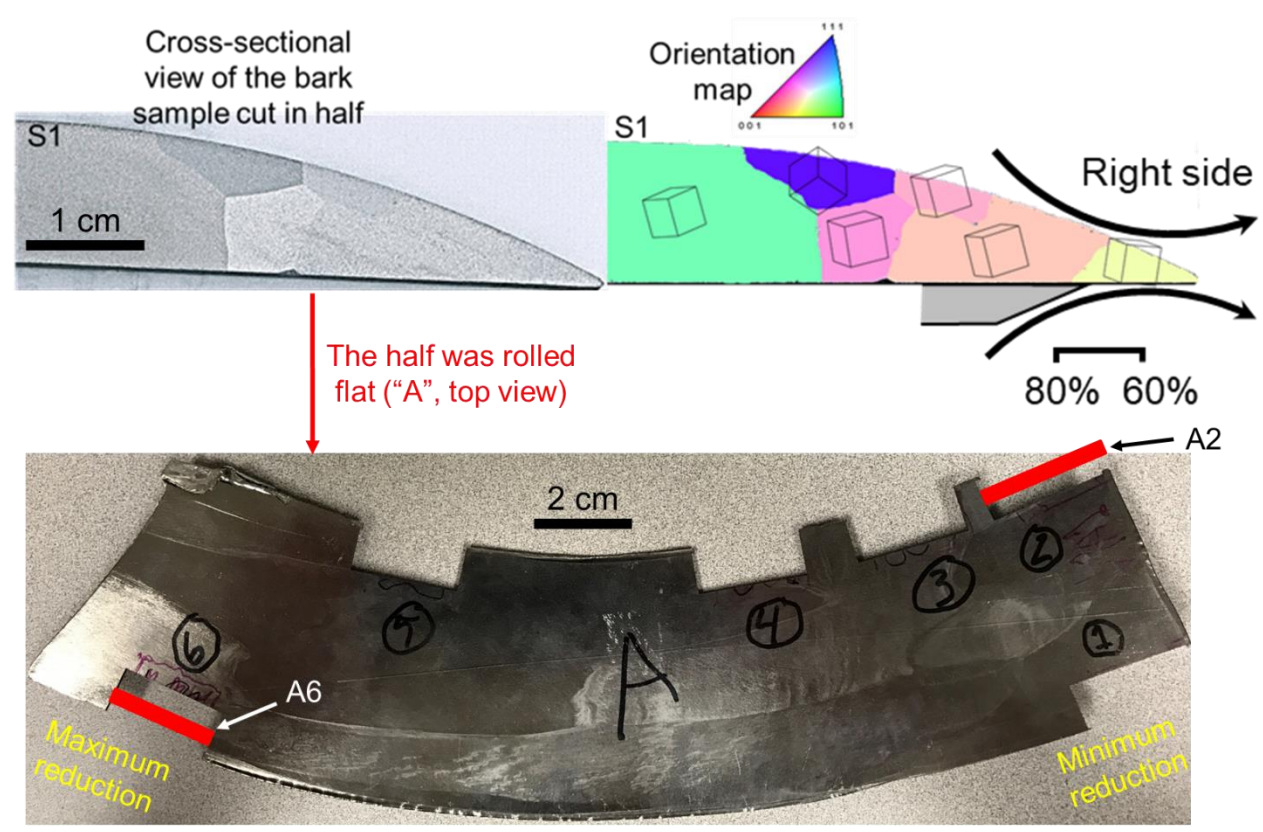


Figure 29: A flat piece ("A") about 1 mm thick rolled from the right half of sample S (Figure 28). End slice S1 was cut next to the top edge of the rolled piece, and its corresponding orientation map and the sense of rolling are shown on the right. The cross-sections of samples A2 and A6 were examined for the effects of rolling and annealing.

d. Nb Cavity Samples Characterized by EBSD

This section and corresponding sections in the Results and Discussion chapters are based upon previously published papers [126, 127], with additional figures and details.

Using EDM, three samples were cut from two rings trimmed from the equator and iris of a large grain half-cell prepared at Thomas Jefferson National Accelerator Facility (JLab). Two of the samples were extracted from the equator ring, and one from the iris ring, as shown in Figure 30. All samples contained a grain boundary, and the two equator samples had "earing" features (heterogeneous deformation) near the grain boundary. The earing may be associated with a higher drag force due to the resistance to thinning at the grain boundary.

Figure 31 shows secondary electron images of the six cross-sectional areas examined by EBSD. The samples were mounted with the outside of the half-cell facing upwards. The cross-sections of the samples are the opposite surfaces of half-cells that would be welded to other half-cells. These surfaces were hand ground using SiC abrasive paper to remove the EDM recast layer. The relatively smooth EDM finish enabled the use of fine abrasive paper to minimize damage from grinding, starting with grit 1200 (particle size ~15.3 μm) and ending with grit 4000 (particle size ~2.5 μm) [128]. After grinding, the samples were given a light etch (BCP) that removed another 10 μm of material to provide a surface suitable for EBSD. The step size used for EBSD was 20 μm. The data were cleaned using the same procedure as described in the previous section, after which orientation maps were generated.

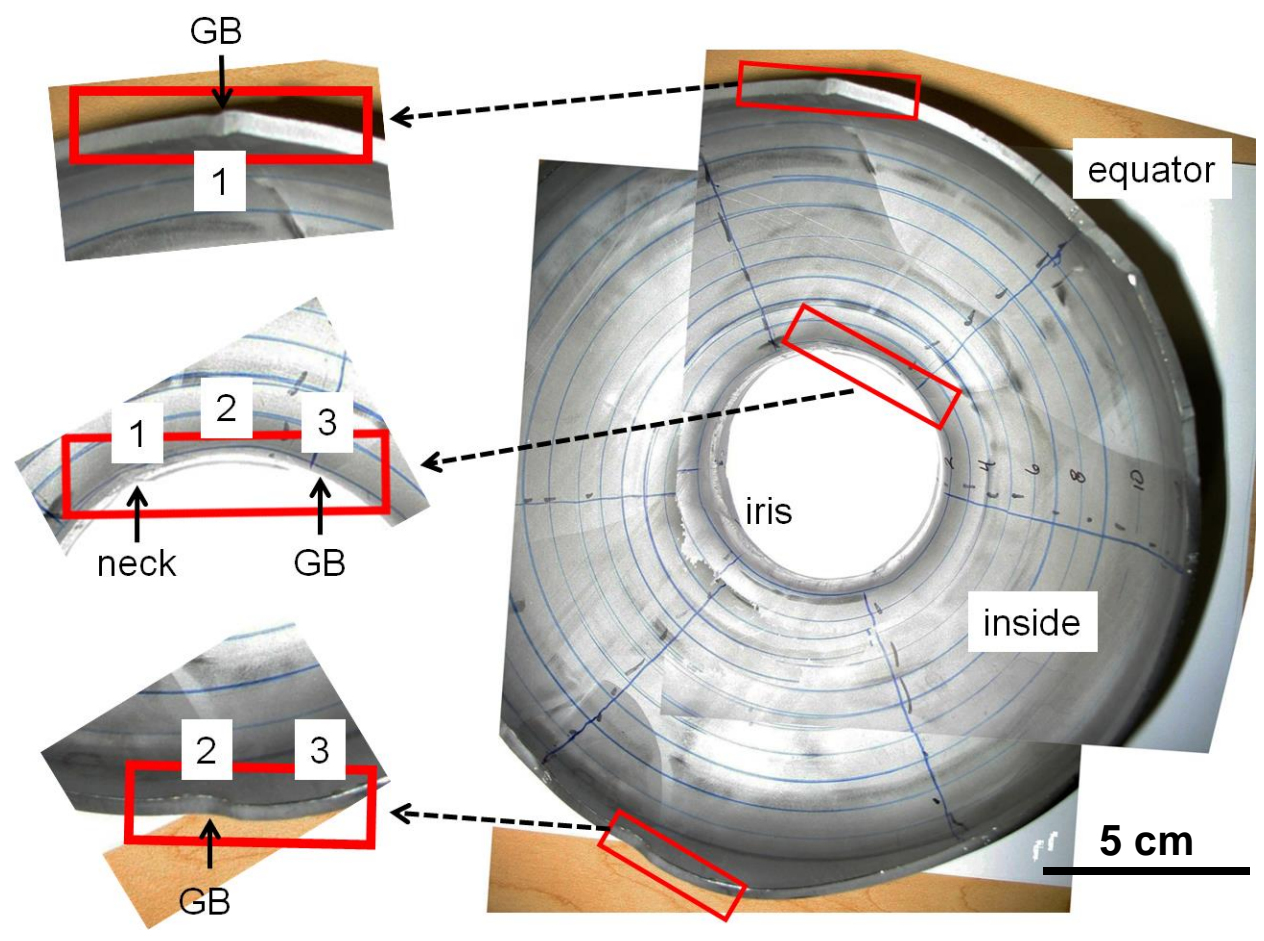
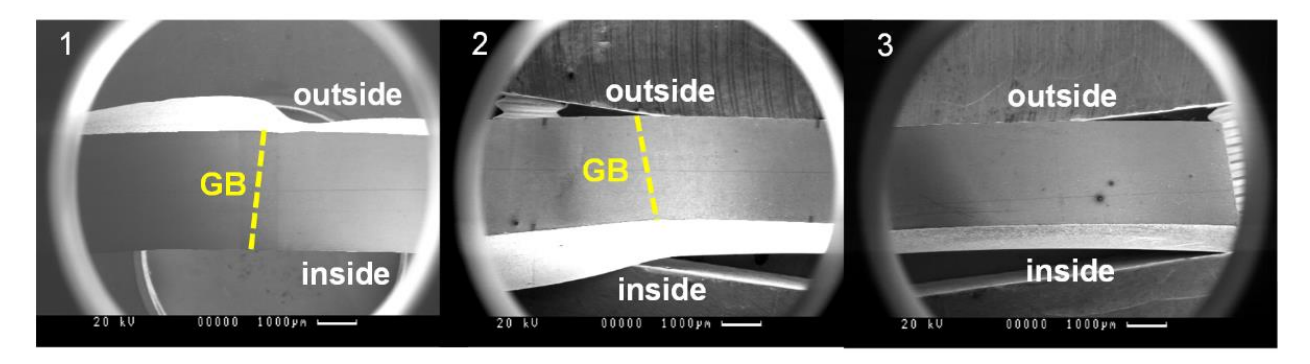
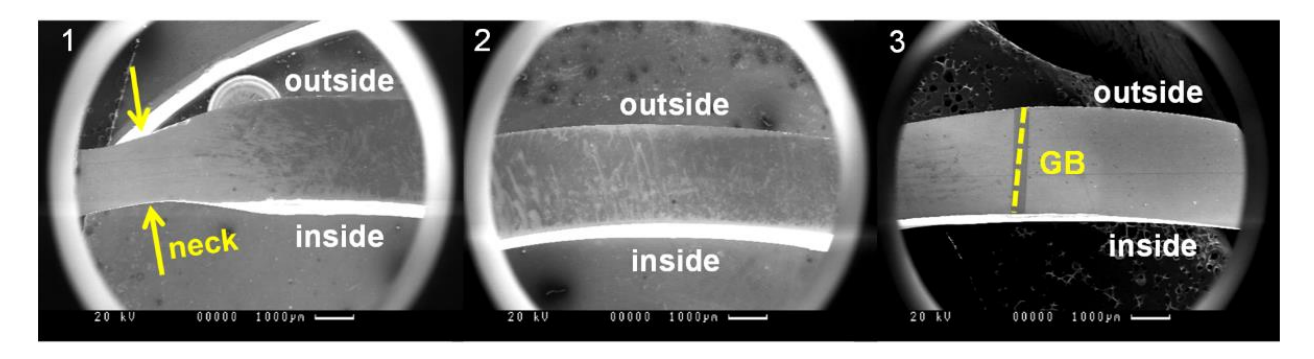


Figure 30: Locations of three samples extracted from a half-cell formed by JLab. The locations of grain boundaries (GB) and a neck are indicated in the blown-up images in Figure 31. Numbers provide approximate locations of EBSD scans on the equator and iris [adapted from Figure 2 in reference [126]].



Cross-sectional areas examined on the equator samples



Cross-sectional areas examined on the iris sample

Figure 31: Secondary electron images of the 6 areas examined by EBSD. Grain boundaries and the neck are marked in accordance with Figure 30. The numbering is also the same as Figure 30 [adapted from Figure 4 in reference [126].

After obtaining the EBSD measurements, the iris sample and one of the equator samples were heat treated at 800 °C/2hr in a vacuum furnace dedicated for Nb, and the other equator sample was heat treated at 1000 °C/2hr. For the 1000 °C anneal, titanium was used as a getter to minimize the uptake of hydrogen and oxygen into Nb. The same areas were scanned again to identify the effects of annealing on the microstructure. Then, the samples were etched with BCP to remove another 10 µm of material from the surface, and the same areas were examined once more to identify changes that occurred in the subsurface region.

The image quality (IQ) of EBSD patterns are an indicator of grain boundaries, defect content, and surface contamination [124]. The IQ parameter is the average height of detected

intensity peaks in the Hough transform (locating the bands) of an EBSD pattern [129]. Any distortions to the lattice within the diffracting volume will produce diffraction patterns with lower IQ as the Bragg condition is no longer precisely satisfied, resulting in a more diffuse diffraction band [124]. As the dominant defect in a crystal, dislocations can be qualitatively assessed by an IQ map, where darker areas indicate higher dislocation content [124]. Nevertheless, IQ is affected by both GNDs and SSDs, while LAM only reflects GNDs. Other factors such as grain boundaries, surface contamination, and the electron channeling depth for the crystal orientation will also affect the IQ. Furthermore, IQ can be affected by EBSD imaging parameters that are often different for each scan, may vary smoothly over the area of a scan, and will differ from grain to grain due to different amounts of backscattered electrons. Thus, the IQ map is informative when interpreted as a relative quantity within a given scan, but less so when comparing between scans.

Like LAM maps, IQ maps are presented in grayscale that varies linearly from black, the minimum IQ on a map, to white, the maximum IQ on a map – which differs for each scan. In the Results chapter, both LAM and IQ maps are used to assess the total defect content.

e. Nb Single Crystals Characterized by in-Situ Tensile Tests

This section and corresponding sections in the Results and Discussion chapters are based upon previously published papers [58, 130], with additional figures and details.

To investigate slip activities in Nb, twelve sets of single crystal samples were extracted from the Ningxia slice after its surface was mechanically cleaned, as shown in Figure 32. Each set contained three parallel samples from the same grain, so the three nominally have the same crystal orientation. The orientations were chosen to initially favor either a single slip system or a combination of slip systems. The methodology for orientation selection is detailed in [16]. A

letter from O to Z is designated to each set, and for the three samples in a set, number 1 denotes the one marked by a black dot, and numbers 2 and 3 follow downwards, as shown in the upper right schematic of Figure 32. The dimensions of the samples are shown on the left side of Figure 32, which is a reduced version of the ASTM E8-04 standard for sub-size samples.

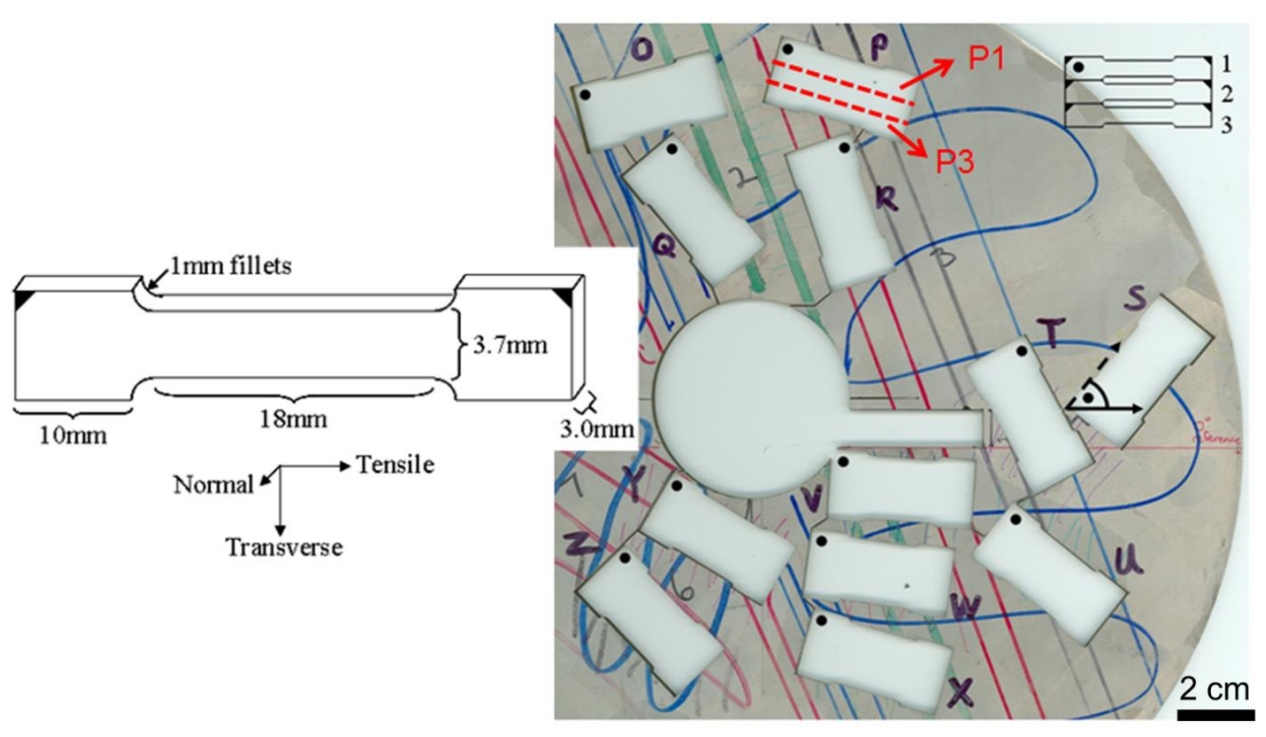


Figure 32: Layout of single crystal tensile samples extracted from the Ningxia ingot slice. The dimensions are shown on the left. The location of samples P1 and P3 are shown as examples of the labeling strategy [adapted from Figure III-3 in reference [16]].

Samples P3, Q2, R2, S3, T3, U3, V3, W3, and X3 (as-received samples) were electropolished by Baars (parameters provided in [16]) and deformed monotonically to 40% engineering strain using a tensile load frame (Instron 4302), with a strain rate of 1 mm/min. Samples O1 through Z1 (set 1) were etched with BCP after being extracted from the ingot slice and annealed at 800 °C/2hr by Compton to remove some of the dislocations formed during ingot production. They were used to assess orientation gradients within the large grains before and after annealing. Samples P2, Q3, R3, S2, T2, U2, V2, W2, and X2 (heat-treated samples) were electropolished by Baars and annealed at 800 °C/2hr by Compton. They were deformed *in-situ* at 0.004 mm/sec inside a Tescan MIRA3 scanning electron microscope using an Ernest Fullam stage, with a strain increment of ~10% followed by characterization, in which slip traces and orientations were recorded at three locations along the gauge length. An example of the test setup is shown in Figure 33 [131]. The deformation behavior of heat-treated samples is compared to that of as-received samples to identify the effects of annealing.



Figure 33: Experimental setup of the *in-situ* tensile tests. Sample W is shown as an example. Left – tensile load frame mounted inside the MIRA3 SEM chamber, right – plan view of the sample [adapted from Figure 3.2 in reference [131].

To understand the evolution of GNDs during uniaxial tension and how they correlate with work hardening and crystal rotation, samples T1 (in the middle of the stereographic triangle) and V1 (near the [100]-[110] boundary) were deformed *in-situ* for CC-EBSD analysis. EBSD patterns with 480×480 resolution over an area of 250×250 µm² were recorded at each 10% strain increment, using a step size of 2 µm and an exposure time of 0.1 s. The EBSD data were processed with the OpenXY software to obtain GND density and distributions at every deformation stage² [132]. The calculation is based upon equations developed by Nye and Kroner that relate derivatives of lattice distortion to dislocation content [121, 133-136].

The experimental methods described above will enable characterization of the physical metallurgy of Nb that governs cavity forming and performance, with emphases on microstructure and slip behavior.

² B. Dunlap and M. Crimp provided training of the CC-EBSD methodology as well as valuable insights.

IV. RESULTS

This chapter presents observations on ingot and sheet microstructures, as well as how they are correlated based on the rolling experiments. Such correlations also provide insights into how the microstructure and performance of a large grain cavity are influenced by forming and annealing. A fundamental study on slip behavior of Nb that influences the microstructural changes is reported at the end.

a. Crystal Orientation of Large Grain Nb Ingots

Table 2 through Table 7 list the orientations in Bunge Euler angles ($\phi 1 \Phi \phi 2$) for each ingot slice at locations indicated on images of the ingots (Figure 24 through Figure 26). While only selected orientations are shown in the tables, all measurements are reflected in the EBSD maps and subsequent analyses. For the CBMM-NSCL ingot slice, the Laue measurements shown in Table 3 are closest to the EBSD sample locations, and the differences between the measurements from the two methods will be addressed later. For the Niowave ingot, orientations of seven locations measured again after etching are shown in Table 7.

Table 2: Orientations in Bunge Euler angles (°) for the Ningxia ingot slice. The numbering is the same as Figure 24.

	Ningxia				
1	78.0	27.2	284.9		
2	105.9	7.8	239.4		
3	322.7	33.1	79.3		
4	294.7	25.1	83.0		
5	327.0	41.9	38.5		
6	186.1	37.2	172.9		
7	202.4	39.2	167.0		
8	132.7	26.0	266.5		
9	270.6	158.5	184.7		
10	244.9	139.8	153.9		

Table 3: Orientations in Bunge Euler angles (°) for the CBMM-NSCL ingot slice. The numbering is the same as Figure 24. There are varying differences between EBSD and Laue measurements of the same grains (discussed later).

	CBMM-NSCL (EBSD)			CBMM-NSCL (Laue)			Difference
1	167.6	140.4	167.6	168.4	142.0	179.8	11.7
2	281.9	123.7	127.8	279.1	138.0	143.2	22.4
3	158.9	143.7	184.7	156.0	148.2	180.0	5.3
4	176.4	133.3	194.7	172.2	144.4	196.5	12.5
5	171.7	159.5	261.7	130.1	146.7	148.7	50.1
6	188.0	136.1	188.0	169.4	140.8	179.9	14.4
7	168.3	118.0	135.3	173.6	147.7	146.5	30.9
8	155.4	142.5	245.4	152.0	138.4	233.9	10.0

Table 4: Orientations in Bunge Euler angles (°) for the CBMM-H1 and CBMM-H2 ingot slices. The numbering is the same as Figure 25. The two slices are nearly identical in orientations.

	CBMM-H1			C	BMM-F	Difference	
1	195.4	140.4	173.0	195.7	140.3	172.9	0.4
2	135.7	154.7	130.6	136.4	153.8	132.0	1.2
3	29.2	134.7	181.6	29.3	135.2	182.2	0.7
4	158.8	147.8	114.8	159.4	147.6	114.2	1.2
5	206.5	158.8	126.5	205.2	158.5	125.4	0.6
6	248.5	128.9	187.9	248.1	128.9	188.3	0.7

Table 5: Orientations in Bunge Euler angles (°) for the TD-1 and TD-2 ingot slices. The numbering is the same as Figure 25. There is a systematic difference only in $\phi 1$ associated with mounting error.

		TD-1			TD-2		Difference
1	318.6	141.2	101.1	321.9	140.7	101.1	3.3
2	346.0	129.6	160.5	348.3	129.1	159.8	2.8
3	166.9	140.6	108.1	170.6	140.7	108.5	3.4
4	166.3	135.9	188.3	169.4	136.2	188.4	3.0
5	337.0	141.0	175.2	340.4	140.9	174.7	3.8
6	177.2	146.4	134.3	180.7	146.4	134.8	3.1
7	273.2	139.7	160.2	276.1	139.8	160.0	3.1

Table 6: Orientations in Bunge Euler angles (°) for the Heraeus ingot at locations shown in Figure 25. Orientation variation in grain 1 is small based upon five measurements.

		Heraeus	
1-a	147.6	113.5	163.8
1-b	147.0	114.5	164.4
1-c	145.0	114.3	163.9
1-d	146.0	114.1	164.9
1-e	143.7	114.8	164.1
2	191.7	134.5	112.9
3	121.1	138.0	186.3
4	113.5	132.4	178.5
5	123.3	137.7	123.0
6	234.8	144.7	159.9
7	228.4	140.7	154.0
8	263.3	138.5	112.2
9	99.5	132.8	149.9
10	265.9	159.7	116.3
11	240.1	150.1	161.3
12	304.0	133.5	187.8
13	8.7	142.8	186.6
14	350.4	130.5	124.3
15	58.9	164.9	122.2
16	340.7	130.4	158.3
17	212.1	129.5	155.4
18	179.4	112.5	122.4

Table 7: Orientations in Bunge Euler angles (°) for the Niowave ingot at locations shown in Figure 26. Orientations do not vary much in the longitudinal direction of the ingot. After etching, the orientation of seven locations changed 1-2°, but the orientation gradients associated with the milling bands are still present.

		Niowave		Nioway	e (after e	etching)
1	324.3	137.3	111.7			
2	323.1	136.5	111.1			
3	98.2	144.0	135.3			
4	323.5	136.7	111.6			
5	324.3	136.1	112.5			
6	323.1	137.0	111.9	323.5	135.4	110.9
7	327.7	131.4	116.6	326.7	133.3	115.3
8	332.0	139.1	123.2			
9	328.1	132.6	117.2	327.6	131.2	116.2
10	309.1	173.1	171.9			
11	328.7	131.6	116.5			
12	324.0	136.9	111.2			
13	264.5	174.2	216.8			
14	97.3	145.1	135.0			
15	97.9	144.4	135.2			
16	322.9	135.6	111.1			
17	324.4	135.7	112.2			
18	322.7	136.4	110.1	324.1	135.2	111.8
19	326.5	132.8	113.8			
20	323.6	136.6	111.8			
21	321.9	135.2	109.0			
22	327.4	132.2	115.7			
23	89.3	144.6	124.8			
24	327.8	132.0	116.7	326.6	132.2	115.1
25	327.1	132.8	115.1	326.2	133.6	114.6
26	322.6	135.9	110.3	323.7	135.1	111.4
27	324.8	136.4	113.5			
28	329.7	140.3	121.1			

It is evident from Table 4 that the CBMM-H1 and CBMM-H2 slices have nearly identical crystal orientations due to them being immediate neighbors (the maximum difference between matching locations is 1.2°). For the TD-1 and TD-2 slices (Table 5), the largest difference (\sim 3°) is in φ 1, which is an error associated with rotation about the slice normal direction during mounting (a noticeable misalignment was later found in the fiducial marker on the two slices). As shown in Table 6, the orientation variation in the large grain 1 of the Heraeus slice is small, based upon five measurements. For the Niowave ingot, there is an orientation change after etching of 1.0 to 2.1° from the seven measurements in Table 7, which could be due to mounting error and chemical removal of a machined surface. Furthermore, crystal orientations do not vary much along the longitudinal direction of the Niowave ingot – the orientation spread is only 6.2° over a length of 70 cm. Orientation variations within the grains will be described later (semi-quantified in Table 8) for measurements made on the same grain in each ingot slice.

From orientations obtained from both EBSD and Laue methods, a 30x30 grid was overlaid on the image of each ingot, and an orientation map was constructed, where each pixel is assigned the measured orientation closest to it within a grain. An illustration of this process is shown in Figure 34, in which an orientation map for the TD-1 slice is generated (Figure 35) using the 19 measured datum points that are two inches apart.

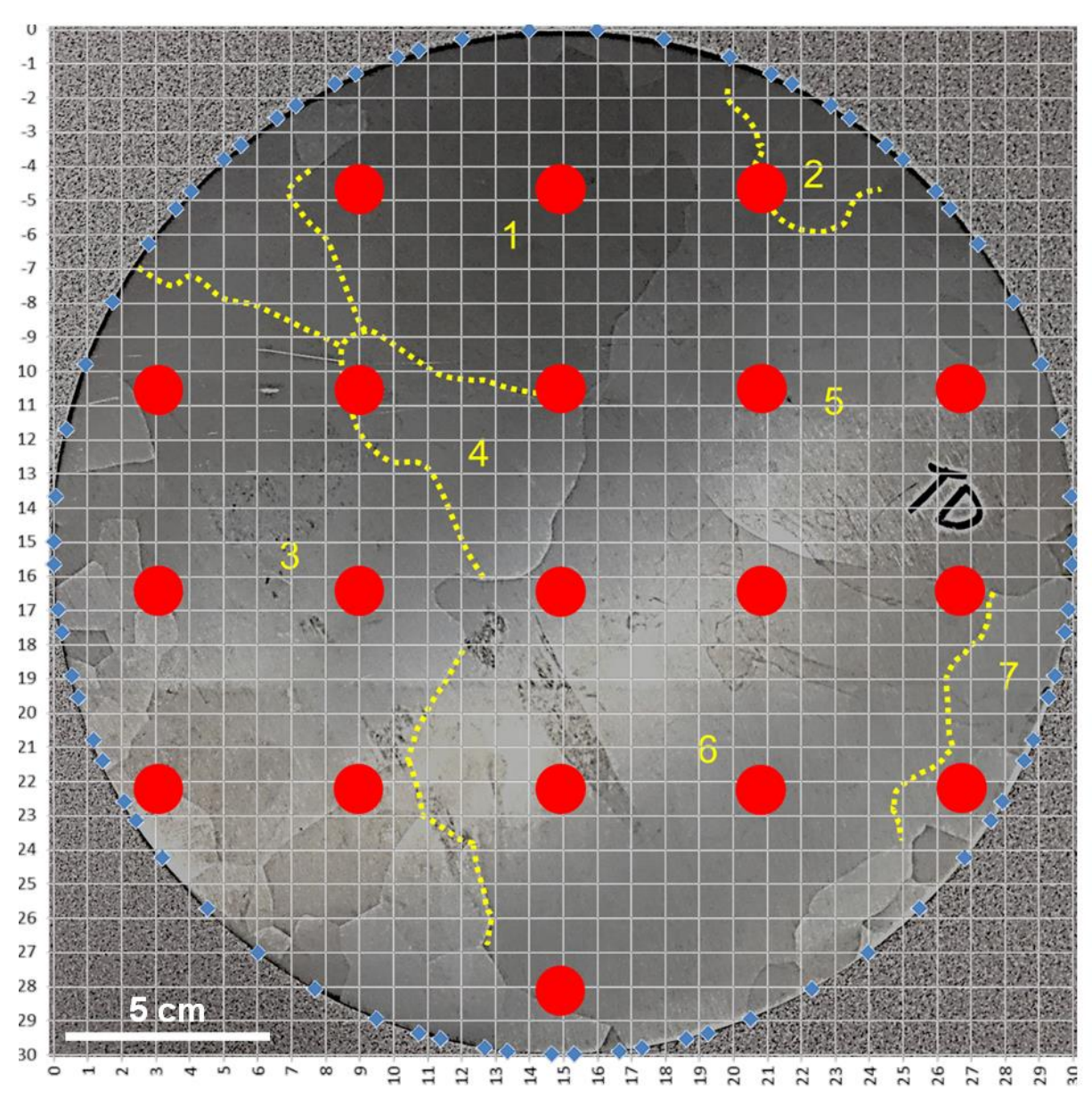


Figure 34: Illustration of how orientation maps were generated using the TD-1 ingot slice. Red dots indicate approximate locations of the 19 measurements that are two inches apart, and each pixel in the 30x30 grid was assigned the measured orientation closest to it within a grain.

Figure 35 through Figure 37 show axial growth direction orientation maps for all ingots. Some small perimeter grains were not measured, corresponding to black areas in the maps (e.g., TD-1). Grain boundary misorientations are annotated in the form of angle [rotation axis] on each map, with coincidence site lattice (CSL) boundaries identified in red lettering. CSL boundaries are high angle grain boundaries (> 15°) that are more energetically favorable than random boundaries, resulting from structural periodicity in the atomic positions within the boundary [137, 138]. Due to the resemblance between the CBMM-H1 and CBMM-H2 ingot slices, only CBMM-H1 is shown in Figure 35 (similarly for the TD-1 slice). For the CBMM-NSCL ingot slice, orientation maps from both EBSD and Laue measurements are shown in Figure 36. The orientation map for the Niowave ingot slab (Figure 37) is presented in the sample [010] (transverse/ingot growth) direction, which corresponds to the [001] directions in the other ingot slices. This perspective also applies to the other maps for the Niowave ingot slab shown later. Both the Heraeus and Niowave ingots have a grain near the perimeter with nearly the same orientation as the center grain.

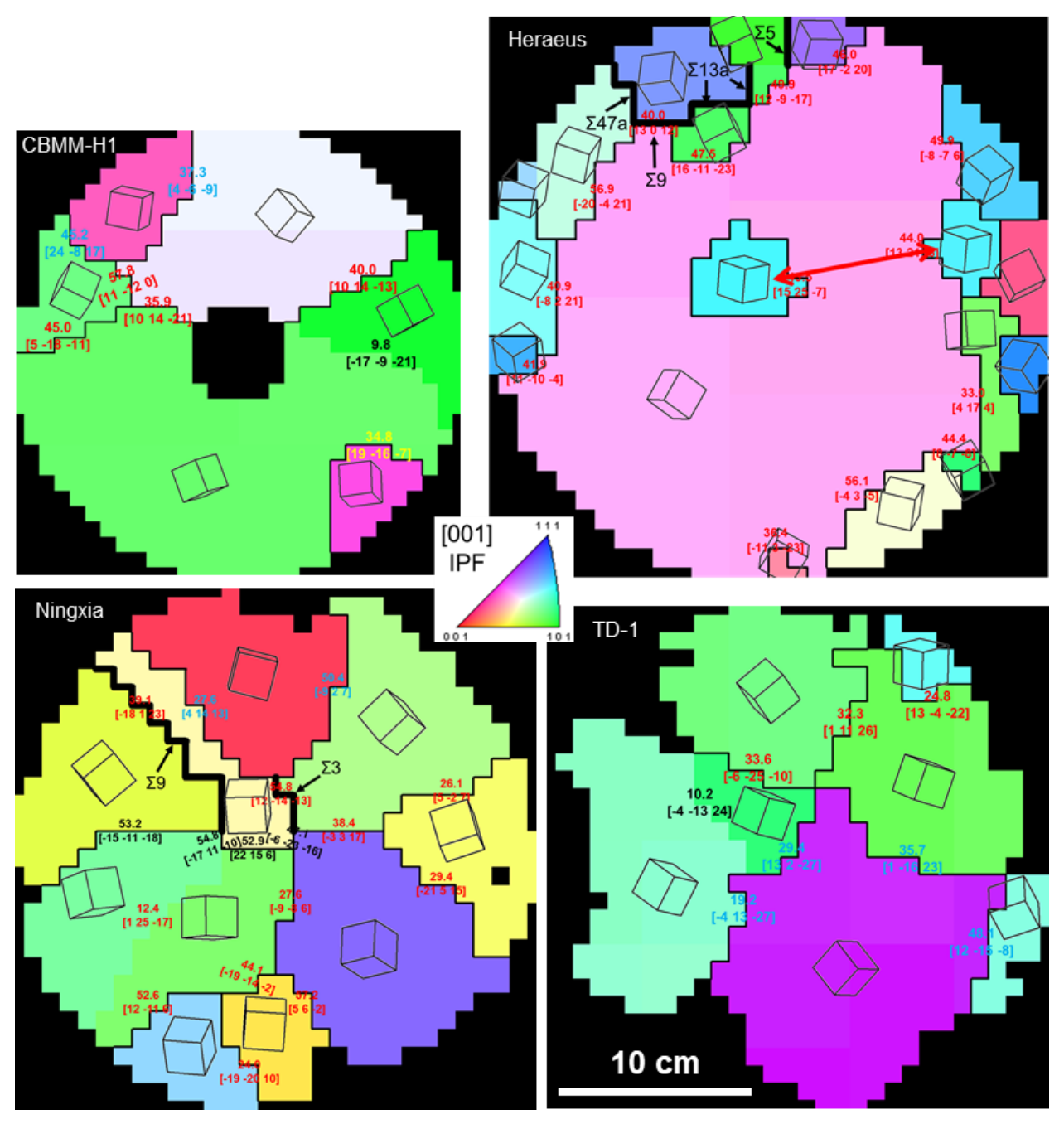


Figure 35: Normal direction orientation maps for the CBMM-H1, Heraeus, Ningxia, and TD-1 ingot slices, as labeled. Annotations provide angle and rotation axis for grain boundary misorientations, with CSL boundaries identified with thick black boundaries and red text. The red arrow on the Heraeus slice identifies the perimeter grain that has the same orientation as the center grain. The high angle ($>15^{\circ}$) grain boundaries are identified with thin black lines. The scale and legend are common to all maps.

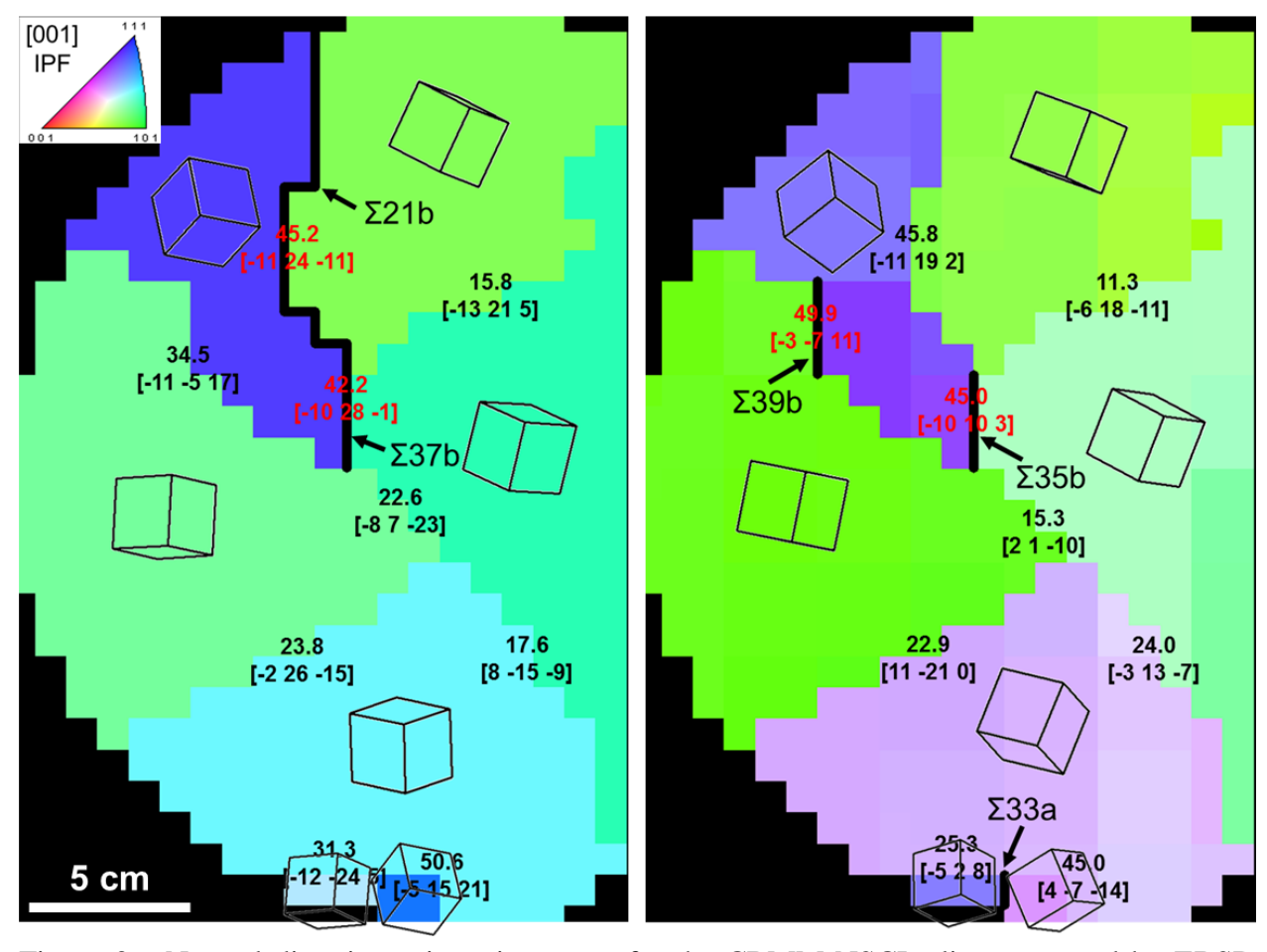


Figure 36: Normal direction orientation maps for the CBMM-NSCL slice measured by EBSD (left) and Laue camera (right). Annotations provide angle and rotation axis for grain boundary misorientations, with CSL boundaries identified with thick black boundaries and red text. The discrepancy between the two methods will be addressed in the Discussion chapter. The scale and legend are common to both maps.

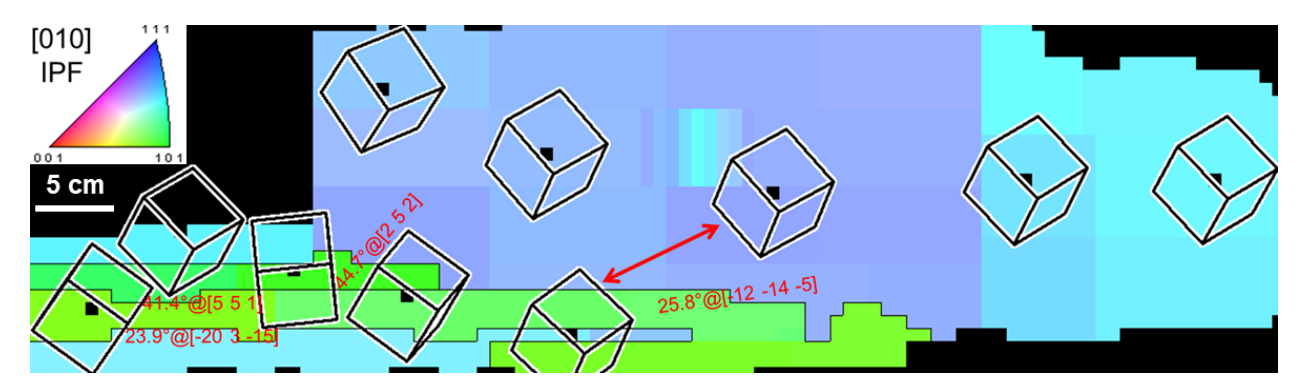


Figure 37: Transverse (ingot growth) direction orientation map for the Niowave ingot slab. Annotations provide angle and rotation axis for grain boundary misorientations. The red arrow identifies the perimeter grain that has the same orientation as the center one. The high angle (> 15°) grain boundaries are identified with thin black lines. There is no CSL boundary in this ingot.

Figure 38 through Figure 40 show misorientation distribution function (MODF) maps for all ingots, where each inverse pole figure (IPF) triangle represents the distribution of rotation axes between neighboring grains for each binned angular range for grain boundary misorientations. The color represents the probability of finding a rotation axis with a misorientation angle range indicated in units of times random, similar to the density pole figures shown in Figure 41. The MODF maps are smoothed density plots that represent the length of grain boundary misorientations, so for comparison, the observed misorientation axes (shown on the orientation maps in Figure 35 through Figure 37) are marked by black X's in Figure 38 through Figure 40.

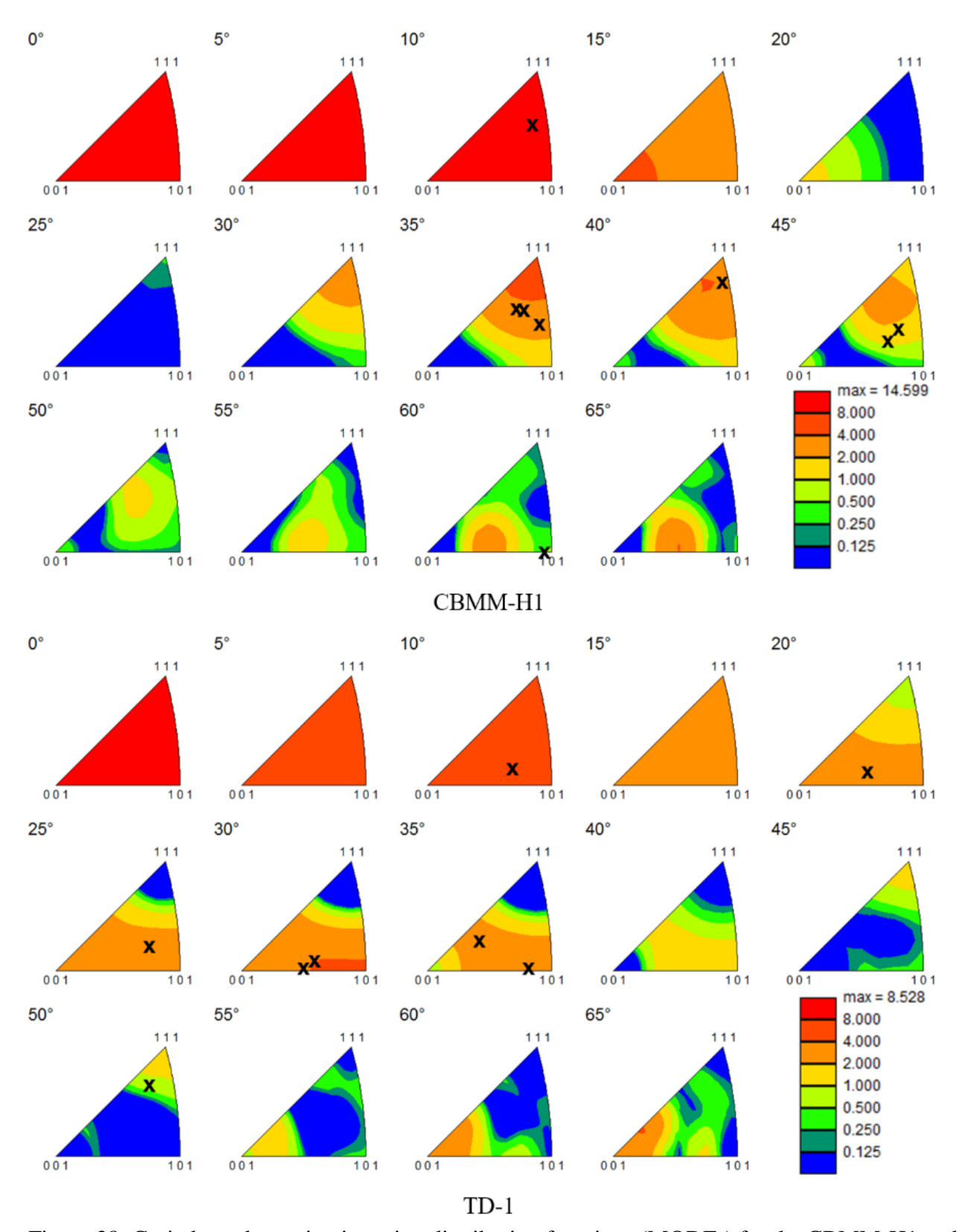


Figure 38: Grain boundary misorientation distribution functions (MODFs) for the CBMM-H1 and TD-1 ingot slices. The specific misorientations identified in Figure 35 are identified by X's. There is a trend for grain boundary misorientations to fall between 35-55°.

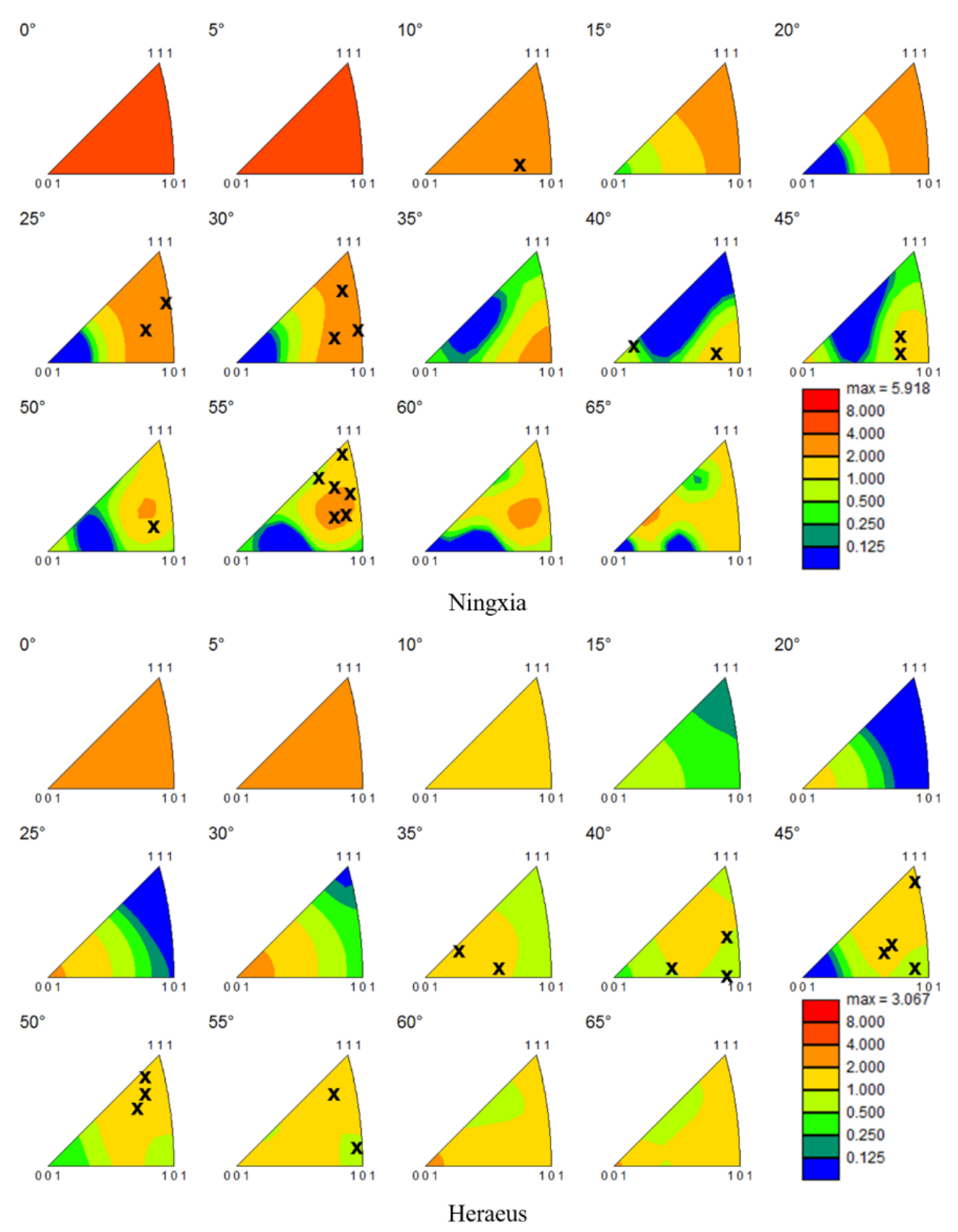


Figure 39: Grain boundary MODFs for the Ningxia and Heraeus ingot slices. Misorientations identified in Figure 35 are identified by X's. There is a trend for grain boundary misorientations to fall between 35-55°.

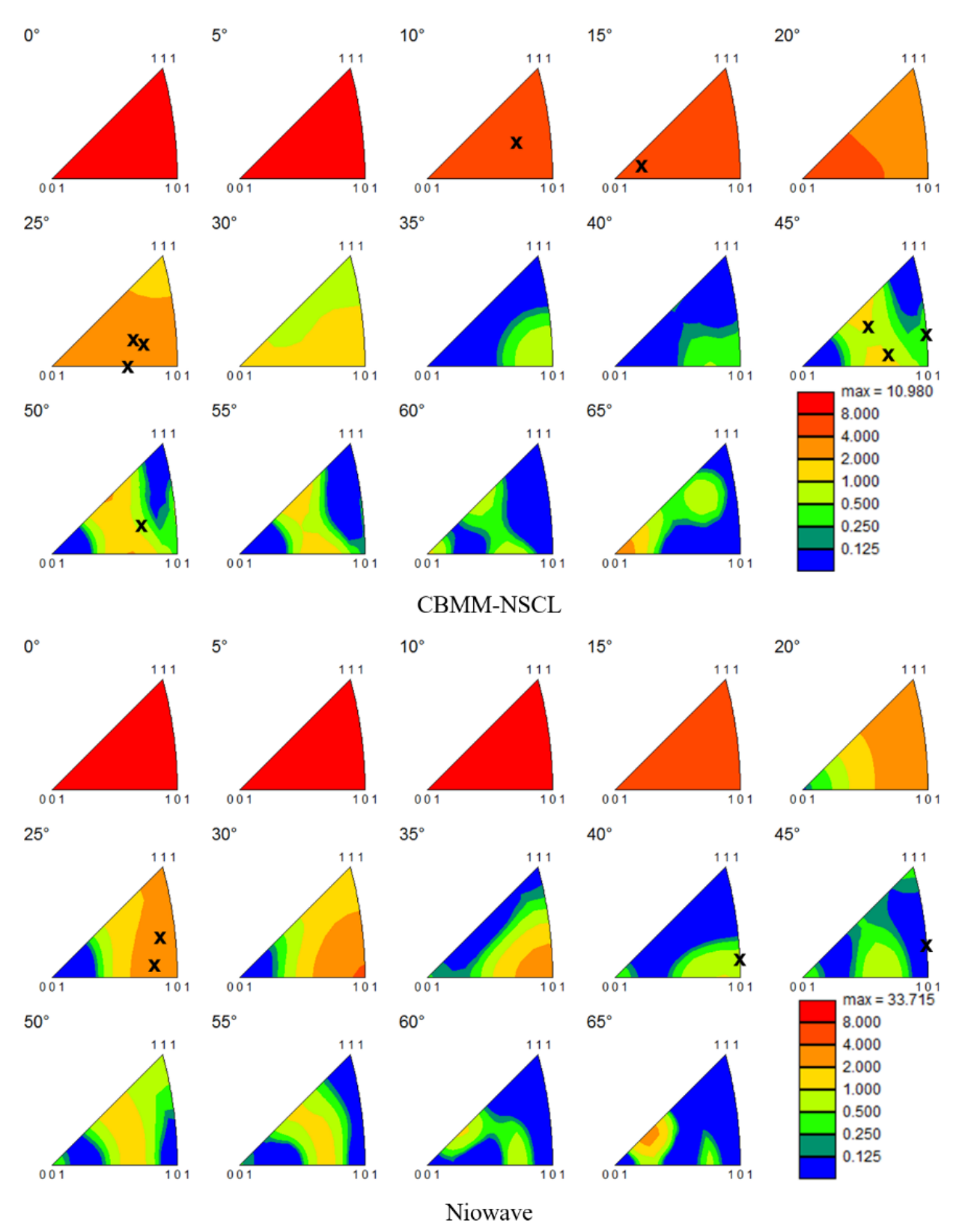


Figure 40: Grain boundary MODFs for the CBMM-NSCL and Niowave ingots. Misorientations identified in Figure 36 and Figure 37 are identified by X's. There is a trend for grain boundary misorientations to fall between 35-55°.

Based on the orientation maps, <001>, <011>, <111> and <112> density pole figures for each ingot are plotted using the same color scale in Figure 41. These pole figures highlight dominant orientations/grains, such as those represented by the three red <001> poles in the Heraeus and Niowave ingot slices. Figure 42 shows discrete IPFs in the ingot growth direction for all ingots. While the orientation distribution appears to be random, there is generally a lack of near <111> orientations aligned with the ingot growth direction.

Orientation variation is commonly observed when multiple measurements are made in the same grain of the ingot slices. This variation can be semi-quantified using the TSL software (EBSD data analysis) as shown in Figure 43, where each point corresponds to the misorientation with respect to the average orientation of a grain. These misorientations are divided into ten 0.5° bins from 0-5°, and the upper bound value for each bin is used as an estimate of the orientation variation.

Table 8 lists the largest variation (orientation spread) for each grain with more than one measurement. The orientation spread is only a couple of degrees in most grains. For example, grain 1 in the middle of the Heraeus slice was measured in 5 places as marked by 1-a through 1-e on the ingot image in Figure 25, showing about 2.5° of misorientation among the orientations. This small variation is consistent with a qualitative assessment of orientation gradients in another Heraeus slice [42], though the nature of the gradients was not assessed in the same way. The TD-1 and CBMM-H1 slices also exhibited consistent orientations, since all grains have an orientation spread of less than 2.5°. The Niowave ingot has a greater spread of 6.2° in grain 1, although it is mainly due to the much bigger area evaluated. This good longitudinal orientation stability is consistent with observations in [44] and is also consistent with the negligible orientation differences between adjacent ingot slices such as TD-1 and TD-2.

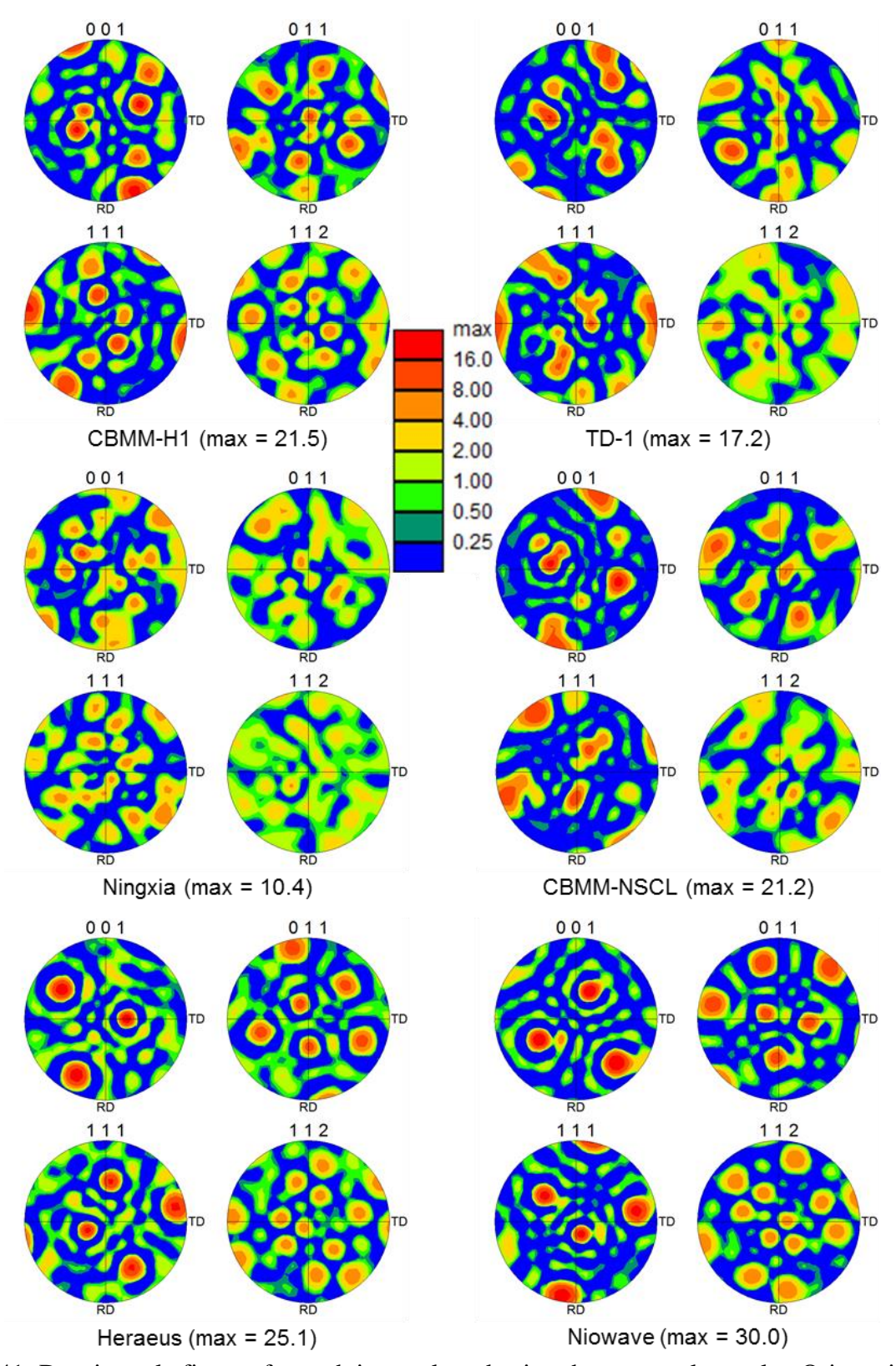


Figure 41: Density pole figures for each ingot plotted using the same color scale. Orientations of dominant grains are evident by the three red <100> poles for the Heraeus and Niowave ingots. The ingots lack commonality in orientation distributions.

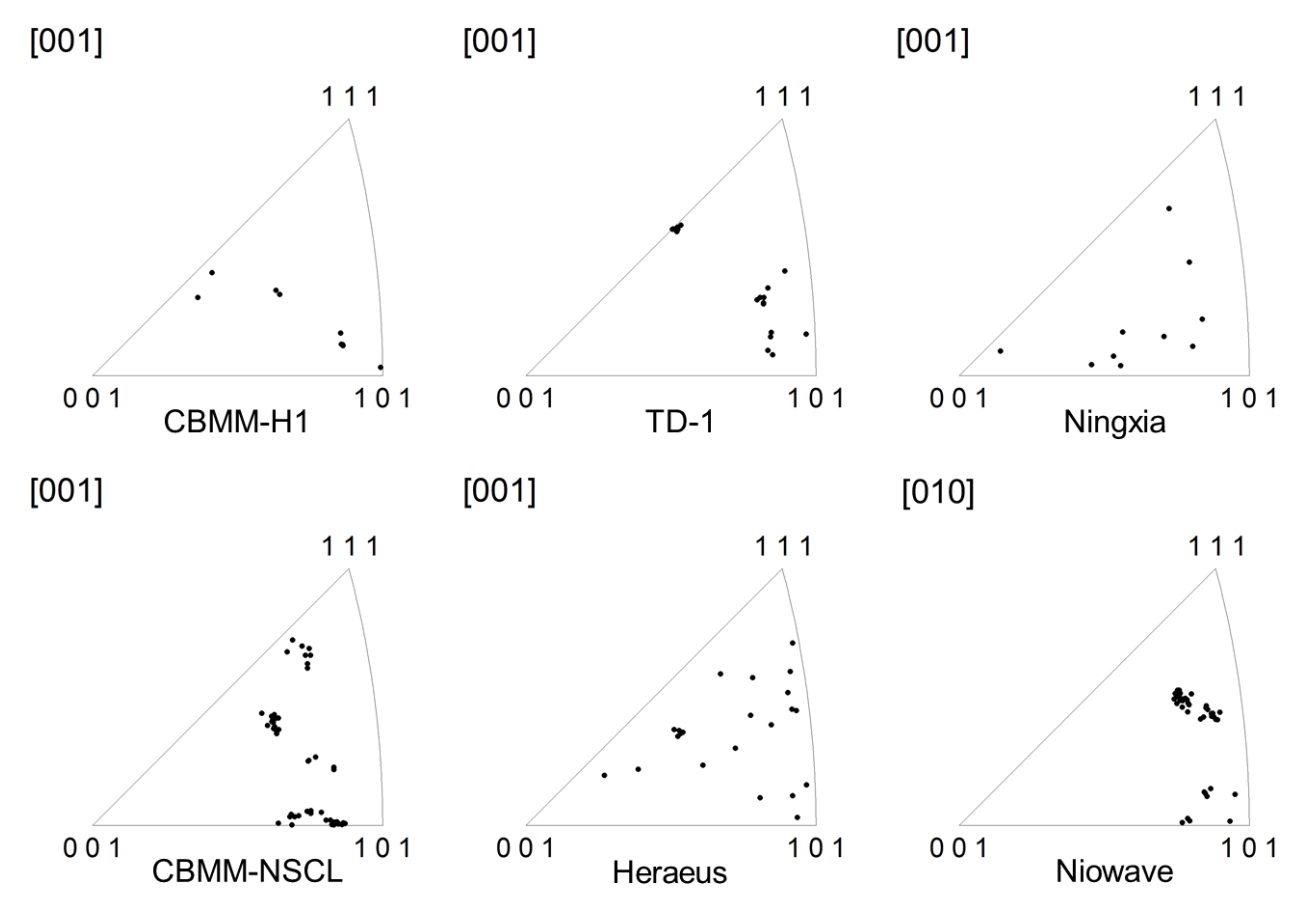


Figure 42: Ingot growth (sheet normal) direction discrete inverse pole figures for each ingot. There is a lack of near <111> orientations among the ingots.

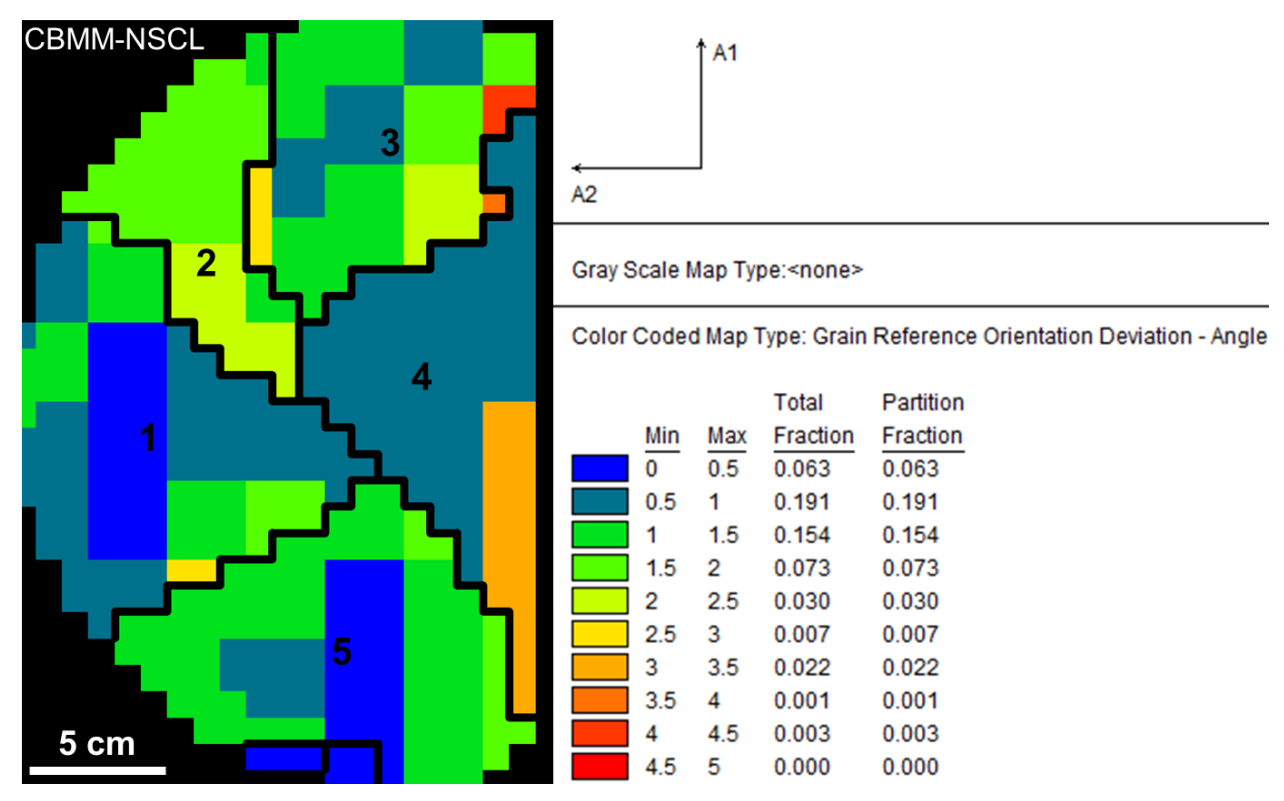


Figure 43: Illustration of how orientation variation is estimated from multiple Laue measurements within a grain. The orientation deviation map on the left uses the average orientation of each grain as a reference. For example, the largest deviation for grain 1 is in the range of $2.5-3^{\circ}$ (dark yellow), and the upper bound value (3°) is assigned to this grain as its orientation spread.

Table 8: Orientation spread for grains with multiple Laue measurements, estimated using the average orientations (Figure 43) as the reference. The intragranular orientation variation is small compared to the Ningxia ingot (shown later).

Ingot	Grain ID	Number of measurements	Orientation spread (°, average)
CBMM-H1	1	3	0.5
CDIVIIVI-III	4	2	1.5
	1	3	1
TD-1	3	5	1.5
1D-1	5	2	1
	6	6	2.5
CDMM	1	16	3
	2	7	2.5
CBMM- NSCL	3	9	4.5
NSCL	4	10	3.5
	5	15	2
Heraeus	1	5	2.5
	1	22	6.2
Niowave	3	4	3.5
	10	2	3

A closer look at the large grain at the center of the Niowave ingot slab shown in Figure 26 reveals that there is a periodic oscillation in orientations that comes from the milling band. For example, if orientation 11 (left side) is used as a reference, the misorientations for orientations 4, 2, and 1 along a milling band near the center are 6.4°, 6.5°, and 6.8°, respectively. Orientations 9, 24, and 22 (right side) along another milling band have much smaller misorientations of 1.6°, 1.2°, and 1.2°, respectively. The six orientations on the right are on the same milling direction pass, which is opposite from measurements on the middle and left side. The orientations are correspondingly similar in bands milled in the same direction.

To more clearly identify this orientation periodicity, a fine step size set of orientations to the left of position 2 were measured. Using orientation 2 as a reference, the misorientation reaches a peak (6.8°) around the center of the adjacent band (position f), and gradually drops to a small value at position j (0.7°) . Orientation j is close to orientation 27, which has the same milling direction. Such oscillation is reflected in the orientation map of the Niowave ingot in Figure 37, which shows a color change that is correlated with the milling pass direction.

A greater orientation spread was observed in the Ningxia ingot slice as evidenced by the EBSD results from the tensile samples. Orientation gradients were observed on two scales. Figure 44 shows how the average orientations vary over the 18-mm gauge length on three of the single crystal samples. This variation is plotted in Figure 45, showing the sum of rotations (ϕ 1+ ϕ 2) about the crystal z-axis and the intervening rotation about the crystal x-axis (PHI). The average orientation gradient for the 12 samples (O1 through Z1) is 4°, although sample Y1 has a striking 14° variation across the gauge length. A closer look at this sample suggests that there is a low angle grain boundary between the rightmost location and the adjacent one. This grain boundary was confirmed by a Laue measurement. Neglecting this boundary, the variation for sample Y1 is about 7°, making sample V1 the one with the largest orientation gradient of about 8° across the gauge length.

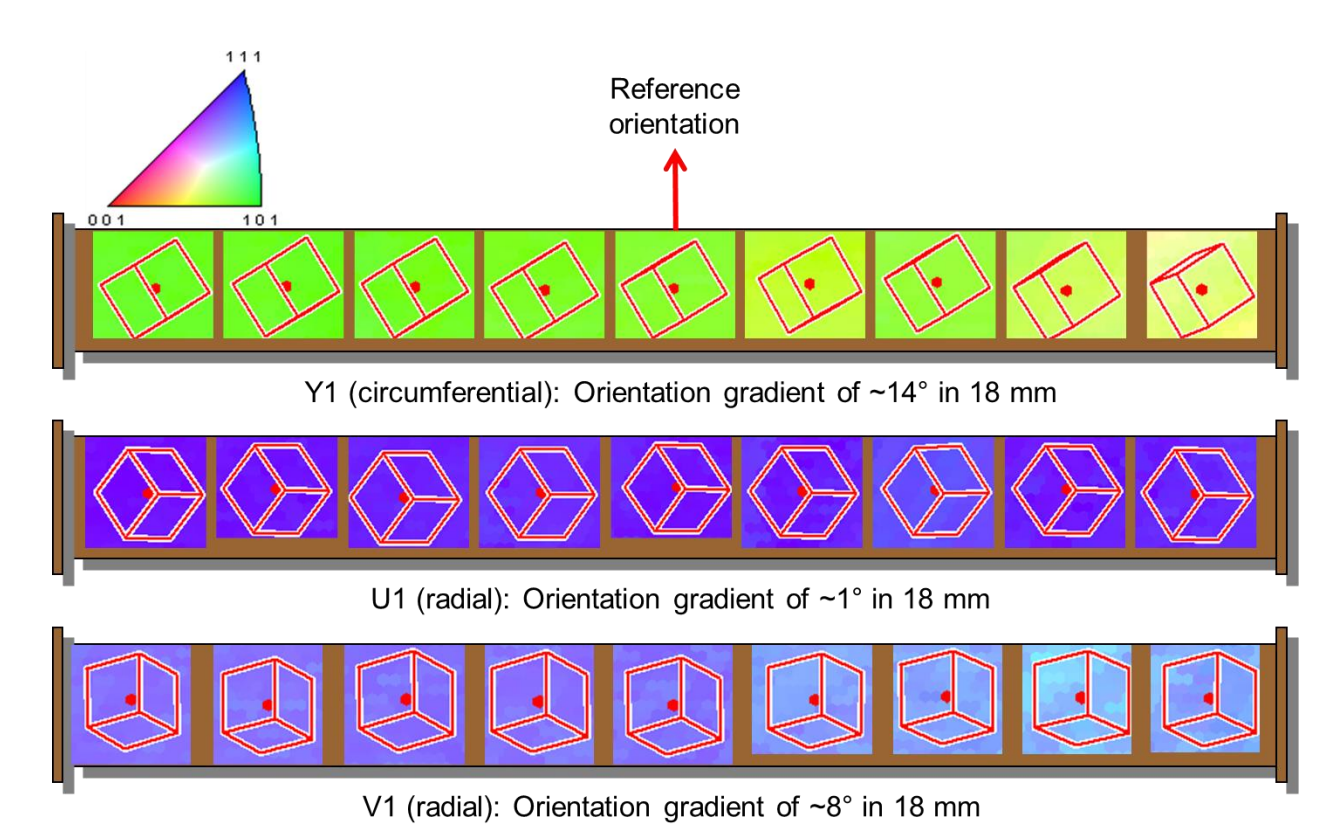


Figure 44: Orientation gradients along the 18-mm gauge length of three tensile samples extracted from the Ningxia ingot slice. Y1 has the largest orientation gradient due to a low angle boundary near its right end.

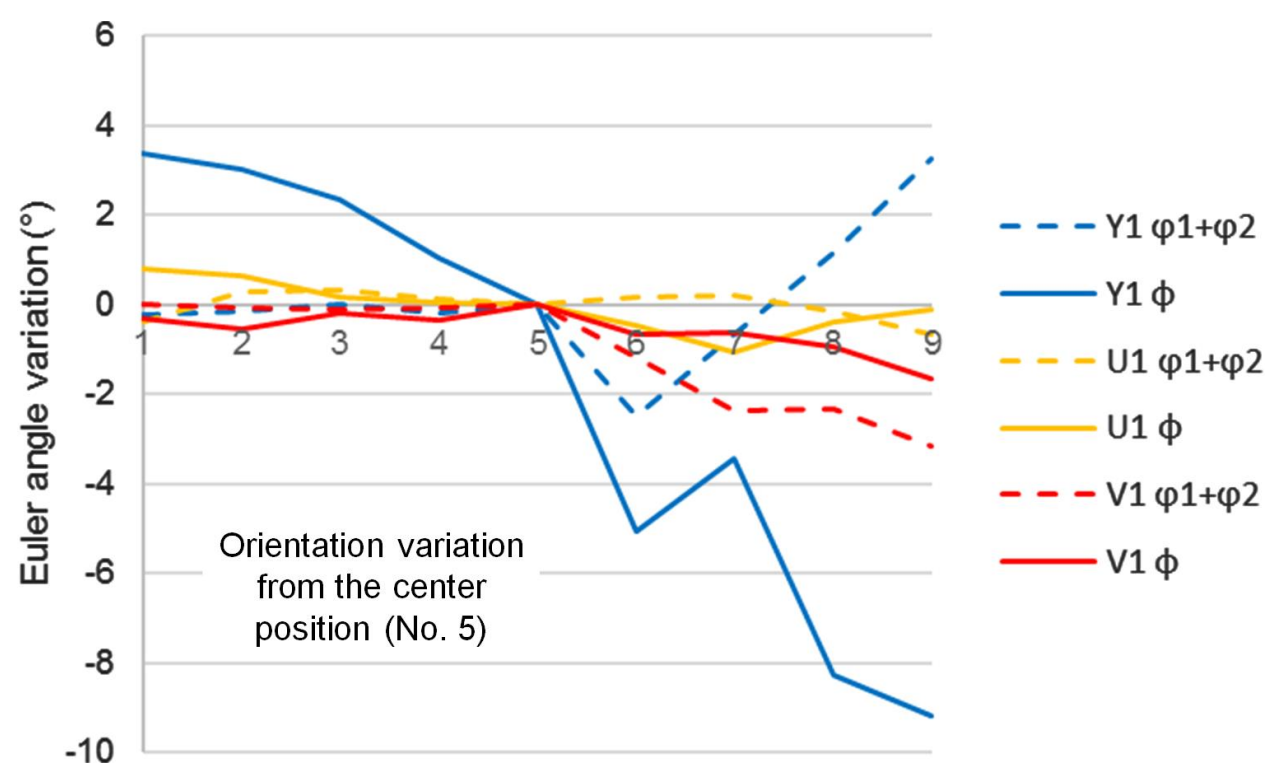


Figure 45: Orientation variation in Euler angles for the three samples shown in Figure 44.

Each of the average orientation values used in Figure 44 comes from an $815x275 \,\mu\text{m}$ scan, in which there are also orientation gradients at the scale of 30-60 microns. Figure 46 shows such fine-scale orientation patterning revealed by the grain reference orientation deviation maps for samples Y1 and U1, with a color scale from blue (0°) to red (5°) (white for >5°). The directionality of orientation banding is consistent for sample U1, but there are several directions for the bands in sample Y1.

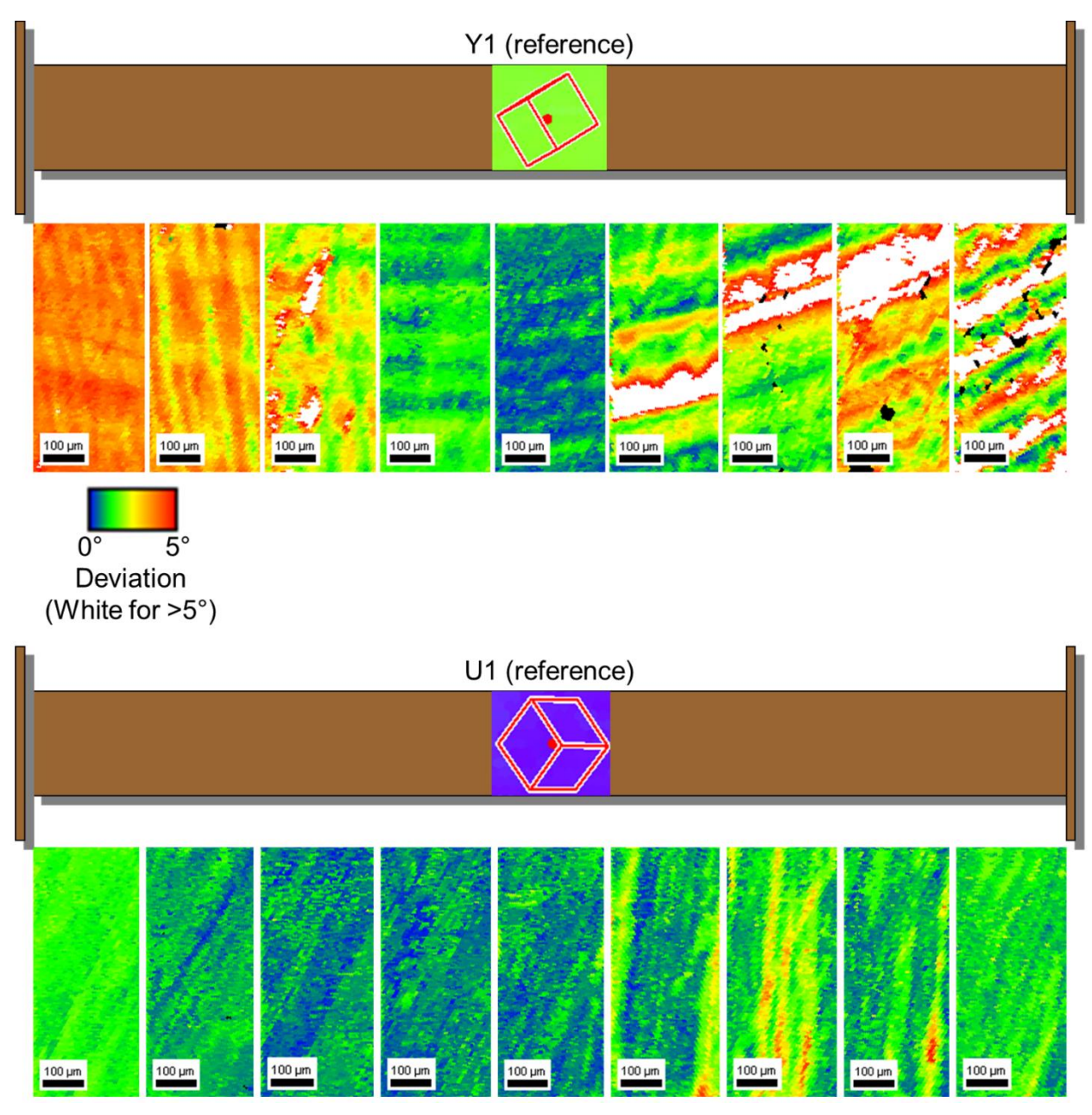


Figure 46: Grain reference orientation deviation maps showing fine scale orientation gradients for samples Y1 and U1 based on the average orientation at the center. The directionality of banding is consistent for sample U1, but less so for sample Y1. The color scale is common to all maps.

Figure 47 shows one fine scale orientation pattern from each sample in set 1 (etched by BCP and annealed, but never electropolished) examined before annealing. While there is no apparent consistency in the directionality or distance between the orientation bands, samples in the same grain tend to have similar directions of banding, with the exception of samples S1 and T1.

This fine-scale orientation patterning did not change much after the set 1 samples were annealed at 800 °C/2hr. Figure 48 shows roughly the same areas examined before and after the

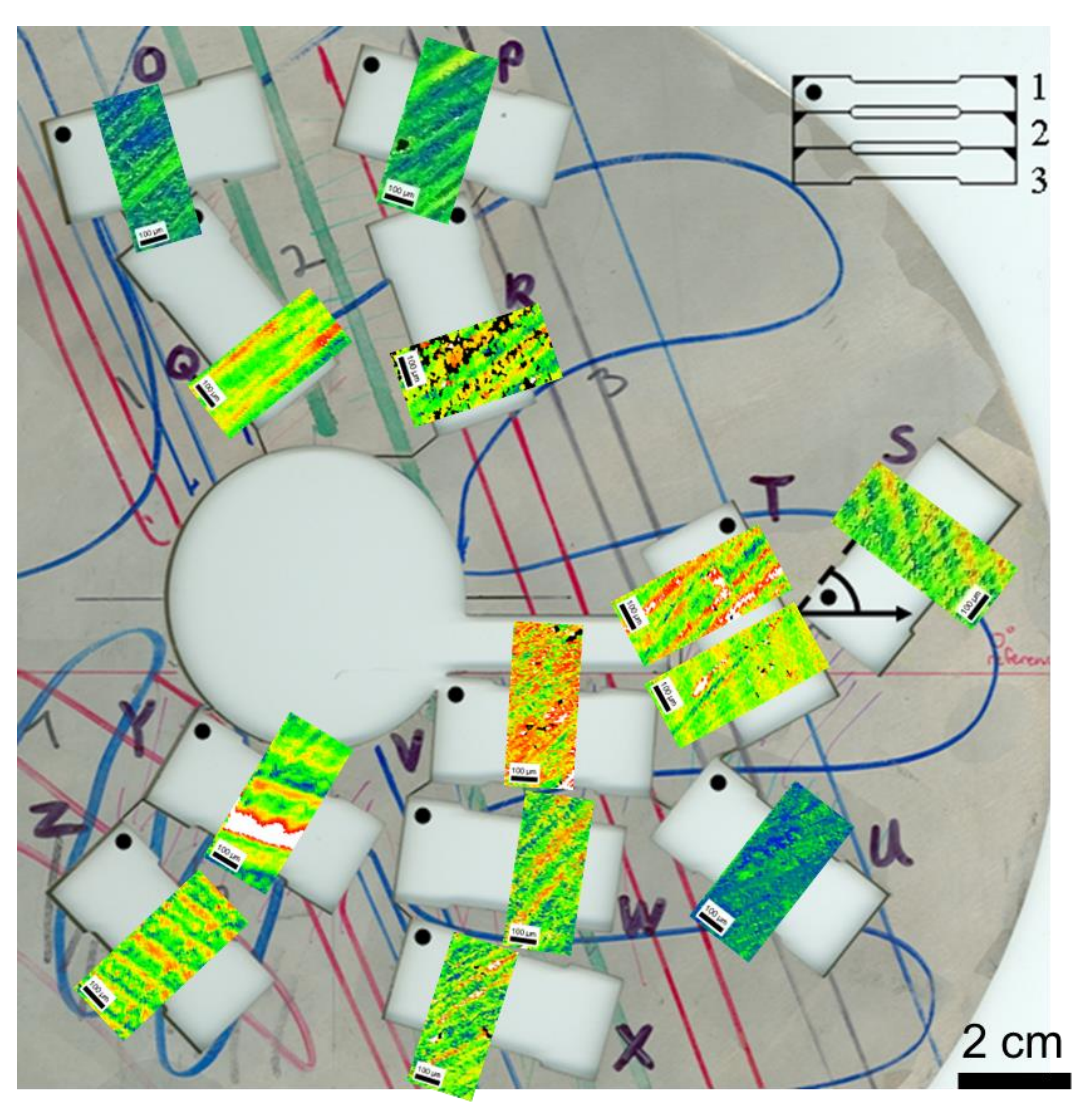


Figure 47: Selected fine scale orientation patterns of the as-cut samples overlaid onto the image of the Ningxia slice. Black dashed lines highlight the original grain boundaries. The color scale for the maps is the same as Figure 46. There is no consistency in the directionality of the banding with respect to the ingot.

anneal for samples P1 and Q1. However, similar patterns are absent on samples from set 2 which were electropolished (parameters provided in [16]) and later annealed, examples of which are shown in Figure 49 for samples S2 and T2 (after annealing).

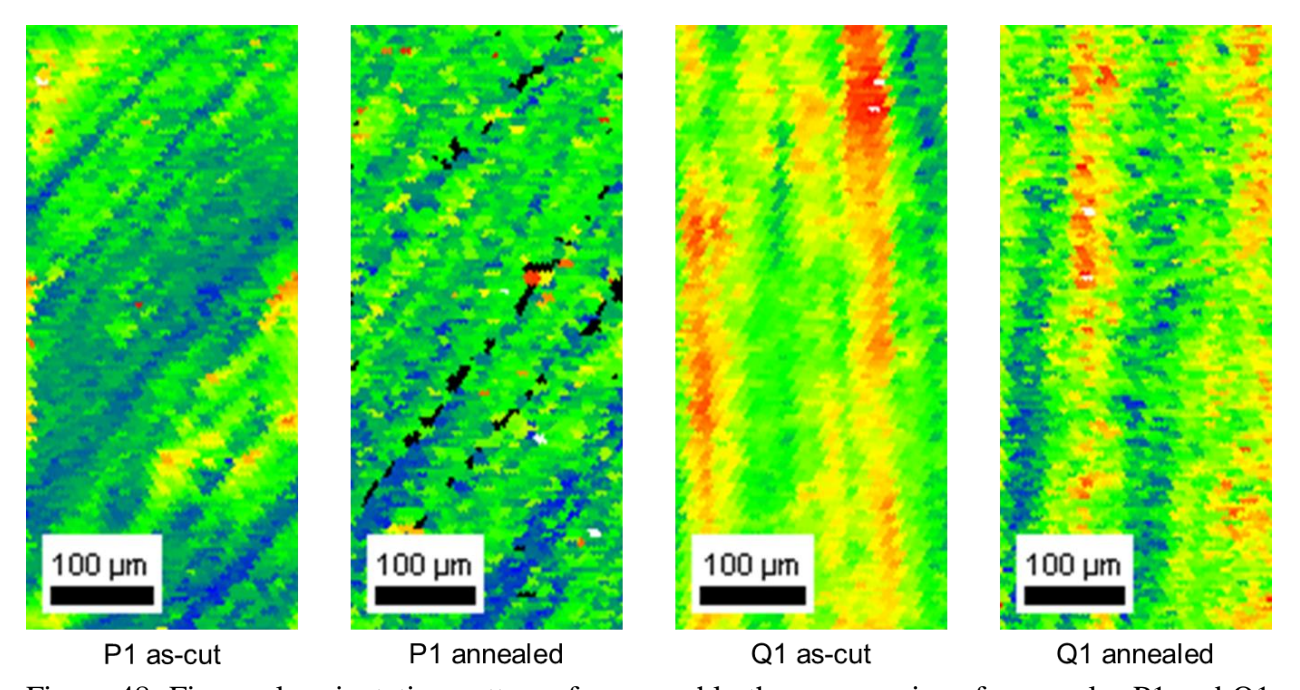


Figure 48: Fine scale orientation patterns from roughly the same regions for samples P1 and Q1 before and after an $800\,^{\circ}$ C/2h anneal. The anneal did not alter the patterning by much. The color scale is the same as Figure 46.

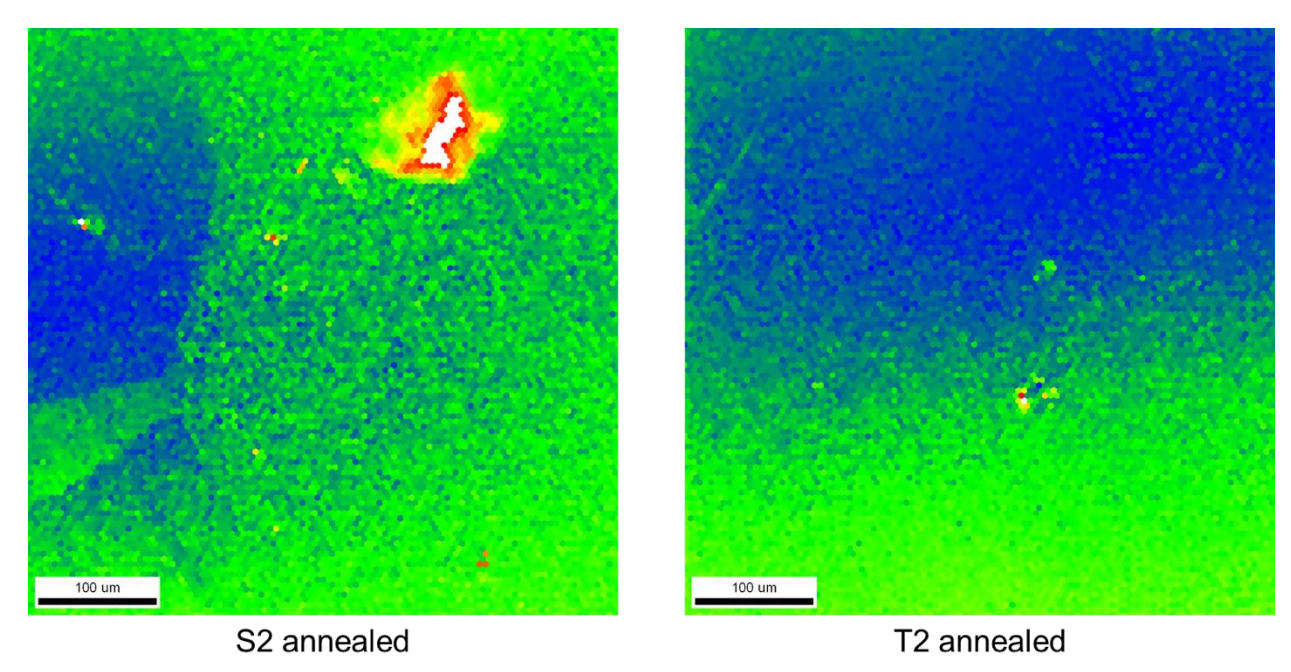


Figure 49: Orientation deviation maps (based upon points with minimum KAM) of the heat-treated samples S2 and T2 before deformation but after electropolishing and annealing. There are no fine scale orientation gradients like those in the as-cut samples. The color scale is the same as Figure 46.

The CBMM-H2 slice was deep drawn into a half-cell, and crystal orientations obtained after deformation are shown in yellow in Figure 50, at locations 1-12 (a different numbering is used as the locations do not always match those on the undeformed ingot slice). For comparison, orientations before deformation at nearby locations are shown in black, and there is only a slight change in orientation in most cases. Orientations within the same grain along the radial direction were also evaluated, in that the stress state varies from iris to equator region. Three such pairs $(12\rightarrow4,~8\rightarrow10,~\text{and}~7\rightarrow6~\text{hand-drawn}$ in Figure 50) were compared to their corresponding orientations before deep drawing. The largest deviation from the original orientation is 9.8° at location 10, while for the other orientations the deviation did not exceed 3.5°.

Even though the crystal orientations did not change much after deformation, the Laue diffraction spots became more smeared. Figure 51 shows three examples of this effect at locations

1 (top), 5 (right), and 7 (bottom) in Figure 50 before and after deep drawing, in which individual spots are no longer discernable after deep drawing.

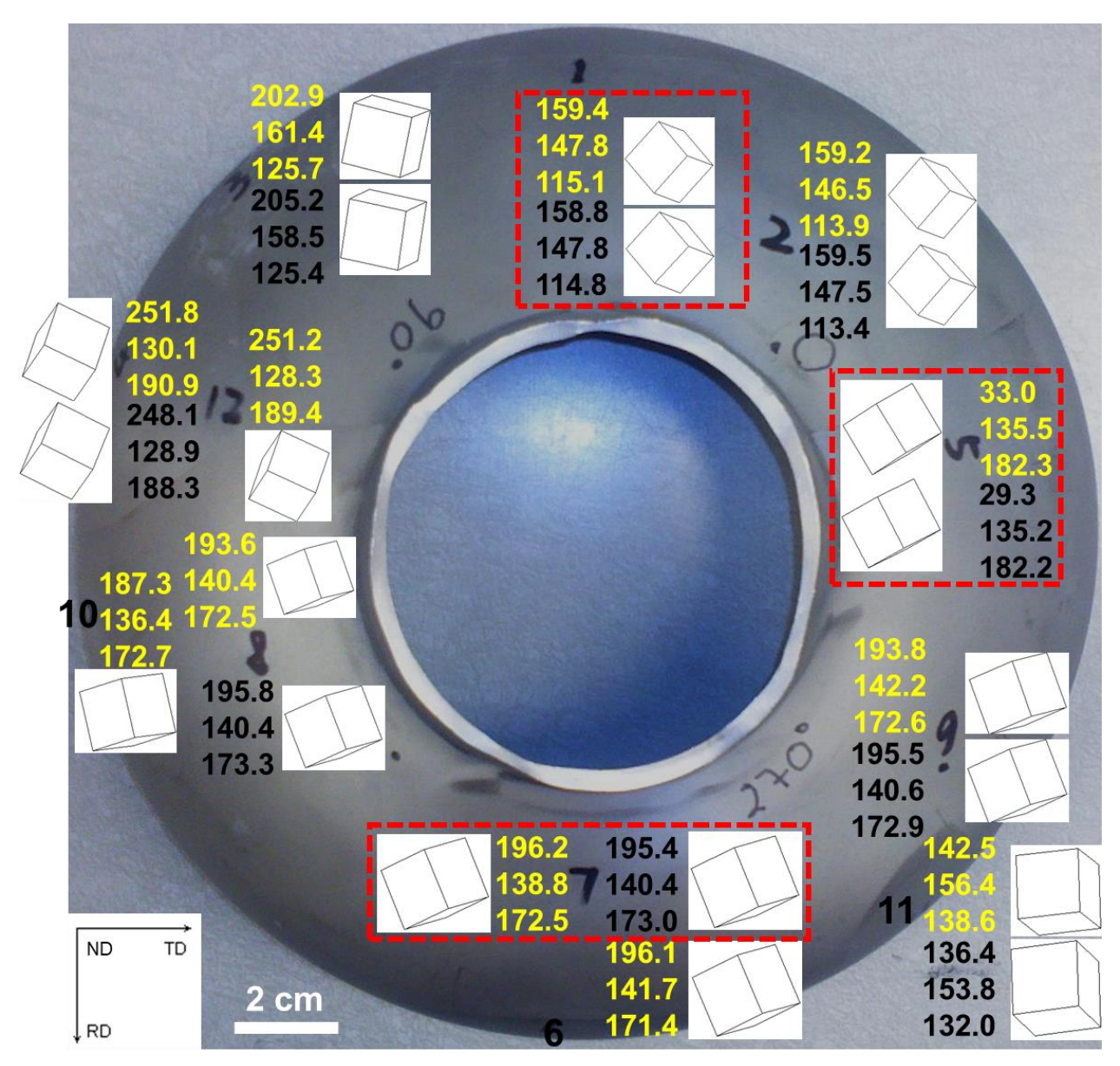


Figure 50: Half-cell deep drawn from the CBMM-H2 ingot slice. Orientations measured before and after deformation are overlaid onto the image (black – before, yellow – after). Note that the numbering of locations (hand-written on the half-cell) is different from Figure 25. The orientations did not change much after deep drawing, except for location 10 (9.8° difference). The red boxes indicate locations for which the Laue patterns will be compared before and after deep drawing (Figure 51) [adapted from Figure 2 in reference [123]].

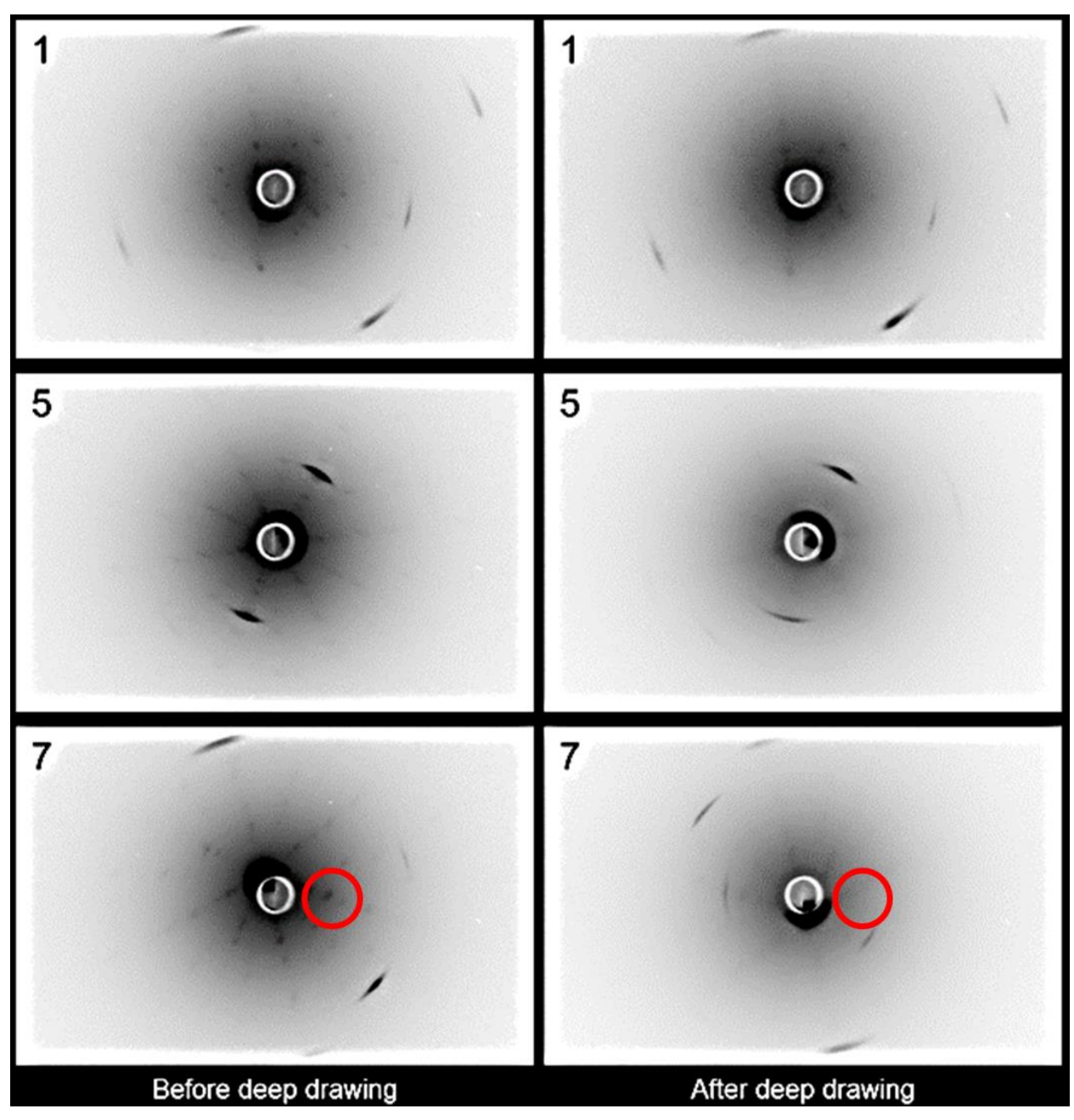


Figure 51: Laue diffraction patterns before and after deep drawing at locations 1, 5, and 7 shown in red boxes in Figure 50. The spots visible on the undeformed ingot slice (left three) are not as visible and more smeared after deformation (right three). A example is shown in red circles at location 7.

In contrast, for the Niowave ingot slab whose surface was end milled, distinct diffraction spots are still visible in the middle of milling bands, and the spots are smeared only at the edges of milling bands. Figure 52 shows an example of this with Laue diffraction patterns near and at a milling band. After a BCP etch that removed about 100 µm from the surface, the diffraction spots became sharper to varying extents at the seven positions examined, examples of which are shown in Figure 53. The spots also moved slightly after BCP, as reflected by a minor orientation change (provided in the Figure).

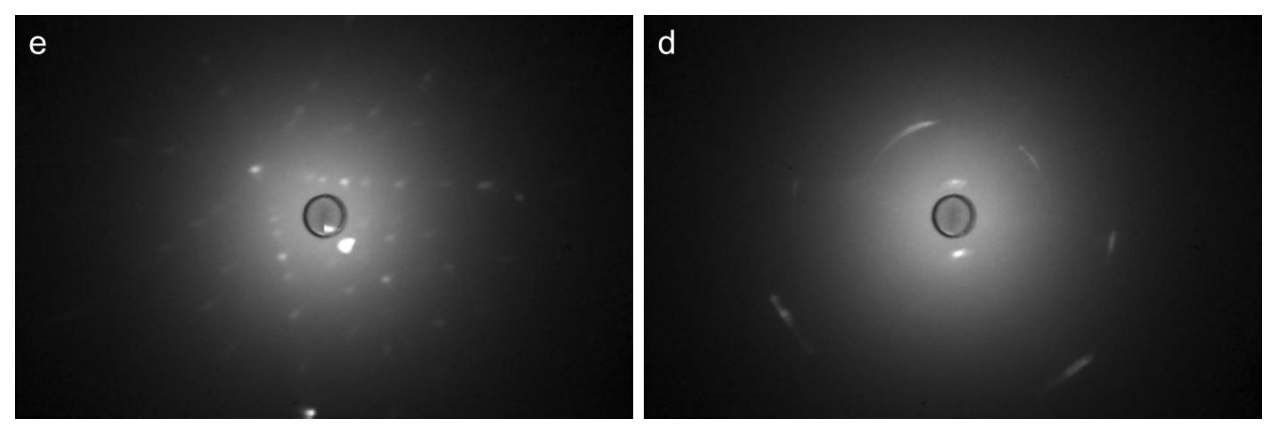


Figure 52: Laue diffraction patterns at positions e and d from the Niowave ingot (Figure 26). The left pattern shows distinct spots in the middle of a milling band, while the right one shows smearing of spots from the edge of a milling band.

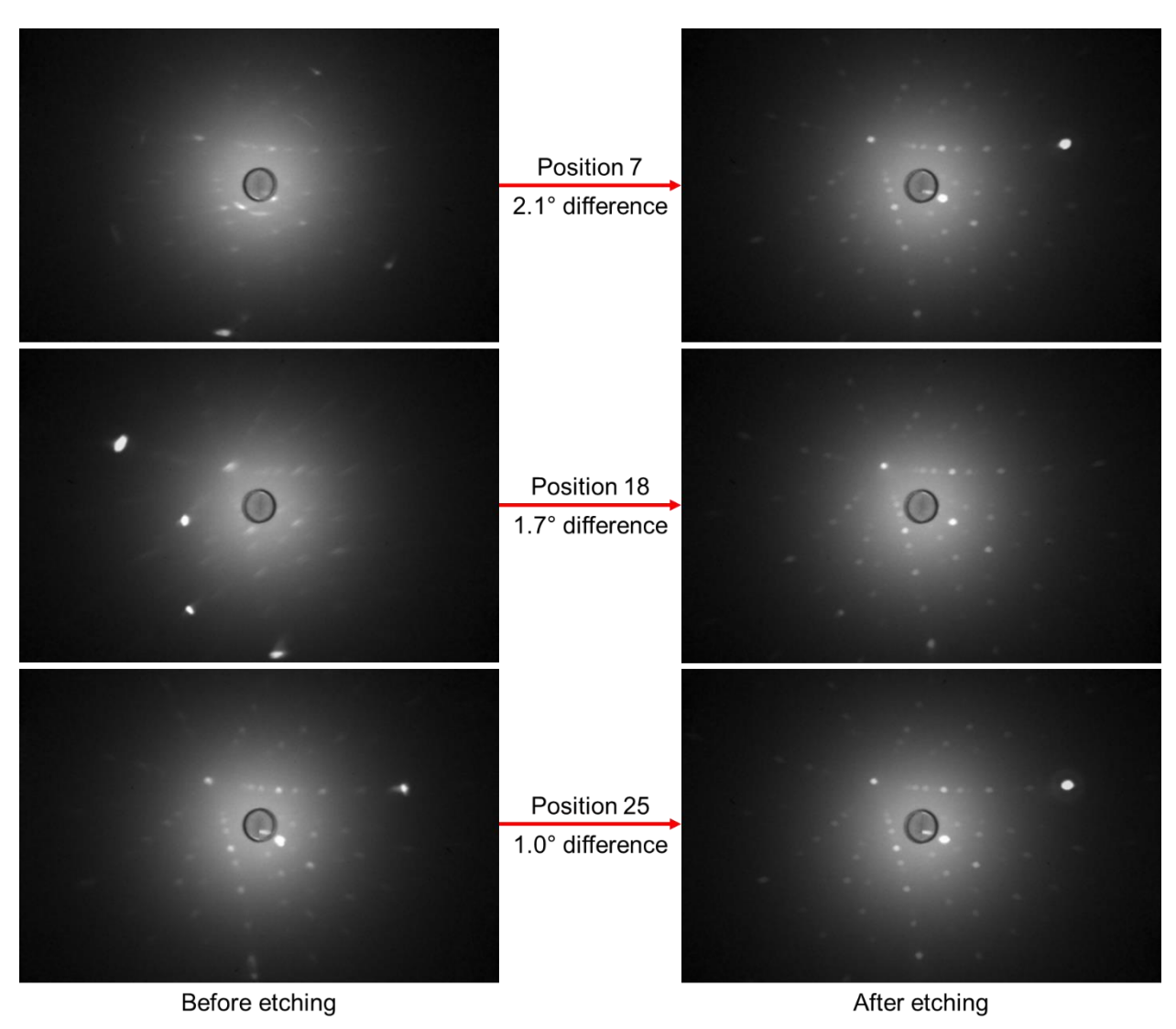


Figure 53: Laue diffraction patterns at positions 7, 18, and 25 from the Niowave ingot (Figure 26) before and after a $100~\mu m$ etch. The spots became sharper after etching. The 1-2° orientation change is due to mounting error and the removal of a machined surface layer.

b. Texture and Stress-Strain Behavior of Fine Grain Nb Sheets

Most of the results of texture assessment of batches of Nb sheet are presented in [61], which provides details on how each map or plot was generated. This section will show extreme cases and a preliminary exploration of correlations between different parameters, as highlighted in [139].

Figure 54 shows sheet normal direction orientation maps, engineering stress-strain curves, and density pole figures for the Tokyo-Denkai samples, with maximum ϵ_f , minimum ϵ_f , maximum UTS, and minimum UTS [139]. The loading direction is either horizontal or in and out of the page with respect to the orientation maps (the ambiguity is due to the symmetry of the square samples and inadequate labeling). The orientation maps are deemed to be representative of the sheets, as additional EBSD scans on grips of the tensile samples (about 10 cm away) show similar microstructure to the square samples [61].

From the orientation maps, the sample with maximum UTS has much smaller grains than the sample with minimum UTS. The sample with maximum ϵ_f has a strong <100> texture component in the pole figures, while the sample with minimum ϵ_f has a dominant <111> component. The texture intensity is higher for samples with maximum ϵ_f and UTS than for samples with minimum ϵ_f and UTS. All four samples lack {110} orientations parallel to the sheet normal.

Figure 55 shows the engineering stress-strain curves for 23 Ningxia samples that were cut either perpendicular or parallel to the rolling direction, and the orientation maps for samples with maximum and minimum UTS. Like the Tokyo-Denkai samples, a smaller grain size corresponds to a larger UTS. However, there is no clear relationship between the stress-strain behavior and sample orientations with respect to the rolling direction. Figure 56 shows the UTS vs. average

grain size (calculated by the TSL software) scatter plots for 23 Tokyo-Denkai and 23 Ningxia samples. Although some degree of correlation is present as expected, there is considerable scatter.

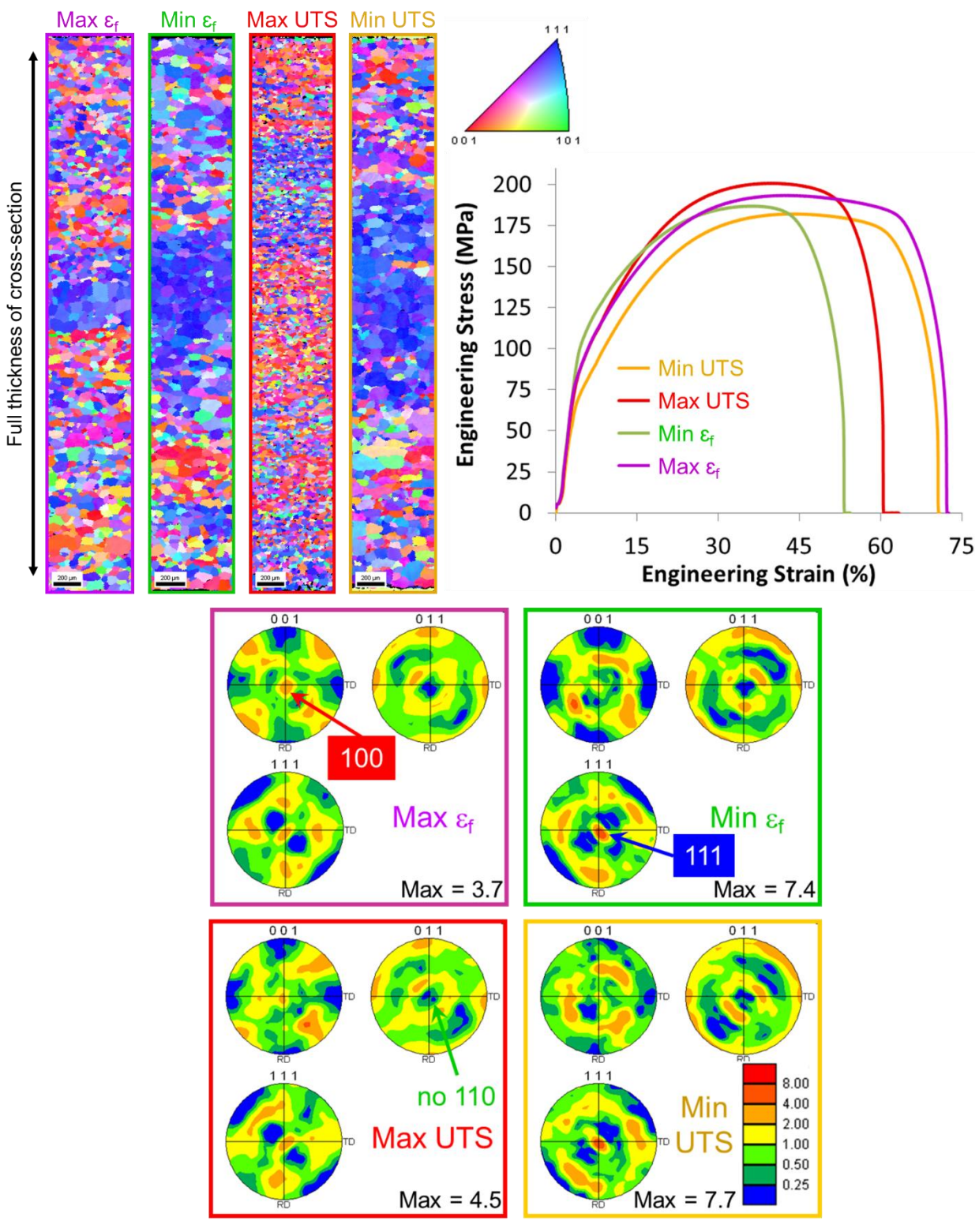


Figure 54: Sheet normal direction orientation maps, engineering stress-strain curves, and density pole figures for the Tokyo-Denkai samples with extreme tensile properties. The loading direction is either horizontal, or in and out of the page with respect to the orientation maps. There is an inverse correlation between grain size and yield strength [adapted from slide 18 in reference [139]].

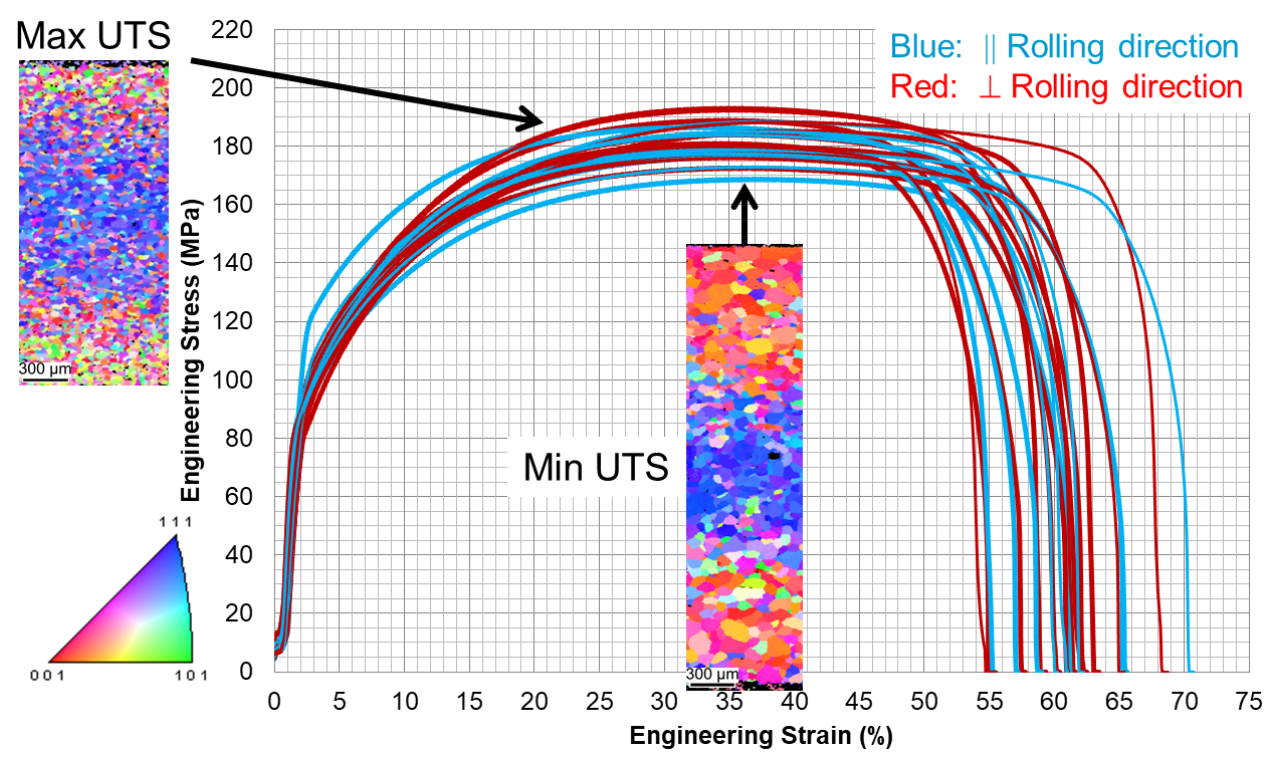
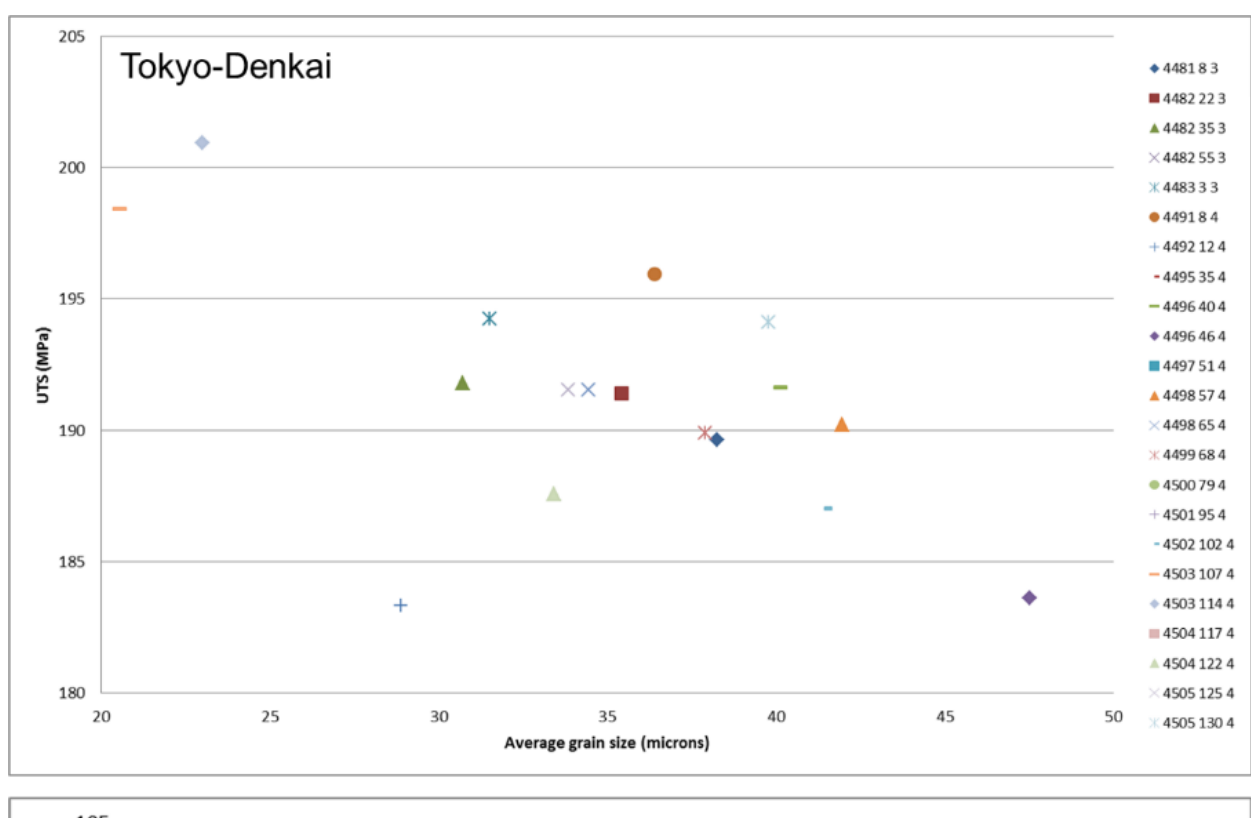


Figure 55: Engineering stress-strain curves for 23 Ningxia samples that were either perpendicular (red curves) or parallel (blue curves) to the rolling direction [adapted from slide 16 in reference [139]]. The yield strength vs. grain size correlation applies to the two extreme samples, but not to every other sample.



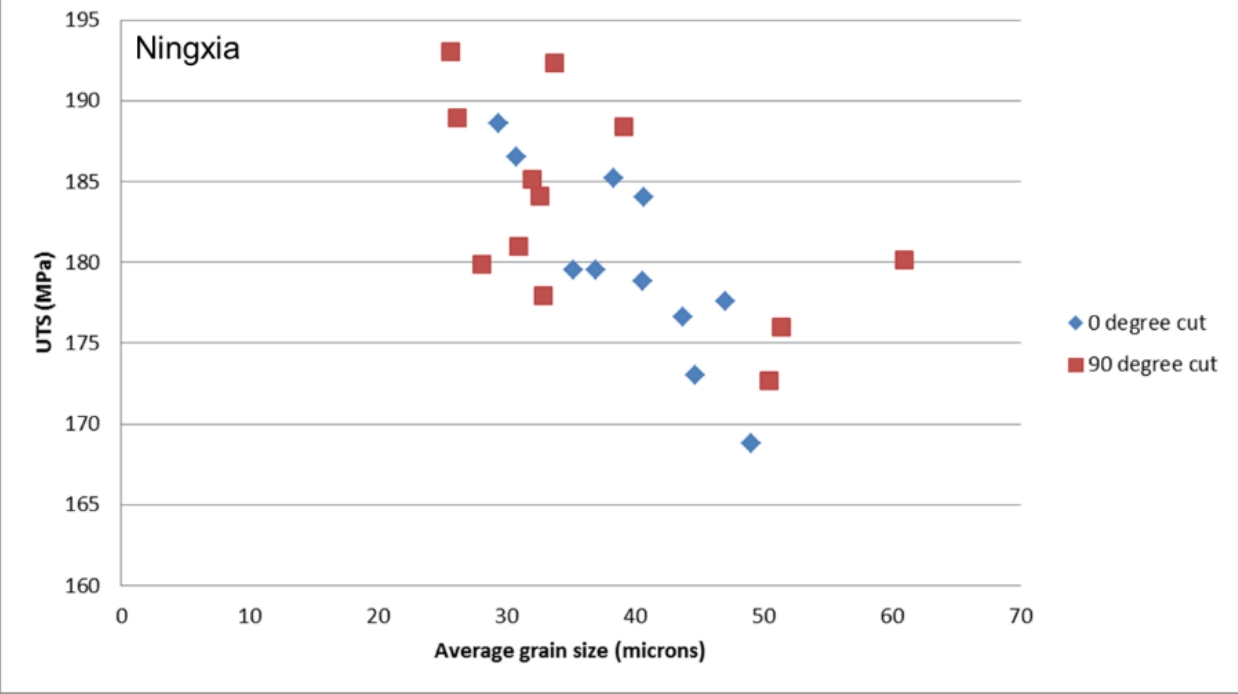


Figure 56: UTS vs. average grain size (equivalent diameter from EBSD analysis) scatter plots for Tokyo-Denkai samples (above) and Ningxia samples (below). A weak negative correlation is present. On average, the Tokyo-Denkai samples have higher UTS than the Ningxia samples [adapted from slide 17 in reference [139]].

Figure 57 shows the maximum orientation distribution function (ODF) intensity at each value of ϕ_2 within a section defined by Φ (45-65°) and ϕ_1 (0-180°) for Tokyo-Denkai and Ningxia samples [139]. The γ -fiber peaks are similar for both materials, with a spread over a range of ϕ_2 between 35° and 60° for Tokyo-Denkai, and between 35° and 55° for Ningxia. The intensity values vary considerably for both suppliers. Figure 58 shows ϵ_f vs. average ODF intensity of the γ -fiber at $\phi_2 = 45^\circ$ for Tokyo-Denkai and Ningxia samples, where there is no apparent correlation. Other plots pursuing correlations between measurable parameters are shown in [61], although the correlations are either weak or absent.

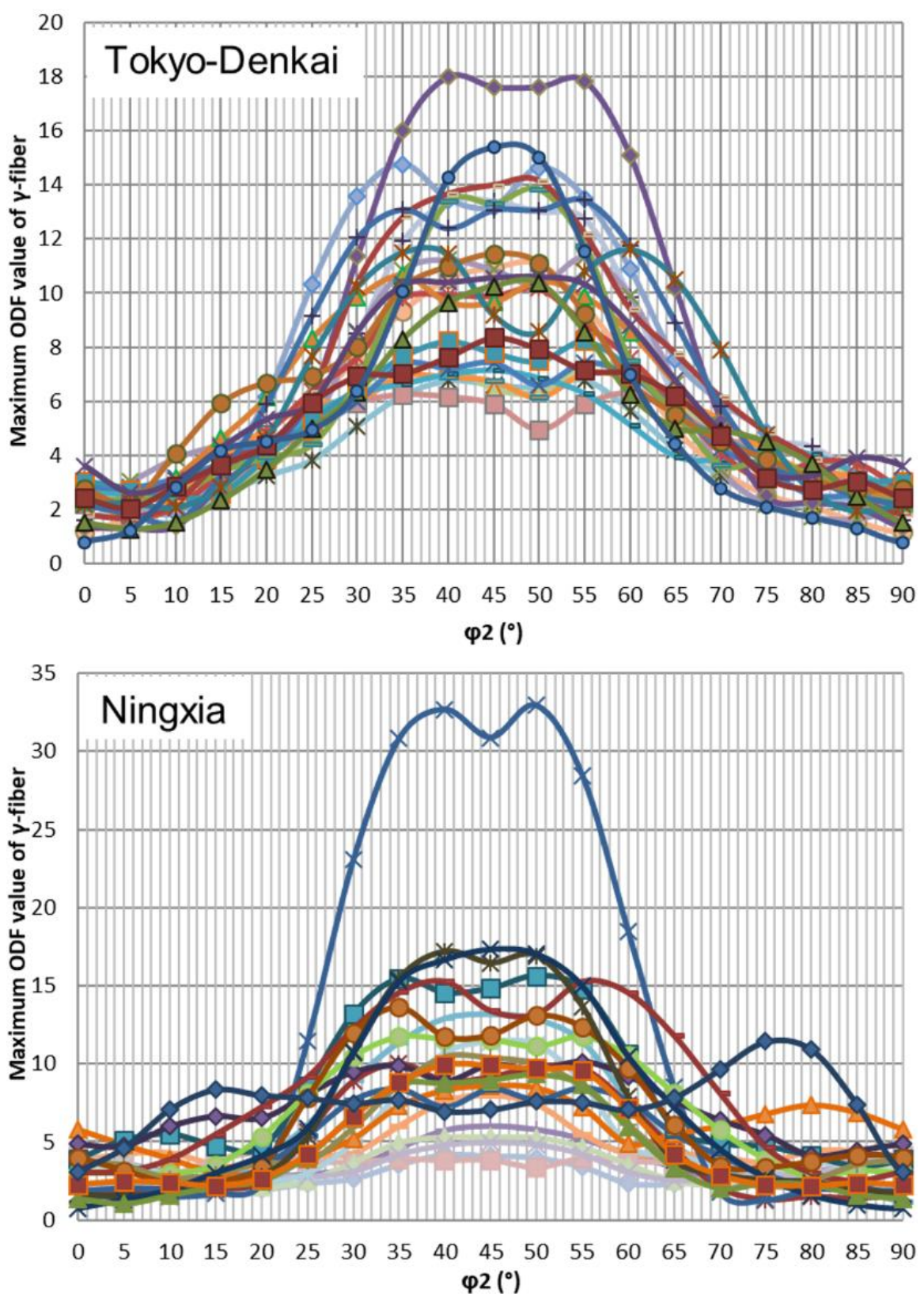
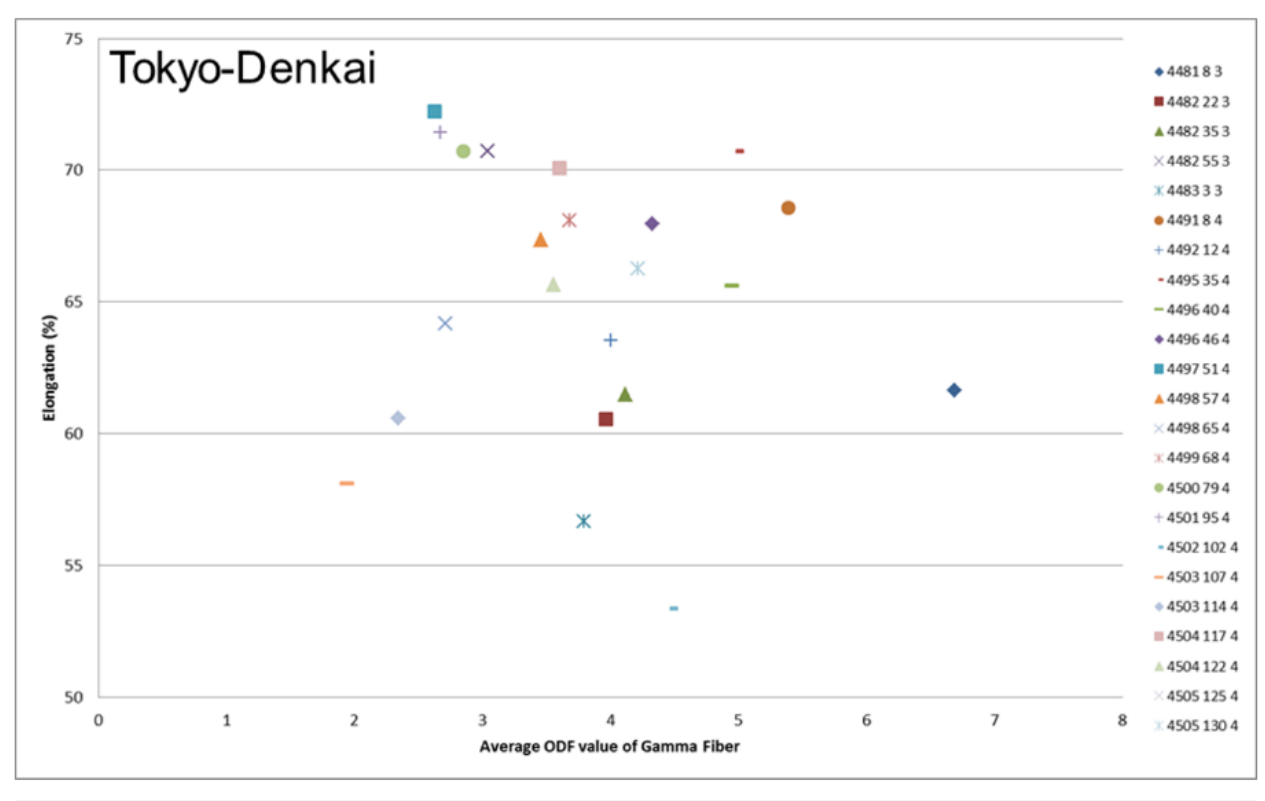


Figure 57: Maximum ODF intensity value of γ -fiber on or near the $\phi_2 = 45^\circ$ slice (from 0-90°) for Tokyo-Denkai (above) and Ningxia (below) samples [adapted from slide 20 in reference [139]].



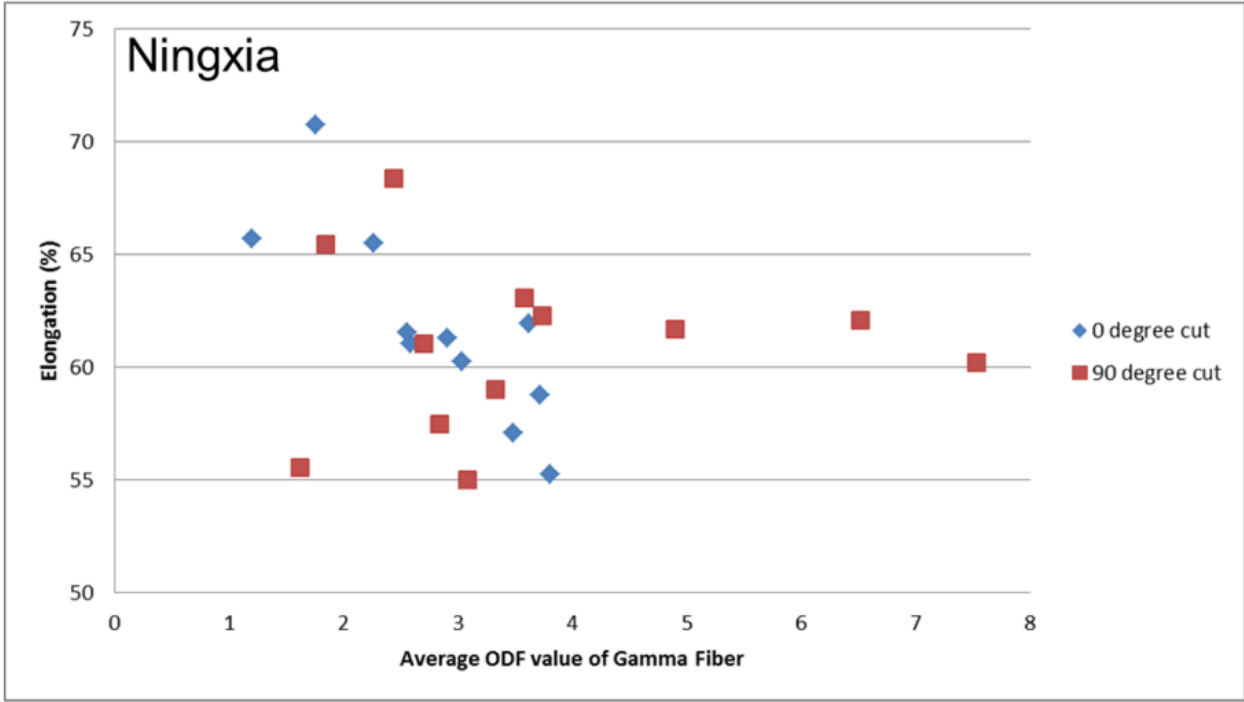


Figure 58: ϵ_f vs. average ODF intensity value of γ -fiber at $\phi_2 = 45^{\circ}$ for Tokyo-Denkai (above) and Ningxia (below) samples. Little correlation is present [adapted from slide 21 in reference [139]].

c. Microstructure of Rolled Nb Samples

Figure 59 through Figure 61 show orientation maps of the cross-sections of the rolled samples, at cold work reductions of about 68%, 76%, and 92%, respectively. In Figure 59, some regions of the lower grain still exhibited the original crystal orientation at the right end of S1 with deformation bands starting to develop, and a different grain is visible along the upper edge. As the reduction increases to 76%, deformation bands begin to dominate, and the initial orientation is hardly present, as shown in Figure 60. At 92% reduction (Figure 61), much of the area is no longer indexable, though the well-defined horizontal bands of different orientations and black zones in the middle resemble the layered structure observed in the sheet material.

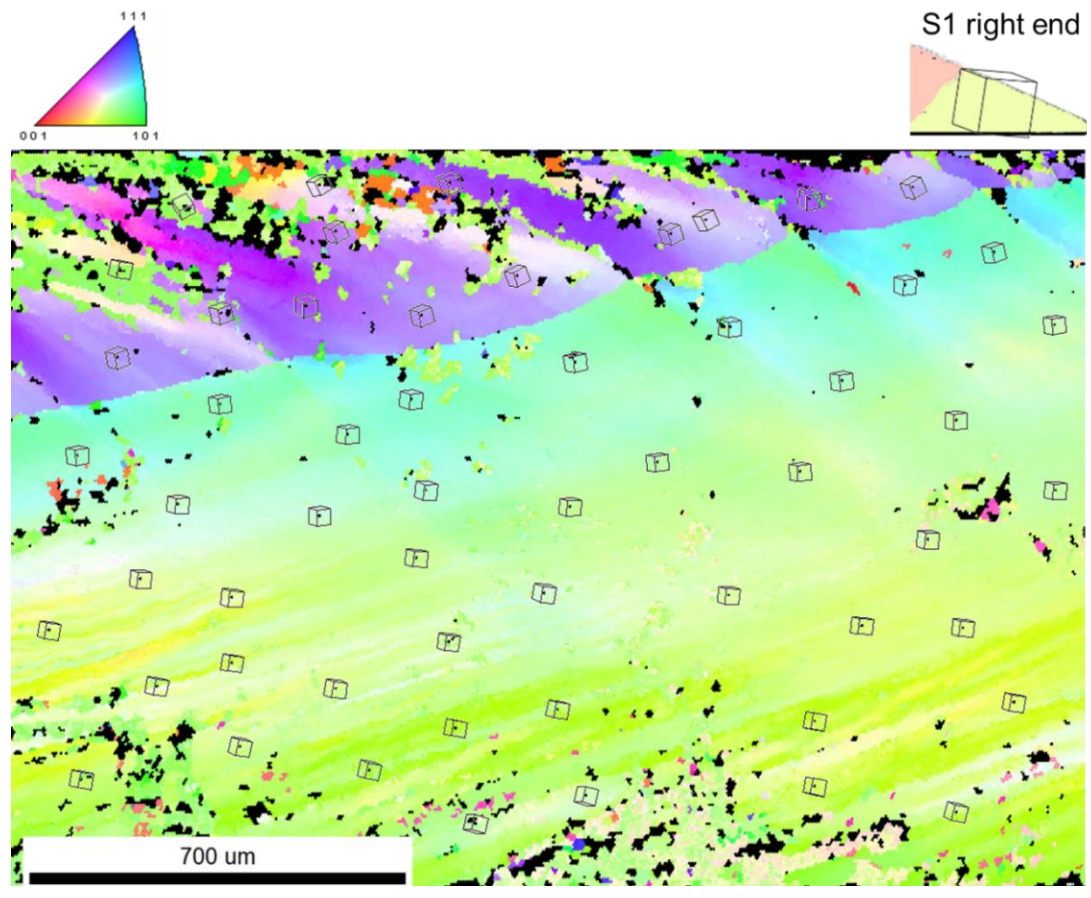


Figure 59: Orientation map of a region on the cross-section of sample A2 with ~68% reduction. The original orientation is shown on the top right corner. An original grain boundary is present in the upper area. The average confidence index (CI) before cleanup is 0.45 for this dataset. The legend on the top left applies to all following orientation maps unless otherwise specified.

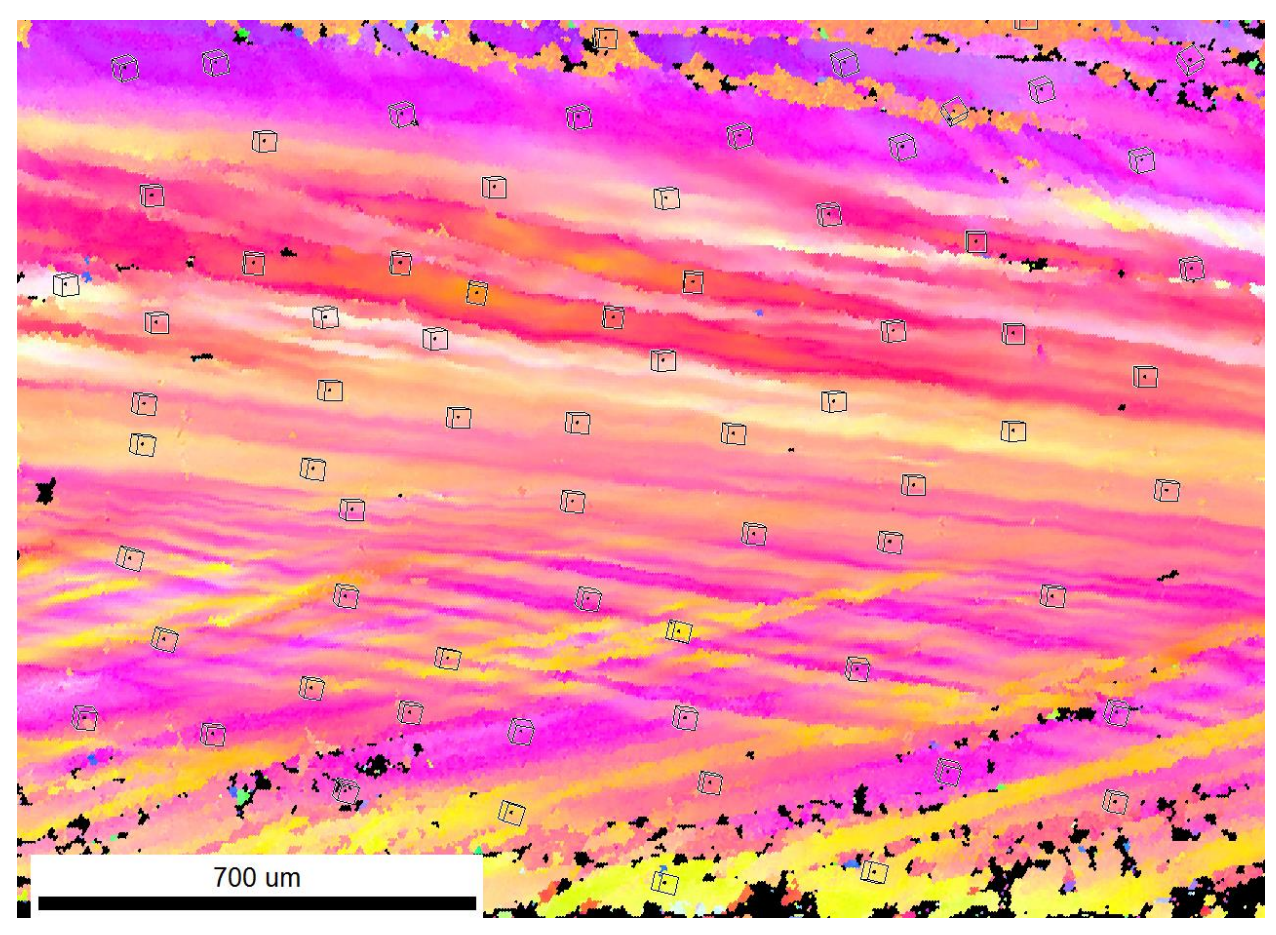


Figure 60: Orientation map of a region on the cross-section of sample A2 with ~76% reduction. Further deformation bands with distinct orientations developed, and the original orientation is no longer traceable. The average CI before cleanup is 0.54 for this dataset.

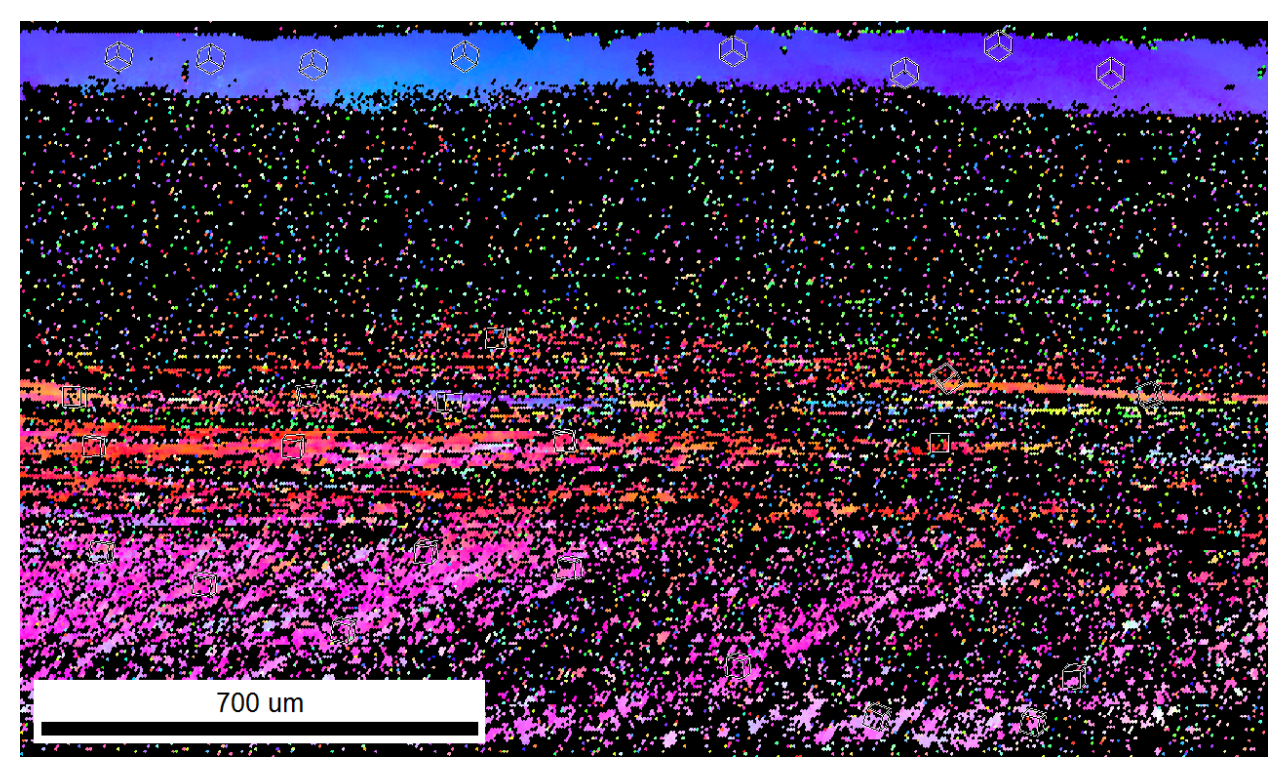


Figure 61: Orientation map of a region on the cross-section of sample A6 with ~92% reduction. The horizontal bands of different orientations and black zones in the middle resemble the layered structure observed in sheet material. The average CI before cleanup is 0.13 for this dataset.

Figure 62 shows orientation maps from matching areas on sample A2 with ~68% reduction before and after annealing at 800 °C/2hr. Small grains in pink and dark green nucleated in the lower large grain as a result of the heat treatment, with orientations different from the parent grain. However, these minority orientations are the same within both the pink and dark green regions, as evident from the prisms shown on the small patches. Also, both new orientations are misoriented about 30° from the parent green orientation, and the rotation axis is close to <111>. The poorer quality in the orientation map after annealing is likely due to the heat treatment plus more time since the last etch which was done before the anneal.

A similar comparison of orientation maps before and after annealing is shown in Figure 63 for sample A2 at ~76% reduction. While recrystallization is less remarkable than in Figure 62, the

new grains on the right still have consistent orientations, which are also similar to the dark green orientations in Figure 62. The new orientations are still about 30° away from the parent orientation, although there is no longer a well-defined rotation axis. The orientation map for sample A6 after annealing is similarly noisy so that it is not possible to discern recrystallized grains, so it is not shown.

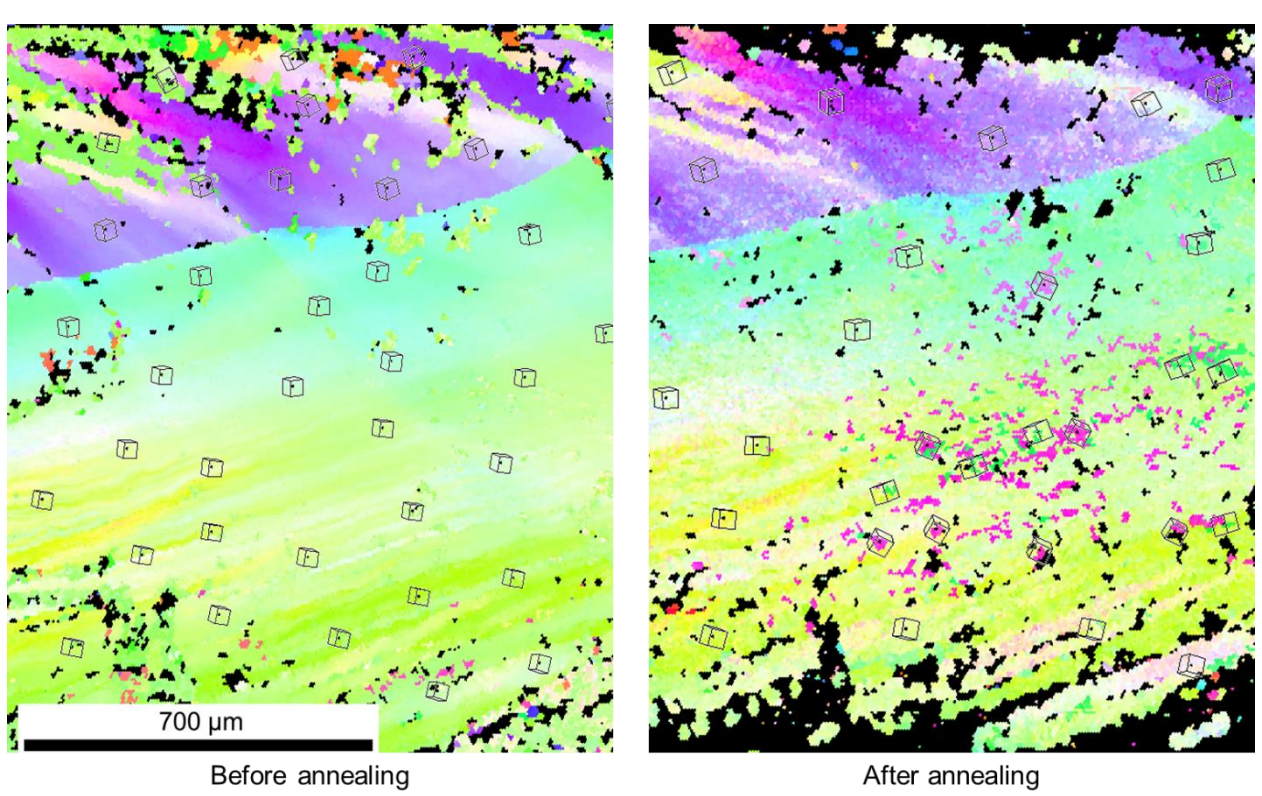


Figure 62: Orientation maps from matching areas on sample A2 with ~68% reduction (shown in Figure 59) before and after annealing at 800 °C/2hr. Small grains emerged inside the lower large grain due to the anneal, with orientations different from the parent grain. However, these minority orientations are the same within the pink and dark green regions.

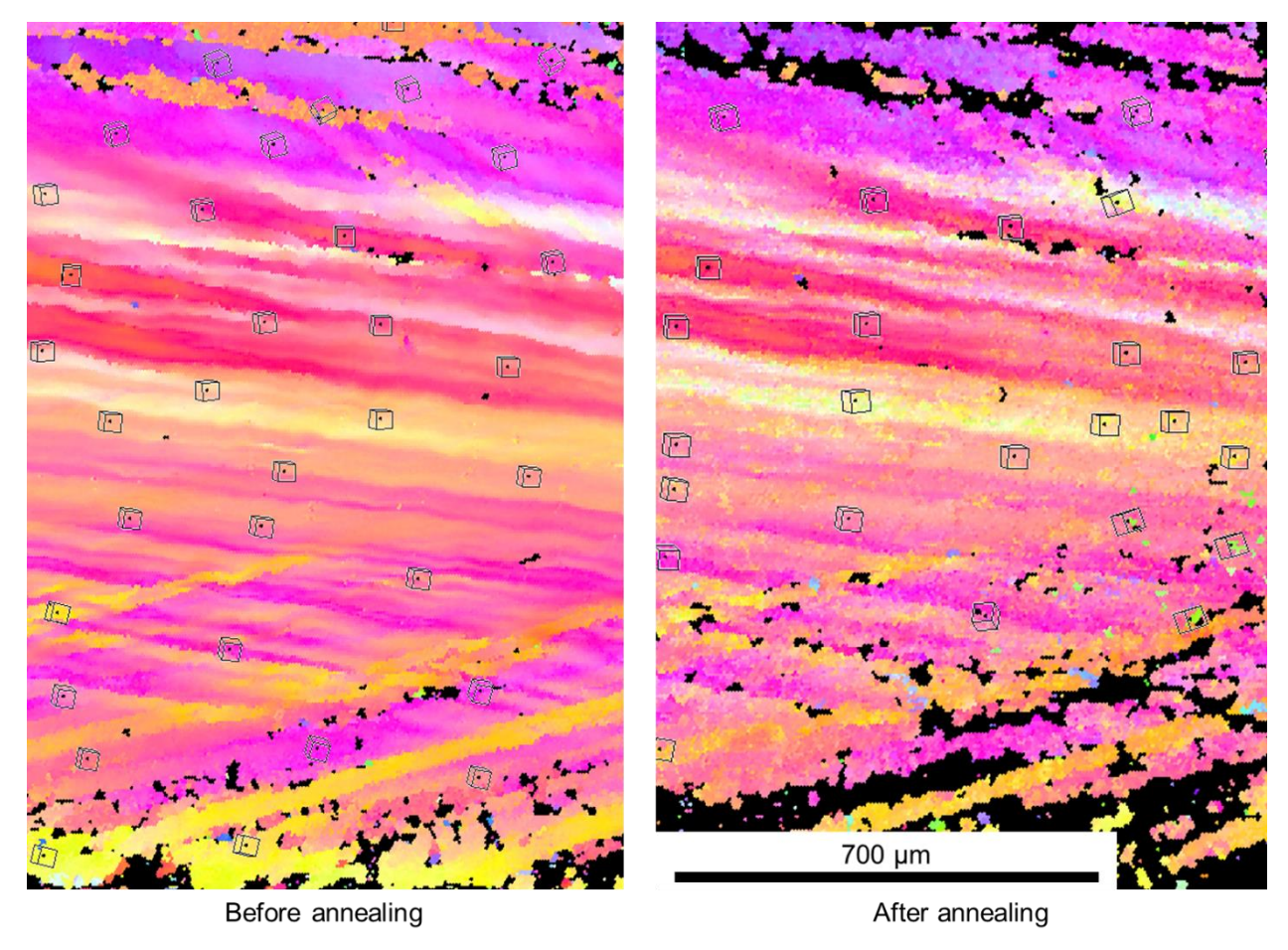


Figure 63: Orientation maps from matching areas on sample A2 with ~76% reduction (shown in Figure 60) before and after annealing at 800 °C/2hr. Similar to Figure 62, small grains with green orientations emerged on the right from the deformation bands because of the anneal. The scattered new grains again have the same orientation.

This work provides initial evidence of how the randomly oriented large grains evolve into the highly variable sheet microstructure upon rolling. While this characterization is preliminary, it is representative of other measurements that are the focus of research projects being conducted by colleagues.

d. Evolution of Microstructure in Nb Cavity Samples

Changes in the microstructure resulting from forming the H1/H2 cavity half illustrated in Figure 30 were assessed using normal direction orientation maps, LAM maps, and IQ maps in the left, middle, and right positions, for the equator and iris in Figure 64 and Figure 65, respectively. Three locations on the equator and three locations on the iris are shown in the top, middle, and lower groups of images in each Figure. Within each group, the images show the as-deep drawn maps above, annealed in the middle, and re-etched following the anneal on the bottom.

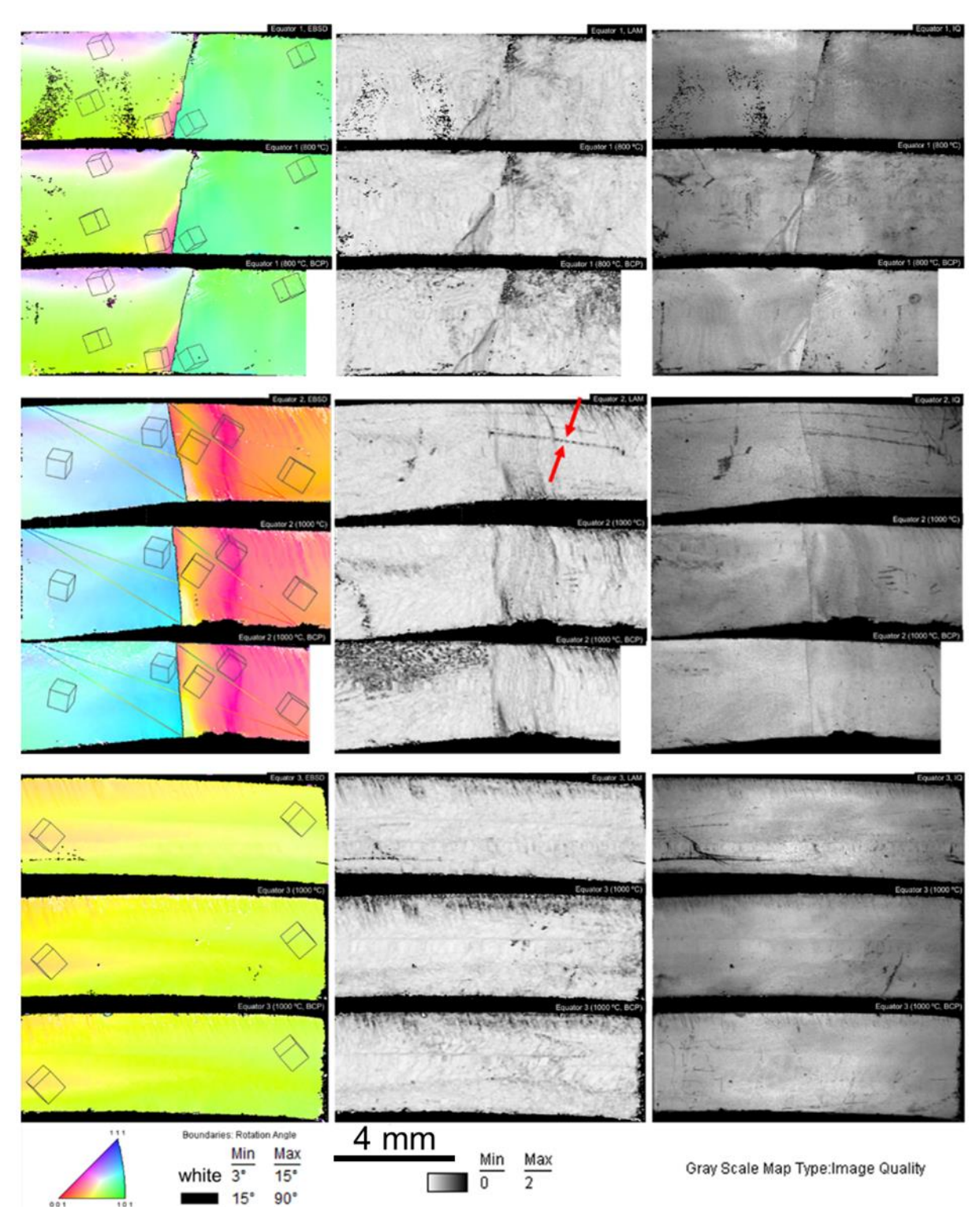


Figure 64: Normal direction orientation maps (left), LAM maps (middle), and IQ maps (right) for the three equator regions indicated in Figure 31. For each region, results for as-deep drawn, after heat treatment, and after BCP conditions are shown from top to bottom. The scale and legends are common to all images. Red arrows on the LAM map of Equator 2 indicates a scratch feature that disappeared after the heat treatment [adapted from Figure 5 in reference [126]].

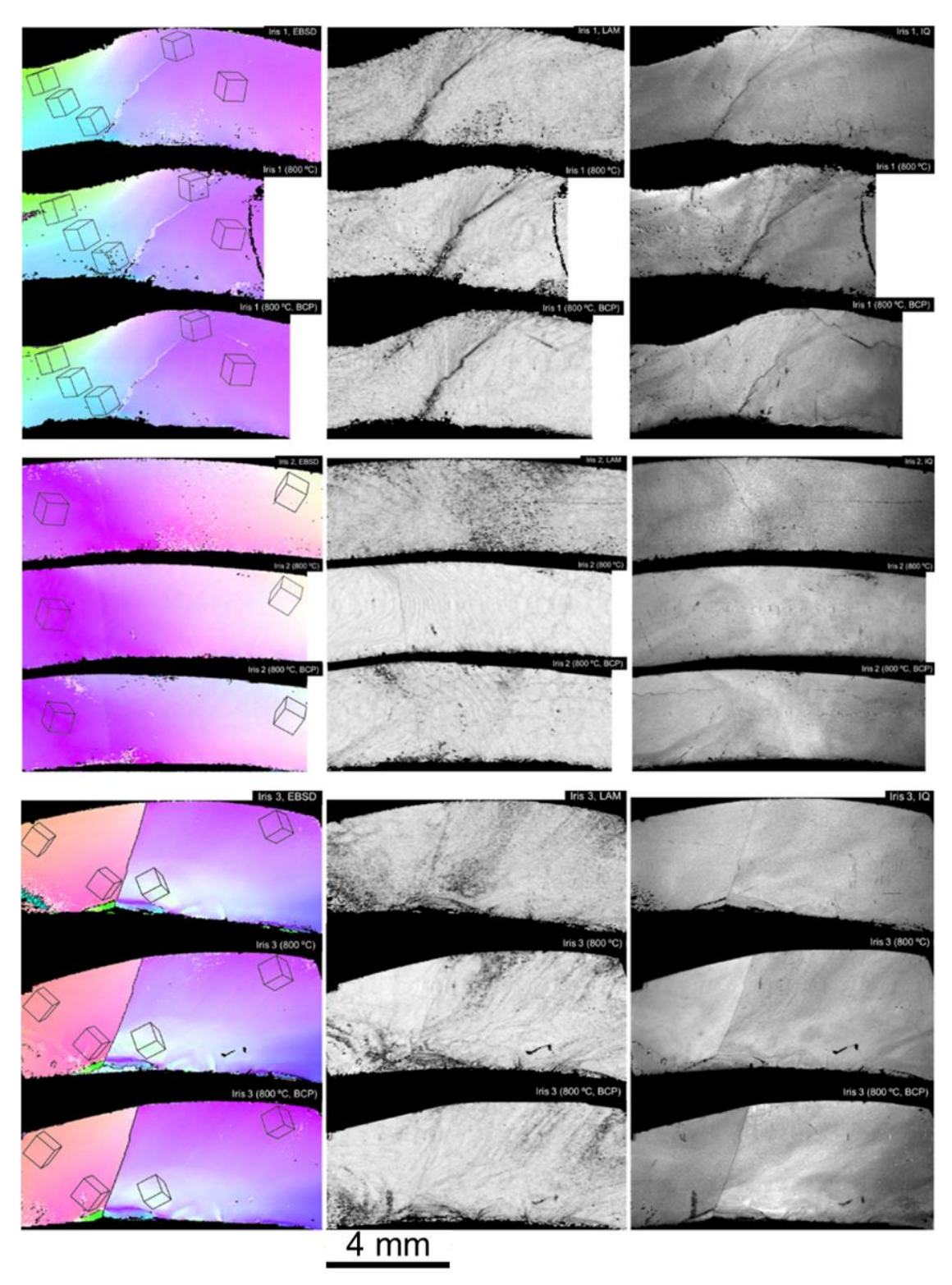


Figure 65: Normal direction orientation maps (left), LAM maps (middle), and IQ maps (right) for the three iris regions indicated in Figure 31. For each region, results for as-deep drawn, after heat treatment, and after BCP conditions are shown from top to bottom. The scale is common to all images and the legends are the same as Figure 64. A grain boundary developed in Iris 1, likely during deep drawing [Figure 6 in reference [126]].

On the orientation maps, low and high angle grain boundaries are marked by white (3-15°) and black (>15°) lines. The 2nd nearest neighbor sampling area (as illustrated in Figure 4) is used for the LAM maps, with a grayscale from white (0°) to black (2°). An individual grayscale from black (minimum IQ) to white (maximum IQ) is used for each IQ map. The LAM maps and IQ maps from matching areas are shown adjacent to each other to aid comparison.

Significant orientation gradients are evident by the large color changes over distances of 100-200 µm in the orientation maps. Surface contamination, grain boundaries, and artifacts such as residual deformation from scratches are visible on the IQ maps. The darker gray regions on the LAM maps near the surface indicate larger LAM values than the lighter gray regions in the interior bulk area, which is evidence for surface damage.

The orientation and LAM maps with grain boundaries show that the magnitude of surface damage depends on crystal orientations. For example, Equator 2 in Figure 64 shows that LAM values on the outside surface are greater (darker) in the right grain than in the left; the difference is even larger after annealing. The heat treatment reduced the magnitude of orientation gradients inside the material, as the LAM maps became lighter, representing a crystal with lower defect content. However, the heat treatment altered the orientation gradients near the surface very little. Furthermore, high LAM values are located near the surface after annealing in all areas except on the outside of the iris to the left of the grain boundary in Iris 3 (Figure 65), in which the left grain was strained (thinned) more than the right grain. The regions that did not initially possess high surface LAM values remained unchanged after annealing (except for Equator 2 in the left grain, where removal of 10 µm revealed much higher LAM values).

A close inspection of the orientation maps suggests that there is often a slight migration of grain boundaries at each stage. For example, the jog in the boundary in Equator 1 (Figure 64) is at a different location in the as-deep drawn and annealed maps and is absent in the etched map.

The heat treatment also led to the removal of defects on the initially polished surface in some cases, notably the disappearance of orientation gradients after annealing that were remnants of a scratch from left to right in Equator 2 (Figure 64). However, what appeared to be similar scratch features in Equator 3 just above the center did not completely disappear with annealing, and the same feature with a wider breadth of misorientations was present after the $10~\mu m$ etch, which implies that this feature is a long-range defect structure that formed during deformation and was stable through the heat treatment.

After etching, the LAM values became higher in several cases, an example of which is shown in the upper third of the left grain in Equator 2 in Figure 64, where many low angle grain boundaries are evident by both the white boundary lines in the orientation map and the extensive black local maxima in the LAM map. Figure 66 provides a quantitative visualization of this, in which the misorientation profiles for the three lines from corresponding places on the orientation maps in Figure 64 are plotted. In the after-BCP condition, the profile for the left grain exhibits a large oscillation of about 2-3° as the line crosses the area with many low angle grain boundaries. This effect is also evident in the etched LAM map of Iris 2 in Figure 65, though less pronounced.

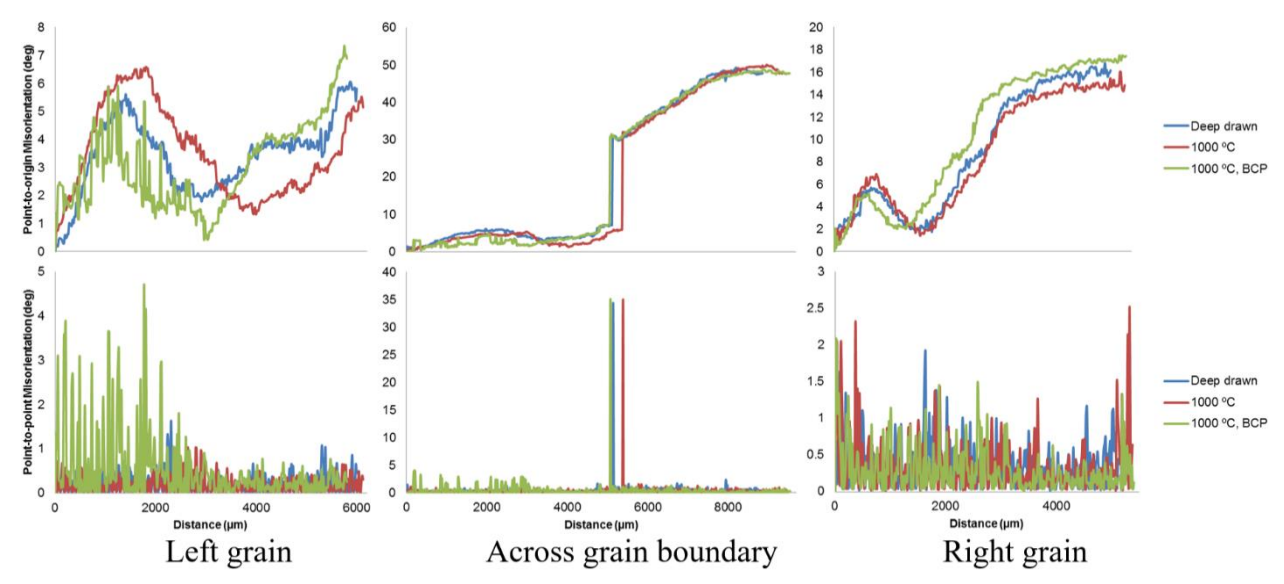


Figure 66: Point-to-origin (upper three) and point-to-point (lower three) misorientation profiles for the three colored lines drawn on Equator 2 in Figure 64. The blue ends of the colored lines in Figure 64 are the origin. In the after-BCP condition (green), the left grain exhibits an oscillation of ~2-3° as the line crosses the area with low angle grain boundaries. [Figure 7 in reference [126]].

Figure 67 shows the LAM histograms for the six scans after deep drawing, after annealing, and after BCP. Before the heat treatment, all iris scans (dashed lines) had higher LAM values than the equator scans (solid lines), which is consistent with the larger strain and greater amount of darker shades of gray in the as-deep drawn LAM maps. Annealing resulted in more dramatic changes in the iris than in the equator, as all LAM peaks for the iris scans moved to the left by about 0.25°. In contrast, LAM peaks for the equator scans shifted in both directions, suggesting that the recovery processes were highly variable. For example, the peak for Equator 3 moved to the right after the 1000 °C/2hr anneal, indicating higher GND content. After etching, the LAM values showed no consistent relationship with the annealed state in the same areas, as a different volume of material was sampled (which was subsurface after annealing).

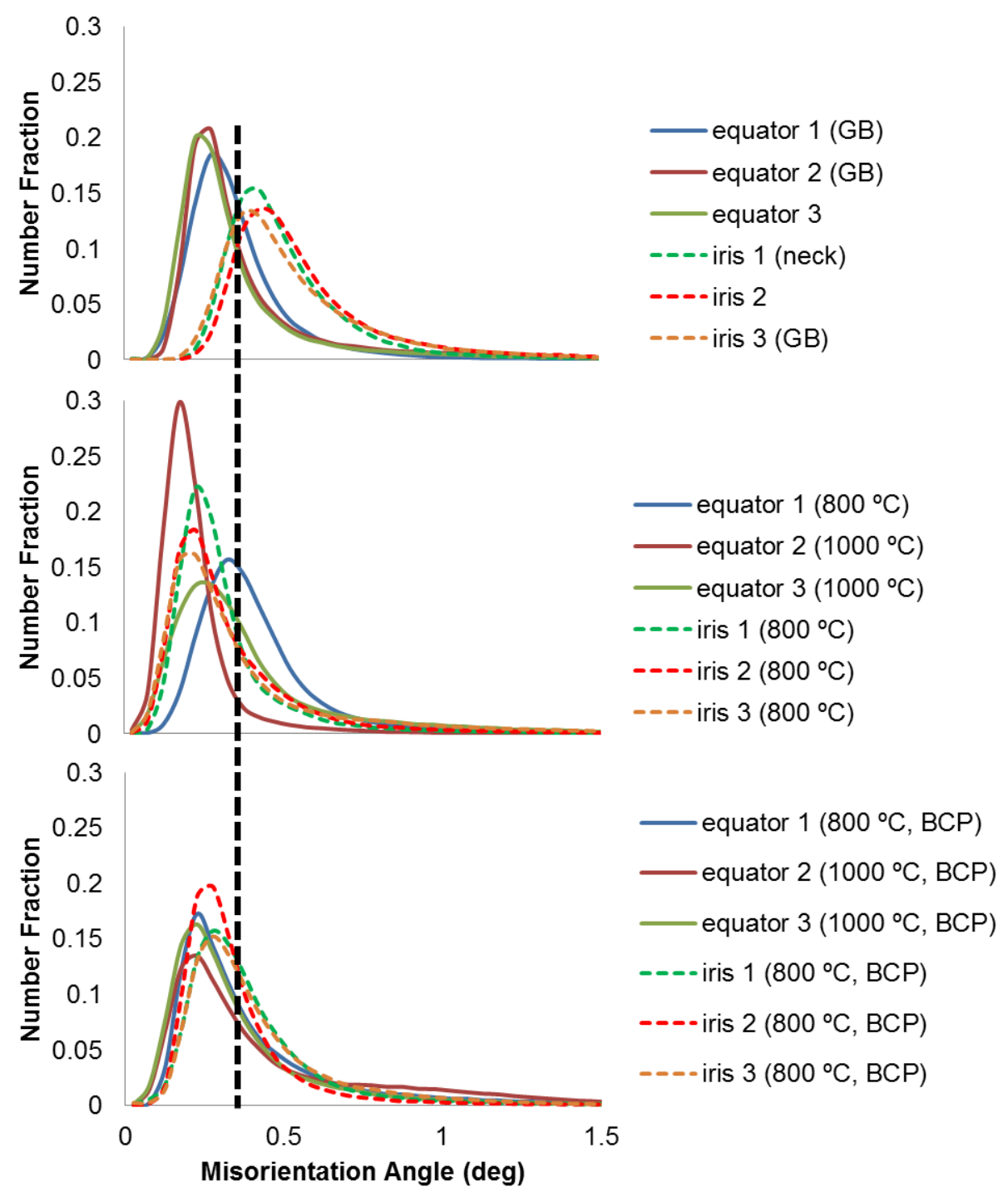


Figure 67: LAM histograms of the six EBSD scans for as-deep drawn (top), after annealing (middle), and after BCP (bottom) conditions. The horizontal scale is common for all three plots. Before annealing, the iris had higher LAM values than the equator, but the iris changed more from annealing [Figure 8 in reference [126].

e. Slip and Crystal Rotation in Heat-Treated Nb Single Crystals

Figure 68 shows the engineering stress-strain curves of the as-received and heat-treated samples side by side [16, 130]. The color code for the orientations is provided on the inverse pole figure on the left plot. Most samples exhibited a stage of easy glide that is characteristic of single crystals, while orientation U showed more work-hardening than a typical polycrystal and necked before reaching the 40% engineering strain. Flow stresses and yield strengths are consistently lower after the 800 °C/2hr anneal. Also, there is no longer a slight drop in the flow stress in the heat-treated samples between yield and ~15% strain, which is most significant in orientation T.

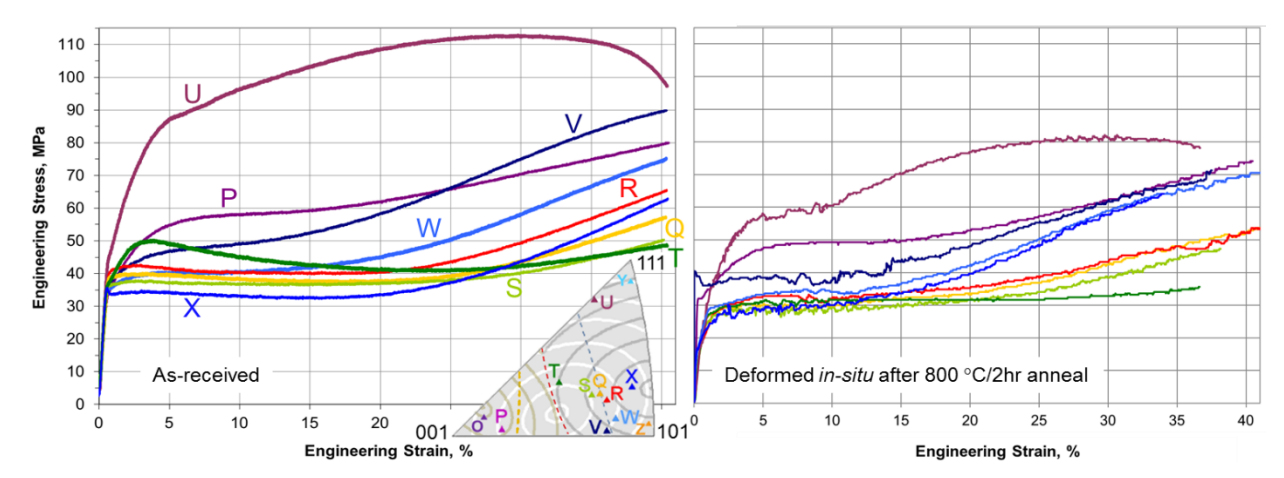


Figure 68: Engineering stress-strain curves of as-received (left) and heat-treated (right) samples. Orientations of tensile axes are indicated by corresponding colors in the triangle inset, which also provides Schmid factor contours in white for $\{110\}$ slip and gray for $\{112\}$ slip, both scaled at 0.5, 0.499, 0.49, 0.47, 0.44, 0.40, 0.36, 0.32. Dashed lines mark boundaries with equal Schmid factors (orange $-\{110\} + \{112\}$ with intersecting slip directions, red $-\{112\}$ with intersecting slip directions, blue $-\{110\} + \{112\}$ with the same slip directions) [Figure 1 in reference [130]].

The IPF triangle inset in Figure 68 provides orientations of tensile axes with respect to the sample coordinate system, overlaid with Schmid factor contours and boundaries. Samples with tensile axes oriented close to the symmetry boundaries where two slip systems have equal Schmid factors (U, P, and V) are more prone to work hardening due to the interactions between intersecting slip systems, while samples with tensile axes oriented away from these boundaries tend to have a low initial hardening rate.

The noisier stress-strain curves for the heat-treated samples resulted from the setting for acquiring the load data. The resolution could have been significantly improved by changing the unit from pounds to grams, thereby making the curves much smoother, but this was discovered too late.

For comparison with the as-received samples, slip trace analyses were performed on the heat-treated samples, an example of which is shown in Figure 69 for sample W. At each strain level (~10% increments), computed slip traces using a MATLAB code [140] based on measured orientations on the top surface were compared with observations for higher Schmid factor slip systems, assuming that the stress tensor was uniaxial tension. Traces for {112} slip are indicated with purple dashed lines, and {110} with green dashed lines on the prisms. The computed traces are in good agreement with the observed traces on SEM images taken at three locations with 1000x magnification.

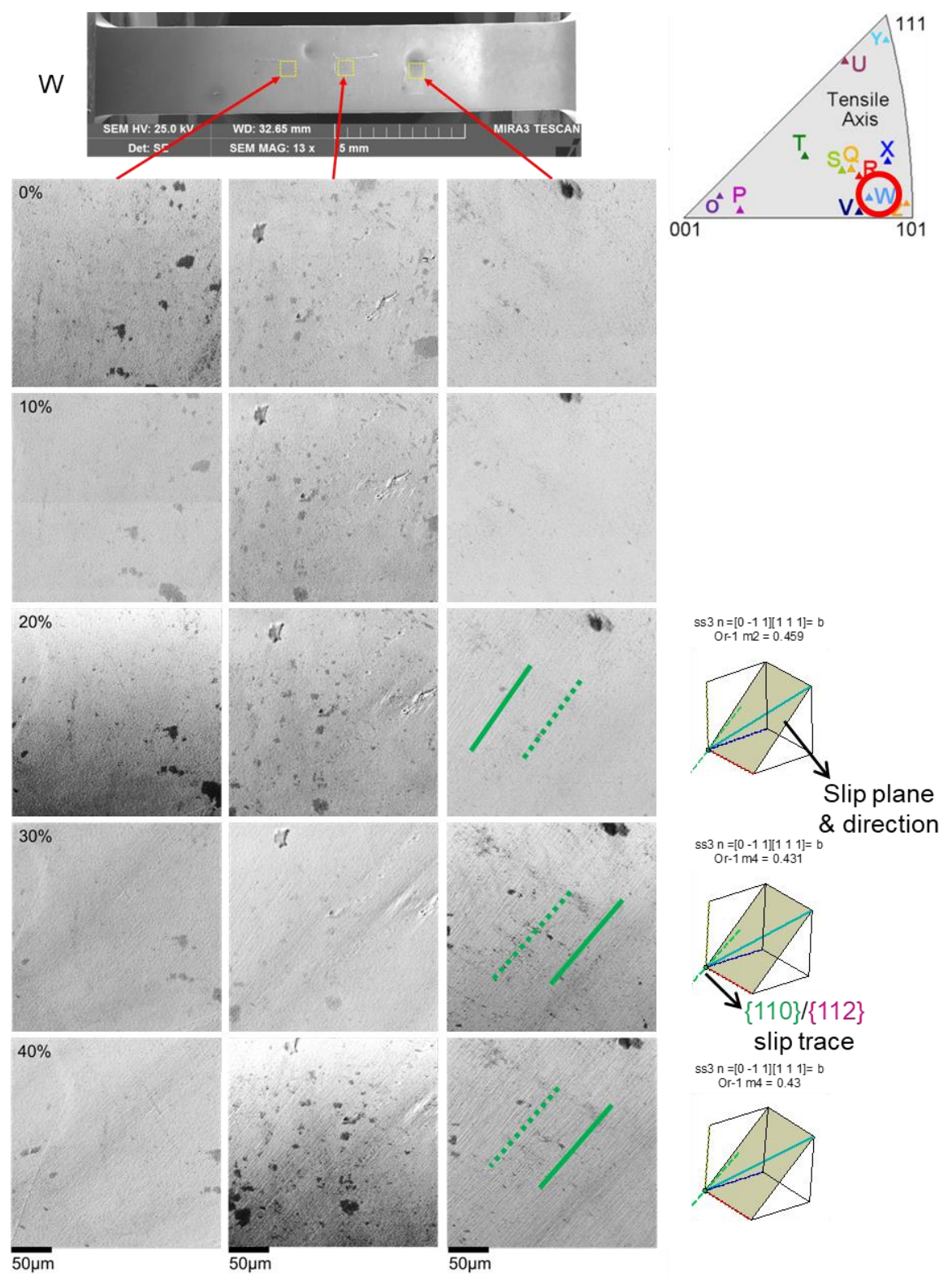


Figure 69: Slip trace identification on the heat-treated sample W in some of the areas examined. Observed slip traces (solid lines) were matched with computed traces (dotted lines) based on the measured orientations, with {110} slip traces in green, and {112} in purple. Slip traces were not apparent until ~20% engineering strain for this sample [adapted from Figure 7 in reference [58]].

Figure 70 and Figure 71 demonstrate how the observed slip traces are related to Schmid factors among the computed slip systems (presented in decreasing Schmid factor order up to the 8th highest), using orientations T and V. For orientation T, the same {110} slip system with the highest Schmid factor was observed in both samples, even though there is a small difference between the initial orientation of T2 and T3 that altered the ranked list of slip system Schmid factors. In contrast, three different slip systems were observed for orientation V in the two samples, even though the samples had the same initial Schmid factor ranking.

The effect of observed slip systems on crystal rotation was assessed using <111>, <110>, and <112> pole figures, as shown in Figure 72 for sample T2. The [$1\bar{1}1$] pole moved towards the tensile axis (pointing out of the page) with deformation, which indicates that slip in the [$1\bar{1}1$] direction was active. Also, the [011] pole (slip plane normal) moved away from the tensile axis. This is consistent with the observed (011) [$1\bar{1}1$] slip system as shown in Figure 70.

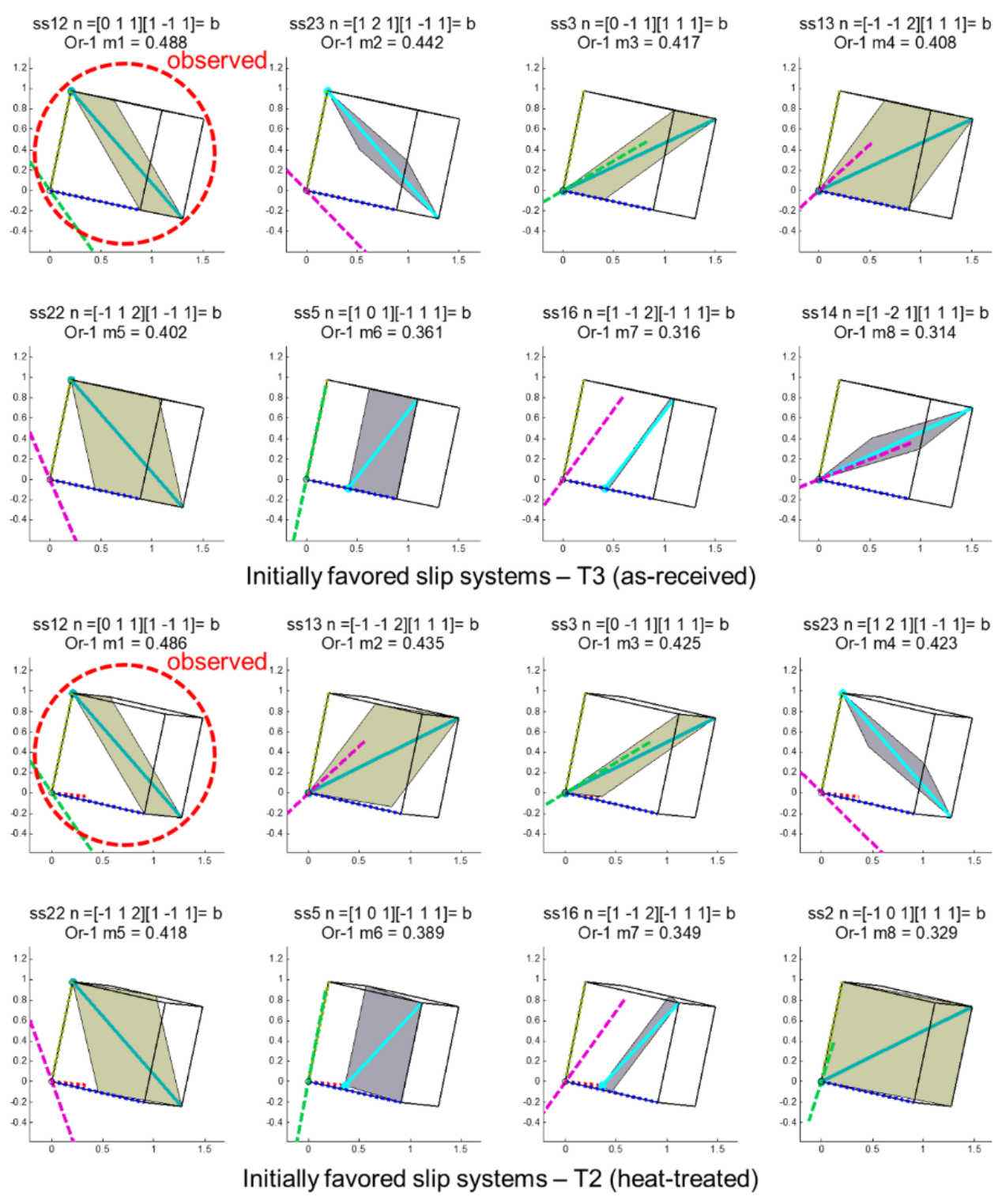


Figure 70: Slip systems ranked by Schmid factors (up to 8th highest) for the as-received sample T3 (above) and heat-treated sample T2 (below). The first {110} slip system was observed in both samples and was the only apparent slip system.

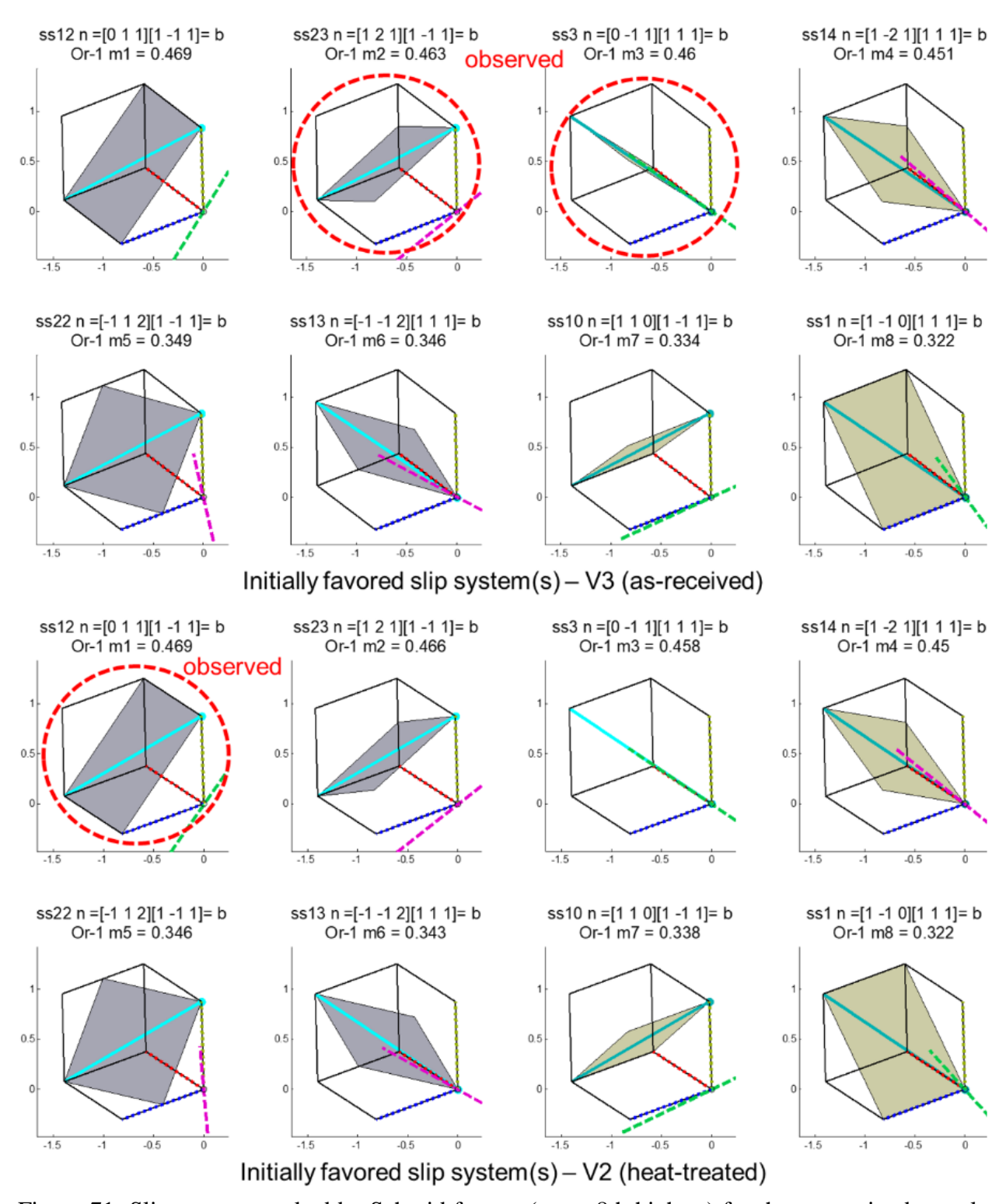


Figure 71: Slip systems ranked by Schmid factors (up to 8th highest) for the as-received sample V3 (above) and heat-treated sample V2 (below). A {110} and a {112} slip system were observed in V3, while only the most highly favored {110} slip system was observed in V2.

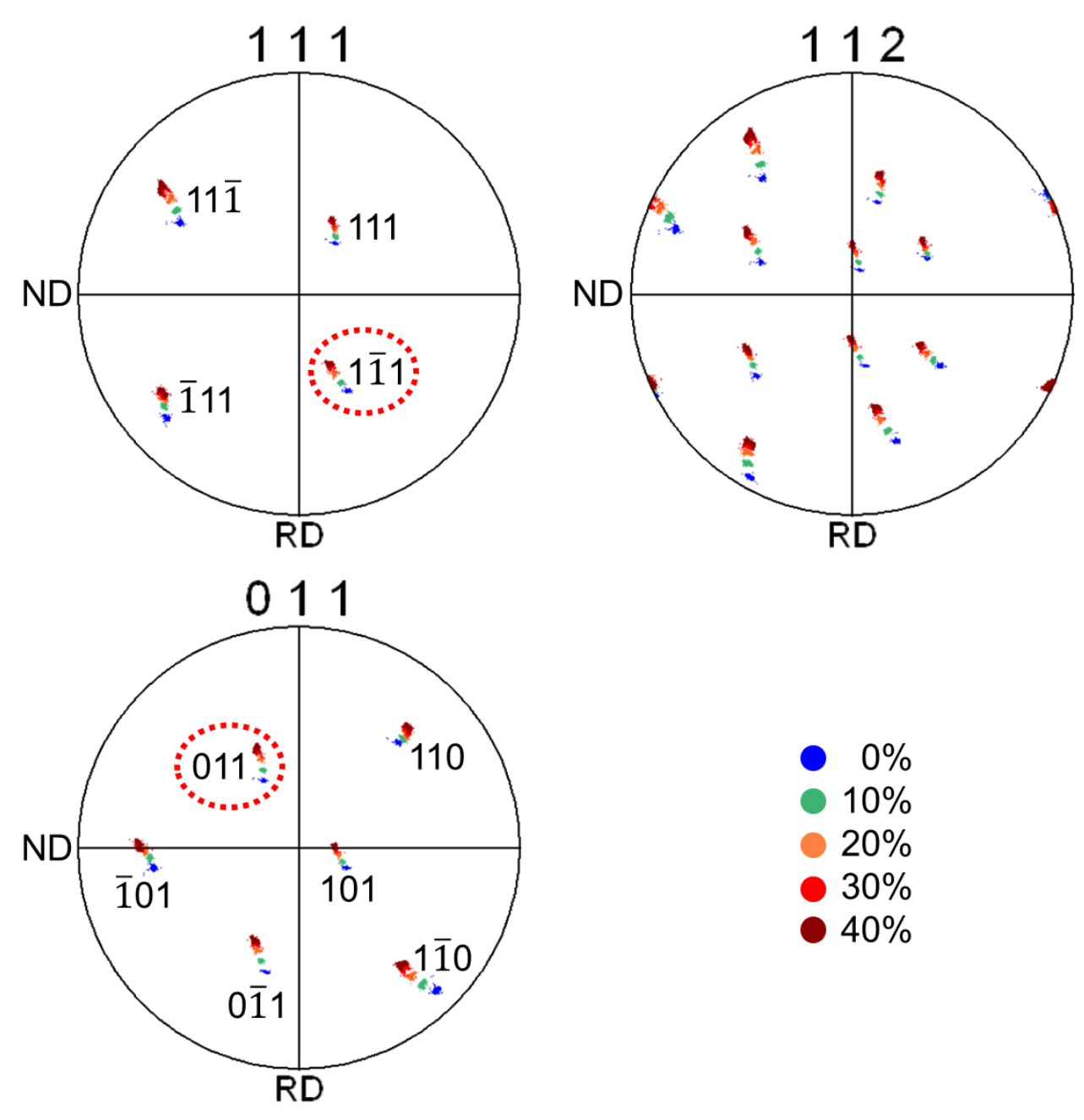


Figure 72: <111>, <112>, and <110> pole figures for the heat-treated sample T2 with the tensile direction pointing out of the page. The $[1\bar{1}1]$ pole moved towards the tensile axis with increasing strain, while the [011] pole moved away from the tensile axis. This is consistent with the observed slip system (011) $[1\bar{1}1]$.

Table 9 summarizes the slip planes associated with observed traces for the as-received and annealed samples. For each orientation, the first slip system whose Schmid factor rank is *different* between the two samples (up to the 8th highest) is indicated in parentheses in the left column. For example, the 2nd highest ranking slip system is different for the two T samples (Figure 70), and the ranking is the same for the V samples (Figure 71). A slip system is red if it was observed in both samples.

Table 9: Summary of observed slip planes from slip trace analyses for as-received and heat-treated samples, with {112} planes in the first line, and {110} planes in the second line for each orientation. The heat-treated samples exhibited more {110} slip than the as-received samples. The numbers in parentheses indicate the Schmid factor rank (as illustrated in Figure 71) for a given slip system, and the first slip system whose Schmid factor rank is different between the two samples is indicated in the left column.

	As-received slip planes	Heat-treated slip planes
	(Schmid factor rank)	(Schmid factor rank)
P (same)	112(2),112(5),112(6)	112(2)
	110(8)	110(4)
Q (8 th)		
<u> </u>	110(3),110(6),110(8)	110(1),110(3)
R (same)	112(4),112(6)	
	110(2)	110(2)
S (4 th)	112(2),112(4)	112(5)
		110(1)
T (2 nd)		
	110(1)	110(1)
U (2 nd)	112(1),112(7)	112(1)
	110(3),110(4)	110(2),110(4)
V (same)	112(2)	
	110(3)	110(1)
W (1 st)	112(1)	
		110(1)
X (4 th)	112(1)	112(1)
		110(2)

The heat treatment led to more slip on {110} planes – there is evidence for slip on 12 {112} and nine {110} planes for the as-received samples and four {112} and 11 {110} planes for the heat-treated samples when slip systems up to the 8th in the Schmid factor rank are considered. No anomalous slip traces (slip on a {110} plane with a low resolved shear stress [141]) were observed in these samples.

Figure 73 shows the orientation evolution with deformation for the as-received sample R2 and heat-treated sample R3, using Euler angles obtained from the center of the gauge length. The two samples initially had a $\sim 1.8^{\circ}$ difference in orientation, but sample R2 rotated much more than sample R3 after the 40% strain. Their final orientations differed from each other by about 14° .

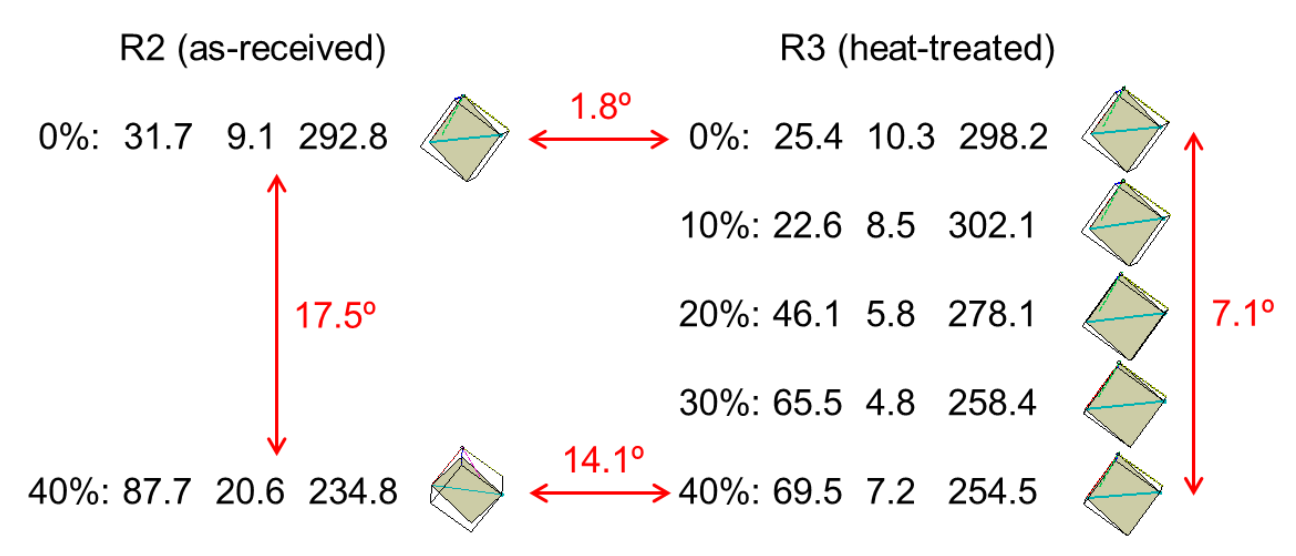


Figure 73: Orientation evolution with deformation for the as-received sample R2 and heat-treated sample R3. R2 rotated more than R3 during deformation [adapted from Figure 6 in reference [58]].

The heat-treated sample P2 is an outlier regarding orientation evolution since it exhibited dramatically different rotations from the three locations spanning ~5 mm along the gauge length. As shown in Figure 74, it started with a slight difference in orientations across the sample, but as deformation proceeded the left and right part of the crystal rotated in opposite directions (the divergence is about 24° after deformation), leaving the center orientation almost unchanged even after 40% strain.

In addition to the orientations obtained from [16], areas corresponding to sample P2 were measured on P3 to evaluate whether similar counter rotations are present. Orientations from the left, middle, and right regions are shown on the bottom of Figure 74 for sample P3. The sense of rotation is similar for P2 and P3, though the magnitudes are different. Also, the orientation at the center of sample P3 is different from the prior measurement at roughly the same location.

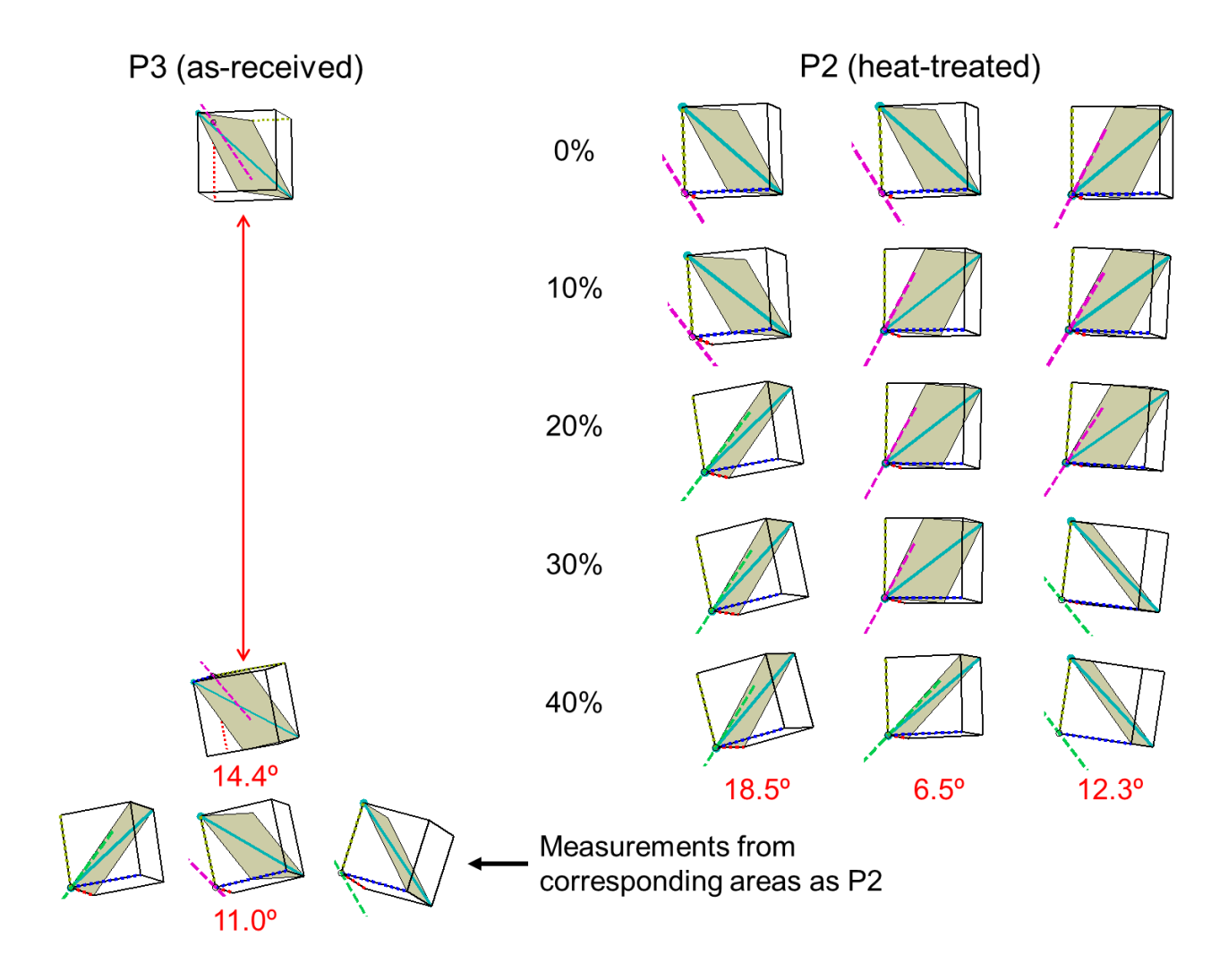


Figure 74: Prisms illustrating how the three locations of the heat-treated sample P2 (right) rotated differently with deformation over a range of ~5 mm along the gauge length. The orientations at 40% strain all differed from that of the as-received sample P3 (left). The left and right regions of sample P3 had similar opposite rotations as P2. Numbers in red show misorientations before and after deformation in corresponding areas.

The heat-treated sample U2 is another outlier since it developed deformation bands with different orientations. Figure 75 shows the orientation maps for sample U2 from three locations before and after deformation. The deformation banding is most evident in the left region, where the rotation between alternating orientations is on the average $\sim 25^{\circ}$, based upon four pairs of datum points evaluated.

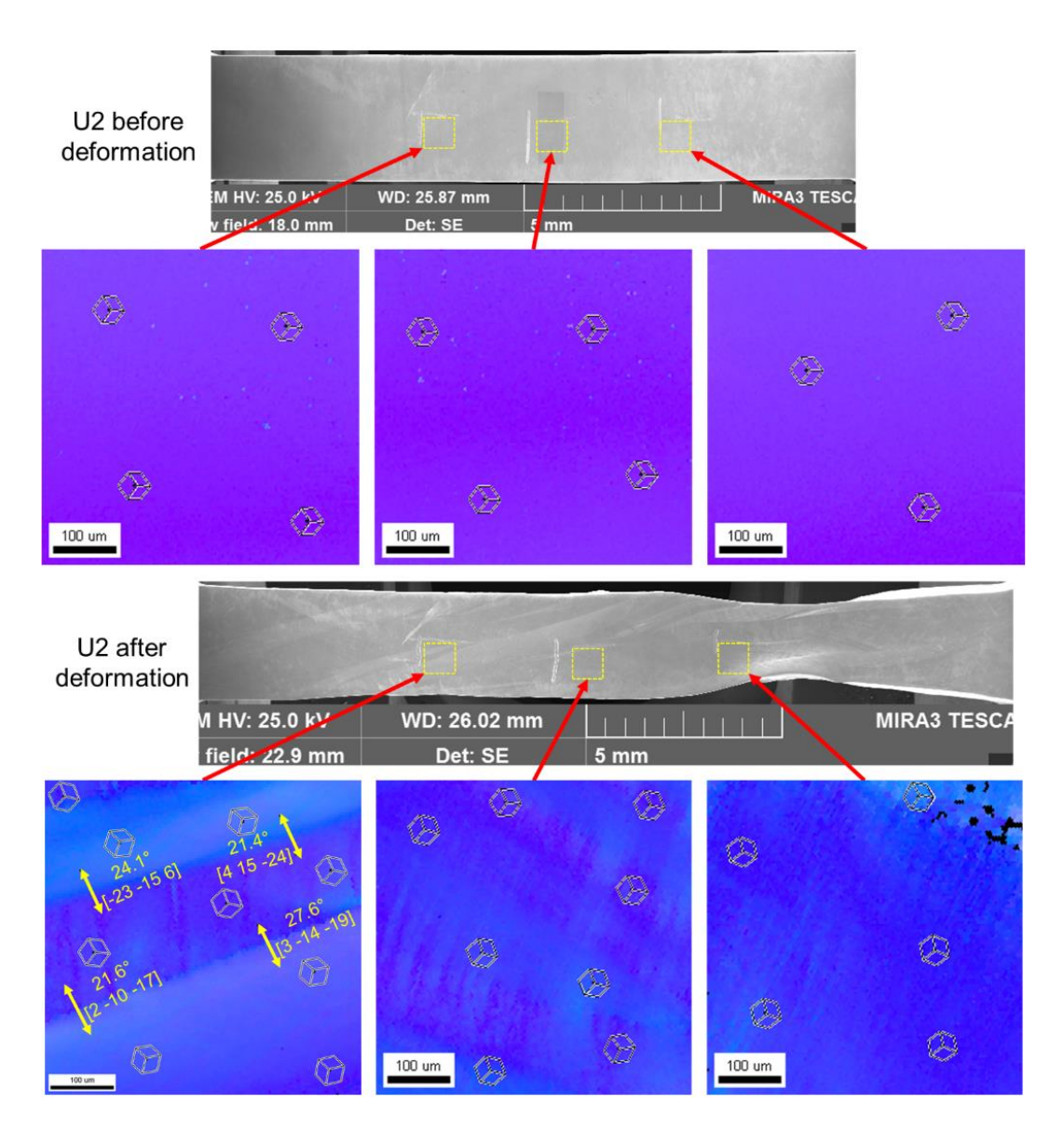


Figure 75: Orientation maps from three regions for the heat-treated sample U2 before and after deformation. The left area developed orientation bands with different rotations after deformation. Annotations on the left map provide angle and rotation axis for misorientations of the deformation-induced grain boundaries.

Figure 76 shows the evolution of tensile axis orientation with deformation in inverse pole figures, using orientations measured at the center of each sample. Triangles connected by dashed lines are used for the as-received samples, and colored dots connected by solid lines are used for the heat-treated samples. The orientation differences before and after deformation are also shown for the heat-treated samples. The trajectories of rotation are similar for orientation S, whereas the other orientations show varying degrees of differences between the as-received and heat-treated samples (X is an extreme).

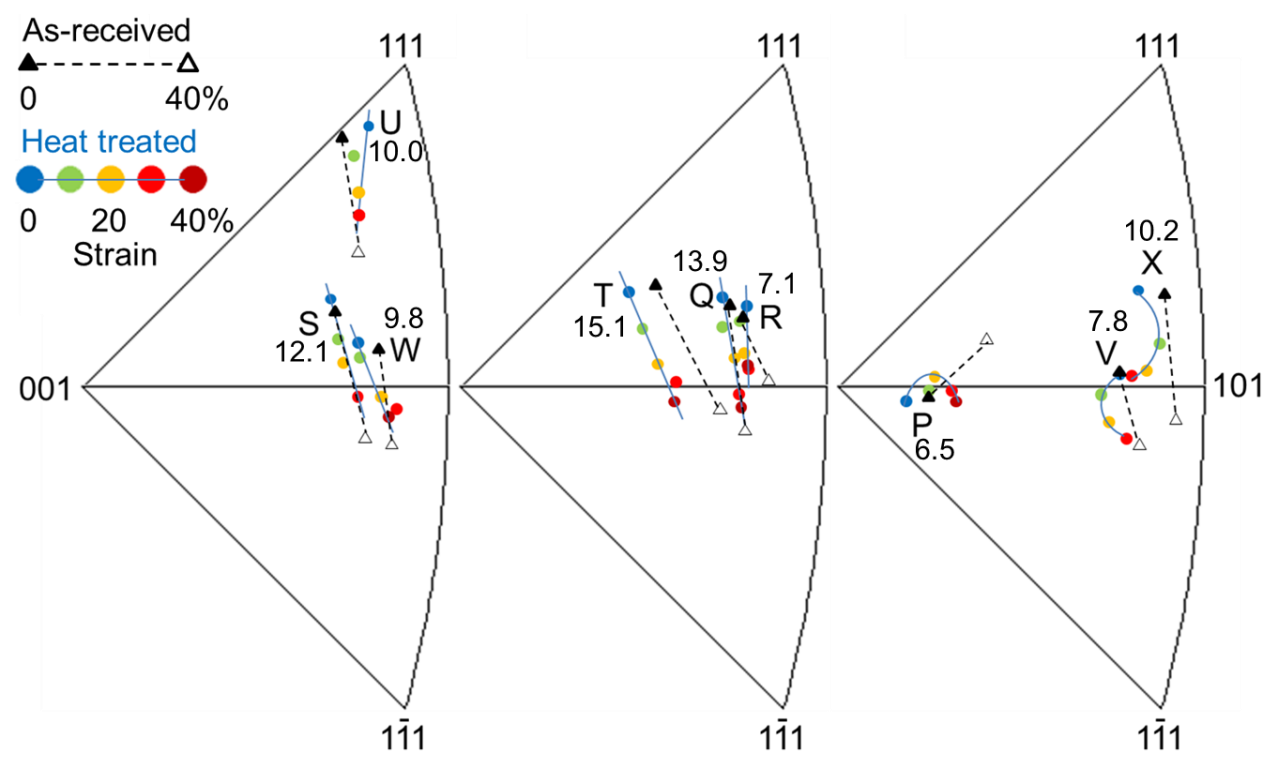


Figure 76: Inverse pole figures showing the evolution of tensile axis orientations with deformation for as-received (triangles) and heat-treated samples (colored solid circles). The orientation change (°) from deformation is shown for each annealed sample. The as-received samples almost always exhibit more crystal rotation than the annealed samples [adapted from Figure 4 in reference [130]].

Figure 77 shows optical images of the as-received and heat-treated samples in pairs taken after deformation. Most samples exhibited similar macroscopic shape changes and shear bands with and without the heat treatment. Both orientation P samples showed an opposite sense of rotation at either end of the gauge length based on the optical reflections, consistent with the orientation data. A notable exception is orientation U, in which necking occurred at different locations for the two samples.

Figure 78 shows the engineering stress-stress curves of samples T1 and V1 deformed *insitu* for CC-EBSD analysis of GND density and distribution. Sample T1 was pre-strained to about 8.7%, as estimated from its geometry. This sample was the first experiment done by Derek Baars in prior work, and because something went wrong with the experiment, it was stopped. The detail had been forgotten, and the anneal also affected the strain state, so interpretation of the stress-strain curve and initial hardening behavior is not straightforward. The 8.7% pre-strain is added to the measured strain for T1 to account for the prior strain. The flow stress is nearly flat for T1 as it is oriented near the center of the stereographic triangle with fewer slip systems interacting with the favored slip systems, while V1 shows more hardening at larger strains because it is oriented near the [100]-[110] symmetric boundary where two slip systems with different Burgers vectors have similar Schmid factors.

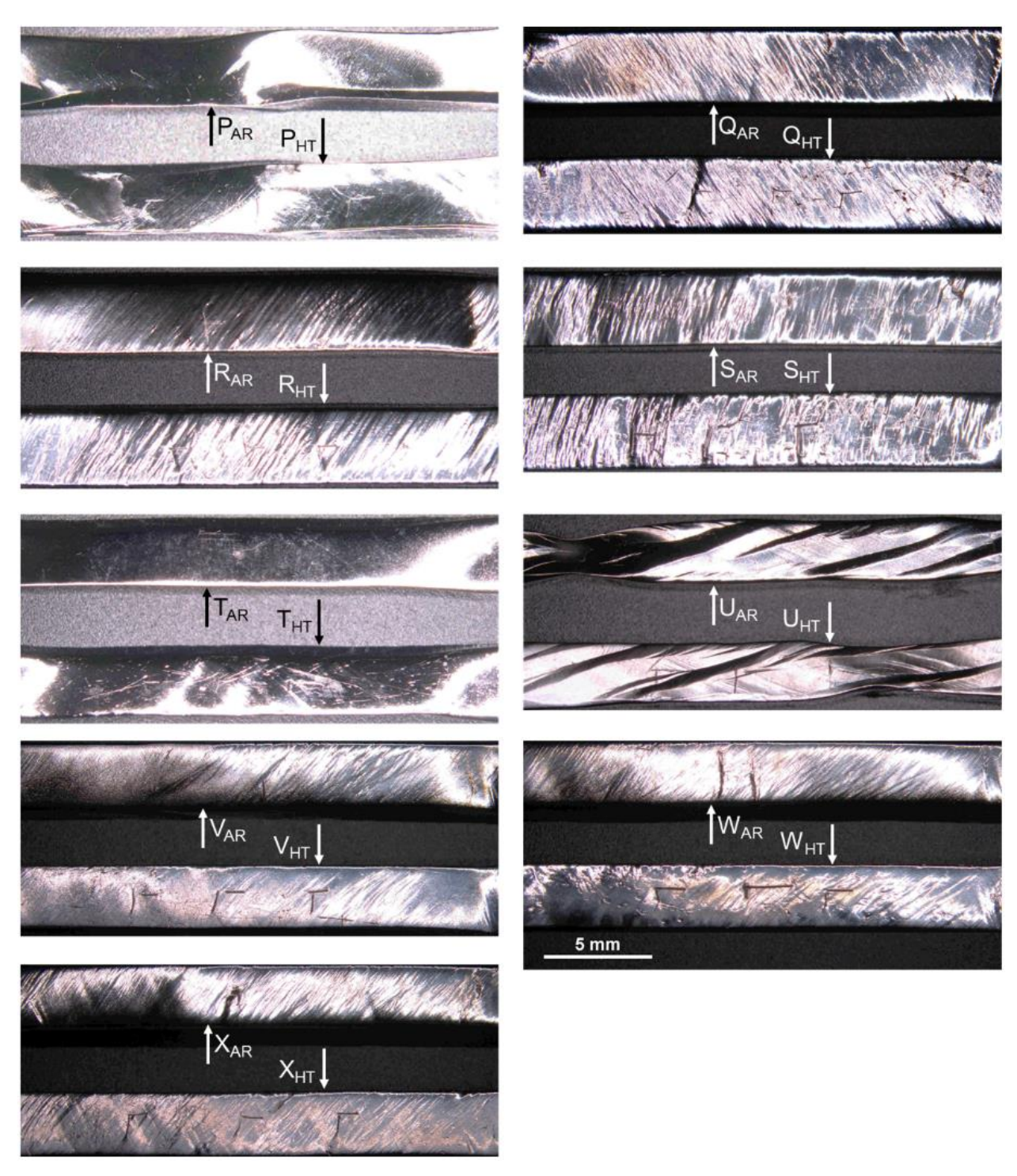


Figure 77: Optical images of the as-received (AR) and heat-treated (HT) samples in pairs taken after deformation. The scale shown for orientation W is common to all images. Both P samples had similarly opposite sense of rotation on either side of the gauge length, based on the reflections. The two U samples necked at different locations near one of the ends of the sample.

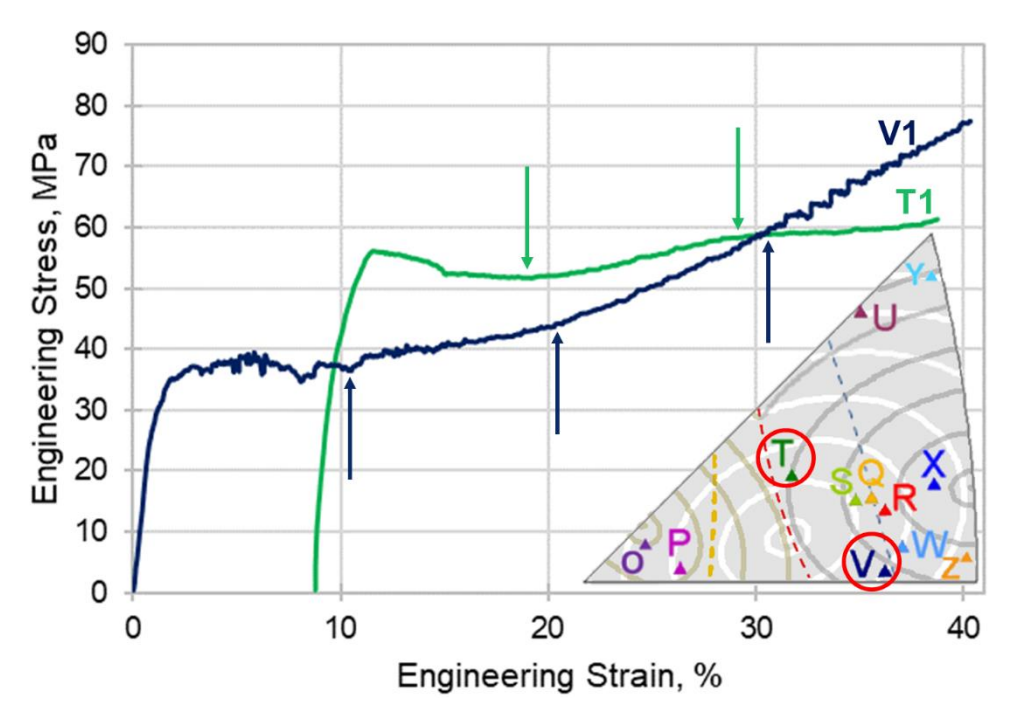


Figure 78: Engineering stress-strain curves of samples T1 and V1 deformed *in-situ*. The arrows indicate where the tensile test was paused to collect CC-EBSD data. The initial hardening behavior for T1 is partly due to the pre-strain (~8.7%), and its plot is shifted to the right accordingly.

Figure 79 shows the GND maps calculated by CC-EBSD using Nye and Kroner equations at each strain level for samples T1 and V1. The map for V1 at 0% strain reflects preexisting GNDs in the sample – some dots and short curves in lighter blue within the circled region suggests higher local GND content. These GNDs could serve as forest dislocations during deformation. The predeformation GND map for T1 is missing because the sample was pre-strained.

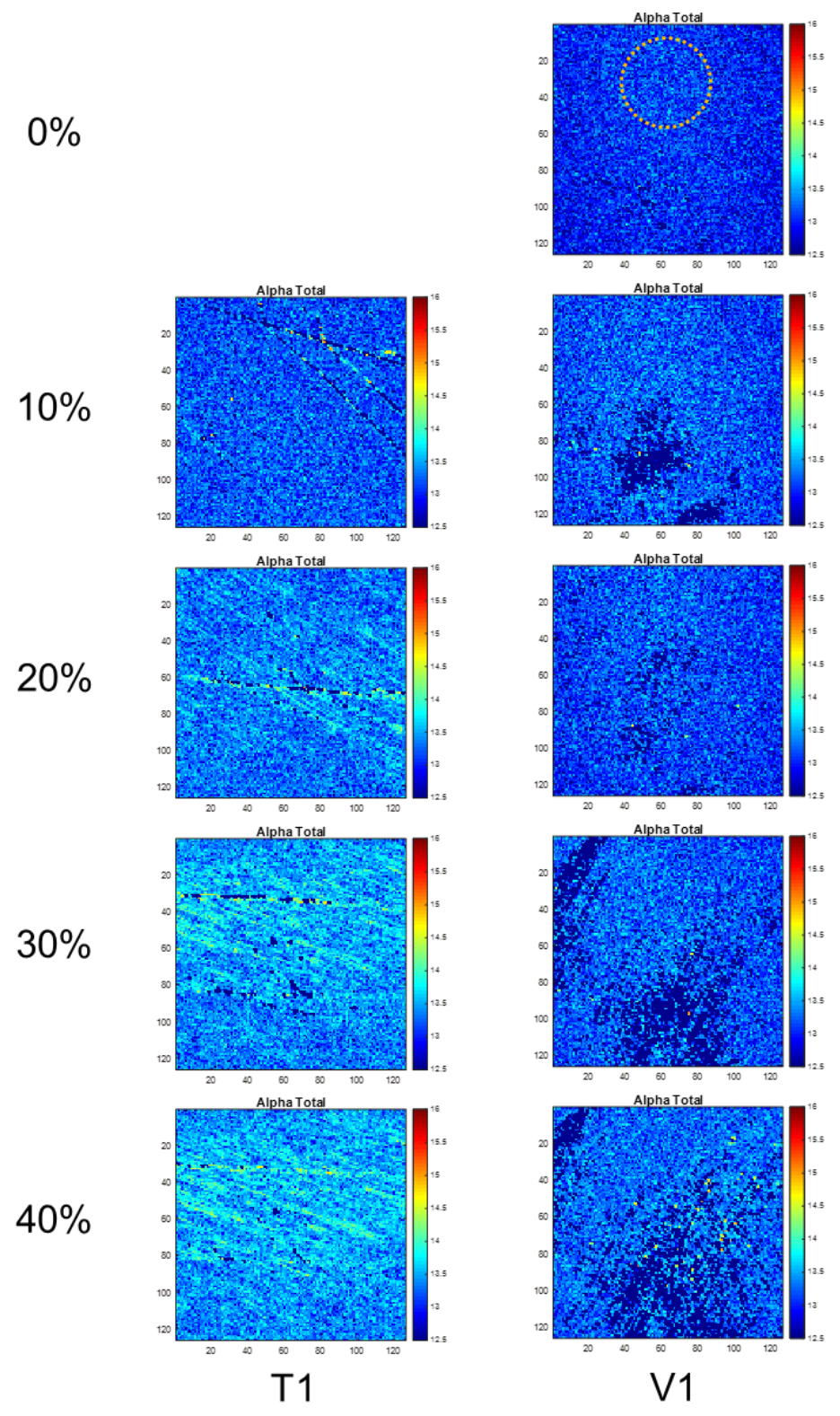


Figure 79: GND distribution maps at each strain level obtained from CC-EBSD for samples T1 and V1. The before-deformation condition for T1 is missing as it was pre-strained to about 8.7%. The orange circle on the top right indicates an area with higher preexisting GND content for V1. There is a noticeable increase in GND density for T1, and little change for V1.

Sample T1 shows a more pronounced increase in GND density with deformation, and the dislocations are mainly aligned with slip traces. On the other hand, hardly any increase in GND content was detected for sample V1, because the color remains nearly constant. This trend in GND density change is consistent with the difference in lattice rotation shown in Table 10 – sample T1 has a greater orientation change than V1 after 40% strain, even though the change was calculated based on the orientation in the pre-strained condition (8.7% instead of 0%) for T1.

Table 10: Orientation evolution with deformation for the annealed samples T1 and V1. Numbers in red are the difference between the initial and final orientation, which shows that T1 has a greater crystal rotation than V1.

T1 (annealed)					V1 (annealed)				
0%					0%	21.6	118.5	124.0	
10%	168.7	67.3	272.9		10%	19.3	121.0	124.8	
20%	180.6	62.9	269.8		20%	16.8	123.9	124.5	
30%	184.0	62.0	269.6		30%	16.5	124.8	125.3	
40%	184.5	61.9	269.7	15.7°	40%	16.4	125.2	126.3	9.5°

The pole figures with respect to tensile axes, slip trace identification, and EBSD results for each tensile sample not shown in this section are provided in the Appendix.

This set of experimental results shown above provides opportunities for exploring the interconnections between various types/states of materials characterized, which will be discussed next.

V. DISCUSSION

This chapter examines the underlying mechanisms which account for the heterogeneous deformation of large grains, variability in sheet texture, microstructural evolution during cavity processing, and differences in slip behavior of single crystals.

a. Preferred Orientation and Orientation Stability in Large Grain Nb Ingots Similarities and Differences of Ingots

To identify variability in the starting material to build cavities, crystal orientations and the distribution of orientations are compared among the eight ingot slices. The density pole figures in Figure 41 show no apparent similarities, which suggests that no preferred orientation is intrinsic to ingot production. This is also supported by the discrete IPFs in Figure 42, indicating that orientation formation is random in the ingots. Another common feature among the ingots is a tendency for grain boundary misorientations to fall between 35° and 55° (denoted by black X's in the MODFs in Figure 38 through Figure 40), which is consistent with the MacKenzie distribution for a completely random texture in cubic poly-crystals that has a misorientation peak at 45° [142]. Furthermore, a different Heraeus ingot slice studied in [42] shows no commonality in orientation, grain boundary misorientation, or grain size with the Heraeus slice examined in this work. These observations taken together suggest that there is a lack of preferential grain boundary mobility or interfacial energy that would lead to a preferred orientation or grain boundary misorientation, even for ingots from the same supplier (e.g., CBMM).

The grain boundary misorientations of the ingot slices are rarely close to CSL conditions. Evaluated by the default settings of the TSL software with CSL boundaries up to Σ 49 and their corresponding tolerances [28], the CBMM-H1, CBMM-H2, TD-1, TD-2, and Niowave ingots

have no CSL boundaries, and the approximate fractions of CSL boundaries for Heraeus, Ningxia, and CBMM-NSCL ingot slices are 8%, 13%, and 5%, respectively (highlighted in black on the orientation maps in Figure 35 and Figure 36). This further supports the hypothesis that orientations are randomly generated, with little low energy configuration being favored.

During fast solidification, dendrites grow along <100> directions for bcc metals [143, 144]. However, there is no preferred orientation for slow solidification condition during ingot production due to the lack of a well-defined heat flow direction. Orientations nucleate randomly because the temperature gradient does not provide adequate driving force to favor certain dendrite orientations. Moreover, grain boundary mobility is high for pure Nb, which leads to high temperature annealing condition that facilitates grain growth. Finally, slow directional solidification favors large grains parallel to the ingot growth direction. These factors combined result in random, elongated grains in the ingots.

An interesting feature from the orientation map of the Niowave ingot (Figure 37) is that one of the perimeter grains (indicated by the red arrow) has the same orientation as the dominant center grain. This suggests that upon the start of solidification, a near single crystal orientation was established, yet some perturbations (perhaps a couple of randomly oriented dendrites that had dislodged from the interface) settled close to, but not at the perimeter. These orientations remained stable as the ingot grew in length, yielding elongated grains near the lower left edge, which led to an island grain within a larger growing parent crystal. The center orientation is also present at the lower perimeter, suggesting that none of the orientations have a growth advantage or disadvantage. There is another similar orientation pair in the Heraeus slice (Figure 35), where the center grain has nearly the same orientation as a grain to its right. This suggests that near the bottom of the ingot, these two areas may have started from the same nucleus.

The good longitudinal orientation stability in the Niowave ingot and in [44] suggests that it is possible to extract many ingot slices with similar orientation profiles, which is an advantage in terms of consistency in volume production of cavities. It may be practical to use a series of adjacent slices to form a set of half-cells that belong to one cavity and align them to match grain boundary locations. Electron beam welding of deformed large grains may cause recrystallization in the heat affected zone as shown in [24, 48, 145], though the influence of welds between matched orientations has not been examined. More ingots need to be examined to determine whether such longitudinal orientation consistency is typical.

The Ningxia ingot slice has the highest orientation gradients among the ingots examined, as evidenced by the series of scans along the gauge length of three tensile samples (Figure 44). It is unclear how such orientation variation within the large grains originated. However, a different Ningxia slice studied in [42] shows similar orientation gradients, which suggests that this may be associated with the ingot production methodology. Such intragranular orientation gradients could complicate deformation behavior in the extracted single crystal samples (discussed later), causing variations in deformation paths that may lead to inconsistent microstructural features, and perhaps, cavity performance. The parallel finer scale (~30-60 µm) orientation gradients present in the asreceived Ningxia samples (Figure 46 through Figure 48) are absent after electropolishing (samples S2 and T2 are shown as examples in Figure 49). This implies that the patterning only existed on the surface and may be an artifact of the mechanical polishing applied to clean the surface of the slice.

Figure 80 and Figure 81 show the maximum Schmid factor maps based on biaxial tension (a simplification of strains likely in a formed half-cell) for each ingot slice for slip on {110}, {112}, or both families of planes (as both are equally facile). These Schmid factor maps provide an

estimate of formability, indicating that some grain orientations are significantly harder than others. The lowest Schmid factor (darkest) orientations have <111> directions normal to the surface. While these orientations require greater stresses to deform, the {111} parallel to the sheet texture results in better formability in other bcc metals, because the strain is more uniform than found in softer grains [24].

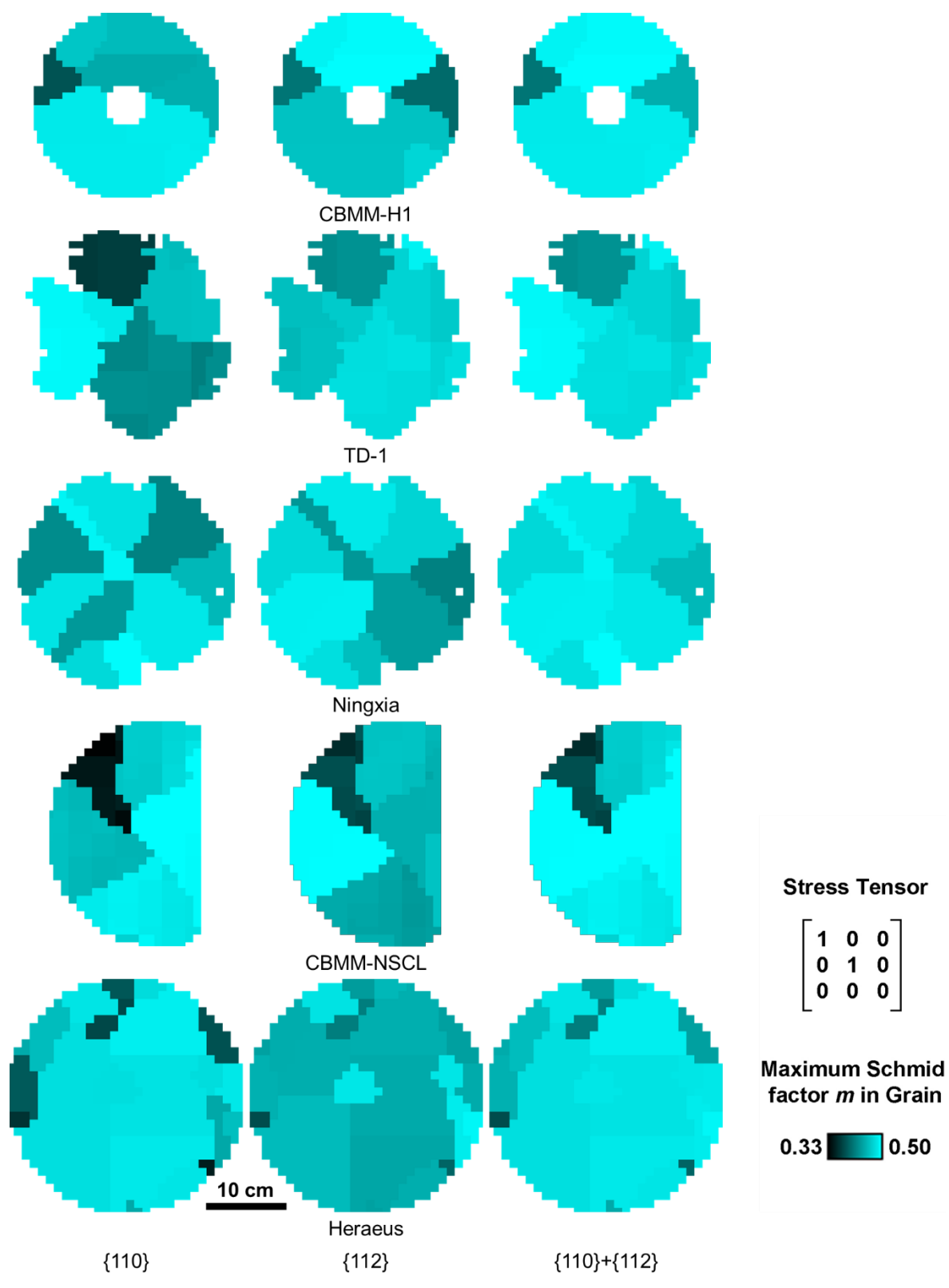


Figure 80: Maximum Schmid factor maps for the 5 ingot slices for slip on {110}, {112}, or both families of planes based on biaxial tension. The scale shown next to the Heraeus slice is common to all maps. These maps provide an estimate of formability based on hard/soft orientations.

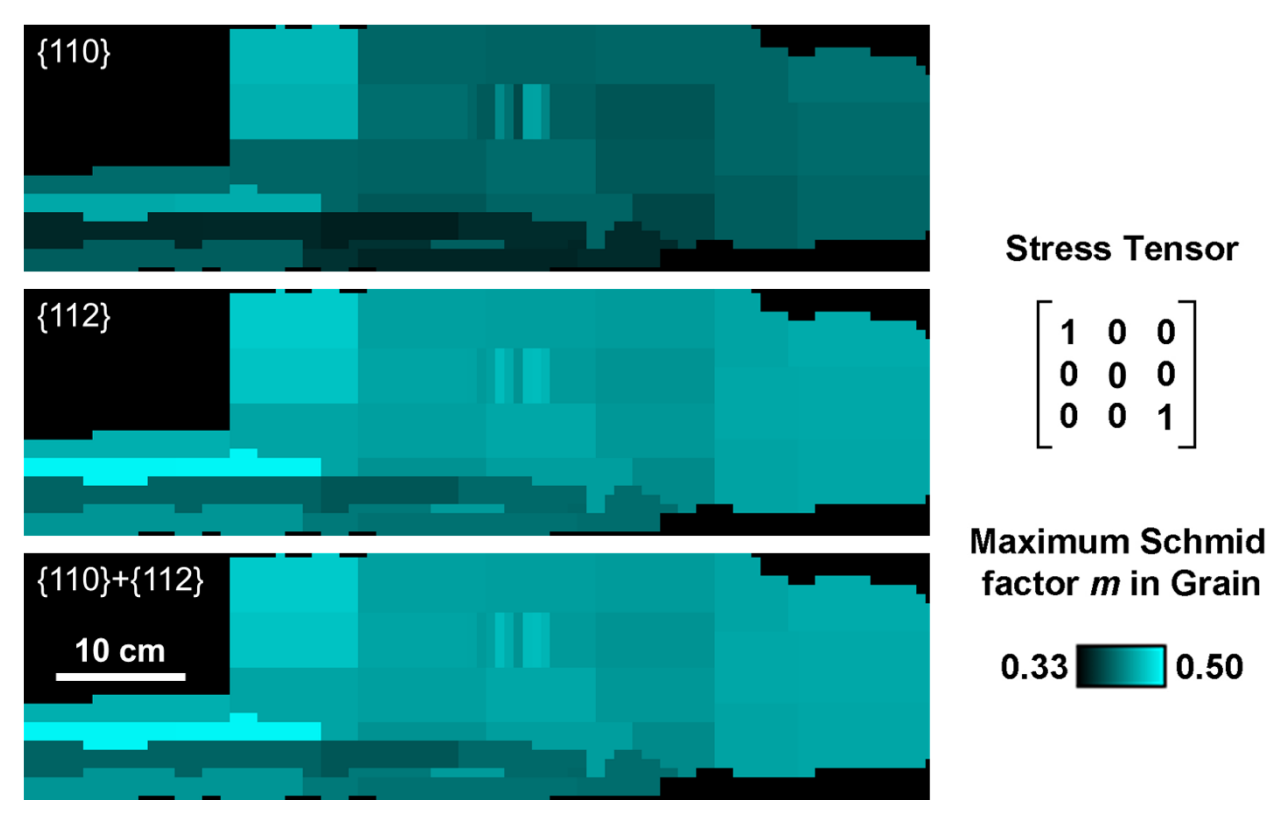


Figure 81: Maximum Schmid factor maps for the Niowave ingot slab for slip on {110}, {112}, or both families of planes based upon biaxial tension in a slice taken perpendicular to the longitudinal direction. Slices from this ingot would likely experience more homogeneous deformation due to the huge grain at the center.

Ideally, for cavity forming the mechanical properties should be isotropic in the plane of a Nb disk [37], which is often not the case for large grain ingot slices as shown in Figure 80 above. It is therefore essential to examine how the initial anisotropy affects deformation.

Ingot slices with more homogeneous shades of blue will presumably experience less heterogeneous strain concentrated along grain boundaries during deep drawing, as the deformation resistance of the grains is similar. Differences in Schmid factors in grains near the center are more important due to the larger strains near the iris. As the perimeter region experiences a complex strain path due to the drawing process (compression-bending-unbending-drawing), the biaxial

maps are not indicative of expected heterogeneous strain evolution (a crystal plasticity model is needed to assess this).

From the Schmid factor maps in Figure 80, the CBMM-H1 and CBMM-H2 slices should deform evenly, since no grain is intrinsically hard (dark). This was partly confirmed by the images of the CBMM-H2 half-cell in Figure 30 (equator) and Figure 50 (iris), which shows mostly similar thickness in the equator and iris cross-sections, though there are several necks/ears (the subsequent weld could even a local thickness variation). There are no severe grain boundary ledges or surface topography either, which again indicates that all grains deformed evenly. Slices from the Niowave ingot would also likely experience more homogeneous deformation due to the huge grain at the center.

Effect of deep drawing/milling on crystal orientation

A preliminary assessment was made by comparing the crystal orientations before and after deep drawing of the CBMM-H2 slice. No significant orientation changes were present after deep drawing at various locations measured by Laue camera on the half-cell (Figure 50). The smearing of Laue diffraction spots in the CBMM-H2 slice after deep drawing (Figure 51) indicates that more dislocations were generated during the forming process. As a result, a subsequent anneal is needed to remove defects and improve RRR and thermal conductivity. The fact that even the brightest diffraction spots were streaked (not sharp) before deep drawing is unexpected and may be related to the EDM surface of the ingot slice.

In contrast to the micro-strain in the surface layer of the deep drawn cavity due to localized friction interactions with the die, longer range macrostrains are present in the Niowave longitudinal ingot. Compared to the Laue patterns of the half-cell (on the right side of Figure 51), diffraction

spots are less smeared in the end-milled Niowave ingot (Figure 53) except at the edge of a milling band (location d in Figure 52). Instead, there was a peak shift on the surface as indicated by the difference in orientations (Table 7) and positions of the diffraction spots before and after etching (Figure 53). This peak shift rather than broadening suggests that milling produces a more uniform macrostrain [125]. Because the mechanical polishing done after milling removed some surface damage, the Laue diffraction spots from the polished surface of the Niowave ingot (Figure 53) are sharper than the undeformed and EDM CBMM-H2 slice on the left side of Figure 51.

Merits and limitations of EBSD and Laue methods

A difficulty with using EBSD to characterize an ingot slice is that small pieces need to be extracted, which prevents further use of the slice to make a cavity. The Laue method serves as a nondestructive alternative of systematically measuring orientations on ingot slices similar to the orientation mapping used to characterize microstructural patches. Therefore, the Laue method is suitable for production evaluation, allowing accept/reject criteria based on anticipated formability requirements. It also allows grain orientations in welds and in heat affected zones to be assessed [145].

Laue measurements do not need to be performed in a vacuum, which considerably loosens the geometrical restrictions imposed by the chamber of an electron microscope. Thus, samples with larger or more complicated dimensions can be characterized. Moreover, unlike EBSD in which only arbitrarily selected locations are measured, the Laue technique enables measurements from virtually anywhere on an ingot slice, and the slice can be evaluated at multiple stages along the cavity fabrication path. Also, X-rays penetrate deeper into materials than electrons, so the

Laue method has a practical advantage of requiring less rigorous surface preparation as compared to EBSD.

As shown in the orientation measurements in Table 3 and the orientation maps in Figure 36 for the CBMM-NSCL ingot slice, the discrepancies in crystal orientations from EBSD and Laue measurements are sometimes significant. This illustrates a couple of more advantages of the Laue method over EBSD. Because the ingot slice was fixed onto a flat stage in front of the Laue camera with movements controlled by a stepper motor, mounting errors were minimized and consistent throughout the characterization process. On the other hand, for EBSD each sample was mounted and measured separately, and the crystal orientations needed to be adjusted to comply with a global coordinate system. Furthermore, it is immediately evident from Laue measurements as to how much orientations oscillate or change within a large grain, while for EBSD, multiple samples would have to be extracted for the same purpose.

The precision of Laue measurements was assessed. Based on multiple operators indexing the same pattern using differently chosen peaks, an orientation was known within 0.25° in each Euler angle, while EBSD measurements on single crystal regions show consistency in obtaining orientations with no smaller than 0.5° of certainty. This indicates that the precision of the Laue method is intrinsically as good as, if not better than EBSD. Both methods depend on reproducibility in sample mounting, but geometrical details may affect accuracy in measurement due to the different sample size and shape.

A limitation of the Laue method is that it lacks the fine spatial resolution available with EBSD, as the illuminated area on the sample is about 1 mm in diameter. This means that grains smaller than a few mm cannot be characterized easily, though this is not a problem for large grain

ingot slices. The disadvantage of the Laue method is that it is much slower and cannot be as easily used to analyze polycrystal grain orientations.

b. Texture/Property Relationship in Fine Grain Nb Sheets

While the microstructures and mechanical properties vary significantly from one sheet to another, little texture/property correlation has been identified. Yield strength and grain size values were extracted from the Ningxia sheet samples shown in Figure 55 to evaluate how well the Hall-Petch equation [146] is satisfied. The fitted line is shown in Figure **. The Hall-Petch constants $(\sigma_0 = 76.3 \text{ MPa} \text{ and } k_y = 1.64 \text{ MPa} \cdot \text{m}^{1/2})$ show reasonable agreement with literature values [], but the R^2 value is quite low, indicating considerable scatter. The gradual slope suggests that the yield strength is not highly sensitive to grain size. These observations imply that other factors such as preferred orientations have a larger influence on the yield strength, and this helps explain why it is hard to find one-to-one correlation between parameters extracted from the tensile tests and microstructural measurements.

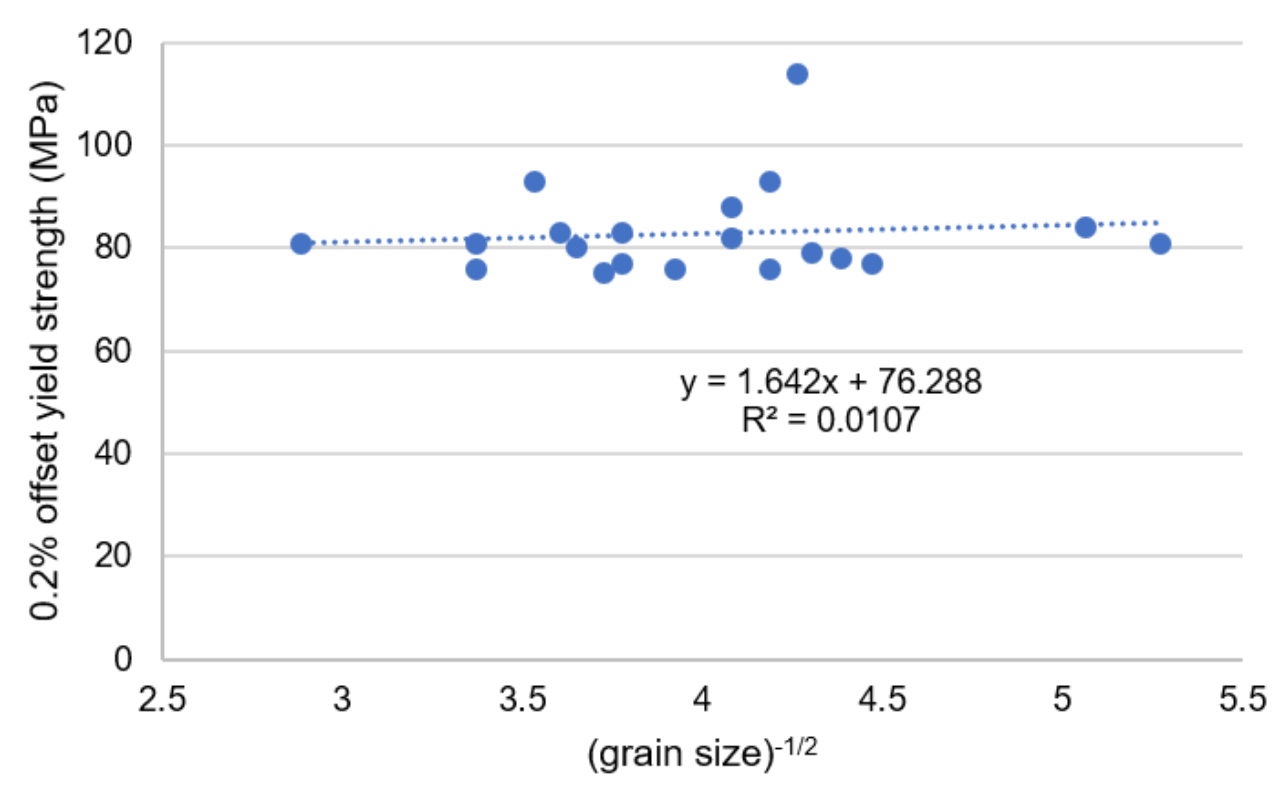


Figure 82: Fitted line of yield strength vs. grain size for the Ningxia samples shown in Figure 55. The shotgun scatter suggests that the Hall-Petch relationship is not well satisfied.

There is sometimes a systematic difference in sample mechanical properties between the two companies. For example, the UTSs of Tokyo-Denkai samples are slightly higher than those of Ningxia samples, as shown in the UTS vs. grain size plots in Figure 56. This may result from their different source material and proprietary manufacturing processes, or from how the samples were cut with respect to the rolling direction (0° or 90° for Ningxia and 45° for Tokyo-Denkai).

Larger LAM values correspond to greater GND content (lattice curvature/low angle grain boundaries) in the sheets, which serves as barriers for plastic deformation and should yield more work hardening and presumably higher UTS. However, the LAM vs. UTS plots exhibit shotgun scattering [61]. This again implies that the mechanical properties are a combined effect of multiple factors that have not been identified.

Despite the scatter in material properties, all samples examined met the ACL specifications. Except for the implications of cost, it may be desirable for a string of cavities to be formed using sheets with similar microstructural profiles. This assessment of texture and mechanical properties provides a means to correlate cavity performance with a specific original materials state, so it is a resource for future learning that may lead to more meaningful ACL requirements.

c. Connection between Ingot and Sheet Microstructure

The multi-crystal rolling experiment provided evidence of how the layer cake microstructure in sheet material originated. Also, as shown in the rolled large grain orientation maps in Figure 59 through Figure 61, dominant orientations that develop from rolling are highly variable and are not always traceable to the original orientations of large grains. However, the similarity in the orientation of recrystallized grains despite being isolated (Figure 62 and Figure 63) implies that the new grains are a systematic (not random) consequence of the deformation process. The inability to consistently index the heavily deformed area for sample A6 with about 92% reduction (Figure 61) suggests a non-uniform stress and strain distribution, which would lead to varying recrystallization behavior in the different layers.

Randomly oriented large grains combined with the complicated deformation state during multiple rolling passes and the not-well-understood orientations of recrystallized grains contribute to the heterogeneity in sheet microstructure. This explains why it is rare to observe similar texture even in sheets from the same manufacturer [24]. This rolling study is an ongoing effort that other researchers are investigating.

d. Effects of Processing History on Cavity Surface Damage

From the shape change due to forming the iris and equator, heterogeneous deformation leads to earing, implying that the equivalent strains are different in different grain orientations. The iris experienced hoop tension and bending that reached an equivalent strain of about 40%. Based upon continuum finite element modeling of the forming process for cavities with similar geometry, the equator experienced a more complex history involving hoop compression and bending to an equivalent strain of about 20% [147]. The difference between the equator and iris LAM maps in Figure 64 and Figure 65 is consistent with the larger strain in the iris – before annealing, the equator scans have large areas that are light gray (lower LAM values), whereas the iris scans are dominated by darker shades of gray (higher LAM values). Because the resulting dislocation density in the iris was probably higher, this provided a larger driving force for recovery, which can account for the more dramatic change in the LAM maps for the iris sample after the heat treatment.

No evidence for recrystallization, i.e., the emergence of new orientations, is present after the 800 °C heat treatment. This suggests that conventional furnace heating facilitates recovery and prevents recrystallization in deformed large grains. In contrast, previous studies on electron beam welding of deformed single crystals [24, 48, 145, 148] showed that recrystallization occurred in the heat affected zone adjacent to the weld, resulting in different grain size on either side of the weld. The samples reached the recrystallization temperature before too much recovery took place due to the high heating rate, so the stored dislocation defect energy was available for nucleation and growth of recrystallized grains.

The grain boundary in Iris 1 in Figure 65 appears to have developed during deformation.

This boundary has the highest misorientation at the inner surface and disappears with distance

toward the outer radius. Since the boundary has large LAM values as indicated by the dark color, it seems to be a consequence of polygonization [29], which leads to a low-energy configuration of dislocations where regularly spaced dislocations organize into low angle boundaries inclined to the slip plane.

The formation of this low angle grain boundary may be a result of the changing driving force for dislocation activity with respect to the crystal orientation, because the hoop stress is in a different crystal direction at every position in the original large grain. A larger bending strain may have occurred at this position during deep drawing, causing an unbalanced population of dislocations of one sign to form the low angle boundary. It is also possible that a preexisting low angle grain boundary became a trap for dislocation accumulation that led to the formation of a sharper grain boundary. Evidence for this possibility is visible in Iris 2 in the middle set of orientation maps of Figure 65, where there is a near vertical very low angle grain boundary to the left of center. This boundary is evident as a subtle color change in the three EBSD maps and the after annealing LAM map, but it is not evident in the as-deep drawn LAM map as it is obscured by the high LAM values.

The slight migration of grain boundaries in all the orientation maps shown in Figure 64 and Figure 65 suggests that the driving force (primarily plastic strain) for recovery was inhomogeneous, so that the defect removal occurred at different rates in various parts of the crystal. The difference in dislocation removal at the equator and iris may explain why the equator is more susceptible to forming hot spots in operating cavities [26], as there are regions where the LAM values become higher after the anneal. This is also consistent with observations of thermal conductivity in [31-33], in which a larger strain is generally associated with a more significant restoration of phonon peaks after annealing. The fact that all the after-BCP LAM histograms are more similar to each

other (Figure 67) may reflect that the observed material was not close to a free surface that could provide surface energy or more degrees of freedom for changes to occur. This implies that defect removal was greater near a free surface than beneath the surface.

The corresponding IQ maps in Figure 64 and Figure 65 for the equator and iris provide a contrast to the LAM maps, as they show a sum of all defect content, including impurities, vacancies, GNDs, and SSDs. In the LAM maps, there is evidence for cell boundaries – distinct networks having regions between them in which there are few GNDs. The IQ maps generally show lower IQ (darker regions) where there is higher GND content, but the cell structures are not evident. This implies that SSDs and other defects overwhelm the contribution from GNDs. Annealing increases the IQ in a way that is consistent with the decrease in the GND content, but there are also regions of high IQ that correspond with high LAM values in most maps.

Because LAM values correspond to GND content, the depth of surface damage can be estimated from the LAM maps. Multiple traces from the surface inward in the six grains measured using EBSD mapping were extracted and averaged. LAM profiles are plotted with depth from the surface in Figure 83 for six areas in the equator and six areas in the iris. As evident by variations in the plot, all six grains responded differently to forming. LAM values for the iris are in general higher than the equator, consistent with overall qualitative observations. At the equator, LAM values come to a low and constant value at a smaller depth than the iris, again indicating that the dislocation content is greater at the iris. Traces starting from the inside and outside behave differently as well; the equator inside and iris outside reach a constant LAM value at \sim 60 μ m, while the LAM values have a more gradual drop from the surface for the equator outside and iris inside.

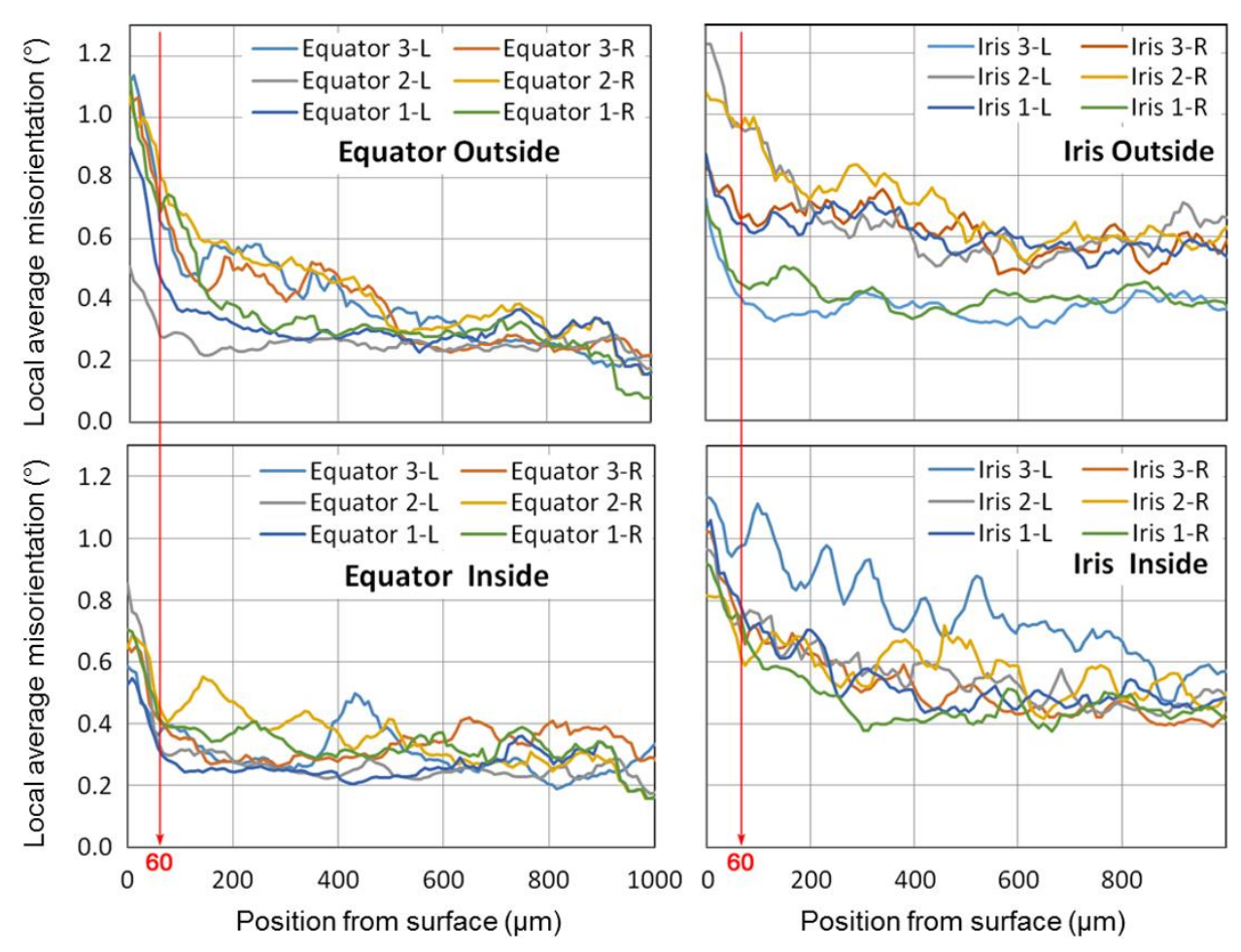


Figure 83: LAM profiles in the 6 grains obtained from averaged traces on the inside and outside of the equator and iris. Damage depths up to about 200 µm is present in some regions, and the magnitude is different for the equator and iris, as well as for the outside and inside [Figure 9 in reference [126]].

Significant dislocation content is present at depths up to about 200 µm at several locations, consistent with the equator and iris LAM maps in Figure 64 and Figure 65. This may explain why the performance of the cavity fabricated from this half-cell was not satisfactory after an initial ~70 µm BCP, but it improved remarkably after a second ~170 µm surface removal with centrifugal barrel polishing, BCP followed by electropolishing as described in [5, 149]. This suggests that the LAM values near the surface can be understood as a metric for damage in cavities, and once the dislocation content drops below a threshold, cavity performance is no longer affected. Comparing

with Figure 14, where fine grain cavity performance was still improving with 180 µm of surface removal, it appears that the damage from deep drawing occurs similarly in fine grain cavities, even though it was estimated using a different approach [76].

Romanenko *et al.* reported that a low-temperature bake at ~120 °C caused a reduction in LAM values in both small and large grain cavities [27], which is unexpected since it is generally believed that dislocations are hard to move at temperatures much below the recovery threshold. In this study, care was taken to observe the same areas before and after the anneal and surface removal, showing that GNDs in large grain Nb are stable and difficult to remove even after the higher temperature anneal. Furthermore, it is puzzling that the data in [27] suggests that more change in LAM took place in large grain material than fine grain material, when one would expect a greater presence of grain boundaries would facilitate removal of dislocations (although there was no indication that the same regions were measured before and after the bake).

In both studies, the trends show a shift of LAM peaks to the left (smaller values) after annealing, and the variability may arise from the heterogeneity in dislocation substructures. Thus, larger statistical sampling may be needed before a quantitative interpretation of the magnitude of the shift can be developed. There are regions with stable and entangled dislocation microstructures that are resistant to the recovery-based removal, and the heterogeneity of these regions may account for the etch pits occasionally observed on large grain cavities that are associated with RF losses [150, 151].

A limitation of this study is that EBSD only provides information about the surface because the penetration depth for the electrons is less than 1 μm . Therefore, it remains an open question as to whether the effects of annealing on the surfaces examined are a good representation of the

bulk. The differences in LAM value histograms before and after the 10 µm BCP in Figure 67 does suggest different recovery behavior between the surface and the bulk, as the surface could serve as a sink for dislocations to exit in large grain material. While the surface condition is vital for superconductivity, reducing defect content is important for bulk properties such as thermal conductivity. Hence, it is necessary to know if dislocations in bulk have been effectively removed.

e. Effects of Heat Treatment on Preferred Slip Systems in Nb

The lower yield strength and flow stress after the 800 °C/2hr heat treatment in the stress-strain curves in Figure 68 are likely due to a reduced density of preexisting dislocations that were barriers to plastic deformation. The lack of a slight drop in the flow stress between yield and ~15% strain for some of the heat-treated samples (most notably T) also suggests lower forest dislocation content.

By comparing the Schmid factor ratio between primary and secondary slip systems (with a different slip direction from primary) with the initial hardening behavior along with the observed rotation axes and slip traces, it was argued in [16] that {112} slip largely accounts for the onset of plastic deformation in the as-received samples. To assess the effects of dislocation removal, a similar analysis was performed on the heat-treated samples, as shown in Figure 84. Here, based on observations of slip traces and rotation axes, the {110} slip systems instead best account for the initial hardening slopes – the smaller the ratio between primary and secondary {110} slip systems (i.e., the more similarly they are favored), the more work hardening a sample tends to have. This change in the preferred slip plane suggests that the anneal may have altered the core structure of screw dislocations in the samples, possibly due to boiling out hydrogen, or that the presence of preexisting forest dislocations in the as-received samples makes slip on {112} planes more

favorable. This is consistent with slip trace observations in Table 9, where {110} slip systems are more prevalent in the heat-treated samples.

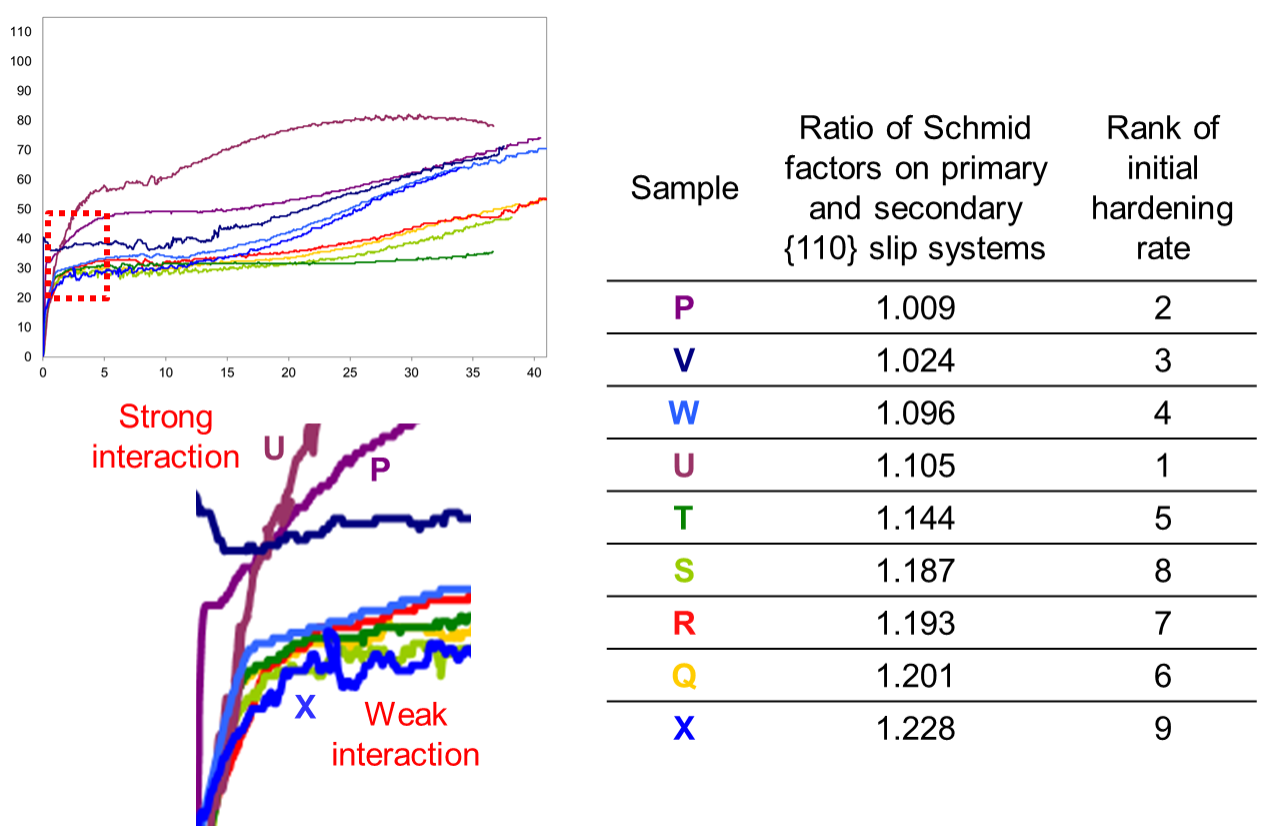


Figure 84: The table on the right lists the annealed samples in the order of increasing ratio between the primary and secondary {110} slip systems, which corresponds roughly to decreasing initial hardening rates as shown in the zoomed image on the lower left [Figure 3 in reference [121]].

Crystal plasticity modeling was used to simulate the deformation of orientations P through X [106, 152]. The modeling attempted to extract parameters describing non-Schmid effects, but if they are there, they appear to be small in Nb. Figure 85: Comparison of experimental and simulation results of several annealed samples using classical, dynamic hardening, and differential-exponential approaches. Without accounting for the Non-Schmid effects, the modeling still shows good agreement with the experiments [Figure 15 and Figure 16 in reference [149]], shows examples that compare the experimental and simulation results of several annealed Ningxia samples [106, 149], indicating that two different hardening rules, the dynamic hardening

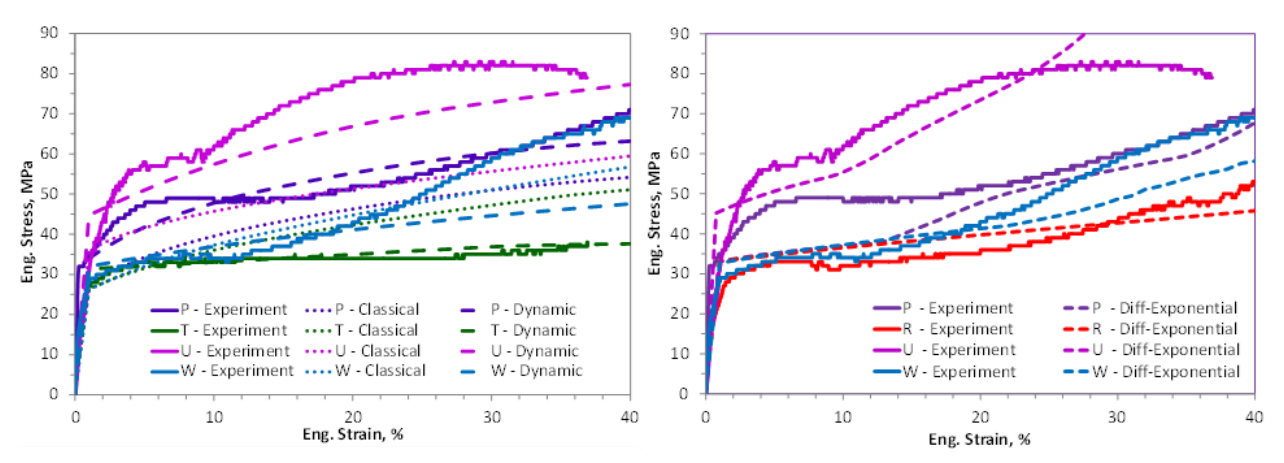


Figure 85: Comparison of experimental and simulation results of several annealed samples using classical, dynamic hardening, and differential-exponential approaches. Without accounting for the Non-Schmid effects, the modeling still shows good agreement with the experiments [Figure 15 and Figure 16 in reference [149]].

and differential-exponential models, can capture the broad effects of hardening but not the evolutionary details (further discussed in [106]), none of which employ the non-Schmid approach. This suggests that these simpler Schmid-based models might suffice for simulating the deep drawing of large grain Nb.

The outcome of slip trace observations summarized in Table 9 is also in line with the implication from modeling that the non-Schmid effects are small in Nb [000]. Even though the

MATLAB code used to calculate slip traces only considers Schmid effects, there is a good agreement between the Schmid theory and experiments – for each heat-treated sample, at least one of the top two ranking slip systems (based on Schmid factor and a global stress tensor) was observed. For the as-received samples, Q is the only exception with the 3rd highest ranking slip system observed.

Slip traces are not visible in most annealed samples until about 20% strain. This may be accounted for by "homogeneous slip," where dislocations move through the crystal uniformly and exit the crystal freely at lower strains. Also, the straight slip lines differ from those observed in the as-received samples, which have a range of inclinations that indicate bursts of slip in the same direction, but on different planes.

Figure 86 shows an example of the slip morphology in samples X3 (as-received) and X2 (annealed) [16]. The slip traces of X3 are wavier with fewer straight portions than X2. This suggests that the presence of preexisting dislocations may have led to entanglements that cause bursts of slip activity on a particular slip plane, and hence, shorter lengths with the same slip trace.

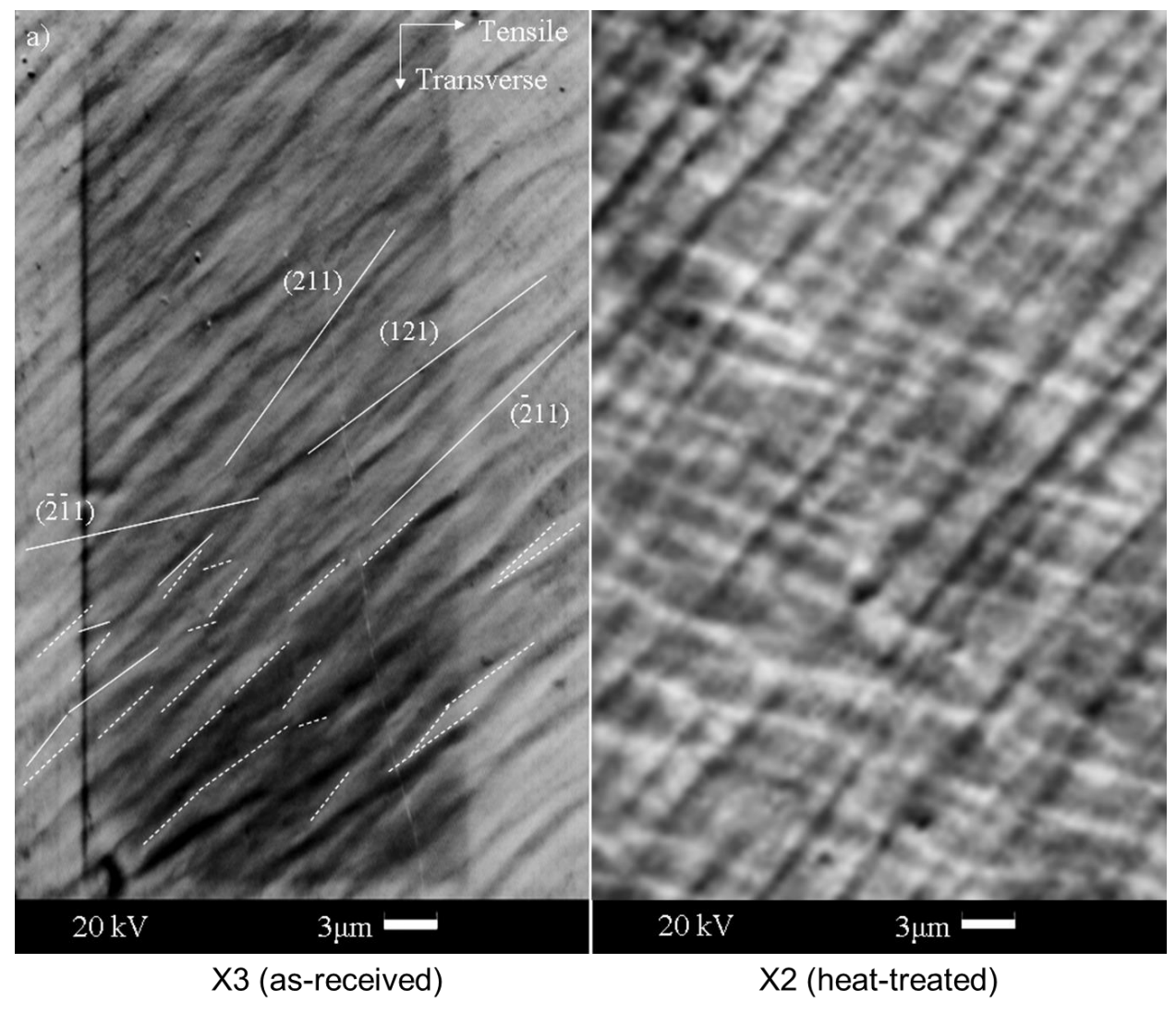


Figure 86: Comparison of slip trace morphology at 40% engineering strain on the as-received and heat-treated sample X. X3 has wavier slip traces than X2.

As shown in the evolution of tensile axes plots in Figure 76 and examples of orientations R and P in Figure 73 and Figure 74, the as-received samples almost always exhibit more crystal rotation than the annealed samples after deformation. This implies that annealing caused changes in slip behavior. For example, if slip occurred alternatively on {112} and {110} planes rather than uniformly on {110} planes, then orientation changes would reflect rotations about two axes rather than one, which may account for larger misorientations in the as-received samples. Moreover, the slightly different initial orientations within each sample pair may have also contributed to the divergence in crystal orientations at larger strains.

In general, the farther away a sample is oriented from symmetric boundaries of the stereographic triangle, the less work hardening and more crystal rotation it exhibits during deformation (stress-strain curves in Figure 68 and rotations on inverse pole figures in Figure 76). This suggests that the single slip condition facilitates lattice rotation, whereas the interaction of slip systems contributes to hardening and suppresses rotation.

Crystal orientations were captured from three areas spanning ~5 mm along the gauge length for the heat-treated samples, which enables assessment of how the initial orientation gradients as illustrated in the serial of scans in Figure 44 affect deformation. However, P2 is the only sample that shows counter rotations in the three regions as shown by the prisms in Figure 74, whereas the other samples all exhibit consistent rotation directions. While this may suggest that the orientation gradients are not significant enough to cause different parts of the samples to deform differently, it may also be due to the relatively short distance (5 mm vs. 18 mm gauge length) over which the orientations were measured, as was imposed by an instrumental limit.

For the CC-EBSD experiment, the differences in work hardening behavior (Figure 78) and GND density (Figure 79) between samples T1 and V1 suggest that GNDs are mainly responsible for crystal rotation, while hardening may be primarily accounted for by SSDs that result from the intersection of slip systems. More tests are needed to confirm this implication. The hints of local preexisting GNDs in sample V1 (Figure 79) could partly explain its high hardening rate despite the prior anneal.

The two U samples both exhibited banding with different orientations diverging from each other with increasing strain, as shown in Figure 75 for U2 (annealed). This phenomenon is similar to that observed in the rolled multi-crystals (e.g., Figure 60). The Schmid factors for rolling or biaxial tension are in general lower than uniaxial tension³. Because U is the orientation with low Schmid factors on multiple slip systems, its stress state may be close to rolling deformation of certain orientations. This perspective may lead to an ability to predict which orientations are more likely to show shear banding in rolling conditions. Simulating the orientation evolution during rolling is a project being conducted by a colleague (Eureka Pai Kulyadi).

For most orientations, the macroscopic shape change and deformation banding are similar between the as-received and annealed samples, as shown in the optical images in Figure 77. This suggests that even though the mechanistic details of deformation are potentially different due to the heat treatment, such microscopic effects may be insignificant from the cavity manufacturing perspective. Nevertheless, changes in dislocation substructures due to varying interactions of slip systems lead to differing defect characteristics that may affect cavity performance.

_

³ This can be demonstrated by comparing the Schmid factors for each slip system based upon uniaxial tension, plane strain compression, or biaxial deformation for the same crystal orientation.

In summary, the connection between randomly oriented large grains and the layered polycrystalline microstructure in rolled sheets has been identified from the rolling experiments. Cavity surface damage results from heterogeneous deformation during deep drawing and leads to different microstructure effects at the equator and iris following heat treatment. Preexisting dislocations play a critical role in the deformation of single crystals. These findings provide a physical basis for developing codes that can simulate the microstructural evolution and recrystallization during cavity processing, which will ultimately contribute to the goal of producing cost-effective SRF cavities with consistent performance.

VI. CONCLUSIONS

The physical metallurgy of Nb for building SRF accelerator cavities with focuses on the microstructure and slip behavior has been investigated to identify sources of variability in cavity performance and to establish a basis for modeling cavity forming and performance. The findings are summarized as follows:

Eight Nb ingots from different suppliers were characterized by the EBSD or Laue method. The ingots have no obvious commonalities in crystal orientation or grain boundary misorientations, suggesting that the ingot solidification process is random and uncontrolled. The slow solidification condition and lack of temperature gradient led to random, elongated grains in the ingots. Typically, the crystal orientations do not vary by more than 1 °/inch along either longitudinal or transverse directions in various ingots, yet the Ningxia ingot shows more orientation gradients than the others, likely due to their ingot manufacturing process (e.g., different thermal gradients). The greater intragranular orientation gradients may have also contributed to the preexisting dislocations in the extracted tensile samples.

The Laue method serves as a nondestructive alternative to EBSD for measuring large grain orientations, allowing crystal orientations to be captured during the cavity fabrication process. It may also be used to examine the heat affected zone of equator welds. Such orientation information is important to establish a database that can be correlated with cavity performance.

Effects of plastic deformation on crystal quality were examined. Machining processes, such as end milling, are likely to introduce a more uniform macrostrain, whereas the friction from deep drawing tends to produce more localized near-surface strains. Both processes can result in surface damage that necessitates heat treatment or chemical removal.

The microstructure and mechanical properties of the Nb material to be used for the Facility for Rare Isotope Beams (FRIB) varied in all samples from the two suppliers. Scatter plots for most pairs of the measured parameters suggest low correlations between the texture, microstructure, and mechanical behavior, even though there is significant variability among sheets. This assessment provides a means to correlate future cavity performance with a specific microstructure.

Preliminary results from the rolling experiment suggest a correlation between the ingot and sheet microstructure – deformation bands parallel to the surface developed from rolling, and grains with random orientations nucleated after heat treatment at 800 °C/2hr. These observations show how the randomly oriented large grains evolve into the highly variable banded/layered sheet texture resulting from the complex stress state of rolling and subsequent heat treatment, suggesting that the variability in cavity performance can be traced all the way back to the ingot, and that recrystallization may be a systematic process determined by prior orientation, strain history, and heat treatment. This implies that a sophisticated material model is necessary to predict variability in cavity performance.

EBSD analyses on the iris and equator samples from a cavity half-cell show that the surface damage from deep drawing depends on crystal orientations, is different at the equator and iris, and is severe even in the bulk at the iris. The iris and equator respond differently to annealing due to their different defect states. While the 800 °C/2hr heat treatment may suffice for recovery near the iris, a longer time or higher temperature may be needed for the equator to achieve a similar degree of defect removal. These heat treatments do not remove GND networks effectively. The damage depth (consisting of higher GND density) is estimated to be 200 µm and removal of this damaged layer proves to be a pratical method to improve cavity performance. The magnitude of surface damage may be similar for large grain and fine grain cavities, but further study is needed to confirm

this. This implies that cavity performance is directly related to the GND content present in the more highly deformed surface regions resulting from the deep drawing process, and that a more strategic deformation path and heat treatment are needed to reduce dislocations and processing cost.

Nb single crystals with different orientations were deformed in uniaxial tension before and after an 800 °C/2hr anneal to study slip activity that is useful in modeling the deep drawing of large grain ingot slices. The results indicate that the stress-strain behavior is strongly dependent on orientations and that annealing lowered the flow stress and usually changed the preferred slip planes from {112} to {110}, due to the removal of preexisting dislocations. This suggests that the prior strain history (hence dislocation content) has a significant impact on which slip systems are favored to operate, which in turn affects the orientation and defect evolution during cavity forming. This implies that for material models to be more effective, they must be capable of tracking the evolution of dislocation content within the material throughout the forming process.

Homogeneous slip could account for the lack of visible slip traces at early stages of deformation in the heat-treated samples. CC-EBSD analysis suggests that GNDs account for crystal rotation during deformation and hardening is caused primarily by SSDs, although more tests are needed to confirm this observation. Initial simulations based on the single crystal stress-strain behavior suggests that a Schmid-based model can capture the anisotropic deformation characteristics.

VII. RECOMMENDATIONS FOR FUTURE WORK

Continuing to characterize the rolling and annealing microstructure of Nb multi-crystals will provide further insights into how sheet microstructure is linked to the original large grains and extend the preliminary studies reported here. Additional rolled samples will be examined using EBSD before and after heat treatment at various temperatures/times. This is an ongoing project conducted by a couple of undergraduate researchers.

The strain tensors obtained from the finite element modeling of deep drawing of Nb can be used to assess which slip systems were activated during deformation. This analysis will provide a means to compare the simulated and measured changes in the shape and crystal orientation of a half-cell, which will assist in constitutive model development.

A synchrotron X-ray study on the half-cell used in this work will address how recovery or dislocation removal occurs in the bulk and if the process is different from the free surface. Samples with grain boundaries or shape irregularities can be extracted from the remainder of the trimmed material and given the same annealing and BCP treatments. This would provide more information on the microstructural evolution during cavity processing.

A similar surface damage study on a fine grain cavity half-cell would reveal the similarities and differences between the damage behavior of large grain and fine grain material. Samples have been extracted from a fine grain cavity provided by JLab, and preliminary EBSD data have been collected. This would supply another perspective on the ongoing debate of whether the large grain or fine grain approach is better for volume production of cavities.

Due to the limited number of single crystal samples studied in this work and in [16], several orientations are still missing in the fundamental triangle. Future tests with new orientations will

supplement the collection of uniaxial tensile deformation of Nb and make the comparison with the D&F set more robust. This would also provide a basis for improving the crystal plasticity models for Nb deformation.

More CC-EBSD experiments can be performed on the tensile samples to confirm the trend of GND evolution during deformation. The GNDs can also be resolved into different types (edge vs. screw) as well as onto slip planes ({110} vs. {112}). This will provide further insights into the deformation mechanism of Nb. GNDs can also be mapped on cavities as a function of processing, reinforcing the link between dislocations and cavity performance.

ECCI provides a means to observe dislocations directly, so it can be used to identify the evolution of dislocation substructure and content with heat treatment and deformation in the tensile samples. The outcomes can be correlated with the stress-strain behavior and slip system activities can be inferred. Fundamental understanding of dislocation evolution is also helpful in modeling the processing of cavities. This may enable strategic heat treatment schedules that would identify an optimized microstructure for cavity performance (e.g., dislocations aligned perpendicular to the heat transfer direction). This analytical approach is the subject of a paper by a colleague (Mingmin Wang) that was published recently [153].

APPENDIX

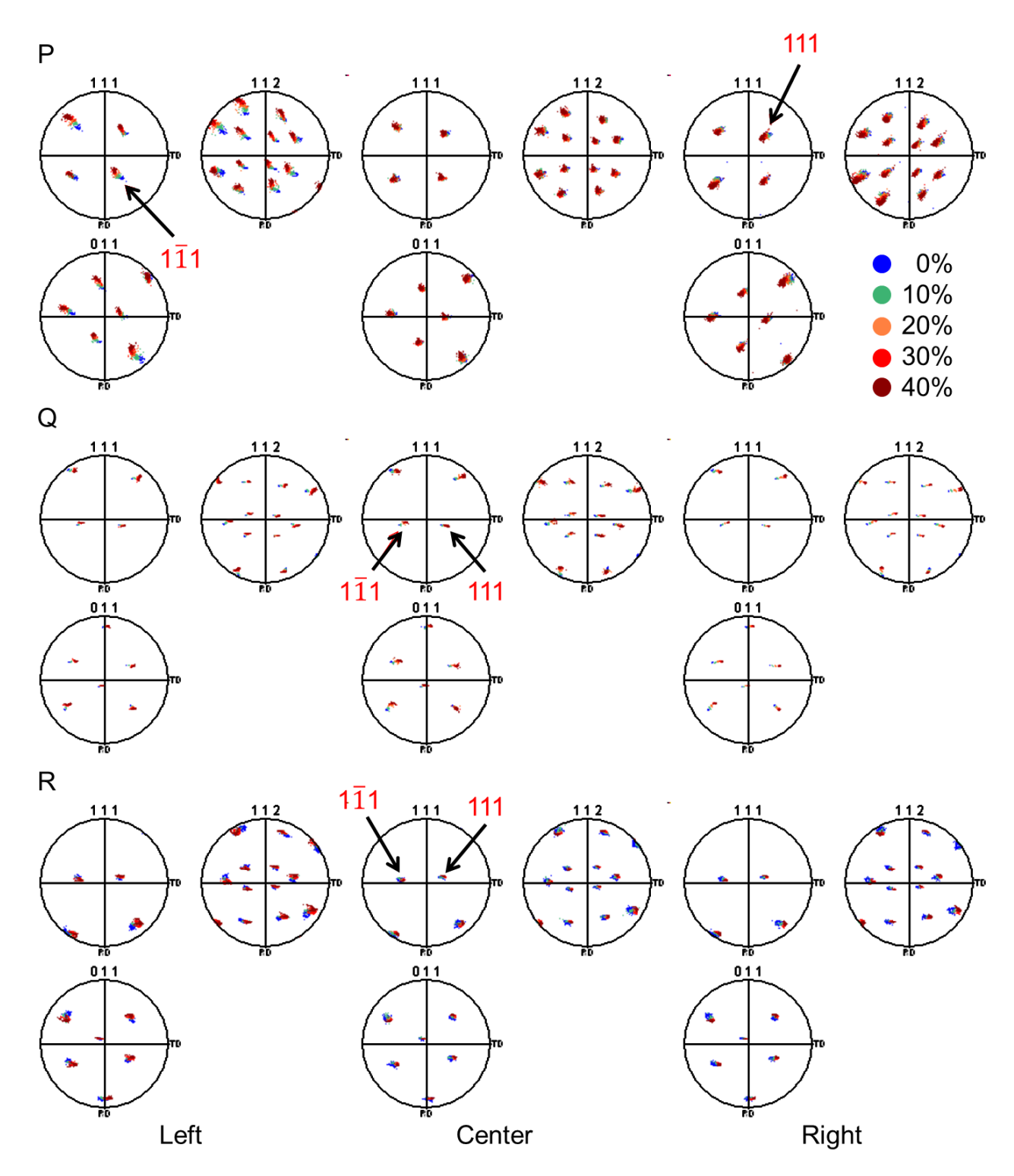


Figure 87: <111>, <112>, and <110> pole figures from three regions on the gauge length for the heat-treated samples P, Q, and R with the tensile axis pointing out of the page. The color scale for engineering strain is common and shown next to sample P.

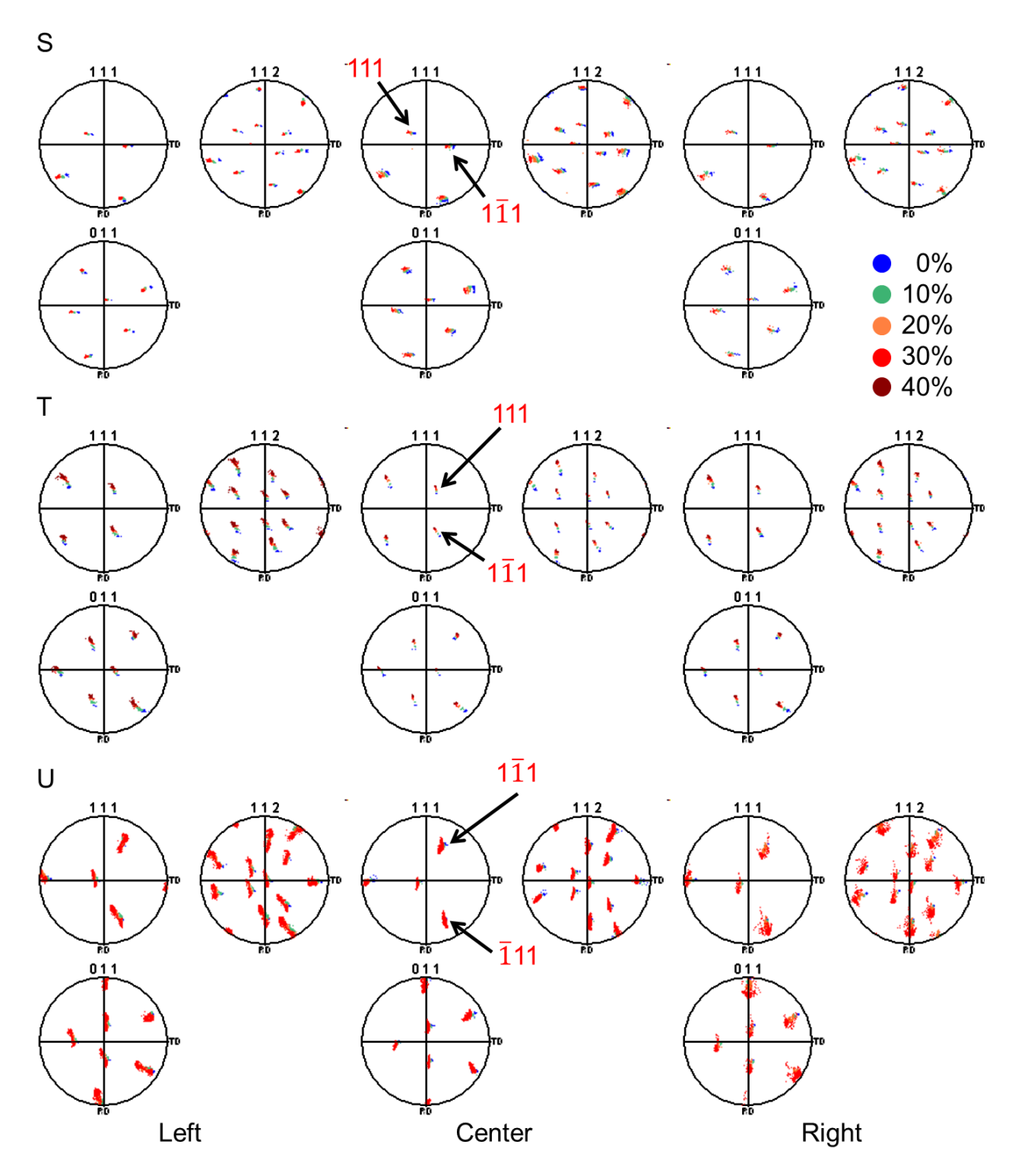


Figure 88: <111>, <112>, and <110> pole figures from three regions on the gauge length for the heat-treated samples S, T, and U with the tensile axis pointing out of the page. The color scale for engineering strain is common and shown next to sample S.

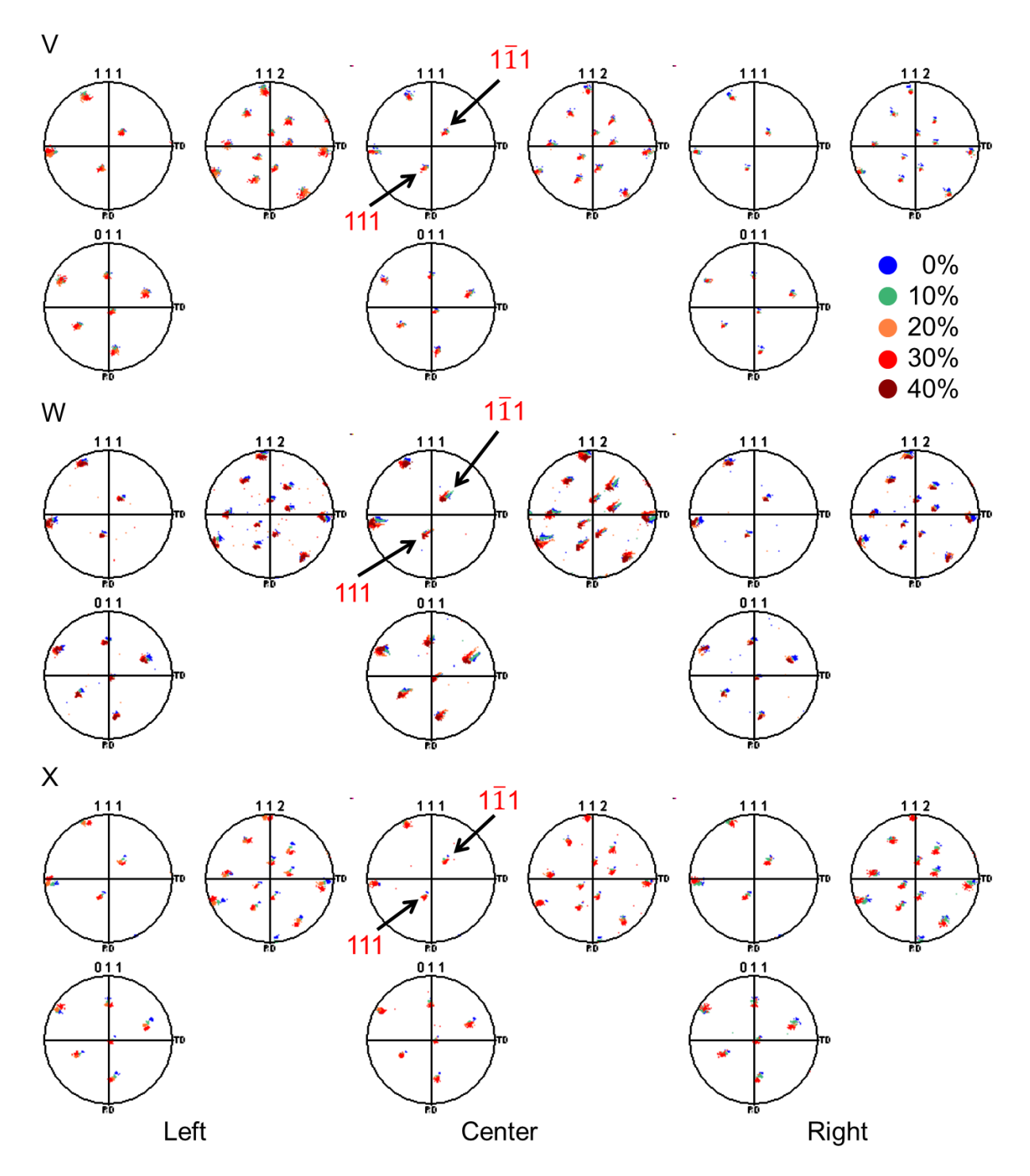


Figure 89: <111>, <112>, and <110> pole figures from three regions on the gauge length for the heat-treated samples V, W, and X with the tensile axis pointing out of the page. The color scale for engineering strain is common and shown next to sample V.

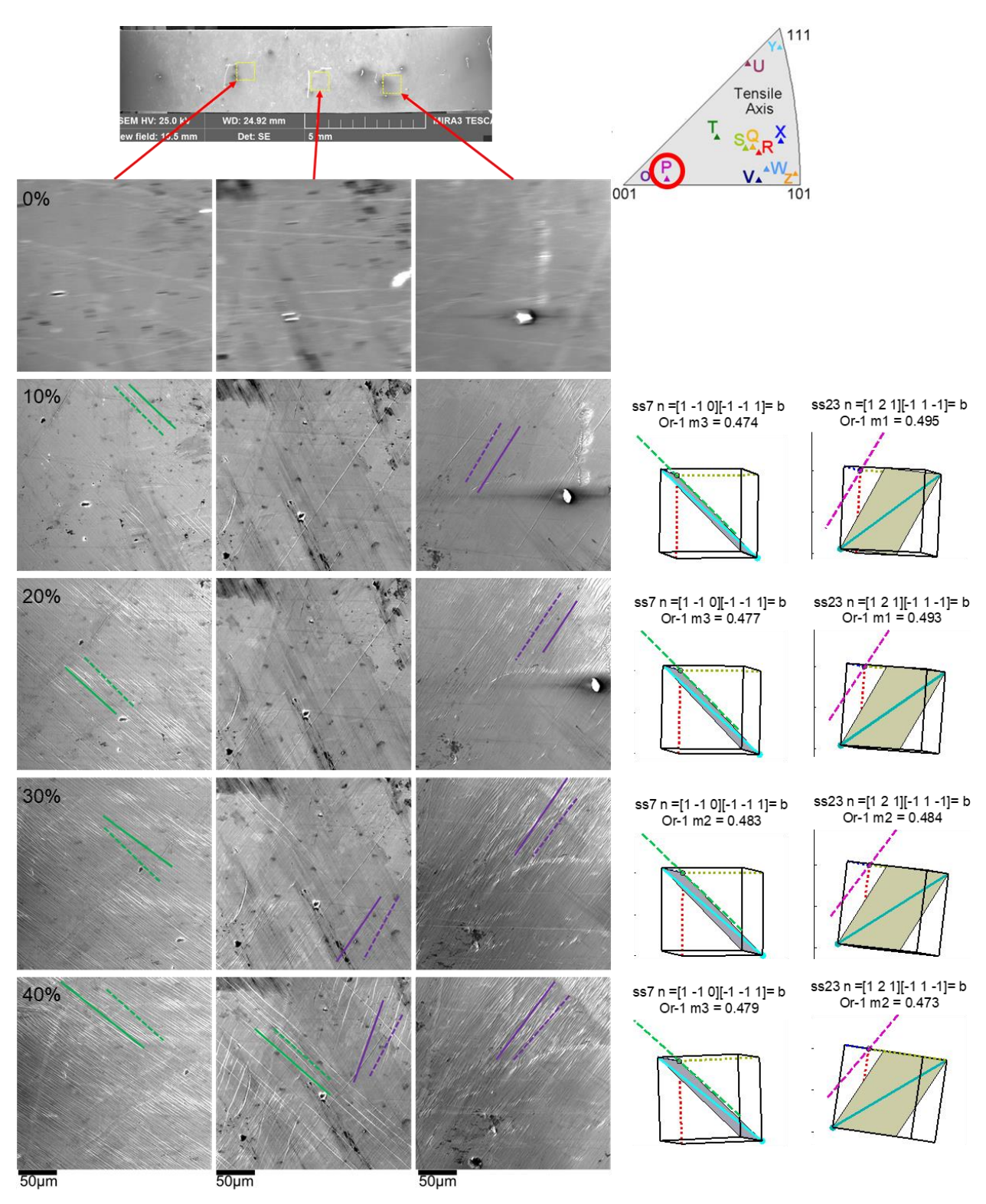


Figure 90: Slip trace identification on the heat-treated sample P in some of the areas examined. Observed slip traces (solid lines) were matched with computed traces (dotted lines) based on the measured orientations, with {110} slip traces in green, and {112} in purple.

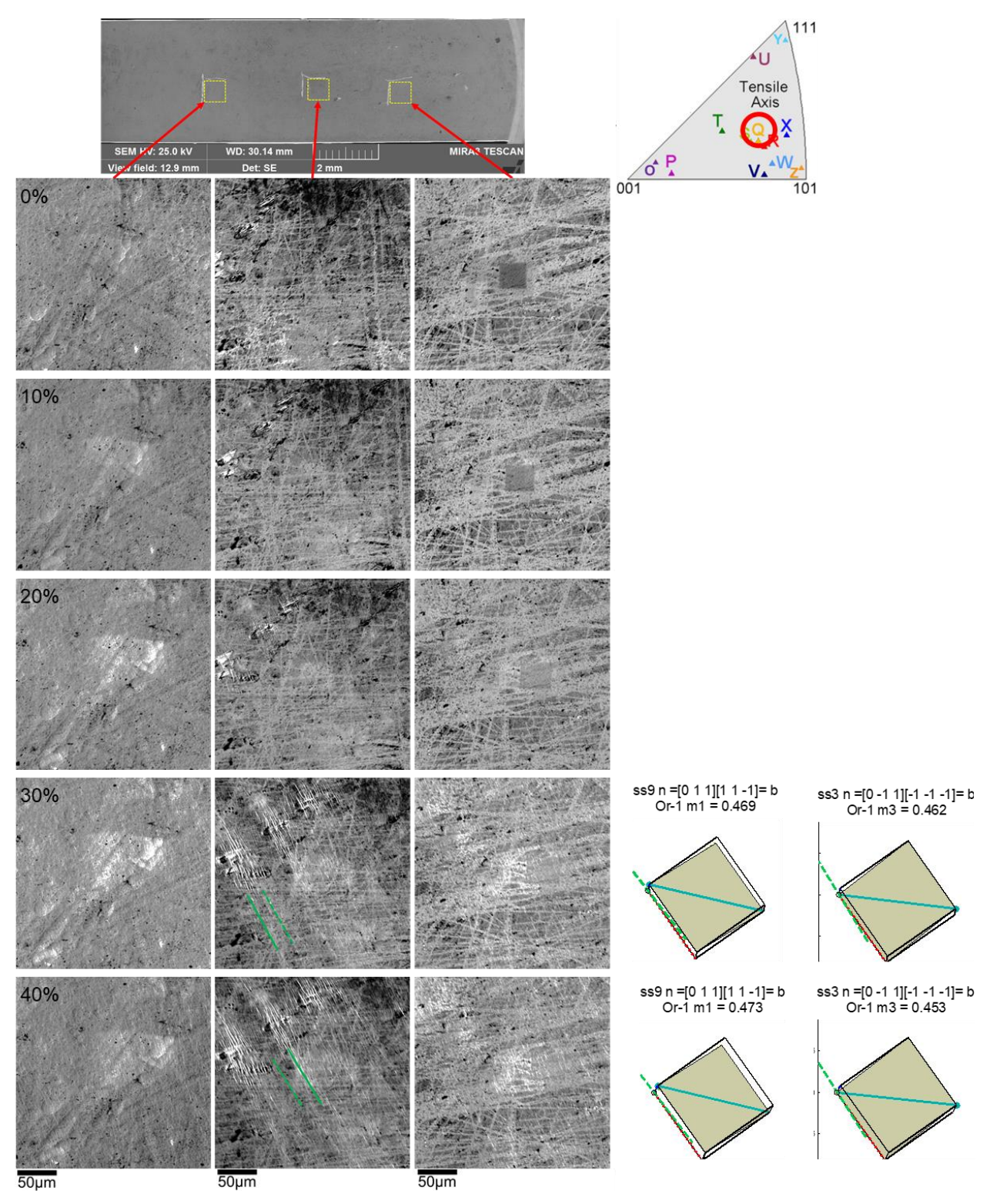


Figure 91: Slip trace identification on the heat-treated sample Q in some of the areas examined. Observed slip traces (solid lines) were matched with computed traces (dotted lines) based on the measured orientations, with {110} slip traces in green, and {112} in purple.

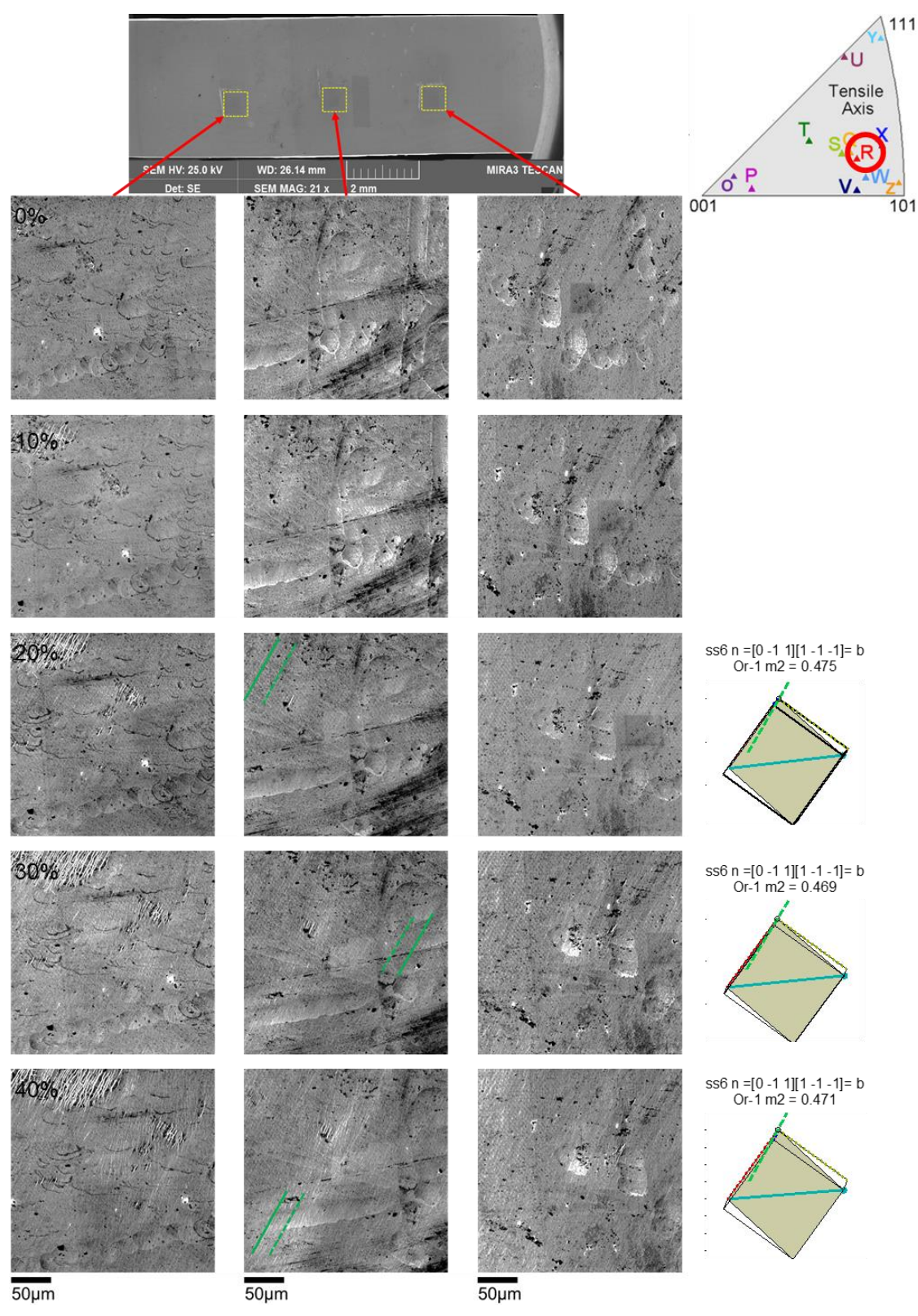


Figure 92: Slip trace identification on the heat-treated sample R in some of the areas examined. Observed slip traces (solid lines) were matched with computed traces (dotted lines) based on the measured orientations, with {110} slip traces in green, and {112} in purple.

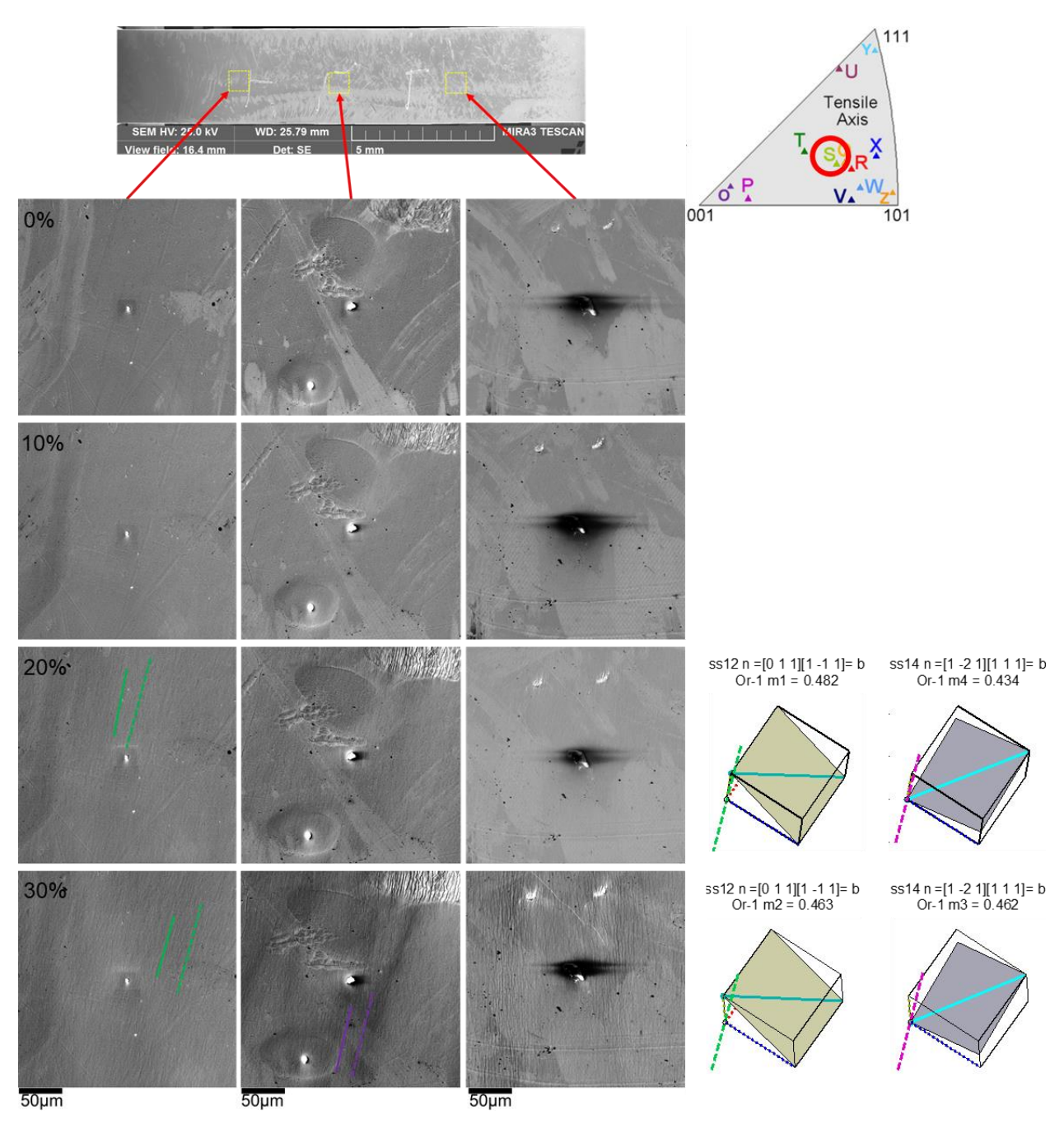


Figure 93: Slip trace identification on the heat-treated sample S in some of the areas examined. Observed slip traces (solid lines) were matched with computed traces (dotted lines) based on the measured orientations, with {110} slip traces in green, and {112} in purple.

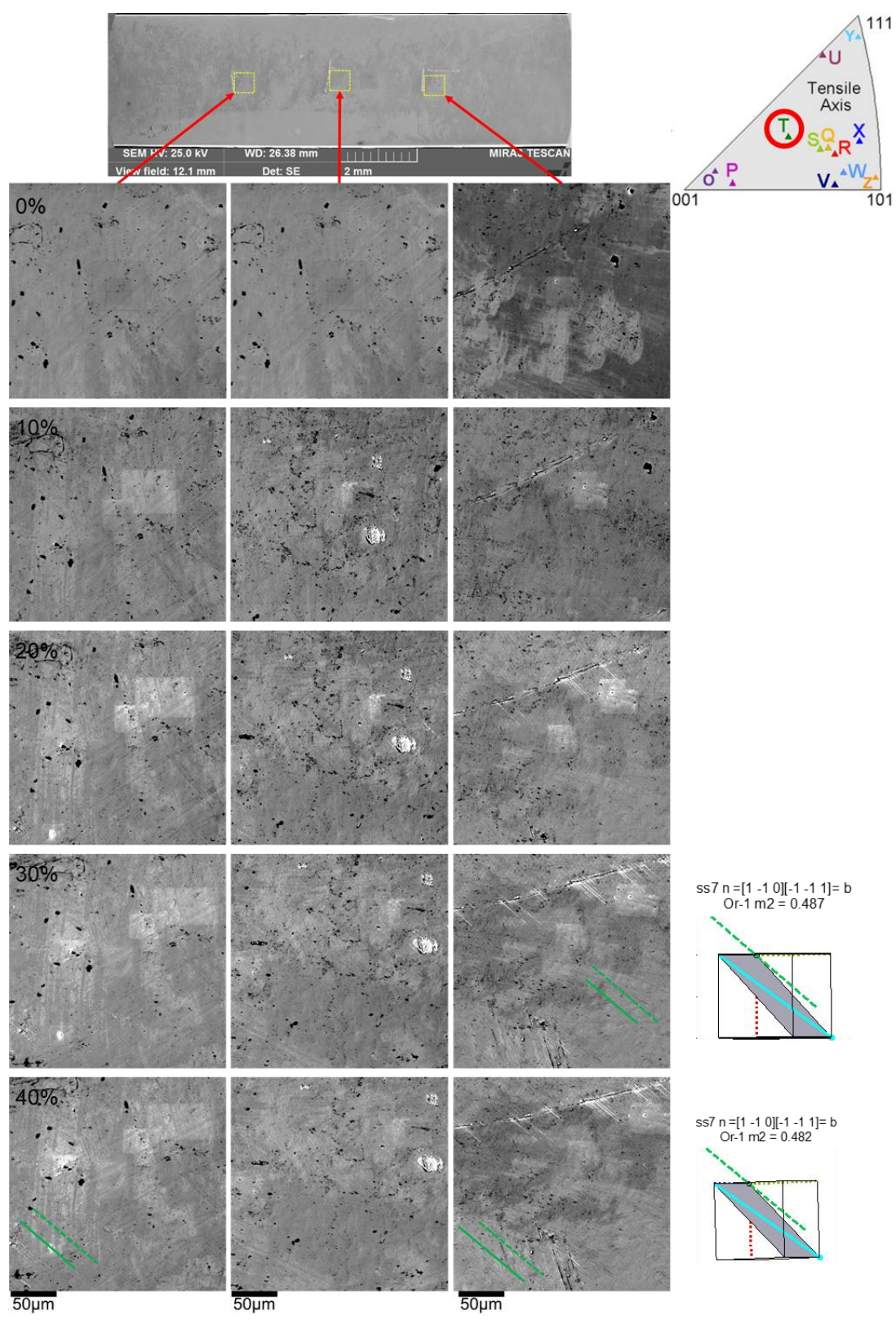


Figure 94: Slip trace identification on the heat-treated sample T in some of the areas examined. Observed slip traces (solid lines) were matched with computed traces (dotted lines) based on the measured orientations, with {110} slip traces in green, and {112} in purple.

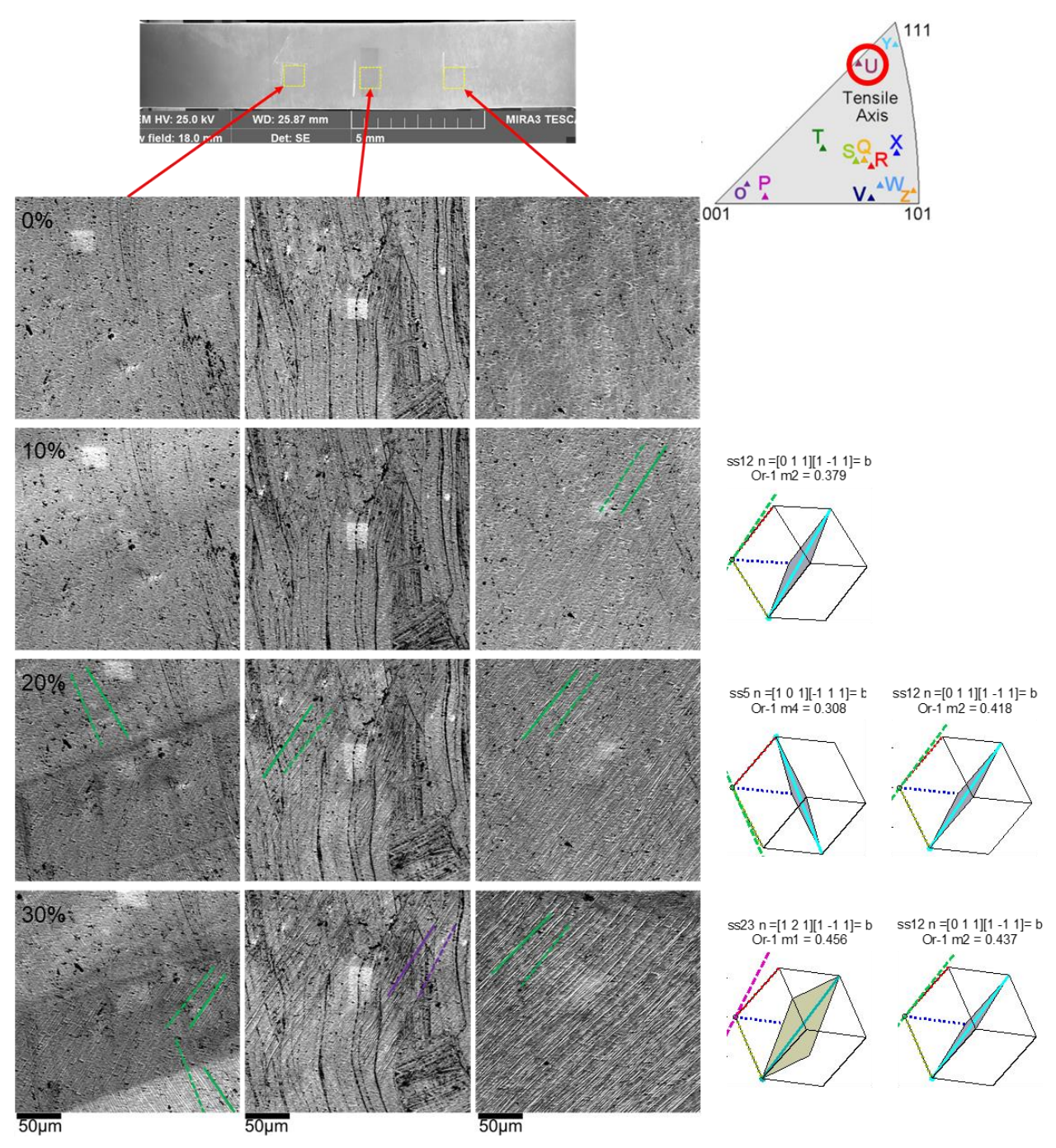


Figure 95: Slip trace identification on the heat-treated sample U in some of the areas examined. Observed slip traces (solid lines) were matched with computed traces (dotted lines) based on the measured orientations, with {110} slip traces in green, and {112} in purple.

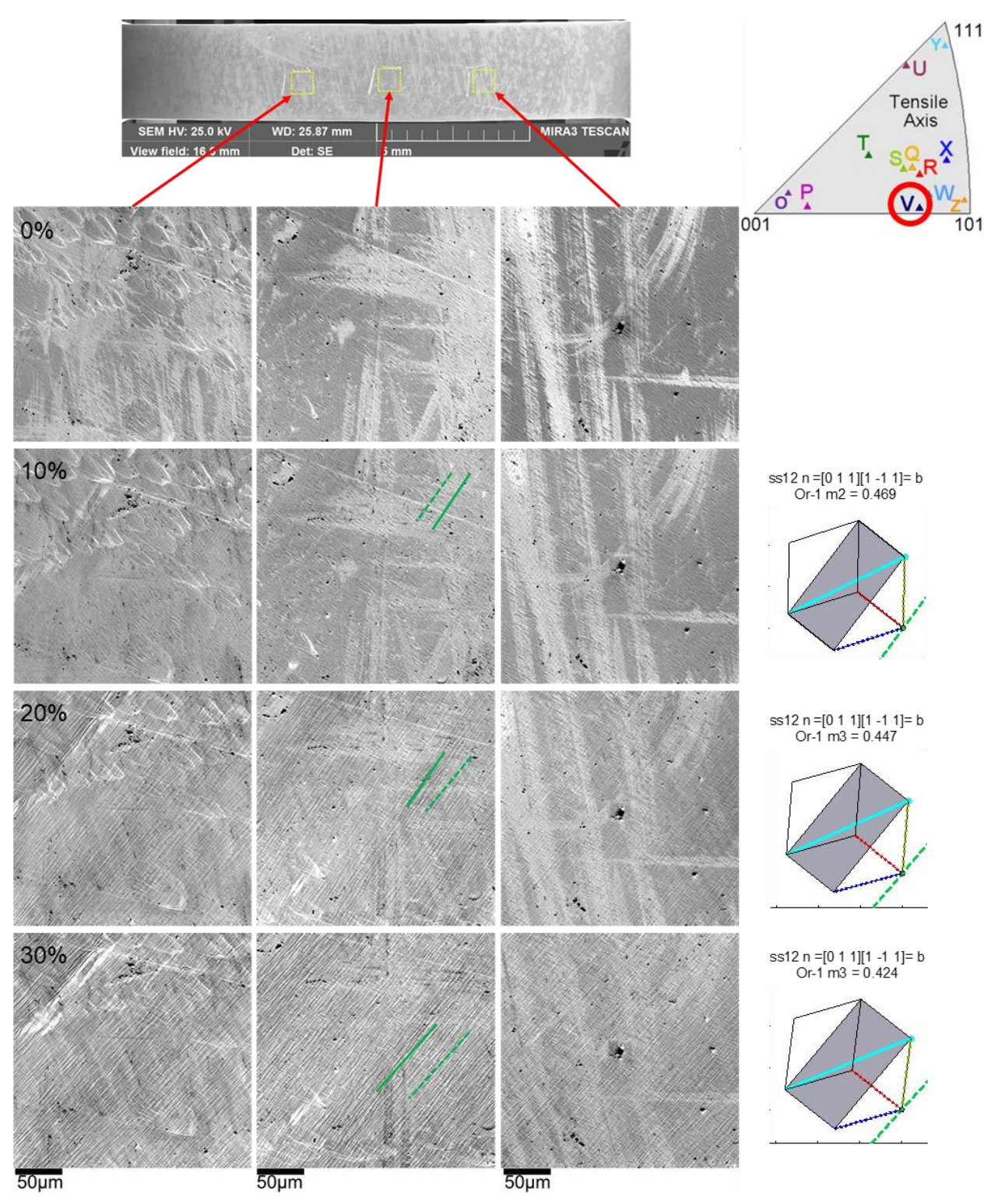


Figure 96: Slip trace identification on the heat-treated sample V in some of the areas examined. Observed slip traces (solid lines) were matched with computed traces (dotted lines) based on the measured orientations, with {110} slip traces in green, and {112} in purple.

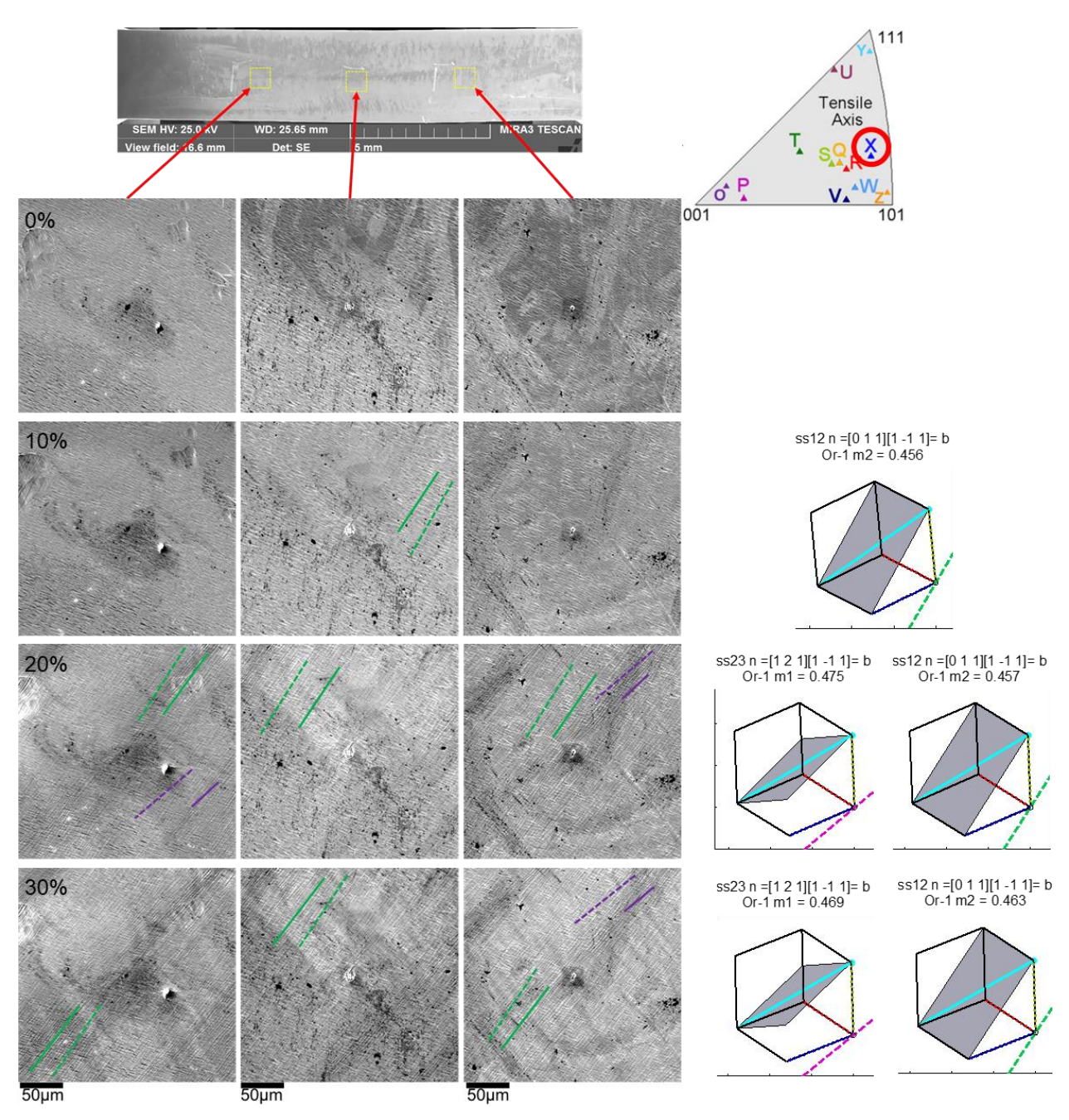


Figure 97: Slip trace identification on the heat-treated sample X in some of the areas examined. Observed slip traces (solid lines) were matched with computed traces (dotted lines) based on the measured orientations, with {110} slip traces in green, and {112} in purple.

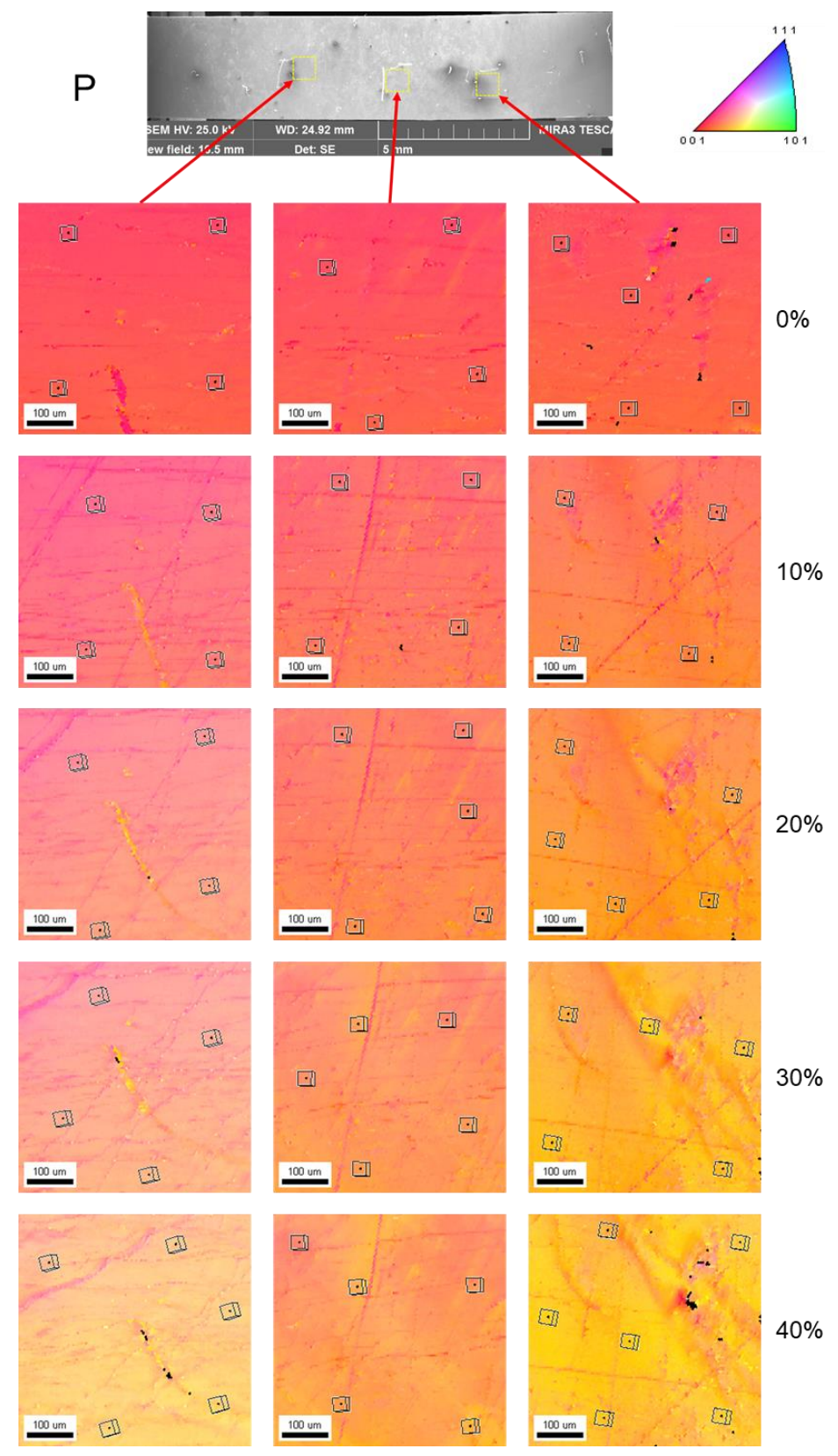


Figure 98: Orientation maps from three regions for the heat-treated sample P before and after deformation.

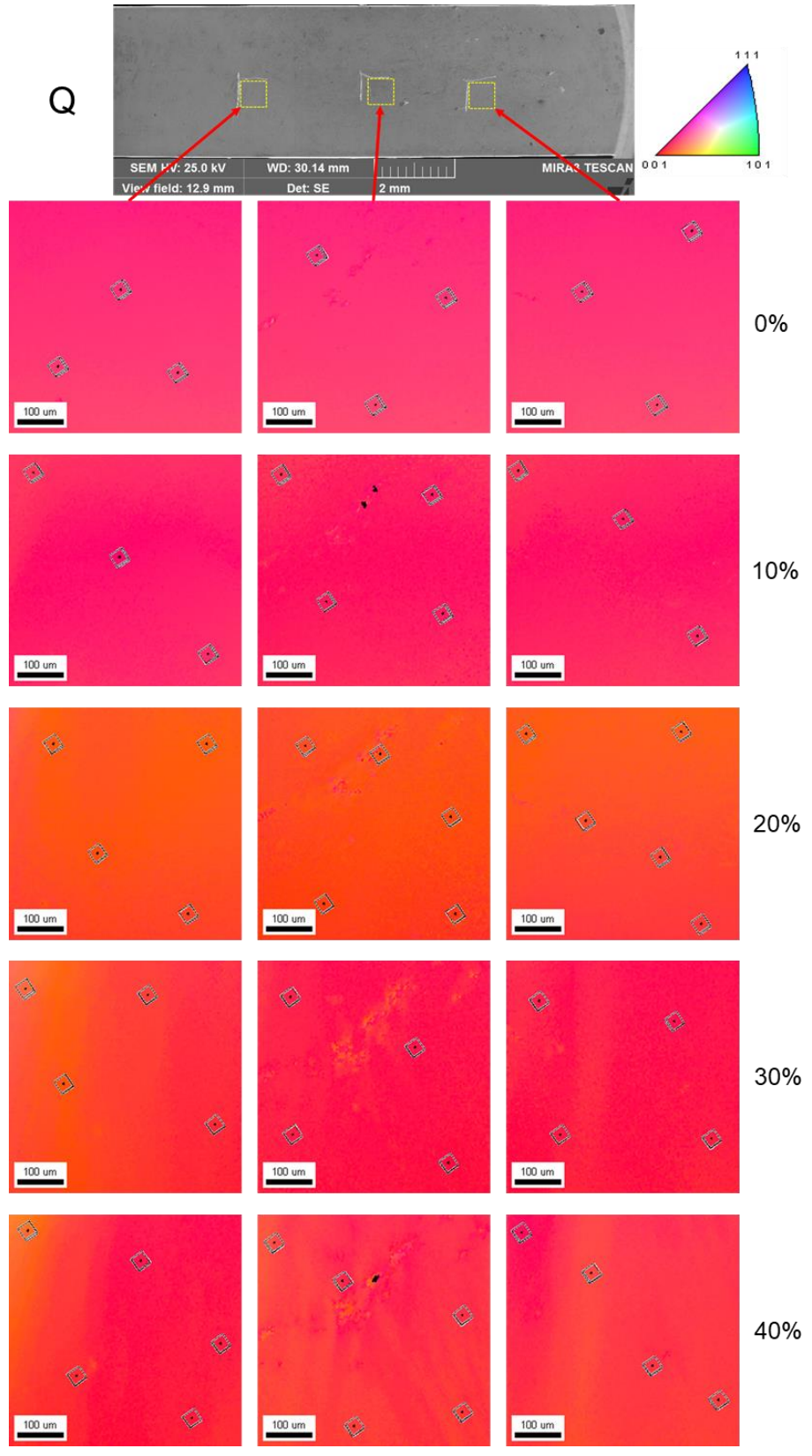


Figure 99: Orientation maps from three regions for the heat-treated sample Q before and after deformation.

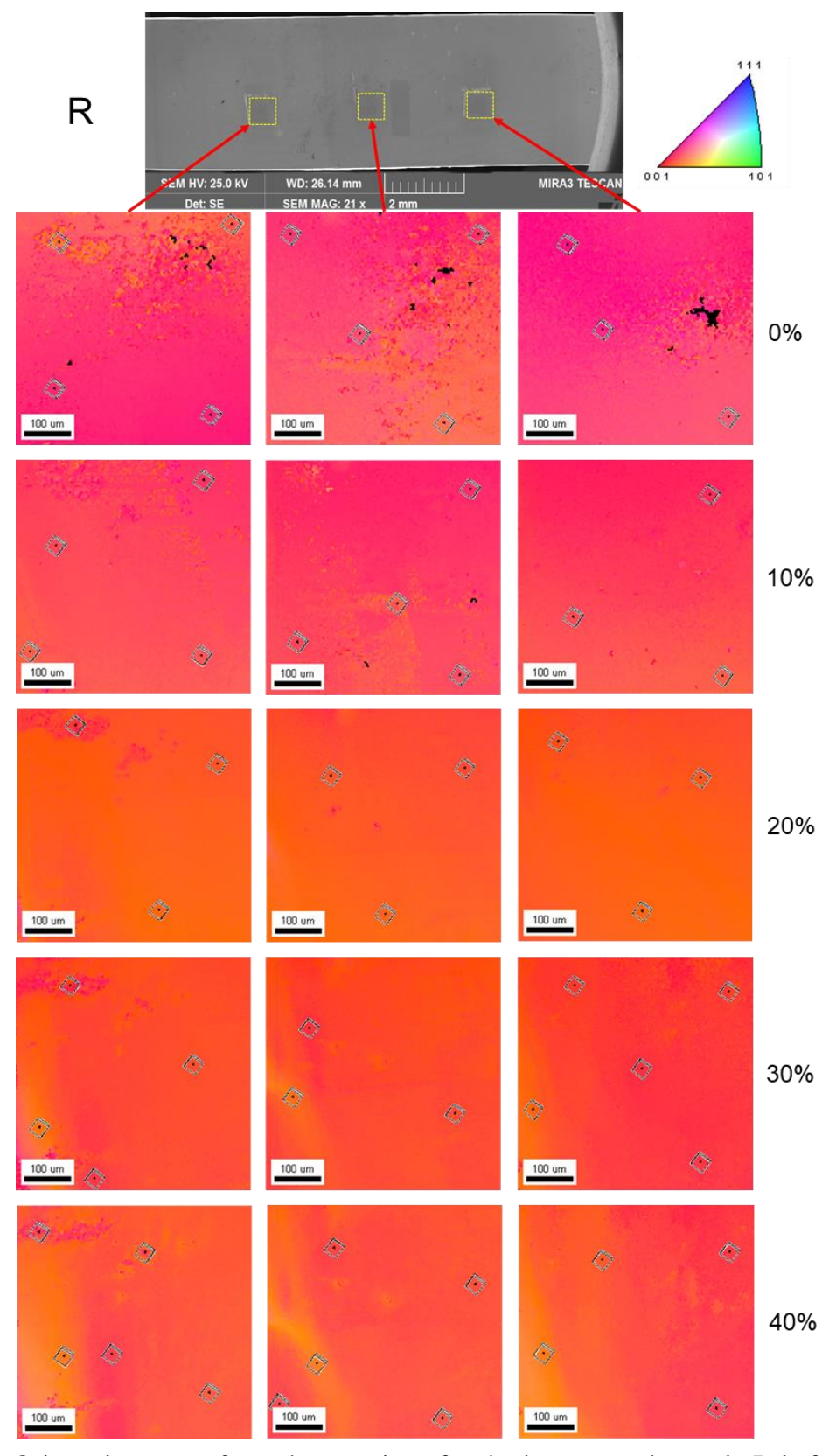


Figure 100: Orientation maps from three regions for the heat-treated sample R before and after deformation.

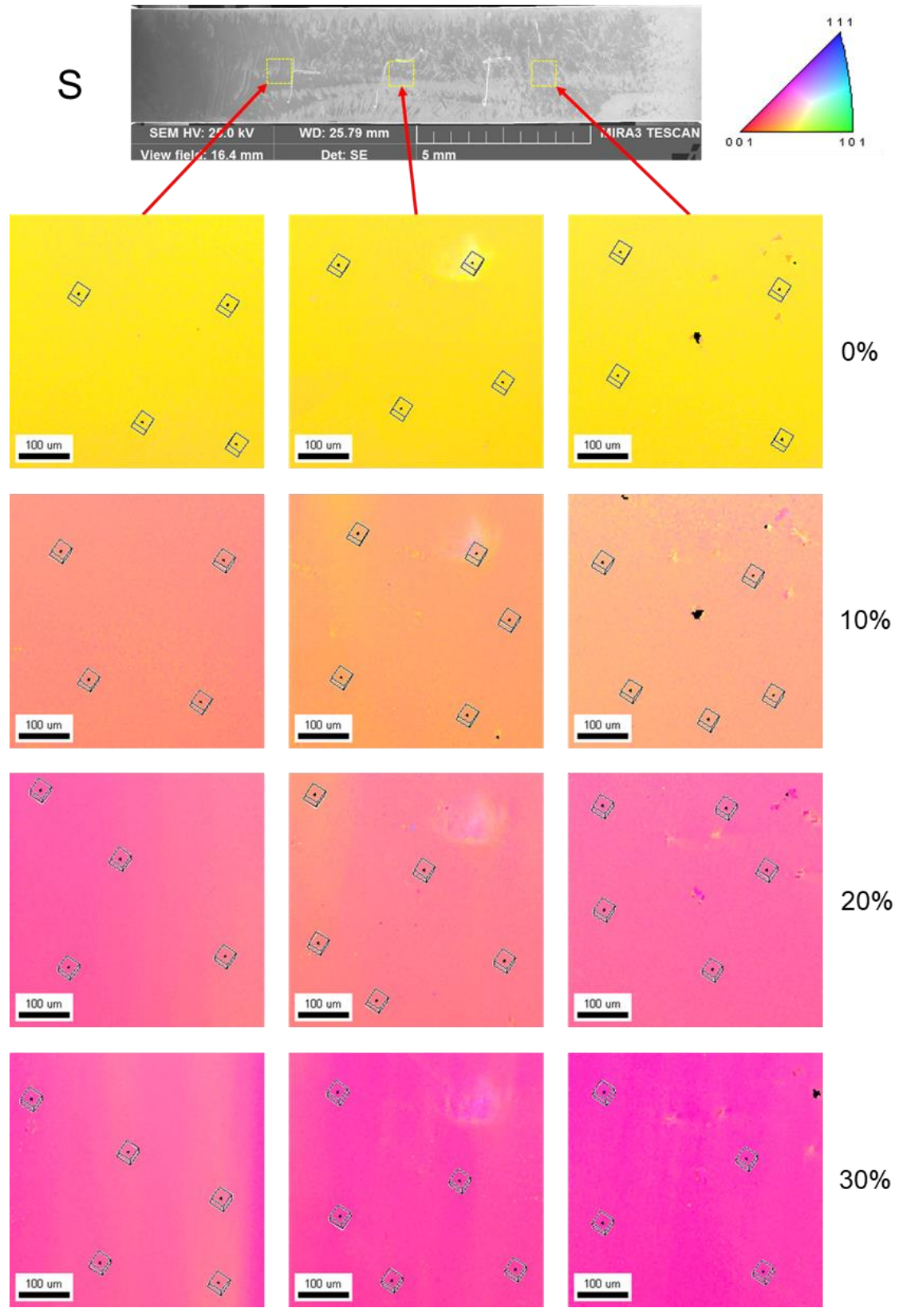


Figure 101: Orientation maps from three regions for the heat-treated sample S before and after deformation.

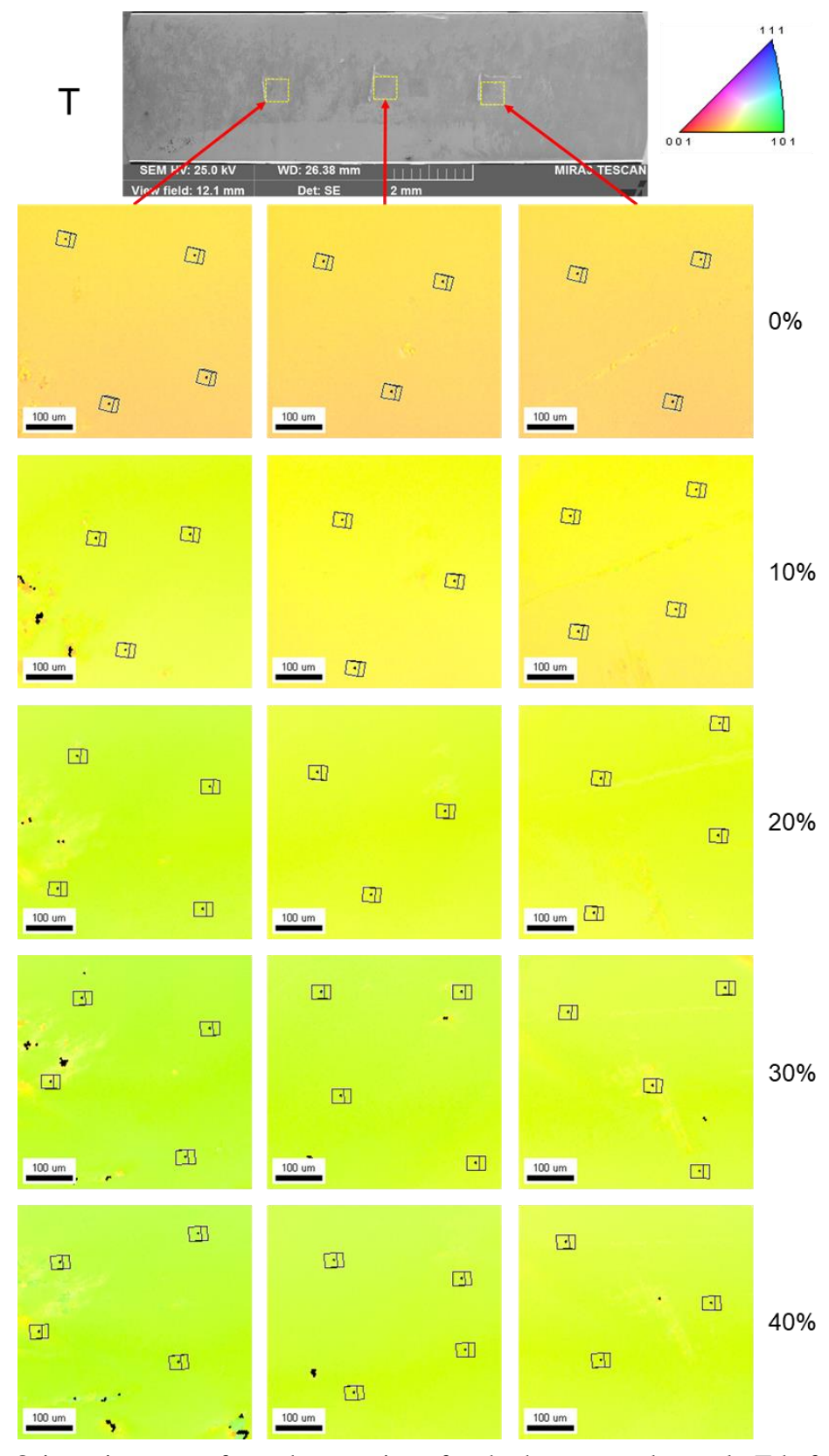


Figure 102: Orientation maps from three regions for the heat-treated sample T before and after deformation.

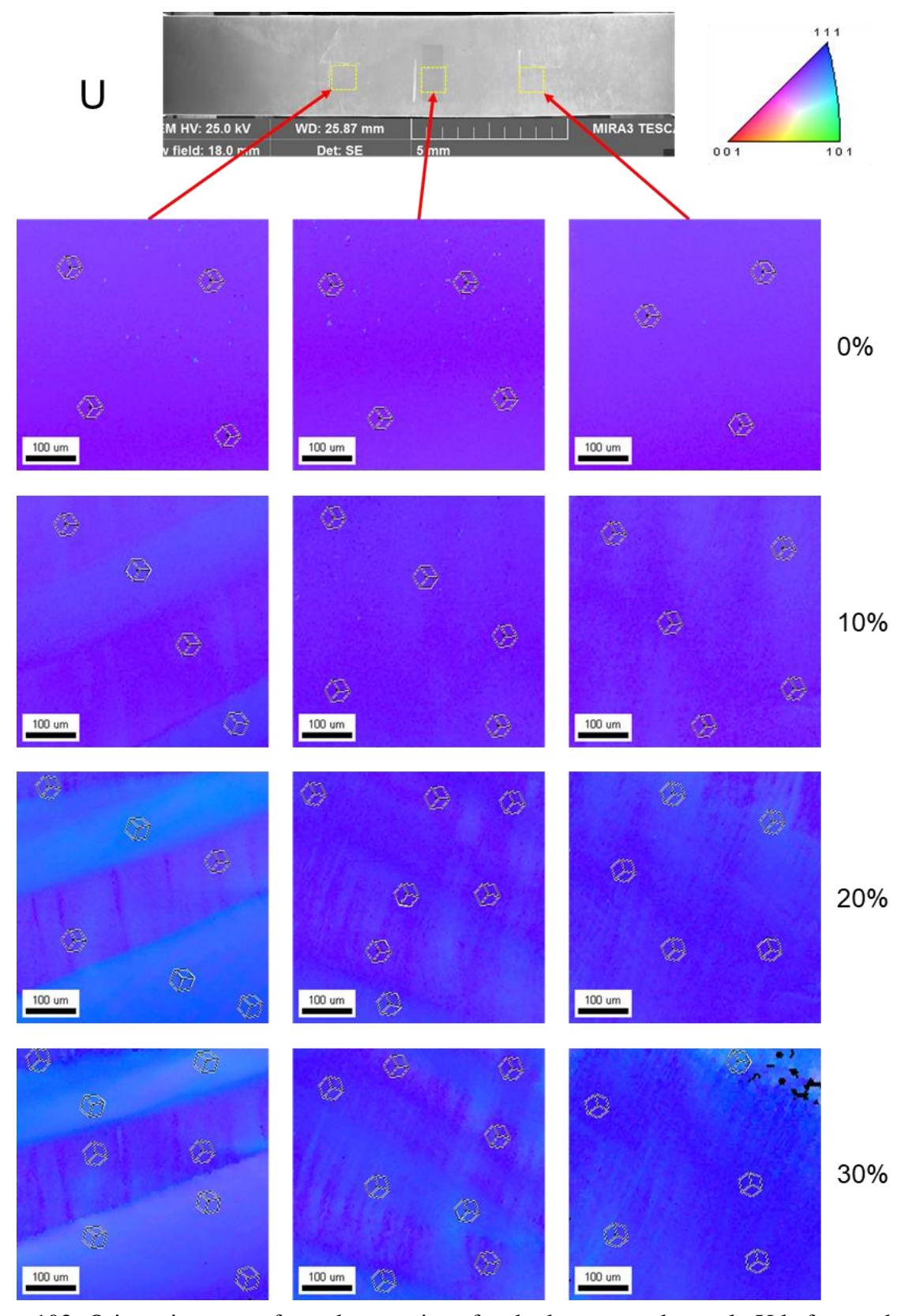


Figure 103: Orientation maps from three regions for the heat-treated sample U before and after deformation.

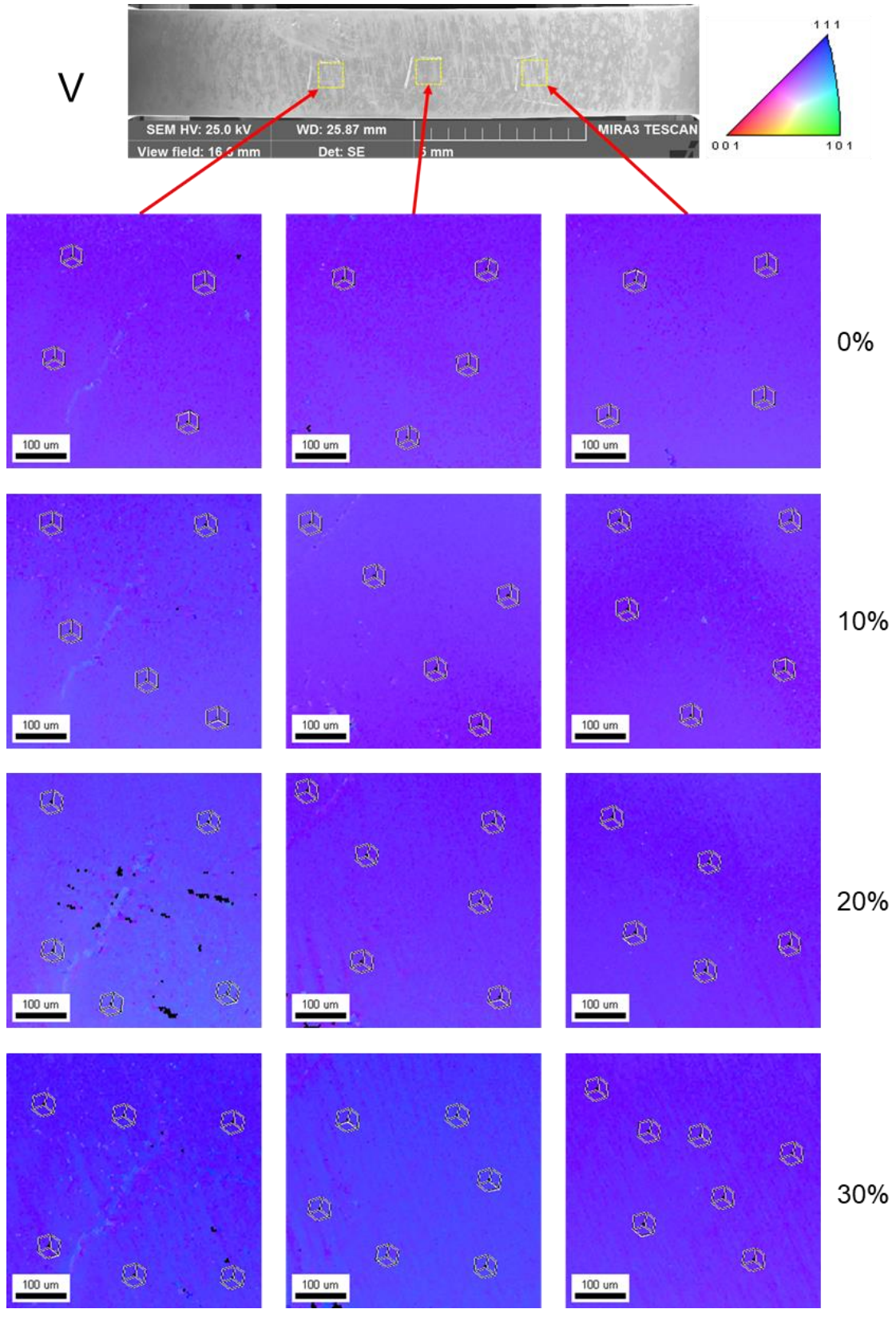


Figure 104: Orientation maps from three regions for the heat-treated sample V before and after deformation.

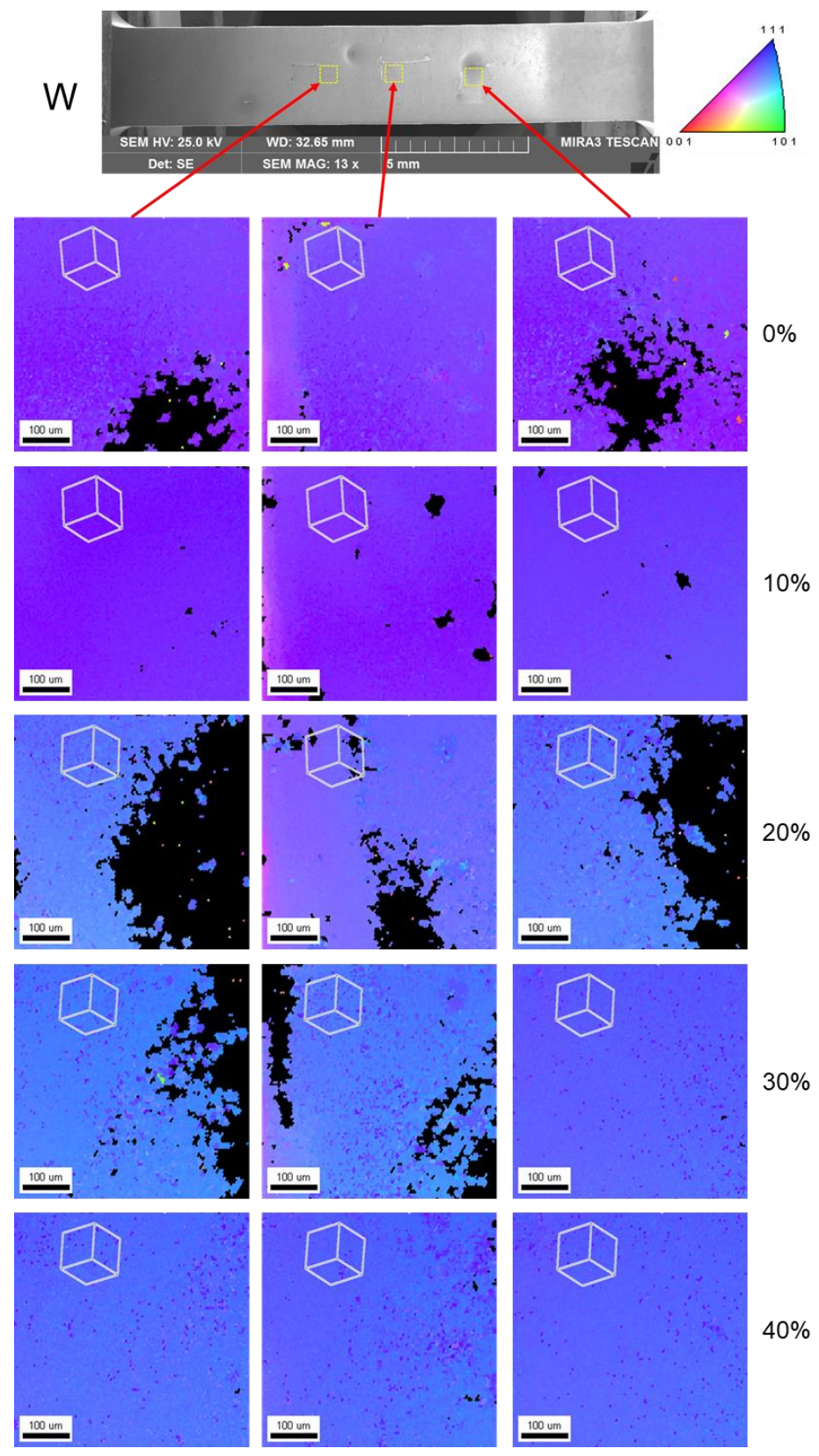


Figure 105: Orientation maps from three regions for the heat-treated sample W before and after deformation.

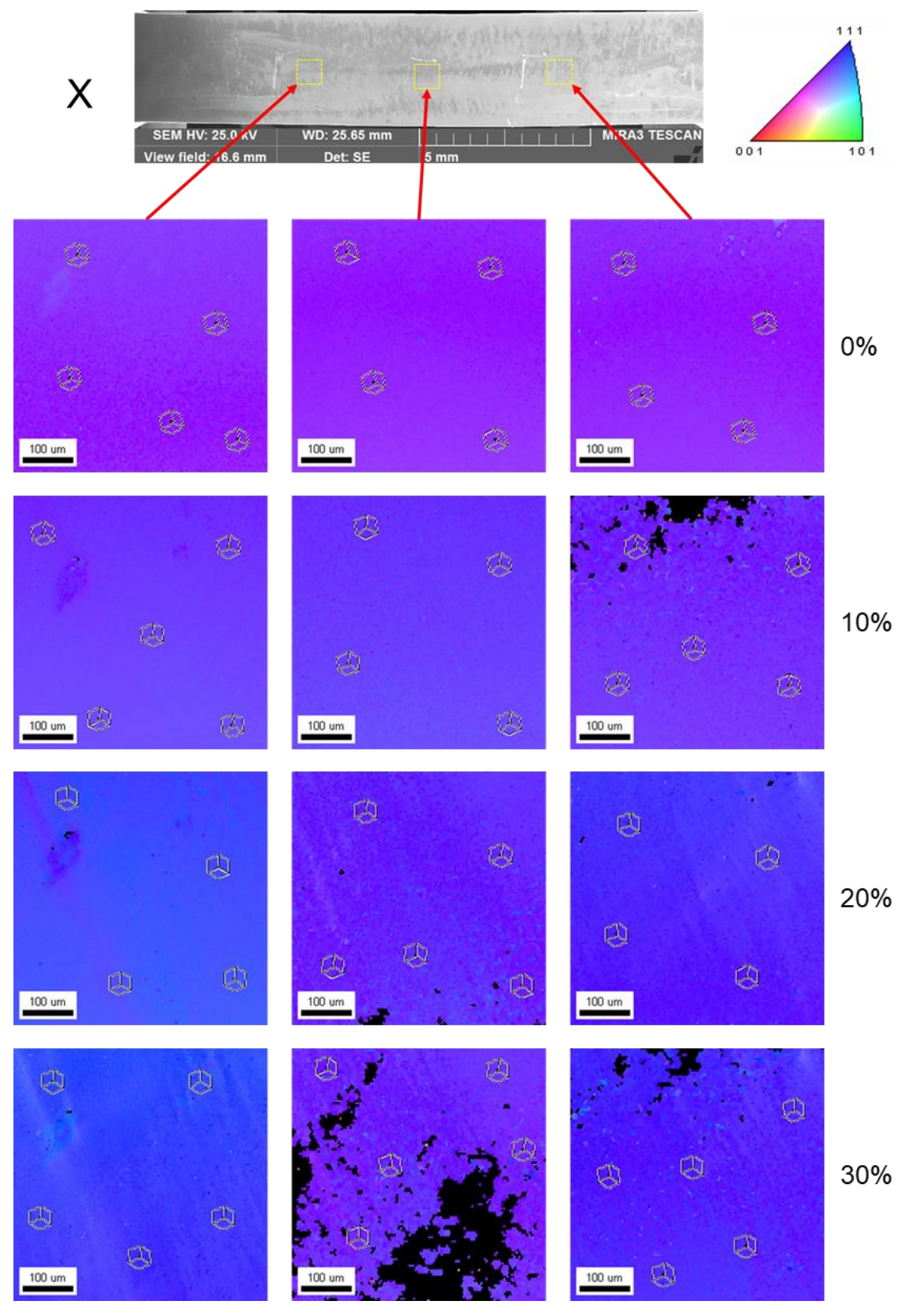


Figure 106: Orientation maps from three regions for the heat-treated sample X before and after deformation.

BIBLIOGRAPHY

BIBLIOGRAPHY

- [1] H. Padamsee, J. Knobloch, T. Hays, RF superconductivity for accelerators, Wiley, John & Sons, Incorporated, 1998.
- [2] H. Padamsee, RF superconductivity: science, technology and applications, John Wiley & Sons 2009.
- [3] C. Antoine, Materials and surface aspects in the development of SRF Niobium cavities, 2012.
- [4] C. Antoine, Influence of crystalline structure on rf dissipation in superconducting niobium, Physical Review Accelerators Beams 22(3) (2019) 034801.
- [5] G. Ciovati, P. Dhakal, G.R. Myneni, Superconducting radio-frequency cavities made from medium and low-purity niobium ingots, Superconductor Science and Technology 29(6) (2016) 064002.
- [6] A. Gurevich, Theory of RF superconductivity for resonant cavities, Superconductor Science Technology 30(3) (2017) 034004.
- [7] H. Padamsee, 100 years of superconductivity & 50 years of RF superconductivity, Banquet Talk at SRF 2011, Chicago.
- [8] D. van Delft, P. Kes, The discovery of superconductivity, Phys. Today 63(9) (2010) 38-43.
- [9] H.K. Onnes, The resistance of pure mercury at helium temperatures, Commun. Phys. Lab. Univ. Leiden, 12, 1 (1911).
- [10] H.K. Onnes, Commun. Phys. Lab. Univ. Leiden 133d (May 1913), reprinted in Proc. K. Ned Akad. Wet. 16, 113 (1913).
- [11] P.J. Bryant, A brief history and review of accelerators, in: S. Turner (Ed.), Cern Accelerator School Fifth General Accelerator Physics Course: Proceedings, Vol 11994, pp. 1-16.
- [12] A. Banford, G. Stafford, The feasibility of a superconducting proton linear accelerator, Journal of Nuclear Energy. Part C, Plasma Physics, Accelerators, Thermonuclear Research 3(4) (1961) 287.
- [13] P. Kneisel, G. Ciovati, P. Dhakal, K. Saito, W. Singer, X. Singer, G. Myneni, The rise of ingot niobium as a material for superconducting radiofrequency accelerating cavities, arXiv preprint arXiv:1304.1722 (2013).
- [14] D. Alesini, Linear accelerator technology, INFN-LNF, Frascati, Rome, Italy.
- [15] H. Padamsee, 50 years of RF superconductivity, Talk at DESY, 2011.

- [16] D. Baars, Investigation of active slip systems in high purity single crystal niobium, Ph.D. dissertation, Michigan State University 2013.
- [17] M.S. Livingston, J.P. Blewett, E. Stickley, Particle accelerators, American Journal of Physics 30(12) (1962) 940-941.
- [18] H. Padamsee, 50 years of RF superconductivity a perspective, Talk at CERN, 2011.
- [19] F. Tecker, Linear colliders (high-energy e+/e- colliders), Talk at CERN, 2011.
- [20] H. Padamsee, Designing superconducting cavities for accelerators, (2004).
- [21] Wikipedia contributors. "Superconducting radio frequency." Wikipedia, The Free Encyclopedia, 5 Feb. 2017. Web. 21 Jun. 2017.
- [22] G. Ciovati, Review of the frontier workshop and Q-slope results, Physica C: Superconductivity 441(1) (2006) 44-50.
- [23] W.D. Callister, D.G. Rethwisch, Materials science and engineering, John Wiley & Sons NY 2011.
- [24] T.R. Bieler, N.T. Wright, F. Pourboghrat, C. Compton, K.T. Hartwig, D. Baars, A. Zamiri, S. Chandrasekaran, P. Darbandi, H. Jiang, E. Skoug, S. Balachandran, G.E. Ice, W. Liu, Physical and mechanical metallurgy of high purity Nb for accelerator cavities, Physical Review Special Topics Accelerators and Beams 13(3) (2010).
- [25] S. Turner, Superconductivity in particle accelerators, CERN, European Organization for Nuclear Research 1996.
- [26] A. Romanenko, Review of high field Q-slope, surface measurements, Proceedings of the 12th Workshop on RF Superconductivity, 2007.
- [27] A. Romanenko, H. Padamsee, The role of near-surface dislocations in the high magnetic field performance of superconducting niobium cavities, Superconductor Science and Technology 23(4) (2010) 045008.
- [28] EDAX-TSL software V5.31 Manual.
- [29] D. Hull, D.J. Bacon, Introduction to dislocations, Elsevier 2011.
- [30] L. Cermelli, Statistically stored dislocations in rate-independent plasticity, Universitae Politecnico di Torino (2000) 25.
- [31] S. Chandrasekaran, T. Bieler, C. Compton, N. Wright, Effect of heat treatment temperature on the thermal conductivity of large grain superconducting niobium, Parameters 3 (2011) 5.

- [32] S. Chandrasekaran, T. Bieler, C. Compton, N. Wright, Recovery of phonon peak in annealed niobium as a function of initial strain and hydrogen concentration, SRFMW2012 (2012).
- [33] S. Chandrasekaran, T. Bieler, C. Compton, N. Wright, Hydrogen saturation and the thermal conductivity of superconducting niobium, (2014).
- [34] C.Z. Antoine, How to achieve the best SRF performance: (practical) limitations and possible solutions, arXiv preprint arXiv:1501.03343 (2015).
- [35] F. Koechlin, B. Bonin, Parametrization of the niobium thermal conductivity in the superconducting state, Superconductor Science and Technology 9(6) (1996) 453.
- [36] W. Singer, Metallurgical and technological request for high purity niobium in SRF application, Hydrogen in Matter(AIP Conference Proceedings)(Volume 837), 2006, pp. 51-63.
- [37] D. Proch, RF cavity fabrication, (2004).
- [38] W. Singer, SRF cavity fabrication and materials, arXiv preprint arXiv:1501.07142 (2015).
- [39] K. Schulze, O. Bach, D. Lupton, F. Schreiber, Purification of niobium, Niobium-Proceedings of the international symposium, 1984.
- [40] R.A. Graham, Single crystal technology for making RRR niobium sheet, AIP Conference Proceedings, AIP, 2007, pp. 21-40.
- [41] P. Kneisel, G. Ciovati, P. Dhakal, K. Saito, W. Singer, X. Singer, G.R. Myneni, Review of ingot niobium as a material for superconducting radiofrequency accelerating cavities, Nuclear Instruments and Methods in Physics Research Section A: Accelerators, Spectrometers, Detectors and Associated Equipment 774 (2015) 133-150.
- [42] W. Singer, A. Brinkmann, A. Ermakov, J. Iversen, G. Kreps, A. Matheisen, D. Proch, D. Reschke, X. Singer, M. Spiwek, H. Wen, H.G. Brokmeier, Large grain superconducting RF cavities at DESY, 927 (2007) 123-132.
- [43] K. Saito, F. Furuta, H. Umezawa, K. Takeuchi, Multi-wire slicing of large grain ingot material, THOAAU05, These Proceedings (2009).
- [44] H. Umezawa, K. Takeuchi, F. Furuta, T. Konomi, K. Saito, K. Nishimura, Single crystal niobium development, Proc. 1st International Particle Accelerator Conference, IPAC10, Kyoto, Japan, 2010.
- [45] W. Singer, S. Aderhold, J. Iversen, G. Kreps, L. Lilje, A. Matheisen, X. Singer, H. Weise, M. Pekeler, J. Schwellenbach, Development of large grain superconducting resonators for the European XFEL, Proc. of the 23rd Particle Accelerator Conference, Vancouver, Canada, 2009.

- [46] W. Singer, X. Singer, Technical specifications for large crystal niobium discs applied for the fabrication of 1.3 GHz superconducting cavities, Version B, DESY April (2006).
- [47] A. Ermakov, I. Jelezov, X. Singer, W. Singer, G.B. Viswanathan, V. Levit, H.L. Fraser, H. Wen, M. Spiwek, Physical properties and structure of large grain/single crystal niobium for superconducting RF cavities, Journal of Physics: Conference Series 97 (2008) 012014.
- [48] D. Baars, T. Bieler, A. Zamiri, F. Pourboghrat, C. Compton, Crystal orientation effects during fabrication of single or multi-crystal Nb SRF cavities, SRF07, Beijing, Oct (2007).
- [49] G.R. Myneni, P. Kneisel, T. Cameiro, Large grain cavities from pure niobium ingot, Google Patents, 2012.
- [50] H. Jiang, T.R. Bieler, C. Compton, T.L. Grimm, Cold rolling evolution in high purity niobium using a tapered wedge specimen, Physica C: Superconductivity 441(1-2) (2006) 118-121.
- [51] W. Singer, S. Aderhold, A. Ermakov, J. Iversen, D. Kostin, G. Kreps, A. Matheisen, W.D. Möller, D. Reschke, X. Singer, K. Twarowski, H. Weise, H.G. Brokmeier, Development of large grain cavities, Physical Review Special Topics Accelerators and Beams 16(1) (2013).
- [52] P. Kneisel, G.R. Myneni, G. Ciovati, J. Sekutowicz, T. Carneiro, Development of large grain/single crystal niobium cavity technology at Jefferson lab, 927 (2007) 84-97.
- [53] G. Ciovati, P. Kneisel, G. Myneni, S. Chattopadhyay, Performances of high-purity niobium cavities with different grain sizes, Proceedings of LINAC, 2006, pp. 318-20.
- [54] P. Kneisel, Review of progress on large grain and single grain niobium cavities, Proceedings of SRF2007, Peking Univ., Beijing, China, paper TH102.
- [55] C. Compton, A. Aizaz, D. Baars, T. Bieler, J. Bierwagen, S. Bricker, T. Grimm, W. Hartung, H. Jiang, M. Johnson, Single crystal and large grain niobium research at Michigan State University, AIP Conference Proceedings, AIP, 2007, pp. 98-105.
- [56] G. Ciovati, P. Dhakal, J. Matalevich, G. Myneni, A. Schmidt, J. Iversen, A. Matheisen, W. Singer, Mechanical properties of niobium radio-frequency cavities, Materials Science and Engineering: A 642 (2015) 117-127.
- [57] D. Baars, T. Bieler, P. Darbandi, F. Pourboghrat, C. Compton, Microstructure studies of niobium, SRF2009, Berlin, Germany, SRF2009 WEB Proceedings, paper TUOBAU05 (2009) 144-48.
- [58] D. Kang, D. Baars, T. Bieler, C. Compton, Study of slip in high purity single crystal Nb for accelerator cavities, TUP017, Proceedings of SRF2013, Paris, France (2013) (2013) 20-40.
- [59] D. Raabe, K. Lücke, Rolling textures of niobium and molybdenum, Zeitschrift für Metallkunde 85(5) (1994) 302-306.

- [60] H. Abreu, S.S. Tavares, S. Carvalho, T. Eduardo, A.D.S. Bruno, M.H.P. da Silva, Texture and microstructure of cold rolled and recrystallized pure niobium, Materials Science Forum, Trans Tech Publ, 2007, pp. 3436-3441.
- [61] M. Zhao, Investigation of correlations between mechanical and microstructural properties of high purity polycrystalline niobium, master's thesis, Michigan State University 2015.
- [62] C. Compton, T. Bieler, S. Chandrasekaran, D. Kang, D. Miller, N. Wright, Quality assurance and acceptance testing of niobium material for use in the construction of the facility for rare isotope beams (FRIB) at Michigan State University (MSU), SRF2013, MOP033, Paris, France (2013).
- [63] H. Jiang, D. Baars, A. Zamiri, C. Antonie, P. Bauer, T. Bieler, F. Pourboghrat, C. Compton, T. Grimm, Mechanical properties of high RRR niobium with different texture, IEEE Transactions on Applied Superconductivity 17(2) (2007) 1291-1294.
- [64] A. Iro, Z. Zhou, H. Utsunomiya, T. Sakai, Reduction in planar anisotropy of pure niobium sheet by asymmetric rolling, Tetsu To Hagane-Journal of The Iron and Steel Institute of Japan 97(11) (2011) 572-577.
- [65] W. Polkowski, Differential speed rolling: a new method for a fabrication of metallic sheets with enhanced mechanical properties, Progress in Metallic Alloys, InTechOpen2016.
- [66] R. Srinivasan, G.B. Viswanathan, V.I. Levit, H.L. Fraser, Orientation effect on recovery and recrystallization of cold rolled niobium single crystals, Materials Science and Engineering: A 507(1-2) (2009) 179-189.
- [67] H.R.Z. Sandim, D. Raabe, EBSD study of grain subdivision of a Goss grain in coarse-grained cold-rolled niobium, Scripta Materialia 53(2) (2005) 207-212.
- [68] H.R.Z. Sandim, D. Raabe, An EBSD study on orientation effects during recrystallization of coarse-grained niobium, Materials Science Forum 467-470 (2004) 519-524.
- [69] H.R.Z. Sandim, J.F.C. Lins, A.L. Pinto, A.F. Padilha, Recrystallization behavior of a cold-rolled niobium bicrystal, Materials Science and Engineering: A 354(1-2) (2003) 217-228.
- [70] V. Palmieri, F. Stivanello, S.Y. Stark, C. Roncolato, M. Valentino, Besides the standard niobium bath chemical polishing, SRF 2001 workshop, Tsukuba Sept, 2001.
- [71] G. Ciovati, P. Kneisel, G.R. Myneni, America's overview of superconducting science and technology of ingot niobium, (2011) 25-37.
- [72] P. Dhakal, G. Ciovati, G. Myneni, K. Gray, N. Groll, P. Maheshwari, D. McRae, R. Pike, T. Proslier, F. Stevie, R. Walsh, Q. Yang, J. Zasadzinzki, Effect of high temperature heat treatments on the quality factor of a large-grain superconducting radio-frequency niobium cavity, Physical Review Special Topics Accelerators and Beams 16(4) (2013).

- [73] C. Antoine, A. Aspart, S. Regnault, A. Chincarini, Surface studies: method of analysis and results, This Proceedings, 2001.
- [74] R.E. Ricker, G.R. Myneni, Evaluation of the propensity of niobium to absorb hydrogen during fabrication of superconducting radio frequency cavities for particle accelerators, Journal of Research of the National Institute of Standards and Technology 115(5) (2010) 353.
- [75] R. Kirby, H. Padamsee, F. King, Residual oxygen on Nb heated to 500 C, 2005.
- [76] P. Kneisel, T. Saito, R. Parodi, Performance of 1300 MHz KEK-type single cell niobium cavities, Jefferson Laboratory 1998.
- [77] A. Grassellino, Muon spin rotation/relaxation studies of niobium for SRF applications, Proceedings of the 15th International Conference on RF Superconductivity, 2011.
- [78] M. Wang, T. Bieler, C. Compton, D. Kang, D. Larbalestier, P. Lee, A. Polyanskii, Z.-H. Sung, Introduction of precisely controlled microstructural defects into SRF cavity niobium sheets and their impact on local superconducting properties, 17th International Conference on RF Superconductivity (SRF2015), Whistler, BC, Canada, Sept. 13-18, 2015, JACOW, Geneva, Switzerland, 2015, pp. 120-124.
- [79] C.R. Weinberger, B.L. Boyce, C.C. Battaile, Slip planes in bcc transition metals, International Materials Reviews 58(5) (2013) 296-314.
- [80] U. Kocks, The relation between polycrystal deformation and single-crystal deformation, Metallurgical and Materials Transactions B 1(5) (1970) 1121-1143.
- [81] E. Furubayashi, Behavior of dislocations in Fe-3% Si under stress, Journal of the Physical Society of Japan 27(1) (1969) 130-146.
- [82] T. Imura, Mechanical properties of bcc metals, Meshii, ed., TMS-AIME, Warrendale, PA (1982) 65-73.
- [83] F. Louchet, L. Kubin, D. Vesely, In situ deformation of bcc crystals at low temperatures in a high-voltage electron microscope Dislocation mechanisms and strain-rate equation, Philosophical Magazine A 39(4) (1979) 433-454.
- [84] H. Saka, K. Noda, T. Imura, Tensile test of foil specimens of Fe single crystals at room and low temperature under observation in high voltage electron microscope, Cryst. Lattice Defects 4(1) (1973) 45-56.
- [85] A. Seeger, U. Holzwarth, Slip planes and kink properties of screw dislocations in high-purity niobium, Philosophical Magazine 86(25-26) (2006) 3861-3892.

- [86] V. Vitek, Theory of the core structures of dislocations in BCC metals, Cryst. Lattice Defects 5(1) (1974) 1-34.
- [87] M. Duesbery, V. Vitek, Plastic anisotropy in bcc transition metals, Acta Materialia 46(5) (1998) 1481-1492.
- [88] A. Seeger, The flow stress of high-purity refractory body-centred cubic metals and its modification by atomic defects, Le Journal de Physique IV 5(C7) (1995) C7-45-C7-65.
- [89] A. Seeger, Why anomalous slip in body-centred cubic metals?, Materials Science and Engineering: A 319 (2001) 254-260.
- [90] R. Maddin, N. Chen, Plasticity of columbium single crystals, Transactions of The American Institute of Mining and Metallurgical Engineers 197(9) (1953) 1131-1136.
- [91] W. Wasserbäch, Anomalous slip in high-purity niobium and tantalum single crystals, Physica Status Solidi (a) 147(2) (1995) 417-446.
- [92] W. Wasserbäch, V. Novak, Optical investigation of anomalous slip-line patterns in high purity niobium and tantalum single crystals after tensile deformation at 77 K, Materials Science and Engineering 73 (1985) 197-202.
- [93] M. Duesbery, R. Foxall, P. Hirsch, The plasticity of pure niobium single crystals, Le Journal de Physique Colloques 27(C3) (1966) C3-193-C3-204.
- [94] R. Foxall, M. Duesbery, P. Hirsch, The deformation of niobium single crystals, Canadian Journal of Physics 45(2) (1967) 607-629.
- [95] A. Seeger, Progress and problems in the understanding of the dislocation relaxation processes in metals, Materials Science and Engineering: A 370(1-2) (2004) 50-66.
- [96] J. Christian, Some surprising features of the plastic deformation of body-centered cubic metals and alloys, Metallurgical Transactions A 14(7) (1983) 1237-1256.
- [97] M. Duesbery, Dislocations in Solids vol 8, ed FRN Nabarro, Amsterdam: Elsevier) p, 1989.
- [98] K. Sangwal, J. Torrent-Burgues, F. Sanz, J. Servat, Observations of cleavage steps, slip traces and dislocation hollow cores on cleaved {100} faces of L-arginine phosphate monohydrate single crystals by atomic force microscopy, Surface Science 374(1-3) (1997) 387-396.
- [99] J. Schneibel, L. Martínez, Atomic force microscopy of slip lines in FeAl, Journal of Materials Research 10(9) (1995) 2159-2161.
- [100] D. Veselý, The study of deformation of thin foils of Mo under the electron microscope, Physica Status Solidi (b) 29(2) (1968) 675-683.

- [101] D. Veselý, The study of slip bands on the surface of Mo single crystals, Physica Status Solidi (b) 29(2) (1968) 685-696.
- [102] A. Luft, L. Kaun, A detailed investigation of slip line pattern and subsurface dislocation structure of molybdenum single crystals, Physica Status Solidi (a) 18(1) (1973) 109-122.
- [103] D. Bowen, J. Christian, G. Taylor, Deformation properties of niobium single crystals, Canadian Journal of Physics 45(2) (1967) 903-938.
- [104] M. Duesbery, R. Foxall, A detailed study of the deformation of high purity niobium single crystals, Philosophical Magazine 20(166) (1969) 719-751.
- [105] U. Kocks, R. Maddin, Observations on the deformation of niobium, Acta Metallurgica 4(1) (1956) 91-92.
- [106] A. Mapar, T. Bieler, C. Compton, D. Kang, F. Pourboghrat, Crystal plasticity modeling of single crystal Nb, 17th International Conference on RF Superconductivity (SRF2015), Whistler, BC, Canada, Sept. 13-18, 2015, JACOW, Geneva, Switzerland, 2015, pp. 228-232.
- [107] K.Y. Xie, S. Shrestha, Y. Cao, P.J. Felfer, Y. Wang, X. Liao, J.M. Cairney, S.P. Ringer, The effect of pre-existing defects on the strength and deformation behavior of α -Fe nanopillars, Acta Materialia 61(2) (2013) 439-452.
- [108] S. Papanikolaou, D.M. Dimiduk, W. Choi, J.P. Sethna, M.D. Uchic, C.F. Woodward, S. Zapperi, Quasi-periodic events in crystal plasticity and the self-organized avalanche oscillator, Nature 490(7421) (2012) 517-521.
- [109] N. Friedman, A.T. Jennings, G. Tsekenis, J.-Y. Kim, M. Tao, J.T. Uhl, J.R. Greer, K.A. Dahmen, Statistics of dislocation slip avalanches in nanosized single crystals show tuned critical behavior predicted by a simple mean field model, Physical Review Letters 109(9) (2012) 095507.
- [110] J. Stiegler, C. Dubose, R. Reed, C. McHargue, Dislocations in deformed and annealed niobium single crystals, Acta Metallurgica 11(8) (1963) 851-860.
- [111] S. Ikeno, E. Furubayashi, Behavior of dislocations in niobium under stress, Physica Status Solidi (a) 12(2) (1972) 611-622.
- [112] S. Thompson, P. Flewitt, The defect structure and superconducting transition of cold-worked niobium, Journal of the Less Common Metals 40(3) (1975) 269-283.
- [113] C. Chang, C. Chen, Observations on interactions of glissile dislocations in niobium by transmission electron microscopy, Physica Status Solidi (a) 39(2) (1977) 549-560.
- [114] M.A. Crimp, Scanning electron microscopy imaging of dislocations in bulk materials, using electron channeling contrast, Microscopy research and technique 69(5) (2006) 374-381.

- [115] T. Ruggles, D. Fullwood, Estimations of bulk geometrically necessary dislocation density using high resolution EBSD, Ultramicroscopy 133 (2013) 8-15.
- [116] A. Wilkinson, E. Clarke, T. Britton, P. Littlewood, P. Karamched, High-resolution electron backscatter diffraction: an emerging tool for studying local deformation, The Journal of Strain Analysis for Engineering Design 45(5) (2010) 365-376.
- [117] A.J. Wilkinson, G. Meaden, D.J. Dingley, High resolution mapping of strains and rotations using electron backscatter diffraction, Materials Science and Technology 22(11) (2006) 1271-1278.
- [118] A.J. Wilkinson, G. Meaden, D.J. Dingley, High-resolution elastic strain measurement from electron backscatter diffraction patterns: new levels of sensitivity, Ultramicroscopy 106(4-5) (2006) 307-313.
- [119] B.E. Dunlap, T.J. Ruggles, D.T. Fullwood, B. Jackson, M.A. Crimp, Comparison of dislocation characterization by electron channeling contrast imaging and cross-correlation electron backscattered diffraction, Ultramicroscopy 184 (2018) 125-133.
- [120] J. Jiang, T. Britton, A. Wilkinson, Measurement of geometrically necessary dislocation density with high resolution electron backscatter diffraction: effects of detector binning and step size, Ultramicroscopy 125 (2013) 1-9.
- [121] T. Ruggles, T. Rampton, A. Khosravani, D. Fullwood, The effect of length scale on the determination of geometrically necessary dislocations via EBSD continuum dislocation microscopy, Ultramicroscopy 164 (2016) 1-10.
- [122] D. Kang, D.C. Baars, T.R. Bieler, C.C. Compton, Characterization of large grain Nb ingot microstructure using EBSP mapping and Laue camera methods, AIP Conference Proceedings, AIP, 2011, pp. 90-99.
- [123] D. Kang, D. Baars, T. Bieler, G. Ciovati, C. Compton, T. Grimm, A. Kolka, Characterization of large grain Nb ingot microstructure using OIM and Laue methods, Thomas Jefferson National Accelerator Facility, Newport News, VA (United States), 2011.
- [124] A.J. Schwartz, M. Kumar, B.L. Adams, D.P. Field, Electron backscatter diffraction in materials science, Springer 2009.
- [125] B.D. Cullity, J.W. Weymouth, Elements of X-ray Diffraction, American Journal of Physics 25(6) (1957) 394-395.
- [126] D. Kang, T. Bieler, C. Compton, Effects of processing history on the evolution of surface damage layer and dislocation substructure in large grain niobium cavities, Physical Review Special Topics-Accelerators and Beams 18(12) (2015) 123501.

- [127] D. Kang, T. Bieler, C. Compton, Surface damage and effects of heat treatment on large grain Nb cavities, Proceedings of the SRF2013, Paris (2013) 455-460.
- [128] D. Zipperian, Silicon carbide abrasive grinding, Quality Matters Newsletter 1(2) (2002) 1-3.
- [129] S.I. Wright, M.M. Nowell, EBSD image quality mapping, Microscopy Microanalysis 12(1) (2006) 72-84.
- [130] D. Kang, D. Baars, A. Mapar, T. Bieler, F. Pourboghrat, C. Compton, Study of slip and deformation in high purity single crystal Nb for accelerator cavities, 17th International Conference on RF Superconductivity (SRF2015), Whistler, BC, Canada, Sept. 13-18, 2015, JACOW, Geneva, Switzerland, 2015, pp. 191-195.
- [131] H. Li, Analysis of the deformation behavior of the hexagonal close-packed alpha phase in titanium and titanium alloys, Ph.D. dissertation, Michigan State University 2013.
- [132] Brigham Young University, OpenXY, 2018, https://github.com/BYU-MicrostructureOfMaterials/OpenXY.
- [133] E. Kroener, Continuum theory of dislocation and self-stresses, FLORIDA UNIV GAINESVILLE COLL OF ENGINEERING, 1971.
- [134] S. Sun, B. Adams, W. King, Observations of lattice curvature near the interface of a deformed aluminium bicrystal, Philosophical Magazine A 80(1) (2000) 9-25.
- [135] B.L. Adams, Orientation imaging microscopy: emerging and future applications, Ultramicroscopy 67(1-4) (1997) 11-17.
- [136] J. Nye, Some geometrical relations in dislocated crystals, Acta Metallurgica 1(2) (1953) 153-162.
- [137] H. Grimmer, W.t. Bollmann, D. Warrington, Coincidence-site lattices and complete pattern-shift in cubic crystals, Acta Crystallographica Section A: Crystal Physics, Diffraction, Theoretical and General Crystallography 30(2) (1974) 197-207.
- [138] S. Ranganathan, On the geometry of coincidence-site lattices, Acta Crystallographica 21(2) (1966) 197-199.
- [139] T.R. Bieler, D. Kang, M. Zhao, C. Compton, Materials quality testing for FRIB, Talk at FRIB, 2016.
- [140] T.R. Bieler, BCC orientation analysis-TSL, MATLAB code, 2010.
- [141] A. Seeger, W. Wasserbäch, Anomalous slip—a feature of high-purity body-centred cubic metals, Physica Status Solidi (a) 189(1) (2002) 27-50.

- [142] J. Mackenzie, Second paper on statistics associated with the random disorientation of cubes, Biometrika 45(1-2) (1958) 229-240.
- [143] W. Kurz, D.J. Fisher, Fundamentals of solidification, (1989).
- [144] S. Tang, Z. Wang, Y. Guo, J. Wang, Y. Yu, Y. Zhou, Orientation selection process during the early stage of cubic dendrite growth: A phase-field crystal study, Acta Materialia 60(15) (2012) 5501-5507.
- [145] D. Baars, H. Jiang, T. Bieler, C. Compton, P. Bauer, T. Grimm, Crystal orientations near welds in high RRR niobium with very large grains, IEEE Transactions on Applied Superconductivity 17(2) (2007) 1295-1298.
- [146] E. Hall, Yield point phenomena in metals and alloys, Springer Science & Business Media 2012.
- [147] M. Johnson, Private communication, FRIB, 2014.
- [148] D. Baars, H. Jiang, T. Bieler, A. Zamirit, F. Pourboghrat, C. Compton, Effects of elastic modulus on deformation and recrystallization of high purity Nb, Applications of Texture Analysis (2008) 391-398.
- [149] T.R. Bieler, D. Kang, D.C. Baars, S. Chandrasekaran, A. Mapar, G. Ciovati, N.T. Wright, F. Pourboghrat, J.E. Murphy, C.C. Compton, Deformation mechanisms, defects, heat treatment, and thermal conductivity in large grain niobium, AIP Conference Proceedings, AIP Publishing, 2015, p. 020002.
- [150] X. Zhao, G. Ciovati, T.R. Bieler, Characterization of etch pits found on a large-grain bulk niobium superconducting radio-frequency resonant cavity, Physical Review Special Topics Accelerators and Beams 13(12) (2010).
- [151] G. Ciovati et al., Unpublished work, 2011.
- [152] A. Mapar, T. Bieler, F. Pourboghrat, C. Compton, Dynamic hardening rule; a generalization of the classical hardening rule for crystal plasticity, 16th Int. Conf. RF Supercond. Paris, France, 2013.
- [153] M. Wang, D. Kang, T. Bieler, Direct observation of dislocation structure evolution in SRF cavity niobium using electron channeling contrast imaging, Journal of Applied Physics 124(15) (2018) 155105.